



UNIVERSITÉ CATHOLIQUE DE LOUVAIN  
LABORATOIRE D'HYPERFRÉQUENCES

*Louvain-la-Neuve*



ROYAL MILITARY ACADEMY  
DEPARTMENT OF ELECTRICAL ENGINEERING  
AND TELECOMMUNICATION

*Brussels*

**Ultra-Wideband Ground Penetrating Radar,  
with Application to the Detection of Anti Personnel  
Landmines**

**Jury**

Prof. P. Sobieski (ELEC), président  
Prof. A. Vander Vorst (EMIC), promoteur  
Prof. M. Acheroy (RMA), co-promoteur  
Prof. D. Vanhoenacker-Janvier (EMIC)  
Prof. M. Piette (RMA)  
Prof. L. P. Ligthart (TU Delft, NL)

**Bart SCHEERS**

*Thèse présentée en vue de  
l'obtention du grade de  
docteur en Sciences Appliquées*

Mars 2001

# Contents

<b>Preface .....</b>	<b>1</b>
List of publications .....	11
<b>Chapter 1. Introduction .....</b>	<b>1-1</b>
<b>Chapter 2. Ground Penetrating Radar.....</b>	<b>2-1</b>
2.1. Brief historical overview .....	2-1
2.2. GPR principles.....	2-2
2.2.1. General .....	2-2
2.2.2. Different types of GPR systems .....	2-7
2.2.3. Propagation in lossy dielectric material .....	2-12
2.2.4. Impulse GPR design parameters .....	2-22
2.3. GPR in demining applications .....	2-35
2.3.1. State of the art.....	2-35
2.3.2. Field trials and conclusions .....	2-37
2.4. Summary.....	2-41
<b>Chapter 3. Development of UWB GPR antennas .....</b>	<b>3-1</b>
3.1. Introduction.....	3-1
3.2. Overview of existing GPR antennas.....	3-2
3.2.1. Conventional antennas.....	3-2
3.2.2. Non-dispersive Ultra-wideband antennas.....	3-6
3.3. GPR antenna design goals for the demining application.....	3-8
3.4. Air-filled TEM horn.....	3-9

3.4.1. TEM horn antennas .....	3-9
3.4.2. Study of the wire Model.....	3-14
3.4.3. Design of air-filled TEM horn.....	3-25
3.5. Dielectric-filled TEM horn .....	3-29
3.5.1. Influence of the filling .....	3-29
3.5.2. Design of the dielectric-filled TEM horn.....	3-32
3.5.3. Results of the dielectric-filled TEM horn.....	3-35
3.6. Summary.....	3-37

**Chapter 4. Time domain characterisation of antennas by normalised impulse response..... 4-1**

4.1. Introduction.....	4-1
4.2. Definitions of terms .....	4-2
4.2.1. Impulse response and frequency response function.....	4-2
4.2.2. Virtual source of a time domain antenna .....	4-3
4.2.3. The far field for time domain antennas .....	4-4
4.2.4. Electrical boresight.....	4-5
4.2.5. Definition of patterns for time domain antennas .....	4-6
4.3. Time domain antenna equations .....	4-7
4.3.1. Transmitting antenna .....	4-8
4.3.2. Receiving antenna.....	4-10
4.3.3. Reciprocity of time domain antennas .....	4-11
4.4. Normalised impulse response .....	4-12
4.4.1. Normalisation of the IR .....	4-12
4.4.2. Measurement of Normalised IR on boresight.....	4-14
4.4.3. Normalised IR off-boresight.....	4-17
4.4.4. Relation between gain and normalised IR.....	4-20
4.5. Results on TEM horns .....	4-21
4.6. Time domain simulations .....	4-24
4.7. Summary.....	4-28

<b>Chapter 5. Modelling of the GPR radar range equation in the time domain.....</b>	<b>5-1</b>
5.1. Introduction.....	5-1
5.2. Radar range equation.....	5-2
5.3. GPR range equation.....	5-3
5.4. Radar range equation in the time domain.....	5-5
5.5. GPR range equation in the time domain.....	5-9
5.6. Calculation of the different terms in the time domain GPR range equation.....	5-10
5.6.1. Transmission coefficients on the air-ground interface .....	5-10
5.6.2. Total path length in the air and in the ground.....	5-13
5.6.3. Ground as a low-pass filter.....	5-15
5.6.4. Impulse Response of objects .....	5-18
5.7. Summary.....	5-27
<b>Chapter 6. Study of the UWB GPR.....</b>	<b>6-1</b>
6.1. Introduction.....	6-1
6.2. General description of the system.....	6-1
6.3. Study of the antenna configuration.....	6-8
6.3.1. Height above the ground.....	6-8
6.3.2. Antenna Coupling.....	6-10
6.3.3. The 3 dB footprint of the antennas .....	6-12
6.3.4. Optimisation of the antenna off-set angle .....	6-13
6.4. Study of the range performance.....	6-17
6.5. Experimental results .....	6-23
6.5.1. Acquisition software.....	6-23
6.5.2. Results .....	6-24
6.6. Summary.....	6-26
<b>Chapter 7. UWB Signal processing .....</b>	<b>7-1</b>
7.1. Introduction.....	7-1
7.2. A-scans processing .....	7-3
7.2.1. Overview of A-scan processing.....	7-3

7.2.2. UWB signal processing on A-scans .....	7-10
7.3. Migration .....	7-15
7.3.1. General .....	7-15
7.3.2. Exploding source model .....	7-17
7.3.3. Overview of existing migration methods .....	7-19
7.4. Migration by deconvolution.....	7-25
7.4.1. Development of the method .....	7-26
7.4.2. Implementation of the migration method .....	7-30
7.4.3. Discussion.....	7-32
7.4.4. Results of the migration method.....	7-39
7.5. Summary.....	7-50
<b>Chapter 8. Conclusions and future work .....</b>	<b>8-1</b>
8.1. Conclusions.....	8-1
8.1.1. UWB antennas.....	8-2
8.1.2. Time domain modelling of the GPR.....	8-3
8.1.3. Migration.....	8-5
8.2. Conclusions on the use of a UWB GPR as a mine detector .....	8-5
8.3. Future work.....	8-6
<b>Appendix A. Measurement of short pulse response and frequency response function of non-canonical 3D objects .....</b>	<b>A-1</b>
A.1. Measurement set-up .....	A-1
A.2. Measurement of the FRF of 3D objects by dual channel analysis.....	A-2
A.3. Measurement results on Teflon cylinders and AP mines in free space .....	A-5
A.4. Discussion.....	A-8
<b>Appendix B. Kirchhoff and Stolt migration.....</b>	<b>B-1</b>
B.1. Kirchhoff migration .....	B-1
B.2. Stolt migration.....	B-5

---

## Preface

---

### *Overview of the world-wide landmine problem*

On the first of September 1999, the ‘Ottawa Convention’ on the prohibition of the use, stockpiling, production and transfer of Anti Personnel Landmines, and on their destruction, has been signed by 135 and ratified by 84 states world-wide. Thereof, 14 EU Members States have signed and 13 ratified. Meanwhile the awful consequences of the Anti Personnel mines contamination must still be overcome. Today, about 60 million of uncleared anti personnel mines (AP mines) and anti tank mines (AT mines) can be found in more than 60 countries. It was previously estimated that as many as 110 million landmines were scattered in 64 countries. Those numbers were based on the limited information available in national archives and military records. In 1998, a growing consensus in the international community was formed that the number may be lower. New calculations, based on a more rigorous counting of the number of landmines in 12 severely effected countries, has led to a new estimation of the number of landmines in the region of 60-70 million. A good overview of the world-wide landmine problem and the Ottawa Convention can be found in [1] and [2]. Table 1 contains an overview of the best estimation of the numbers of landmines in the 10 countries with the highest number of casualties (source: [1]).

Country	Number of mines	
	Low estimation	High estimation
Bosnia-Herzegovina	600 000	1 000 000
Croatia	400 000	400 000
Afghanistan	5 000 000	7 000 000
Iraq	10 000 000	10 000 000
Cambodia	4 000 000	6 000 000
Somalia	1 000 000	1 000 000
Mozambique	1 000 000	1 000 000
Angola	6 000 000	15 000 000
Eritrea	500 000	1 000 000
Sudan	1 000 000	1 000 000
<b>TOTAL</b>	<b>29 635 000</b>	<b>43 535 000</b>

Table 1: Best estimation of the numbers of landmines in the 10 countries with the highest number of casualties

The map in Fig.1 shows the world distribution of the problem. This map also represents countries suffering from an UneXploded Ordnance (UXO) problem, which explains the presence of for instance Belgium and Germany. Attention must be drawn on the fact that most of the polluted developing countries are not landmine producers. The opposite is also true, most of the producing countries are not suffering from a landmine problem themselves.

More important than the actual numbers, however, is the far-reaching impact of the landmines on the people living in those affected countries. It has been estimated, that every year more than 26.000 persons are killed (about one person every 20 minutes). In Cambodia, for example, the estimated number of amputee's is 36.000, which is, in other words, 1 amputee for every 236 citizens.

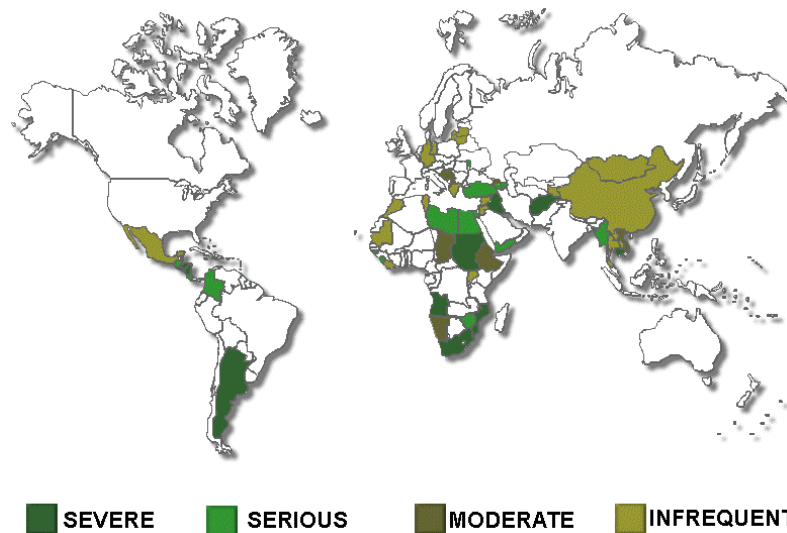


Fig.1: World-wide distribution of the landmines and UXO problem

The presence of landmines not only directly affects people's health, but has also a negative influence on the economic life of the country, by preventing access to precious rural land and other resources. Without mines, agriculture production could increase by 88-200% in Afghanistan, 11% in Bosnia and 135% in Cambodia (source: [1]).

So it is clear that, even if the 'Ottawa Convention' can prevent new mines to be laid, there is a real and even more challenging problem to be solved: the reduction of landmine contaminated areas and the assistance to mine victims. One aspect in this challenge is the detection, identification and clearance of landmines, called humanitarian demining.

Humanitarian demining differs from military mine clearance operations in many aspects. The military mine clearance as applied in conflict situations accepts low rates of clearance efficiency and a higher rate of casualties. For these purposes it is often sufficient to punch a path through a minefield. The costs of these kinds of operations is usually not an issue, time is. For the humanitarian demining purposes, on the contrary, a high clearance efficiency is required (99.6% is required by UN). This can until now only be achieved using the hand clearing method. Also the cost of the clearance operation and the safety of the deminers becomes important. In this work, only humanitarian demining will be considered.

### ***Humanitarian demining today***

In present-day situations the classical humanitarian demining is done using metal detectors and prodding sticks, to manually detect and clear the mines. The demining procedure varies in function of the mine clearance scenario, depending on the climate, the type of vegetation, the variety of mines, etc. The procedure as applied in Cambodia by the bomb disposal unit (EOD) of the Belgian Army is as follows: The deminers work in groups of two and in corridors of 1m large. In a first stage deminer number 2 is on stand-by at a safety distance behind deminer 1. Deminer 1 starts with the execution of the tripwire drill, using a long stick. He will lift the stick up and look for wires. When there is no danger he cuts the vegetation. Deminer 1 will then step back and the demining process is proceeded by deminer 2. Deminer 2 manually scans with a metal detector an area of one meter large and 50 cm deep. When no signal is given, the zone is declared mine free and the procedure will start all over again. If there is a signal, deminer 2 will try to localise and mark the exact position of the signal. Deminer 2 will then step back and deminer 1 comes in again. He will probe the marked area, *i.e.* finding the object by sticking a dagger every 2 cm carefully in the ground and gently remove the topsoil from the suspicious object (Fig.2). This way the exclusion is made between a false target (false alarm) and a mine, and if it is a mine, its actual position and circumference is determined. The process is continued by excavating carefully the ground around the mine and by marking it with a red 'mine-danger' tetrahedron. The lane is now closed and the two deminers will continue on another lane. At the end of the day the explosion team will destroy all the detected mines *in situ*, to make sure the mines will not enter in circulation again.

A platoon of 30 well-trained deminers is able to demine approximately between 500 and 2500 m<sup>2</sup> a day. This method has not been changed since the Second World War.



Fig.2: Deminer prodding and gently removing the topsoil

The manual demining procedure is very time consuming and not without danger. Hence, manual demining is extremely costly. It has been estimated that an average of 1000 US \$ is needed for a manual demining of the 10 US \$ mine. The reason for it is the high false alarm rate of the metal detector. For each piece of metal detected by the metal detector, the procedure with the first deminer is initiated. Minefields are often situated in post conflict areas where the contamination with metal can be very high (grenade fragments, cartridges, etc.). Typical values are 100 false alarms for 1 real mine. There is an obvious need for a more efficient portable demining device in order to achieve a more cost-effective demining process.

### ***Mine detector requirements***

An ideal portable mine detector must meet severe user requirements. Some of these user requirements are listed below. The detector must:

1. Detect metal as well as plastic mines with very low metal content
2. Detect anti-tank and anti-personnel mines
3. Meet the UN-norm safety requirement of 99.6% clearance efficiency
4. Detect mines in all kinds of soils
5. Detect mines from 0 cm (surface laid) up to a of depth of 20 cm
6. Work on rough, vegetation overwhelmed terrain

7. Work in all seasons, in all climatic conditions
8. be able to operate 8 hours a day, 250 days a year
9. for safety reasons be held some cm above the ground
10. be light weighted
11. be reliable ( mean time between failure of at least 1000 hours and a reliable self test)
12. not interfere with other sensors when used within 10 m from each other
13. easy to maintain
14. be simple to use (for local people, having a minimum of special training)
15. have a reasonable false alarm rate, in the order of 20 to 1.

The only technique that does meet almost all of these requirements (except requirement 15) is the combination of the metal detector and the prodding stick, but, as already mentioned, this method is too slow and not without risk.

The demining community is well aware of this problem and of the lack of good alternative mine detectors. Therefore, there is a call from the demining community towards the scientific world to contribute in solving this world-wide problem by looking to new and better demining techniques.

Table 2 lists some sensor types, together with their advantages and disadvantages, which are potential techniques for the demining application. At the moment, none of these sensors meet all of the user requirements and probably never will, at least not without limiting the number of demining scenarios.

<b>Sensor type</b>	<b>Advantages</b>	<b>Disadvantages</b>
<i>metal detector</i>	<ul style="list-style-type: none"> <li>• has proven its usability in most conditions</li> </ul>	<ul style="list-style-type: none"> <li>• High false alarm rate</li> <li>• can not detect pure plastic mines</li> <li>• limited sensitivity in ferruginous soils.</li> </ul>
<i>conventional ground penetrating radar</i>	<ul style="list-style-type: none"> <li>• good for locating and depth estimation</li> <li>• can detect non-metallic objects</li> </ul>	<ul style="list-style-type: none"> <li>• limited depth resolution</li> <li>• poor object classification</li> </ul>
<i>ultra-wideband ground penetrating radar</i>	<ul style="list-style-type: none"> <li>• Good depth resolution and better object classification</li> </ul>	<ul style="list-style-type: none"> <li>• poor penetration in very wet conditions and in clayey soils.</li> </ul>
<i>microwave radiometer</i>	<ul style="list-style-type: none"> <li>• Good resolution and object classification</li> </ul>	<ul style="list-style-type: none"> <li>• poor penetration in very wet conditions and in clayey soils.</li> <li>• sensitive to external noise sources</li> </ul>
<i>IR 3-5 and 8-12 <math>\mu</math>m-band</i>	<ul style="list-style-type: none"> <li>• good object recognition</li> </ul>	<ul style="list-style-type: none"> <li>• need of thermal contrast</li> <li>• only for shallow buried and surface laid mines</li> </ul>
<i>Polarimetric IR</i>	<ul style="list-style-type: none"> <li>• discrimination between natural and man-made objects</li> </ul>	<ul style="list-style-type: none"> <li>• only surface laid mines</li> </ul>
<i>Multi-spectral imager</i>	<ul style="list-style-type: none"> <li>• good object recognition</li> </ul>	<ul style="list-style-type: none"> <li>• only for surface laid mines</li> </ul>
<i>x-ray diffraction and neutron bombardment</i>	<ul style="list-style-type: none"> <li>• searches only for explosives</li> <li>• good explosive classification</li> </ul>	<ul style="list-style-type: none"> <li>• High power consumption</li> <li>• can be hazardous for the deminers health.</li> </ul>
<i>nuclear quadrupole resonance</i>	<ul style="list-style-type: none"> <li>• searches only for explosives</li> <li>• good explosive classification</li> </ul>	<ul style="list-style-type: none"> <li>• High power consumption</li> <li>• sensitive to external noise sources</li> </ul>
<i>biosensors (dogs, rats,..)</i>	<ul style="list-style-type: none"> <li>• can smell the presence of buried explosives at the surface</li> </ul>	<ul style="list-style-type: none"> <li>• long training</li> <li>• only operational for a limited period during the day</li> </ul>
<i>Mechanical deminer</i>	<ul style="list-style-type: none"> <li>• fast in clearing roads and flat areas</li> </ul>	<ul style="list-style-type: none"> <li>• heavy</li> <li>• too low clearance efficiency (&lt;80%)</li> <li>• Can not reach all terrain</li> </ul>

Table 2: Promising techniques for demining

A more schematic approach to the problem can be found by representing the Receiver Operating Characteristic (ROC) of the mine detector. For a given scenario, each mine detector is characterised by its ROC, representing the detection probability ( $p_d$ ) of the detector as a function of the probability of false alarm ( $p_{fa}$ ). A typical ROC of a metal detector is represented in fig. 3, curve A. The region in which the detector operates is close to  $p_d=1$ . What is needed for a more cost-effective mine clearance, is to obtain for a given probability of detection a lower probability of false alarm, such as represented by curve B. Such an improvement can be achieved in two ways: first it is always possible to enhance existing sensors or to investigate new sensor techniques. Secondly an improvement can be found in fusing the data of different sensors. It is commonly accepted by the research community that data fusion will be indispensable if all of the user requirements must be satisfied in all demining scenarios.

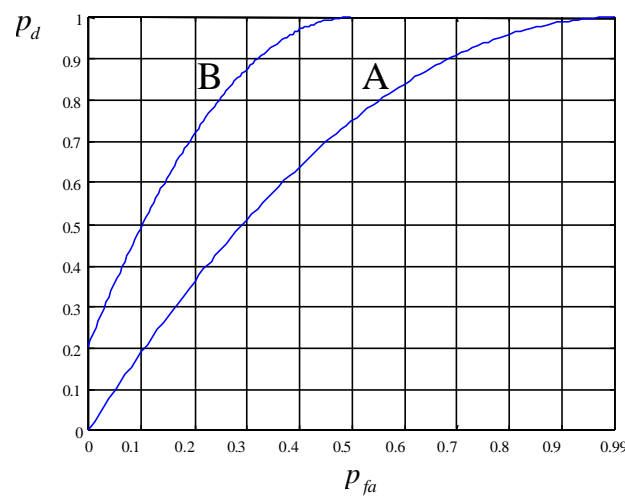


Fig. 3: Typical receiver operating characteristic of a detector

From the mid 90's, several research groups supported by national and international programs have concentrated their work on the humanitarian demining. In 1998, for example, the European Union has committed more than 16.7 M EURO to support research and development of enhanced mine detection systems [3]. The Belgian government has also taken its responsibility in this matter, resulting in a project called "HUDEM".

***The HUDEM project***

Late 1996, a Belgian project on humanitarian demining (HUDEM) has been initiated by the Belgian Ministry of Defence and is supported by the Belgian Ministry of Defence and the Belgian State Secretariat for Development Aid [4]. It is carried out in collaboration with laboratories of other Belgian universities, *i.e.* the ‘Facultés universitaires Notre-Dame de la Paix’ (FUNDP), the ‘Katholieke Universiteit Leuven’ (KUL), the ‘Universiteit Gent’ (RUG), the ‘Université catholique de Louvain’ (UCL), the ‘Université de Liège’ (ULg), the ‘Université libre de Bruxelles’ (ULB), the ‘Universitaire Instelling Antwerpen’ (UIA) and the ‘Vrije Universiteit Brussel’ (VUB), and it is co-ordinated by the Royal Military Academy (RMA). The research project aims at contributing in solving the anti personnel landmine problem by funding research grants devoted to basic research on mine detection. Research is focussed on increasing the knowledge on sensors and on sensor/ground characteristics, on designing new sensors or tuning old ones and on processing the data produced by sensors. Furthermore, it considers the detection as a global process wherein the outputs of the sensors, considered as skilled specialists, are integrated in a fusion operation. There is also a group working on a realistic design of a rough terrain robot for a platform mounted system.

From the list of promising sensors in table 2, only a limited number is addressed in the scope of the project. The work performed on the ultra-wideband (UWB) ground penetrating radar as a possible demining sensor is reported in this thesis. It has to be clear that, in accordance with the philosophy of the project, the intention of this work is not to produce a ready-to-use mine detector. The work consists in a contribution to one type of sensor, the UWB GPR. In some parts of the work a feasibility study will be done, in other parts the advantages and shortcomings of the sensor will be shown, as to help industrial designers in the development of this kind of sensor for the demining application.

## REFERENCES

- [1] U.S. Department of State, *Hidden Killer 1998 : The Global Landmine Crisis*. Washington D.C., USA, 1998.  
[http://www.state.gov/www/global/arms/rpt\\_9809\\_demine\\_toc.html](http://www.state.gov/www/global/arms/rpt_9809_demine_toc.html)
- [2] International Campaign to Ban Landmines, *Landmine Monitor Report 1999*. USA, April 1999.  
<http://www.hrw.org/reports/1999/landmine/>
- [3] Commission of the European Communities, *Action against Anti Personnel Landmines : Reinforcing the Contribution of the European Union*, Communication from the Commission to the European Parliament and the Council.
- [4] M. Acheroy, M. Piette, Y. Baudoin and J.-P. Salmon, “Belgian Project on Humanitarian Demining (HUDEM), Sensor Design and Signal Processing Aspects,” HUDEM Symposium, Brussels, BE, April 1999.



# List of publications

## Journal papers

B. Scheers, "Ground penetrating radar for antipersonnel mine detection," *Revue HF*, no. 3, pp. 25-33, 1998.

B. Scheers, M. Acheroy and A. Vander Vorst, "Time domain simulation and characterisation of TEM horns using normalised impulse response," *IEE Proceedings - Microwaves, Antennas and Propagation*, vol. 147, no. 6, pp. 463-468, Dec. 2000.

## Conference papers

B. Scheers and M. Piette, "Short-pulse response of antipersonnel landmines to UWB GPR signals," *Seventh International Conference on Ground Penetrating Radar*, Kansas, USA, pp. 337-341, May 1998.

B. Scheers, M. Piette and A. Vander Vorst, "The detection of AP mines using UWB GPR," *IEE Second International Conference on the Detection of Abandoned Land Mines*, Edinburgh, UK, pp. 50-54, Oct. 1998.

B. Scheers, "Development of a laboratory UWB GPR system for mine detection," *HUDEM Symposium*, Brussels, BE, April 1999.

N. Milisavljevic, B. Scheers, Y. Yvinec and M. Acheroy, "3D visualisation of data acquired by laboratory UWB GPR in the scope of mine detection," *Mine'99, Proc. of EUROCONFERENCE ON: Sensor systems and signal processing techniques applied to the detection of mines and unexploded ordnance*, Florence, IT, pp. 149-154, 1999.

N. Milisavljevic, B. Scheers and Y. Yvinec, "Laboratory UWB GPR for 3D data acquisition and shape extraction of AP landmines," *PHOTOMECH'99-ETE'99*, European Workshop, Hotel Bedford, Liège, BE, pp. 65-70, Nov. 1999.

B. Scheers, M. Piette and A. Vander Vorst, "Development of dielectric-filled TEM horn antennas for UWB GPR," *Millennium Conference on Antennas & Propagation AP-2000*, Davos, Switzerland, vol. II, p. 187, April 2000.

B. Scheers, Y. Plasman, M. Piette, M. Acheroy and A. Vander Vorst, "Laboratory UWB GPR system for landmine detection," *Eight International Conference on Ground Penetrating Radar*, Gold Coast, Australia, pp. 747-752, May 2000.

B. Scheers, M. Acheroy, A. Vander Vorst, "Time domain modelling of UWB GPR and its application on landmine detection", *Proceedings of SPIE, Detection and Remediation Technologies for Mines and Minelike Targets V*, Orlando, USA, vol. 4038 II, pp.1452-1460, Apr. 2000.

### **Poster sessions and presentations at workshops**

N. Milisavljevic, B. Scheers, O. Thonnard and M. Acheroy, "Current contribution of the RMA/SIC to the HUDEM project," Poster for Second International Symposium on Operationalization of remote sensing, ITC Enschede, NL, 1999.

WEU, CEPA 1, "Ground Penetrating Radar for use in Demining," Rome, IT, Jan. 2000.

European Commission, Joint Research Centre, "Research on Demining Technologies," Joint Workshop, Ispra, IT, July 2000.

B. Scheers, M. Acheroy and A. Vander Vorst, "Time modelling and signal processing for UWB GPR in close-in mine detection," EuMW workshop and short courses, WS2, Paris, FR, Oct. 2000.

## **Related projects**

Joint Multi-sensor Mine Signature Measurement Campaign (MsMs). The aim of the project is to provide the researchers and developers with multi-sensor data of mines and objects laid out in different soil types. Therefore, a first measurement campaign was held at the test minefield at the European Commission's Joint Research Centre in Ispra, Italy at the end of 2000. All national research centres were (and still are) invited to participate with the measuring campaign. The multi-sensor data is made freely available through the web.

The author developed for this project a positioning target. The positioning target will be placed in the minefield and is specially designed so that it can be detected by all the sensors (metal detector, GPR, IR camera and microwave radiometer). The positioning target will serve as the basis for the co-registration of the data recorded by different sensors.



---

## Chapter 1. Introduction

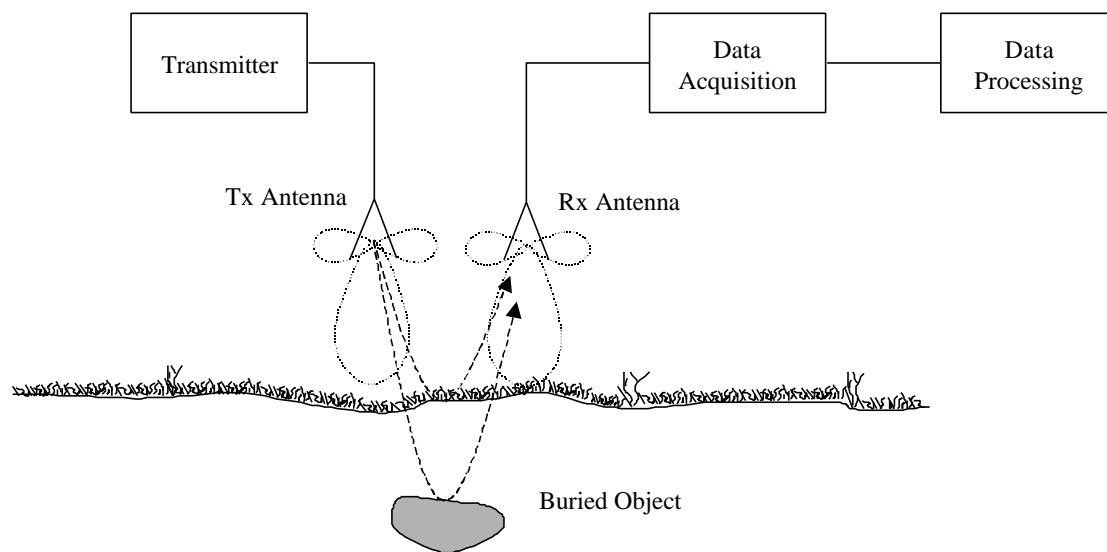
---

Ground Penetrating Radar (GPR) is considered as being one of the most promising technologies for close detection and identification of buried Anti Personnel (AP) Landmines, due to its ability of detecting non-metallic objects in the sub-surface.

Ground Penetrating Radar is the name for the family of radar systems that image the sub-surface. Some authors prefer to speak of Surface Penetrating Radar (SPR) instead of Ground Penetrating Radar, but there is no essential difference between those two terms. Nowadays, Ground Penetrating Radar is a wide used technique and the number of its applications is still growing. Locating pipes and cables, civil engineering (bridge inspection, finding voids), security, archaeology investigation, geophysical survey and ice mapping are a few examples of its use.

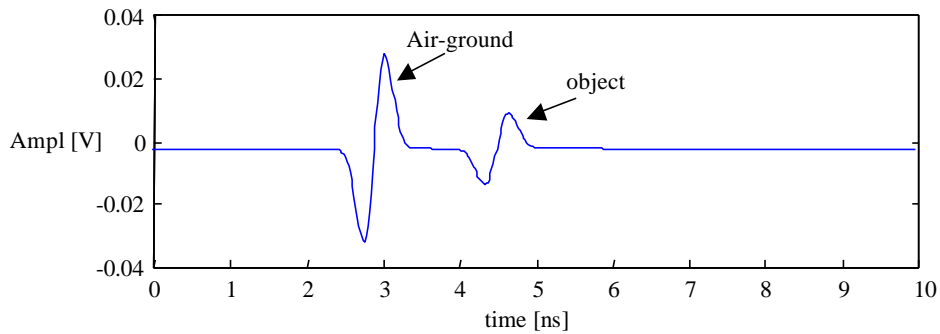
The operating principle of Ground Penetrating Radar is straightforward. A GPR couples EM waves in the ground and samples the backscattered echoes. The EM wave will be backscattered on any electrical parameters contrasts in the ground. The special property of GPR is that it can detect echoes from all three types of electrical parameters contrasts, *i.e.*  $\epsilon_r$ ,  $\mu_r$  and  $\sigma$ . This means that a GPR system has potential for locating and identifying both metallic and non-metallic buried targets on the echo characteristics. The relative permittivity  $\epsilon_r$  of a medium describes the behaviour for electric field propagation; the relative permeability  $\mu_r$  describes the behaviour for magnetic field propagation and  $\sigma$  defines the conductivity. All these three macroscopic parameters are in general function of frequency.

Fig. 1-1 shows a block diagram of a generic GPR system. The antennas are normally scanned over the surface in close proximity to the ground. An EM wave sent into the ground will backscatter on any electrical parameter discontinuity. The backscattered echoes that reach the receiving antenna are sampled and processed by a receiver. GPR systems always use different antennas for transmit and receive functions. The difficulty of using a single antenna arises because there are no sufficiently fast switches available to protect the receiver from the transmitted power.



**Fig. 1-1 :** Ground Penetrating Radar block diagram

Fig. 1-2 shows a typical time representation of a signal, received by the GPR at a given fixed position. The first and normally the largest echo is due to the air-ground interface. Other echoes, appearing later in time are reflections on target or clutter present in the subsurface. Two or three-dimensional images can be produced by moving the antennas on a line or a two dimensional grid.



**Fig. 1-2 :** Typical signal, received by the GPR

The potential of detecting non-metallic targets makes the GPR complementary to a metal detector in the application of AP landmine detection. The additional information on location and other target features could drastically reduce the number of false alarms and thereby speed up the mine clearance. In spite of this promising potential, the use of GPR in real demining operations for the moment is negligible. This is mainly due to four reasons or drawbacks:

1. The first drawback is the limited range resolution. The range resolution of a radar system is defined as “ the ability to distinguish between two targets solely by the measurement of their ranges (distance from the radar); usually expressed in terms of the minimum distance by which two targets of equal strength at the same azimuth and elevation angles must be spaced to be separately distinguishable” (IEEE Std 686-1990). The range resolution (in this case depth resolution) of a GPR is just like in any other radar system directly related to the bandwidth of the system ( $B$ ) and the propagation velocity  $v$  by

$$\Delta R = \frac{v}{2B} \quad (1.1)$$

In most of the conventional GPR systems, the bandwidth is inferior to 1 GHz. Using the quantitative definition (1.1) the depth resolution is limited, depending on the permittivity of the ground, to 9.4 cm for dry soil ( $\epsilon_r = 2.55$ ) and to 3.4 cm for very wet soil ( $\epsilon_r = 20$ ). The depth resolution problem is also illustrated on fig. 1-2. Trace (a), (b) and (c) represent the response of three impulses on one layer. Trace (d), (e) and (f) represent the total response of the same impulses on a two layered structure, with equal reflection amplitude on both layers. In case (d) the

pulse duration is short compared with the two-way travel time between the layers. In case (e) the pulse duration is about equal to the two-way travel time between the layers, which means that the separation  $\Delta d$  between the two layers equals the depth resolution  $\Delta R$  as defined in (1.1). In case (f) the pulse duration is longer than the two-way travel time, and the two layers can not be distinguished in the response.

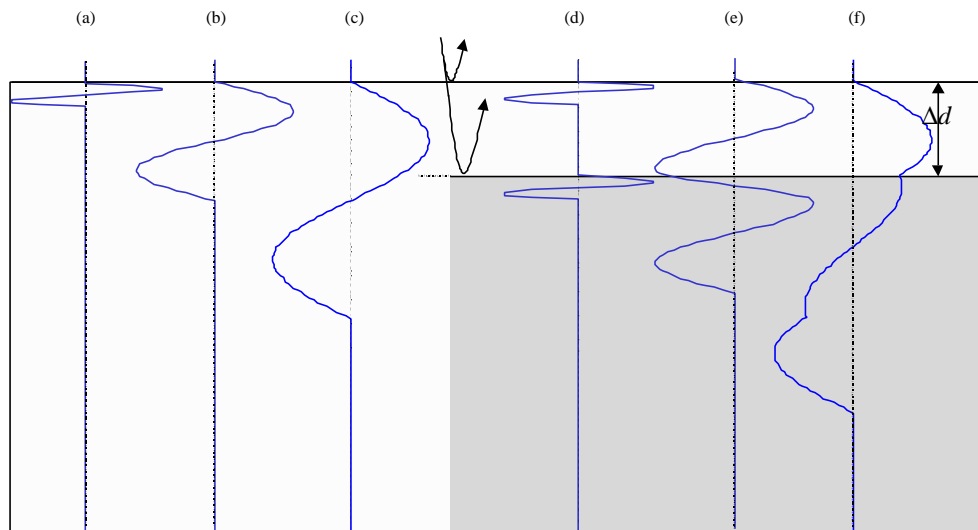


**Fig. 1-3 :** Illustration of the depth resolution problem

As anti personnel landmines are often laid shallow, conventional GPR can have difficulties discriminating the target echoes from the air-ground interface. If the air-ground interface is smooth and flat, simple image processing techniques can enhance the depth resolution. Post-conflict areas however have often a rough surface and are covered with a lot of vegetation. In this case, the performance of these simple image-processing techniques will be insufficient and just more depth resolution is needed, which means larger bandwidth. The choice of the lower and the upper cut-off frequencies of the frequency band is not straightforward. Using an ultra wide-band involves the use of higher frequencies, which are strongly attenuated by the lossy soil. Low frequencies ( $< 1\text{GHz}$ ) on the other hand have a good penetration in the ground, but a poor resolution. So when mines are buried too deep and the frequency band is chosen too high, it is possible that we don't detect anything at all because of the dramatically increased attenuation of the soil with frequency.

2. A second problem with the GPR systems is the ability of discriminating between a mine and a mine-like target. This problem is like the first one related to the frequencies used by the GPR system. The wavelengths radiated by the GPR have the same order of magnitude as the size of the landmines. As a consequence, the backscattering on the mine is very complex and the backscattered signal is a combination of different backscattering mechanisms.

Many authors suggest that there is a lot of information in the late-time response (resonant part) of buried objects to short EM impulses. Looking to the buried mine as a linear system, the larger the bandwidth at the input of the system, the more information one can get on the system. This additional information can be very useful for clutter reduction and/or classification of targets. So again a UWB approach imposes itself.

3. The third drawback concerns the antennas used in commercially available GPR systems. Antennas are a critical point in a GPR system. Most of the GPR systems are designed for applications other than the demining application and the antennas do not meet the specific requirements as needed for this application. The most apparent example is the element antenna. Element antennas, like dipoles, are widely used in GPR systems. Unfortunately they have a low directivity and therefore perform best when they are in contact with the ground, to couple as much energy as possible into the ground. For safety reasons, deminers do not want to use a sensor that is in direct contact with the ground. Further, minefields have often a very rough surface and are covered with a lot of vegetation. So the mobility and hence the dimensions and weight of the antenna become an issue. In the demining application, antennas that can be used off-ground are needed.
4. The last drawback is a more practical one. The output of a GPR is usually an image representing a vertical slice in the subsurface. These images are sometimes difficult to analyse and expert knowledge of the system and the physics behind the operating principle of the system is needed for correct interpretation of the results. In demining operations the deminers are usually not highly educated and they are anyway under too much stress to perform such a complex interpretation.

In this research we want to investigate the feasibility of possible solutions for all of these four drawbacks. It is not our intention to present an enhanced demining tool nor to build a field usable system. The research will not be limited to some hardware aspects of the system nor just to the development of new image processing algorithms, but a more overall system approach is searched for. In this research we will also try to demonstrate that the complete knowledge of the hardware system, which is in fact an *a priori* knowledge, can be used to enhance or tune image processing algorithms. The latter is probably one of the most original parts of the work.

The outline of the work is as follows. In Chapter 2 we will give a general description of the conventional GPR. The history of the GPR, possible applications and the physics behind the operation principle are described. In a second part of the chapter the state of the art in demining applications and field trials with commercially available systems are presented and conclusions are drawn.

In Chapter 3 the development of antennas adapted for the demining application is described. After a short introduction and an overview of existing GPR antennas, we will discuss some design goals for the antennas we need in this application. The design goals are mainly a product of field trials. Further in this chapter the step by step development of TEM horn antennas for UWB GPR will be treated. We will show that the dielectric-filled TEM horn antenna is capable of radiating and receiving very short, but still clean pulses. We also study a model for prediction of antenna impedance and radiated far-field for air-filled and dielectric filled TEM horns.

In Chapter 4 we present a method for characterising the antennas by considering the antenna as a convolution operator. It is always important to select a domain that presents a solution in the easiest and most compact manner. For UWB antennas this domain is the time domain. In this chapter we show how the antennas can be characterised by their normalised impulse response and how this impulse response can be measured. Further we show that this compact way of describing the antennas can be used for simulations and comparing performances of different time domain antennas.

In Chapter 5 we model the whole radar system as a cascade of linear responses, which gives a lot of advantages and possible applications. The study results in an equivalent time domain expression of the radar range equation. The model will also be the basis of the link between the system and the image processing.

At the start of the HUDEM project in 1996, there was no UWB GPR system commercially available. Therefore we decided to develop an indoor laboratory version of an impulse UWB GPR to investigate the feasibility of enhancing the depth resolution and classification rate of UWB systems. In Chapter 6, a detailed description of the UWB GPR is given together with a study of its range performance, using the time domain model from the previous chapter.

In Chapter 7 we give an overview of some possible UWB signal processing techniques and investigate to which extent they can enhance the classification capability of an UWB GPR. Further we investigate some migration techniques. In this chapter we present a novel 3D migration method that takes into account the complete time domain model of the system. We will show that the migration method is able to reconstruct the 3D shape of small targets, in some cases even with the correct dimensions.

Finally some conclusions are drawn and possible future work is suggested.



---

## **Chapter 2. Ground Penetrating Radar**

---

The aim of Chapter 2 is to give an overview of the GPR basic principles and technology. A lot of definitions and often-used terms that will be used throughout the whole work will be explained here. Readers who are familiar with GPR and the demining application can skip parts of this chapter. Section 2.2.4 however can be interesting since a description of the hardware and the design parameters of a time domain GPR are given there. The description is far from complete, but it gives a good overview of the technological difficulties encountered in GPR systems.

### **2.1. Brief historical overview**

The first use of electromagnetic pulses to determine the structure of buried features appeared in 1926 in the work of Hülsenbeck. He noted that any dielectric variation would also produce reflections and that the technique had advantages over seismic methods. The first ground penetrating radar survey to be reported was the determination of the depth of a glacier in 1929 by Stern [1]. Then the technology seemed to have lost interest until the late 1950's. From the beginning of the 1970's a lot of commercial applications using a GPR are mentioned in the literature, for example by Morey [2]. The systems used in that time were exclusively impulse time domain systems. The applications were mainly found in the domain of civil engineering: location of voids, containers, tunnels and rocks, detection of cables and tubes, measuring the thickness of ice and coal layers, probing the profiles of lakes and rivers, etc. From then until today, the range of applications has been growing steadily.

New applications as non-destructive testing, archaeology, roads and tunnel quality assessments, remote sensing, etc. appeared. In 1988, D. J. Daniels, D. J. Gunton and H. F. Scott published a tutorial paper entitled “Introduction to subsurface radar” [3], giving a good overview of the GPR technology at that time. In 1996, D. J. Daniels published his book on surface penetrating radar [4]. Many engineers and researchers who are active in the domain consider the tutorial paper and the book to be reference works. Every two years, an International Conference on GPR is organised. At the last two conferences, in 1998 and 2000, the author presented a paper describing his work (see List of Publications).

## 2.2. GPR principles

### 2.2.1. General

The operating principle of Ground Penetrating Radar is straightforward. A GPR couples EM waves in the ground and samples the backscattered echoes. An EM wave will be backscattered on any electrical parameter contrast in the ground, *i.e.* the permittivity  $\epsilon$ , the permeability  $\mu$  or the conductivity  $\sigma$ . All these three macroscopic parameters are in general a function of frequency. In practice it will be primarily the contrast in permittivity, which leads to a reflection of the radiated EM waves. Earth materials are mostly nonmagnetic materials, having a relative magnetic permeability  $\mu_r = \mu/\mu_0$  of 1, with  $\mu_0 = 4\pi \cdot 10^{-7} \text{ H/m}$  being the permeability of free space. This means that no contrast in permeability will be encountered. The change in conductivity primarily affects absorption of the radar signal by the medium. The variation in permittivity has the largest impact on the variation of the characteristic impedance of the medium (see also Section 2.2.3), so the encountered contrasts in permittivity  $\epsilon$  between materials in the ground will lead to a reflection.

The data recorded by a GPR are generally represented as a one, two or three dimensional dataset, denominated by the acoustic terminology A- B- and C-scans.

**A-scan**

A single waveform  $b(x_i, y_j, t)$  recorded by a GPR, with the antennas at a given fixed position  $(x_i, y_j)$  is referred to as an A-scan (Fig. 2-1). The only variable is the time, which is related to the depth by the propagation velocity of the EM waves in the medium.

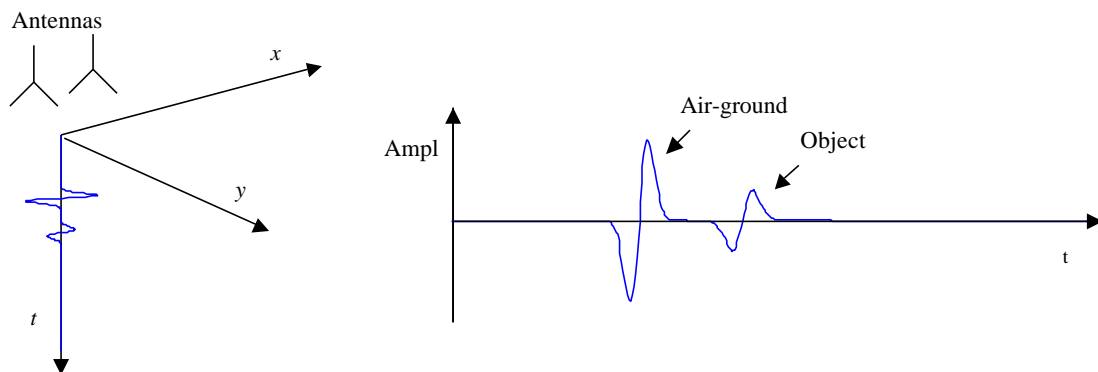


**Fig. 2-1:** Configuration and representation of an A-scan

**B-scan**

When moving the GPR antennas on a line along the x-axis, one can gather a set of A-scans, which form a two dimensional data set  $b(x, y_j, t)$ , called a B-scan (Fig. 2-2 (a)). When the amplitude of the received signal is represented by a colour scale (or grey-scale), a 2D image as shown in Fig. 2-2 (b) is obtained. The 2D image represents a vertical slice in the ground. The time axis or the related depth axis is usually pointed downwards.

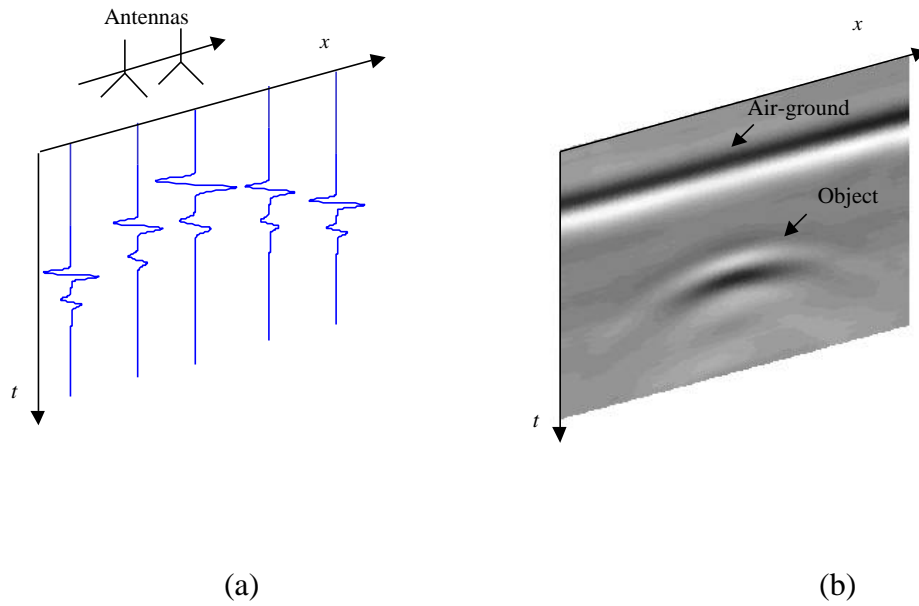


**Fig. 2-2:** (a) Multiple A-scans forming a B-scan

(b) Representation of a B-scan on a grey-scale

Reflections on a point scatterer located below the surface appear, due to the beamwidth of the transmitting and the receiving antenna, as **hyperbolic** structures in a B-scan. This can be easily verified, using the geometry shown in Fig. 2-3 (a). Suppose a homogeneous half-space with a propagation velocity equals  $v$  and the transmitting- and receiving antenna close to each other, so that they can be considered as one antenna ( monostatic case). The co-ordinate system is represented on Fig. 2-3 (a). A point scatterer at a position  $(0, z_0)$  in the half space, will be located by the antenna pair, situated in  $(x,0)$  at a distance  $\sqrt{x^2 + z_0^2}$ . So in the recorded data  $b(x,t)$ , represented in Fig. 2-3 (b), the reflection on the point scatterer appears in each A-scan after a time

$$t = 2\sqrt{x^2 + z_0^2} / v \quad (2.1)$$

Equation (2.1) represents a hyperbola with a vertical axis and an apex in  $(0, 2z_0 / v)$ . The shape of the hyperbola is function of the antenna configuration (monostatic, bi-

static), the depth of the point scatterer  $z_0$  and the propagation velocity profile of the ground. The hyperbolic defocusing of an object can be corrected for in the data processing, this is called migration or SAR processing (see Chapter 7).

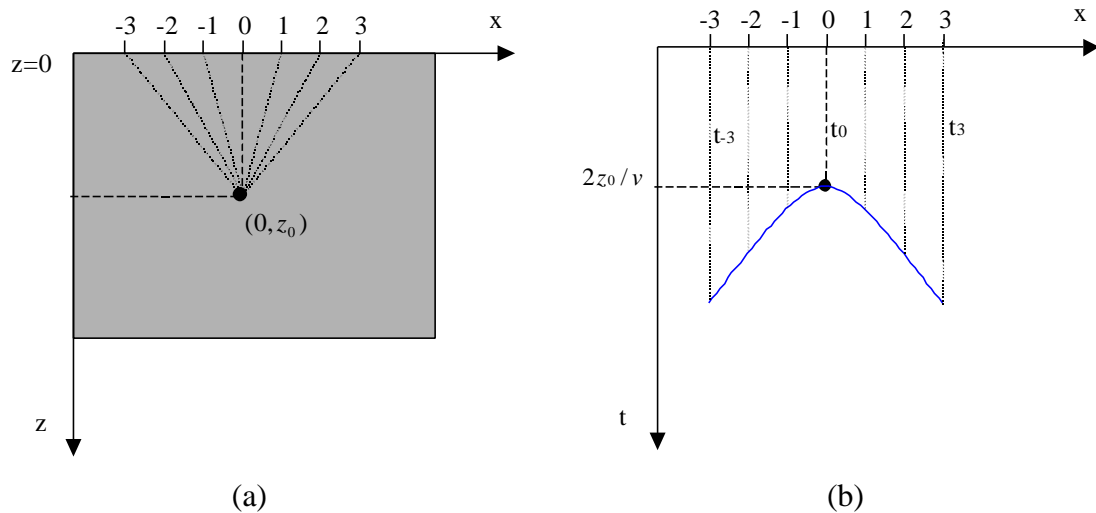


**Fig. 2-3:** (a) Point scatterer at position  $(0, z_0)$ , (b) recorded data  $b(x, t)$

### *C-scan*

Finally, when collecting multiple parallel B-scans or in other words, when moving the antenna over a (regular) grid in the  $xy$ -plane, a three dimensional data set  $b(x, y, t)$  can be recorded, called a C-scan (Fig. 2-4). Usually a C-scan is represented as a two dimensional image by plotting the amplitudes of the recorded data at a given time  $t_i$ . The image  $b(x, y, t_i)$  represents then a horizontal slice at a certain depth, parallel to the recording plane (Fig. 2-5). Nowadays, many user-software packages have integrated functions to plot directly three-dimensional representations of the recorded C-scans. In this case, an arbitrary cut in the 3-D volume (Fig. 2-6 (a)) or an iso-surface (surface with the same amplitude) is usually represented (Fig. 2-6 (b)).

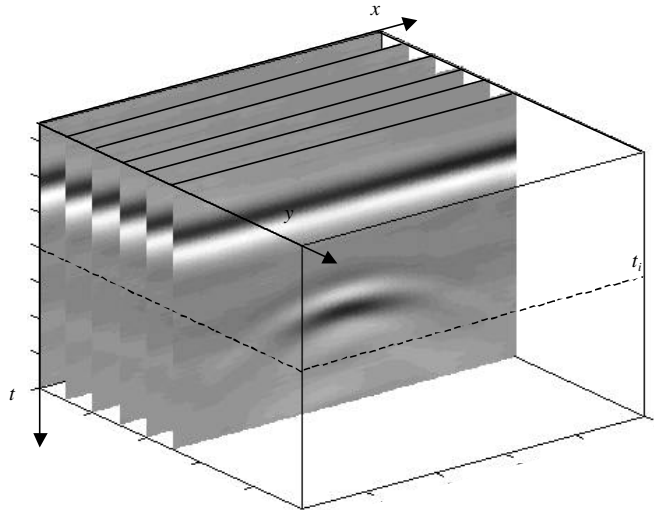


**Fig. 2-4:** Multiple parallel B-scans forming a C-scan

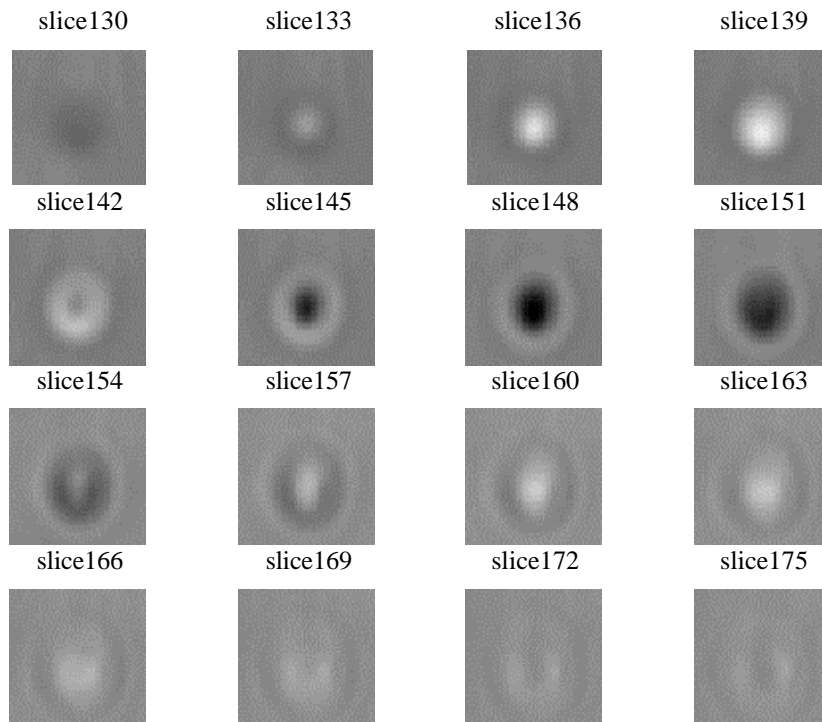


**Fig. 2-5:** Representation of a C-scan by horizontal slices at different depths

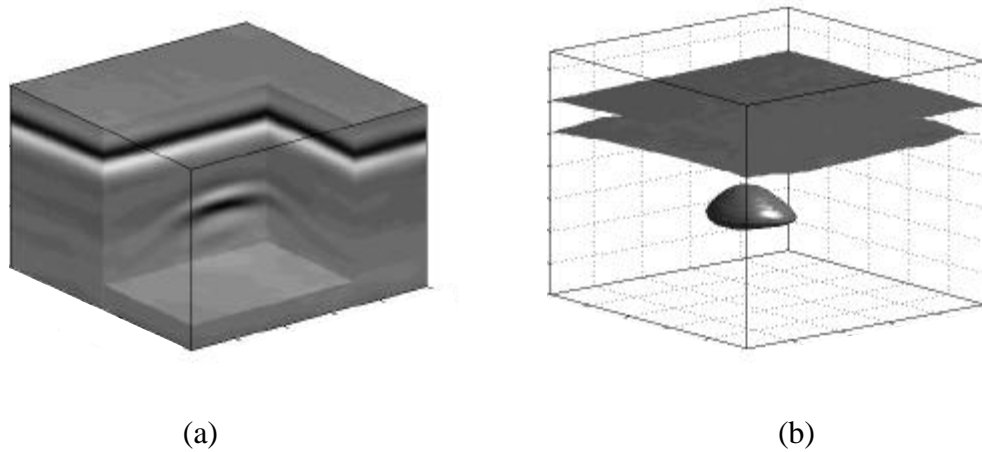


**Fig. 2-6:** (a) Arbitrary cut in the 3-D volume, (b) iso-surface representation

### 2.2.2. Different types of GPR systems

Fig. 2-7 gives a schematic overview of the various possible types of GPR systems that exist today. GPR systems can be classified by the domain in which they work and by the type of modulation.

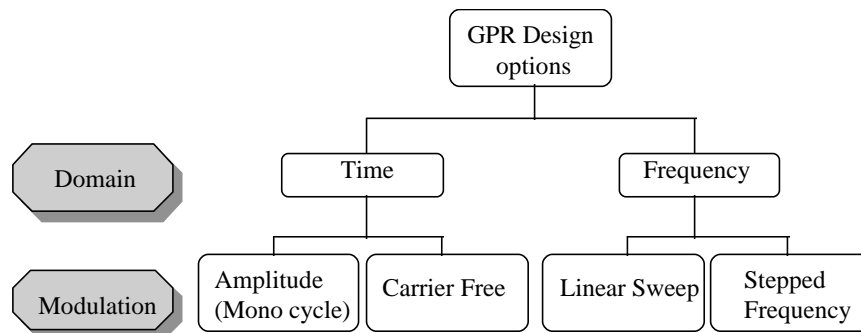


**Fig. 2-7:** Different types of GPR systems

The first family of GPR systems is the time domain GPR. The principle of a time domain GPR is to send a pulse at a given pulse repetition frequency (PRF) into the ground and then listen to the backscattered echoes. In the time domain GPR there are two major categories: the amplitude modulated and the carrier free GPR. The first one sends a pulse with a carrier frequency. This carrier frequency is modulated by a

(square) envelope. In order to achieve a good depth resolution it is important that the duration of the pulse is as short as possible. Therefore a monocycle is used. Most of the commercially available GPRs belong to this family. The central frequency of the monocycle can vary from some MHz up to some GHz as a function of the application. The 3dB bandwidth of the emitted pulse is equal to the central frequency  $f_c$  of the monocycle. Fig. 2-8 shows a monocycle of 1ns. The central frequency and the 3dB bandwidth is 1 GHz.

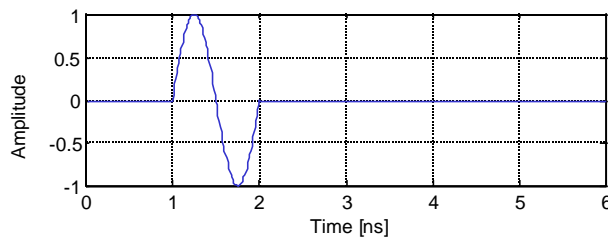


**Fig. 2-8:** A monocycle of 1ns

The need for larger bandwidth has led to the development of a second category of time domain GPR: the carrier-free GPR. The pulse sent by the GPR has no carrier. The width of the carrier free pulse is of the order of some 100 ps. The shape of the pulse can vary, but typically a Gaussian pulse is used. The carrier-free radar is also called an **UWB GPR** (Ultra-WideBand) because of the large bandwidth. The use of the term UWB is slightly different than in conventional air radar systems. A radar system is defined by the Defence Advanced Research Project Agency's (DARPA) [5] to be UWB if its fractional bandwidth is larger than 25%. The fractional bandwidth BW of a system, also defined by DARPA, is given by

$$BW = \frac{2(f_{\max} - f_{\min})}{f_{\max} + f_{\min}} 100\% \quad (2.2)$$

where  $f_{\max}$  and  $f_{\min}$  are the higher and lower limits of the frequency range within which some specified fraction (90-99%) of the total signal energy lies. With this definition, almost all the GPR systems would be UWB. There is no alternative definition for GPR systems, but it is generally accepted that UWB GPR must have a

fractional bandwidth larger than 100%. In this work we will hold to this definition. So UWB GPRs have a fractional bandwidth larger than 100%.

The block diagram of a time domain GPR (Fig. 2-9) is much less complicated than the classic pulsed air radar. In the diagram one can see four major parts: the transmitter, the receiver, the timing circuit and the processing part. The fast sampling in the receiver part is done with a sequential sampler (see Section 2.2.4).

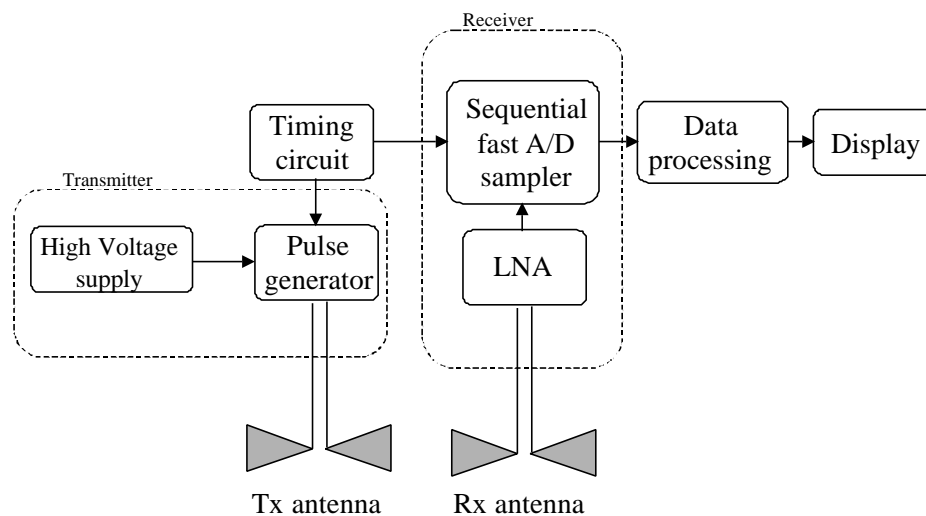


**Fig. 2-9:** Block diagram of a time domain GPR

The majority of the GPR systems use a time domain waveform, although the last decades GPRs are also developed in the frequency domain. In the frequency domain there are also two possible modulation types: either the continuous wave is frequency modulated with a linear sweep, named FMCW GPR, or the frequency of the continuous wave changes in fixed steps, called stepped frequency GPR.

A FMCW system transmits a continuously changing carrier frequency by means of a VCO over a chosen frequency range. The frequency sweeps according to a sawtooth or a triangular function within a certain dwell time. After reception, the backscattered wave is mixed with the emitted wave. The difference in frequency between the transmitted and received wave is a function of the depth of the target. A major limitation of the FMCW radar is the poor dynamic range of the system. The FMCW radar is receiving signals at the same time as it is transmitting. The leakage signal

between the antennas can mask the smaller backscattered signals. Therefore the development of FMCW for the GPR application was abandoned and from the late 1970's on, more attention has gone to the stepped-frequency radar.

A stepped frequency GPR uses a frequency synthesiser to step through a range of frequencies equally spaced by an interval  $\Delta f$ . At each frequency, a CW is radiated with a high stability and mixed with the received signal using a quadrature mixer. The I and Q baseband signals can be sampled using high precision, low speed A/D converters. This means that for each frequency, the amplitude and phase of the received signal is compared with the transmitted signal. A good overview of this technique is found in [6]. The stepped frequency radar is shown schematically in Fig. 2-10.

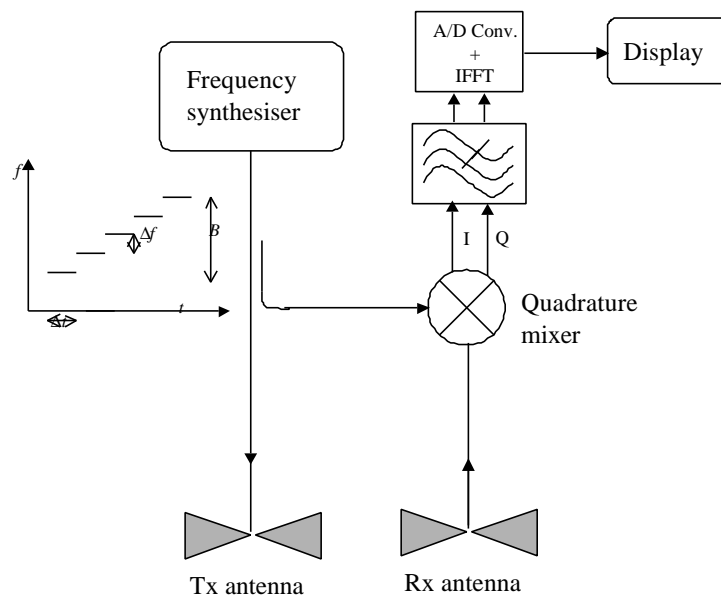


**Fig. 2-10:** Block diagram of a stepped frequency GPR

The transmitted CW signal of a stepped frequency radar at frequency  $f$  can be written as

$$E_t(f) = E_t e^{-j2\pi ft} \quad (2.3)$$

When only one object is present, the received signal is

$$E_r(f) = |\Gamma_0| E_{r0} e^{-j(2\pi ft - 2Rb - f_0)} \quad (2.4)$$

where  $|\Gamma_0|e^{jf_0}$  is the reflection coefficient of the target,  $R$  the distance between the antennas and the target and  $b$  the phase constant of the medium.  $E_{r0}$  is a phasor that contains all the modifications of the transmitted signal, except the phase change related to the distance and the reflection on the object, so it contains for example the free-space loss  $1/R$  and the losses in the ground. The coherent receiver measures the received signal with respect to the transmitted signal. If multiple reflectors are present, the received signal will be a combination of these different reflections. This is repeated for all frequencies. The measured frequency data can afterwards be transformed to an equivalent time domain representation by an inverse fast Fourier transformation (IFFT).

The stepped frequency GPR has some advantages over a time domain GPR. Its dynamic range can be designed to be greater and a narrow band coherent receiver can be used. Further, for two systems yielding the same bandwidth, the S/N ratio will be much higher for the stepped frequency system, because the mean radiated power radiated by a stepped frequency GPR is much higher compared to the mean radiated power radiated by a time domain GPR. The disadvantage of the stepped frequency GPR is the acquisition time. A stepped frequency GPR has to step through a number of frequencies for an acquisition of one A-Scan and for each A-scan an IFFT has to be calculated. With today's technology, the time issue becomes less of a problem. The University of Queensland (Australia) [6] has developed a stepped frequency GPR that only needs 3.6 ms for the acquisition of one A-scan. Impulse systems often have to average several A-scans to enhance their dynamic range, so that the difference in acquisition time is negligible.

### 2.2.3. Propagation in lossy dielectric material

For a good understanding of the physics behind GPR, it is indispensable to study the EM wave propagation in a lossy dielectric material. Without loss of generality, the study is limited to the propagation of uniform plane waves. More complicated wave fronts can always be described as a combination of plane waves.

Earth materials, and soils in particular, can be considered as a conductive (lossy) dielectric medium. Maxwell's equations describing the wave propagation in a conductive dielectric are

$$\nabla \times \vec{E} = -\frac{\partial(\vec{B})}{\partial t} \quad (2.5)$$

$$\nabla \times \vec{H} = \vec{J} + \frac{\partial \vec{D}}{\partial t} \quad (2.6)$$

In harmonic regime, equation (2.5) and (2.6) can be written as

$$\nabla \times \vec{E} = -j\omega \vec{H} \quad (2.7)$$

$$\nabla \times \vec{H} = (\mathbf{s} + j\omega \epsilon) \vec{E} \quad (2.8)$$

with  $\mathbf{s} = \mathbf{s}' - j\mathbf{s}''$  the complex conductivity of the medium, describing how well the medium conducts electric current. At higher frequencies the response time can become significant, resulting in an out of phase component. The imaginary part of the conductivity is related to this out-of-phase polarisation component and is usually small at most radar frequencies.

$\epsilon = \epsilon' - j\epsilon''$  the complex permittivity. The real part of the permittivity  $\epsilon'$  is a measure of the ability of the medium to be polarised under an electric field. For the high frequency range the dipoles can not follow the fast change in magnitude of the electric field, and the polarisation will be out of phase, there is a relaxation phenomena. The imaginary part of the permittivity relates to this out-of-phase polarisation component and can usually not be neglected at most radar frequencies.

$\mu$  the permeability of the medium. If the material is non-ferrous, the approximation  $\mu \approx \mu_0$  is valid.

In equation (2.8) we notice that for conductive dielectrics, the macroscopic parameters  $\mathbf{s}$  and  $\mathbf{e}$  always occur in the combination  $\mathbf{s} + j\omega\mathbf{e}$ . Splitting up the two parameters in their real and imaginary part, this combination can be rewritten as

$$\mathbf{s} + j\omega\mathbf{e} = (\mathbf{s}' + \omega\mathbf{e}'') + j\omega(\mathbf{e}' - \frac{\mathbf{s}''}{\omega}) \quad (2.9)$$

$$= \mathbf{s}_e + j\omega\mathbf{e}_e \quad (2.10)$$

where  $\mathbf{s}_e = \mathbf{s}' + \omega\mathbf{e}''$  is defined as the real effective conductivity,

$\mathbf{e}_e = \mathbf{e}' - \mathbf{s}''/\omega$  is defined as the real effective permittivity.

The real effective conductivity determines a current in phase with the electric field and the real effective permittivity is related to a current out of phase with the electric field.

It is also useful to define  $\mathbf{e}^*$ , the complex apparent permittivity, as

$$j\omega\mathbf{e}^* = \mathbf{s}_e + j\omega\mathbf{e}_e \quad (2.11)$$

and the loss tangent  $\tan \mathbf{d}$  as

$$\tan \mathbf{d} = \frac{\mathbf{S}_e}{\mathbf{w}e_e} \quad (2.12)$$

By substituting (2.12) in (2.11), the complex apparent permittivity can be expressed as a function of the loss tangent:

$$\mathbf{e}^* = \mathbf{e}_e (1 - j \tan \mathbf{d}) \quad (2.13)$$

Thanks to the definition of the complex apparent permittivity, equation (2.8) can be written as

$$\nabla \times \vec{H} = j\mathbf{w}\mathbf{e}^* \vec{E} \quad (2.14)$$

By substitution of (2.7) in (2.14), the wave equation describing the electric field wave propagation in a lossy dielectric medium is found as

$$\nabla^2 \vec{E} + \mathbf{e}^* \mathbf{m}\mathbf{w}^2 \vec{E} = 0 \quad (2.15)$$

The solution of equation (2.15) representing an harmonic plane wave, propagating in the direction  $\vec{k}$ , is

$$\vec{E} = \vec{E}_0 e^{-j\vec{k}\vec{r}} \quad (2.16)$$

with the wave number  $k = |\vec{k}|$  given by

$$k = \omega \sqrt{\epsilon^* \mathbf{m}} \quad (2.17)$$

The wave number  $k$  is complex and may be separated into real and imaginary parts:

$$jk = \mathbf{a} + j\mathbf{b} \quad (2.18)$$

The plane wave solution (2.16) can be written as

$$\vec{E} = \vec{E}_0 e^{-\mathbf{a}\bar{r}} e^{-j\mathbf{b}\bar{r}} \quad (2.19)$$

The first exponential term represents the attenuation of the plane wave in a lossy medium. The rate is specified by  $\mathbf{a}$ , the *attenuation constant*. The second exponential term represents the propagation, the phase is controlled by the *phase constant*  $\mathbf{b}$ . The constants are given by

$$\mathbf{a} = \omega \sqrt{\mathbf{m}\epsilon_e} \sqrt{0.5(\sqrt{1+tg^2\mathbf{d}} - 1)} \text{ , the attenuation constant (Np/m) of the medium} \quad (2.20)$$

$$\mathbf{b} = \omega \sqrt{\mathbf{m}\epsilon_e} \sqrt{0.5(\sqrt{1+tg^2\mathbf{d}} + 1)} \text{ , the phase constant (rad/m)} \quad (2.21)$$

It can be seen in (2.20) that the attenuation of the EM wave in a conductive medium is due to both the conductive and dielectric effects. In table 2.1 the attenuation, the loss tangent and the relative permittivity of some soil types, measured in the scope of the HUDEM project are given for a frequency of 2 GHz [7]. Similar tables, reporting the attenuation and relative permittivity of various materials and soils at radar frequencies can be found in [4][8].

Material	Relative permittivity	Loss tangent	Attenuation [dB/m]
Air	1	0	0
Sandy soil , 0% of moisture content	2.55	0.004	1.22
Sandy soil, 15% of moisture content	11.58	0.087	54.06
Loamy soil, 0% of moisture content	2.82	0.018	5.38
Loamy soil, 15% of moisture content	11.13	0.09	54.82

Table 2.1: The relative permittivity, loss tangent and attenuation of some soil types

The complex parameters  $\epsilon$  and  $s$  and hence  $a$  and  $b$  are primarily function of frequency and water content. To illustrate this, we show in Fig. 2-11 the attenuation constant of sand as a function of frequency in the range from 2 GHz to 18 GHz and the water content expressed in a percentage of volume. The measurements were performed by the University of Louvain-la-Neuve in the scope of the HUDEM project [7]. It can be seen that the attenuation in the soil increases dramatically with frequency. Hence the choice of the frequency band of a GPR system will strongly influence the maximum penetration depth of the system.

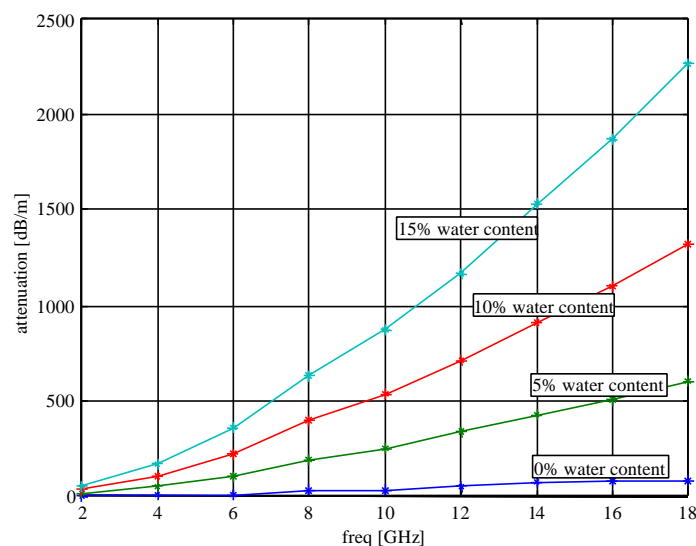


**Fig. 2-11:** The attenuation constant of sand as a function of frequency and water content.

### *Approximations*

In the literature, many approximations are found to simplify the parameters that characterise the propagation of EM waves in a lossy media. The approximations depend on the kind of application and the frequency band of interest. For GPRs, *i.e.* propagation in earth material and for frequencies in the range from MHz to some GHz, the following approximations are generally accepted.

1. The influence of the imaginary part of the conductivity can be neglected with respect to the influence of the real part of the permittivity, or

$$\mathbf{e}' \gg \frac{\mathbf{s}''}{\omega} \quad (2.22)$$

In other words, the conductivity of the soil is taken to be the conductivity at DC:  $\mathbf{s} = \mathbf{s}_{DC}$ . This means that the effective conductivity and effective permittivity may be assumed to be

$$\begin{cases} \mathbf{s}_e = \mathbf{s}_{DC} + \omega \mathbf{e}'' \\ \mathbf{e}_e = \mathbf{e}' \end{cases} \quad (2.23)$$

2. Earth materials are considered to be a low-loss dielectric, having a small loss tangent:

$$(\tan \mathbf{d})^2 \ll 1 \quad (2.24)$$

This is usually the case if the moisture content of the soil is not too high.

In this research we will consequently use these two approximations. Under these approximations, the attenuation constant and the phase constant can be simplified to

$$\mathbf{a} = w\sqrt{m\mathbf{e}'} \frac{\tan \mathbf{d}}{2} \quad (2.25)$$

$$\mathbf{b} = w\sqrt{m\mathbf{e}'} \quad (2.26)$$

The propagation velocity  $v$  of the wave is related to the phase constant by

$$v = \frac{w}{b} \quad (2.27)$$

Using the two approximations (2.22) and (2.24), the velocity of EM waves in earth material can be expressed as

$$v \approx \frac{c}{\sqrt{\mathbf{e}'_r}} \quad (2.28)$$

with  $c$  the propagation velocity in free space and  $\mathbf{e}'_r$  the real part of the relative permittivity. Expression (2.28) is generally accepted in GPR applications and is even accurate for soils with higher losses (like for water saturated soils) as far as  $\tan \mathbf{d} < 1$  [4].

### *The constant Q model*

$Q$  or quality factor, is defined by IEEE Std. 145-1983 as the ratio of  $2p$  times the energy stored to the energy radiated and dissipated per cycle. In Fig. 2-12 (a) and (b) we show the attenuation coefficient of 2 different types of soils, each type with a water content of 5% and 10%. Subplot (a) represent the attenuation in sand, (b) represents the attenuation in a loamy soil. The lines (in green) fitted through the measured points suggest that the attenuation in the soils is almost linear with frequency in a large frequency band. It is this property that is explored in the constant  $Q$  model.

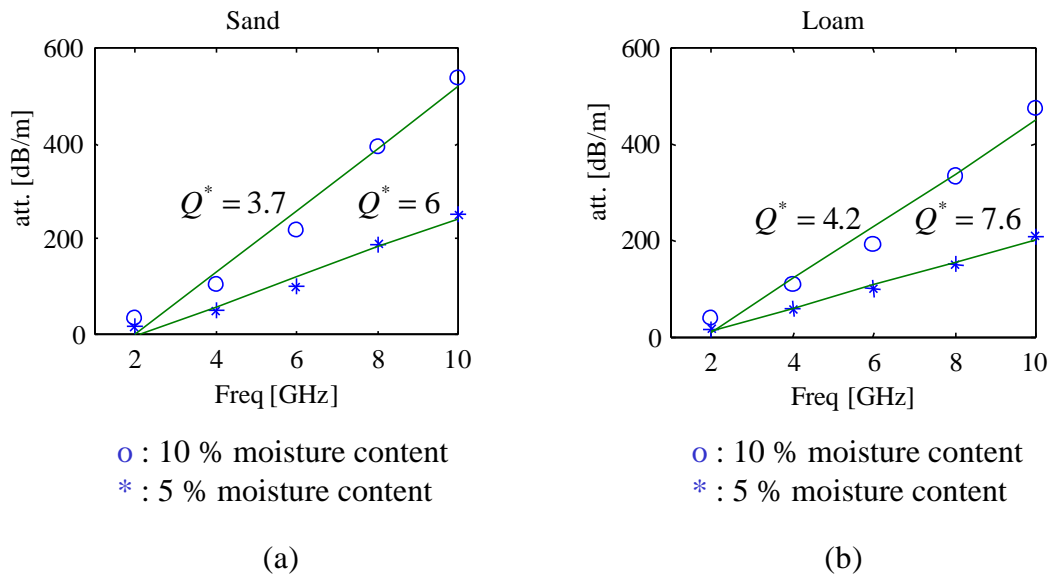


**Fig. 2-12:** Attenuation in (a) sand and (b) loamy soil versus frequency, measurements performed at UCL

If the attenuation is almost linear with frequency, the attenuation and distortion of EM waves in the material can be successfully described by the constant  $Q$  model [6][9]. For seismic waves,  $Q$  has been found to be frequency independent over a large frequency band and is given by

$$Q = \frac{w}{2\nu a} \quad (2.29)$$

with  $a$  the attenuation coefficient and  $\nu$  the propagation velocity. This implies that the attenuation is linear with frequency. In [9] it is suggested that this property can be extended to EM waves in earth materials with low losses and that the definition of  $Q$  in (2.29) holds in this specific case. In [9] they also define a parameter  $Q^*$ , which is a generalisation of the  $Q$  parameter. The  $Q^*$  parameter describes the gradient of the best fit line for each attenuation curve, where the attenuation at zero frequency can be non-zero. In Fig. 2-12 the  $Q^*$  factor is given for the different lines that are fitted through the measured attenuation points. For earth materials, the  $Q^*$  factor is usually

in the range from 2 to 30. The  $Q$  factor is related to the electric parameters of the soil. Combining (2.29) with (2.25) results in

$$Q = \frac{\mathbf{w}}{2\nu\mathbf{a}} = \frac{\mathbf{w}}{2\nu(\mathbf{w}\tan\mathbf{d}/2\nu)} = \frac{1}{\tan\mathbf{d}} \quad (2.30)$$

As a consequence, it is assumed that for constant  $Q$  the loss tangent is independent of frequency and that the real part of the permittivity  $\mathbf{e}'$  is independent of frequency (because  $\mathbf{a}$  is linear with frequency). The latter assumption is generally true for radar frequencies. In the measurements on different soils we noticed however that the first assumption ( $\tan\mathbf{d}$  independent of frequency) is not always correct, certainly not when soils have a higher water content. Anyway, the most important observation is that the frequency dependence of all the electrical parameters together produces a form of attenuation that is nearly linear with frequency.

The constant  $Q$  model provides a mechanism to describe the attenuation and the dispersion of EM waves in earth material by one single parameter  $Q$ . The attenuation constant and the phase constant are linear with frequency and given by

$$\mathbf{a} = \frac{\sqrt{\mathbf{m}\mathbf{e}'}}{2Q}\mathbf{w} \quad (2.31)$$

$$\mathbf{b} = 2\mathbf{a}Q \quad (2.32)$$

We introduce the constant  $Q$  model in this section, but we will use it in Chapter 5. It allows us to calculate an analytical expression of the impulse response of the ground, *i.e.* an impulse response that describes the propagation of an EM wave through a lossy ground over a certain distance.

Table 2.2 summarises the most important terms and ground properties that are introduced in this section. In the last column, the approximated expressions used in this work are given.

Term	Expression	Approximation
Permittivity of free space	$\mathbf{e}_0 \approx 8.85 * 10^{-12} F / m$	
Permeability of free space	$\mathbf{m}_0 = 4\pi * 10^{-7} H / m$	
Complex dielectric permittivity	$\mathbf{e} = \mathbf{e}' - j\mathbf{e}''$	
Real part of dielectric constant	$\mathbf{e}'$	constant with freq.
Imag. part of dielectric constant	$\mathbf{e}''$	
Complex conductivity	$\mathbf{s} = \mathbf{s}' - j\mathbf{s}''$	
Real part of conductivity	$\mathbf{s}'$	$= \mathbf{s}_{DC}$
Imag. part of conductivity	$\mathbf{s}''$	$= 0$
Magnetic permeability	$\mathbf{m}$	$= \mathbf{m}_0$ for earth mat.
Real effective conductivity	$\mathbf{s}_e = \mathbf{s}' + \mathbf{w}\mathbf{e}''$	
Real effective permittivity	$\mathbf{e}_e = \mathbf{e}' - \mathbf{s}''/\mathbf{w}$	$= \mathbf{e}'$
Loss tangent	$\tan \mathbf{d} = \frac{\mathbf{s}_e}{\mathbf{w}\mathbf{e}_e}$	$= \frac{\mathbf{s}_{DC} + \mathbf{w}\mathbf{e}''}{\mathbf{w}\mathbf{e}'}$
Complex apparent permittivity	$\mathbf{e}^* = \mathbf{e}_e (1 - j \tan \mathbf{d})$	$= \mathbf{e}' (1 - j \tan \mathbf{d})$
Complex wave number	$k = \mathbf{w}\sqrt{\mathbf{e}^* \mathbf{m}} = \mathbf{b} - j\mathbf{a}$	
Attenuation constant	$\mathbf{a} = \mathbf{w}\sqrt{\mathbf{m}\mathbf{e}_e} \sqrt{0.5(\sqrt{1 + \tan^2 \mathbf{d}} - 1)}$	$= \mathbf{w}\sqrt{\mathbf{m}\mathbf{e}'} \frac{\tan \mathbf{d}}{2}$
Phase constant	$\mathbf{b} = \mathbf{w}\sqrt{\mathbf{m}\mathbf{e}_e} \sqrt{0.5(\sqrt{1 + \tan^2 \mathbf{d}} + 1)}$	$= \mathbf{w}\sqrt{\mathbf{m}\mathbf{e}'}$
Velocity in free space	$c \approx 3.10^8$	
Phase velocity	$v = \mathbf{w} / \mathbf{b}$	$= \frac{1}{\sqrt{\mathbf{m}\mathbf{e}'}} = \frac{c}{\sqrt{\mathbf{e}'_r}}$

Table 2.2: Summary of the most important terms and ground properties

### 2.2.4. Impulse GPR design parameters

In Section 2.2.2, an overview of the different types of GPR systems was given. In this section we will describe the family of the time domain GPR into some more detail. A general overview of the technology for the transmitter and receiver, as well as some system design parameters will be discussed. In Fig. 2-13 we repeat the block diagram of a time domain GPR. Besides the data processing and display we distinguish 3 parts: the transmitter, the receiver and the timing circuit which triggers both the transmitter and receiver.

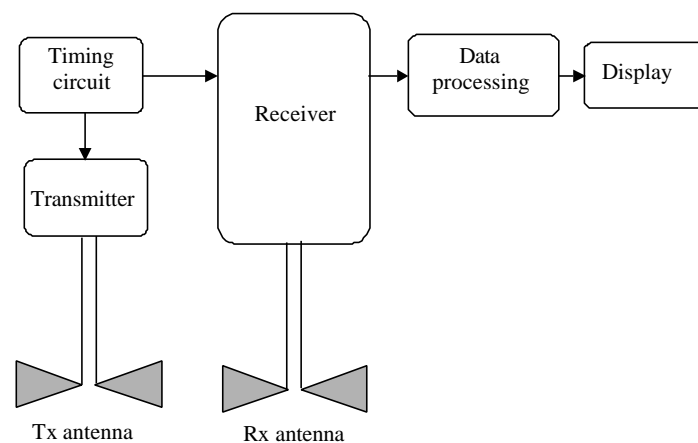


**Fig. 2-13:** Block diagram of a time domain GPR

#### *Transmitter*

The transmitter is a pulse generator, producing short transient pulses with a certain periodicity. This periodicity is called the pulse repetition frequency (PRF). The shape of the pulse is usually a monocycle or a Gaussian pulse, but other shapes like a derivative of a Gaussian pulse or even a step are possible. The impulse generator is generally based on the technique of rapid discharge of stored energy in a capacitor or short transmission line. A block diagram of the principle is shown in Fig. 2-14.

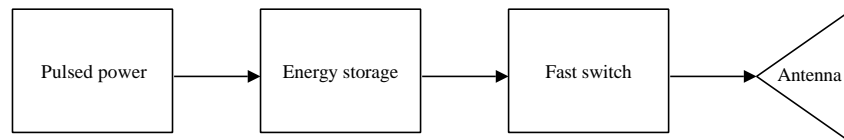


**Fig. 2-14:** Block diagram of pulse generator

The fast switch is an important component in the diagram. The most commonly used technologies for fast switches in GPR are semiconductor switches based on avalanche transistors, step-recovery diodes (SRD) or a combination of these two. In the latter, the SRD is then used to enhance the rise-time of the transition. The avalanche transistor and the SRD are characterised by a high figure of merit in the order of 100-1000 V/ns. The figure of merit is defined as the maximum variation of a signal amplitude per unit of time. It is this characteristic that is needed to generate a transition with a very short rise-time. Fig. 2-15 shows a simplified schematic of a step generator using a transmission line to store the energy and an avalanche transistor as a fast switch [10]. The driving pulse will put the avalanche transistor in a conductive stage so that the transmission line will discharge over the output resistor  $R_L$ .

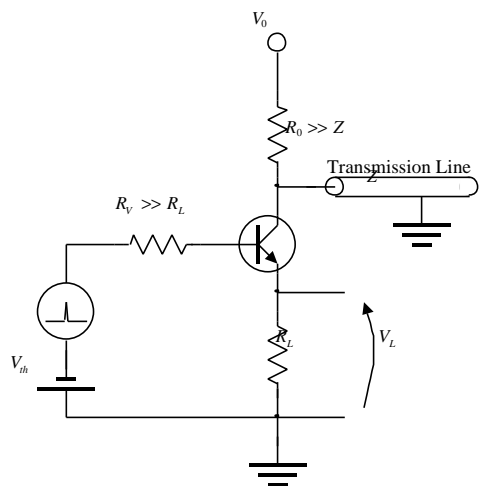


**Fig. 2-15:** Simplified schematic of a step generator

The maximum amplitude of the waveform generated by a pulse generator decreases with the pulse duration or rise time. Typical values for GPRs are between 20 V and 100 V. The transmitter receives an external trigger from a timing circuit. The storage of the energy or the recovery of the fast switch can take a certain time, so in general

the transmitter will limit the pulse repetition frequency of the system. Another important feature of the transmitter is its stability in time. For a pulse generator it is primarily the variation in time between the external trigger and the start of the transition that has to be as small as possible. This delay uncertainty is also called jitter (Fig. 2-16).

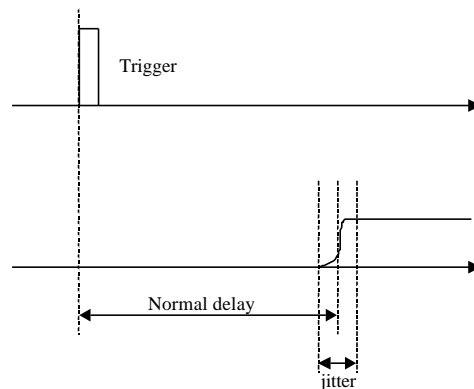


**Fig. 2-16:** Delay uncertainty or jitter

A good overview of different impulse generators is found in [10].

### *The receiver*

From the hardware point of view, the receiver is the most difficult block to build. Its performance has a direct impact on the over-all system performance. The receiver has to be very sensitive, possess a large fractional bandwidth, a large dynamic range and a good noise performance. In Fig. 2-17 we show the block diagram of the receiver. From the left to the right we have a time-varying gain (TVG) amplifier, a low noise amplifier (LNA), a sample and hold circuit (S/H) and an analog-to-digital converter (A/D converter). In the following, a brief description of the blocks will be given.

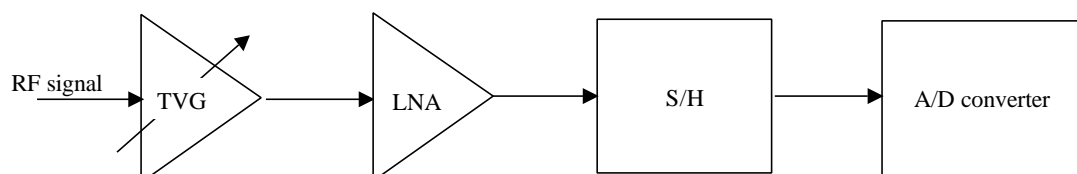


**Fig. 2-17:** Block diagram of receiver

**(a) A/D conversion**

With today's technology, conventional A/D converters like a flash converter or Sigma-Delta converters are limited to conversion rates of about 200 MHz for a 8 bit conversion and 10 MHz for a 16 bit conversion. As the received signals in GPR systems are in the frequency range of some GHz, it is impossible to use a standard A/D converter to sample the received echoes in real time, in order to respect Shannon's theorem. The solution is to slow down sampling rate by a stroboscopic or sequential sampling technique. The principle of sequential sampling is represented in Fig. 2-18. The timing control circuit of a sequential sampler is based on two ramp signals: a fast and a slow ramp. The position (in time) at which an A/D conversion is made is determined by the intersection of the fast and the slow ramp. The fast ramp is at the same rate as the PRF. The slow ramp is set to provide the desired number of samples in one A-scan. As the fast ramp is at the same rate as the PRF and a conversion is done on each intersection, it will take as many emitted pulses as points needed in one A-scan. Hence the number of points per A-scan and the PRF will limit the number of A-scans one can take per second. This number of A-scans has his importance. It will lead to a trade off between number of A-scans one can use to integrate the scans, in order to reduce noise, and the speed at which the antennas can be moved. With the technique of sequential sampling one can reduce the sampling rate from GHz to MHz or even kHz. To be exact, the time between two samples  $T_s$  is given by

$$T_s = T_p \pm \Delta T \quad (2.33)$$

with  $T_p = \frac{1}{PRF}$  and  $\Delta T$  = the equivalent sampling period (see Fig. 2-18). The ' $\pm$ '-sign depends on the orientation of the slow ramp.

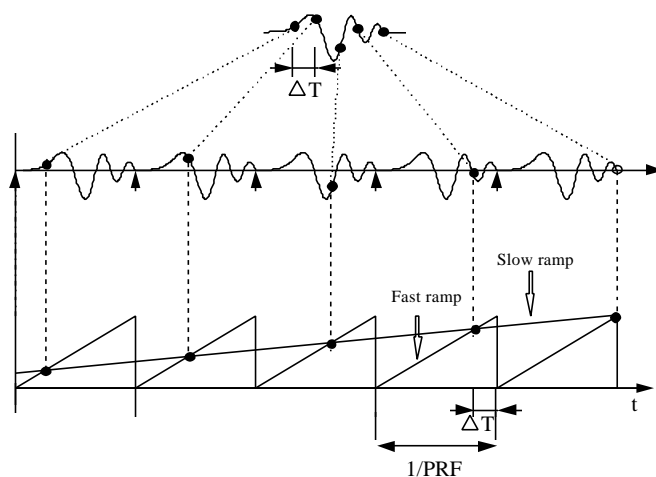


**Fig. 2-18:** Sequential sampling

The A/D conversion itself can be done by a conventional A/D converter. Normally 12 or 16 bits are used for conversion. A 16 bit converter will have a dynamic range of 96 dB. The dynamic range of the receiver is the ratio of the maximum detectable signal to the minimum detectable signal .

### (b) Sample and hold circuit

For a correct A/D conversion the signal at the input of the A/D converter has to be stable for a certain time. The principle is that the maximum rate of signal variation must be smaller than the quantisation step of the converter during the conversion time. To provide this constant signal value to the A/D converter, a sample and hold (S/H) circuit is used.

The working principle of a S/H circuit is based on the charging of a capacitor  $C_s$  to a voltage that is proportional to the input signal so that the sample corresponds to a specific portion of the input signal.

Due to the sequential sampling the input bandwidth of the A/D converter is limited to some MHz. For the S/H circuit this is not true. The input bandwidth of this device has to be of the same order as the highest frequency in the received signal. For an UWB

system, this means that the S/H will have an input bandwidth of some GHz, which makes the design of the circuit very demanding.

In time domain GPRs, two types of S/H circuits are often found: the full-bridge sampler and the half-bridge sampler. The full-bridge sampler is commonly used in systems working with frequencies below 1 GHz. The schematic is equivalent to the schematic of a half-bridge sampler, where only 4 diodes are used in the bridge. The full-bridge sampler is characterised by a good linearity and noise performance [11]. If higher frequencies are used in a system, the preference is given to a half-bridge sampler. It has a faster response but the noise performance is worse [11]. The schematic of the half-bridge sampler is given in Fig. 2-19.

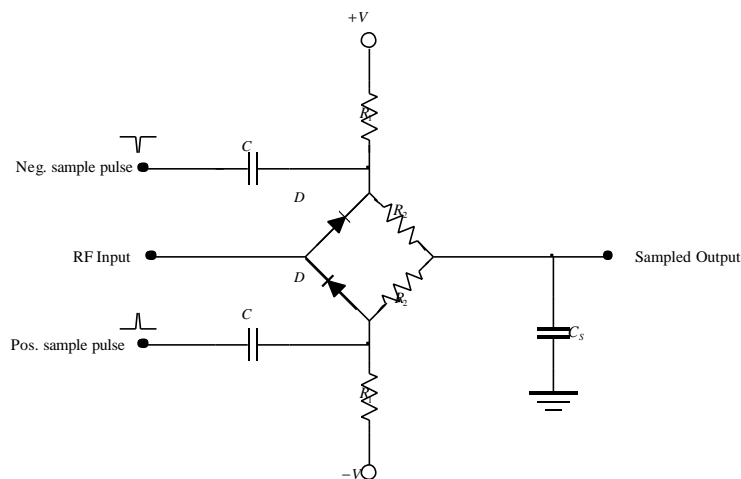


**Fig. 2-19:** Schematic of the half-bridge sample

The aim of the circuit is to charge the capacitor  $C_s$  to a voltage proportional to the RF input. The capacitor  $C_s$  is usually the input capacitor of an amplifier following the S/H circuit. The 2 diodes are reverse biased (blocked) by the voltages  $+V$  and  $-V$  during the hold status of the circuit. These voltages have to be large enough so that the RF input signal does not cause the diodes to conduct. The sampling is initiated by the 2 symmetrical and very narrow sample pulses, which will overcome the inverse bias and put the two diodes in a conducting state. During this time, the RF signal charges the capacitor  $C_s$ . As the diodes have to switch very fast from a blocked stage to a conducting stage, Schottky diodes are frequently used. For an optimum performance

of the sampler, the bridge has to be completely balanced. This means that the 2 diodes and resistors have to be matched, the two reverse bias voltages  $+V$  and  $-V$  have to be exactly equal and opposed in sign, and the shape of the sample pulses have to be totally symmetric. That is why S/H circuits are often implemented in hybrid ICs. The frequency response of a half-bridge sampler can be increased by using shorter sample pulses and by using diodes with a lower capacitance. These diodes however have often a higher series resistance, so both measures will increase noise.

The performance criteria of a S/H circuit are very demanding. The circuit is often designed and optimised for a specific application or system, as the S/H circuits belong to the know-how of a few companies that produce them. It is almost impossible to buy an off-the-shelf sampling head.

### **(c) The low noise amplifier (LNA)**

Before the RF signal enters the S/H circuit, it is conditioned to make use of the whole dynamic range of the A/D converter. The signal conditioning elements consist as usual of a LNA, *i.e.* an amplifier with a very low noise figure. Remarkable about GPR receiver, as represented in Fig. 2-17, is the order of succession of the elements. The LNA is not put as first element as one would expect, but after the TVG. The explanation for this sequence is found in the utility of the time varying gain.

### **(d) Time varying gain (TVG)**

The spherical waves radiated by the transmitting antenna and backscattered by an object are both subject to spreading loss. This means that in the far field the amplitude of the received echo of a given target decreases with  $R^{-2}$ , where  $R$  is the one-way path between the antennas and the object. Further, the objects that we are looking for are buried in a lossy medium. The deeper the object is buried, the more losses will be introduced by the ground. In other words, the later the echo appears in an A-scan, the more it will be attenuated due to these two losses. To compensate for this attenuation in function of time (or depth  $R$ ), a time varying gain is introduced, giving a fixed

gain in dB per unit of time (or per meter) as represented on Fig. 2-20. The curve would approximately compensate for a loss of 50 dB/m (spreading loss + attenuation in the ground).

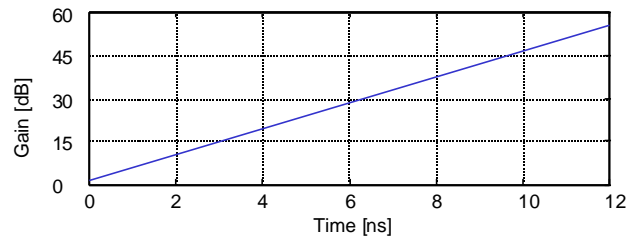


**Fig. 2-20:** Gain curve as a function of time

In practice the TVG is not an amplifier whose gain changes as a function of time, but an attenuator whose attenuation is changed as a function of time. The time varying attenuator is based on PIN diodes. PIN diodes have the property of having a variable resistance as a function of voltage and they have a low junction capacitance. In Fig. 2-21 a schematic is given of a TVG. Two times three diodes are put in a “T” configuration. Two different DC currents respectively forward bias the four series diodes and the two shunt diodes and hence control their dynamic resistance so that the attenuation of the input RF signal can be set.

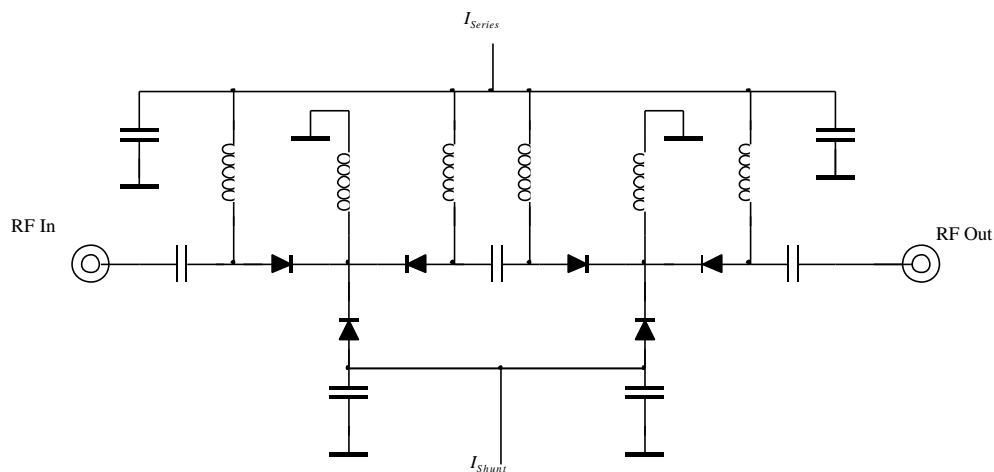


**Fig. 2-21:** Schematic of a time varying gain using PIN diodes

The TVG based on a time varying attenuation has an additional advantage. The first and often the largest reflection in an A-scan is produced by the air-ground interface. Reflections from objects in the ground will appear later in time and hence will be less attenuated by the TVG. By doing so, the LNA following the TVG can be designed more sensitive without saturating on the air-ground reflection. As a consequence the dynamic range of the whole receiver will increase, which would not be the case if the TVG were put after the LNA. This explains why, from the engineering point of view, it is better to put the TVG before the LNA.

### ***Timing circuit***

As explained earlier, the receiver in a time domain GPR is based on a non-coherent acquisition of the backscattered RF signal. This means that the acquisition must be controlled by a very stable and precise timing circuit that synchronises the work between the different parts in the system.

The timing circuit is responsible for mainly three things. First, it has to trigger the impulse generator. Secondly, the timing circuit has to generate the timing signals as needed for the sequential sampler, *i.e.* a trigger for the A/D converter at the intersection of the fast and the slow ramp. Third, it has to control the timing for the TVG.

The stability of the timing circuit is characterised by its time jitter, *i.e.* the uncertainty in time or the random deviation in time of its normal value. Although the sampling is slowed down by the sequential sampling, we obtain a sample of the input RF signal every  $\Delta T$  (see Fig. 2-18), with  $\Delta T$  in the order of some ps, so great care has to be taken to limit the time jitter of the receiver part. As a rule of thumb, one can say that system jitter has to be at least less than  $\Delta T / 2$  to clearly separate two successively samples (see Fig. 2-22).

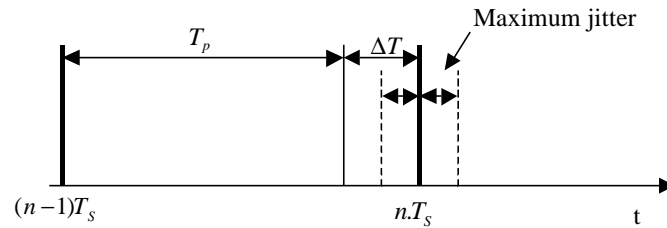


**Fig. 2-22:** Maximum time jitter

For example, a GPR takes 500 points in a time window of 10 ns (which corresponds to an equivalent sample period  $\Delta T$  of 20 ps). The system jitter has to be less than 10 ps, which is a severe and hard to obtain condition.

There exist integrated circuits that generate the necessary timing signals for a sequential sampler. The AD9500 from Analog Devices is such a programmable delay generator. The delay is selected through an 8 bit code. The resolution of the delay is as small as 10 ps and the delay uncertainty or jitter is also typically 10 ps.

### *Some design parameters*

In the design of a time domain GPR, there are certain parameters that can be set as a function of the application. In the following part we discuss several of these parameters. It is important to understand the influence of the parameters on the data and the acquisition time as in commercial systems they can generally be set by the user.

#### **(a) Frequency range**

The choice of the central frequency and of the bandwidth of the GPR is an important issue, and depends primarily on the type of application. For each application a set of frequency constraints can be developed. The parameters influencing the frequency range are: the size of the object, the wanted depth resolution, the maximal penetration depth, and the properties of the soil.

The basic criterion for depth resolution is that the spatial separation between two events (discontinuities in dielectric constant) must be equal to the spatial half-width of the incident pulse. Notice that the half-width in this definition has to be considered in the ground, where the velocity of propagation  $v$  is smaller than in free space, so that the pulse width in the ground is smaller than in free space. The depth resolution is given by (1.1). In Table 2.3, depth resolution is given for a mono-cycle GPR in two different kinds of ground: respectively with a  $\epsilon_r$  of 4 (sandy dry soil) and 15 (sandy wet soil). In the case of a mono-cycle the pulse-width is  $1/f_c$ .

Central frequency	Pulse-width	Depth resolution	
		$\epsilon_r=4$	$\epsilon_r=15$
500 MHz	2 ns	15 cm	7.7 cm
1GHz	1 ns	7.5 cm	3.9 cm
2GHZ	0.5 ns	3.75 cm	1.9 cm
3GHz	0.33 ns	2.5 cm	1.3 cm

Table 2.3: Depth resolution versus central frequency

In conclusion, for good depth resolution, short pulses are needed, which means larger bandwidth.

In Section 2.2.3 we saw that the depth of penetration strongly decreases for higher frequencies in a given soil. The electrical properties of the soil together with the wanted maximum depth penetration imply an upper limit for the used frequencies. Once frequencies above 1 GHz are used, depth penetration decreases dramatically. So if large penetration depth is needed, lower frequencies are preferred.

Besides depth resolution and attenuation, there is also the problem of clutter. Clutter can be defined as backscattered signals that are not from possible targets of interest, but occur in the same time window and have similar spectral characteristics. The smaller the wavelengths in the emitted pulse the larger the quantity of possible clutter sources in the heterogeneous ground. As a general rule it is desirable that the wavelength of the central frequency in the ground of the GPR is ten times larger than

the size of the heterogeneities in the ground to reduce clutter. This also sets a constraint for high frequencies.

### (b) Time window

The time window represents the zone of interest that is to be sampled or in other words, the duration of one A-scan. The beginning and the duration of the timing window can be set by the slow and the fast ramp timing signals.

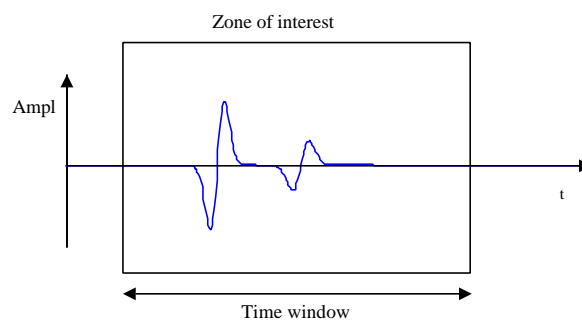


**Fig. 2-23:** The time window

In the application of antipersonnel mine detection the zone of interest is the top layer of the ground, between 0 and 20 cm of depth. The duration of the time window  $T_g$  is in direct relation with the maximal depth of investigation  $s_{\max}$  by

$$s_{\max} = \frac{v \cdot T_g}{2} \quad (2.34)$$

The problem is that the velocity of propagation depends on the permittivity of ground. The velocity of propagation in the ground is approximately given by (2.28). In the next Table some worst case values of  $T_g$  are represented in function of  $s_{\max}$  for a velocity of propagation of  $c/5$ .

$s_{\max}$ (cm)	$T_g$ (ns)
18	6
30	10
60	20

Table 2.4: Maximal depth of investigation

As AP mines are not deeper than 20 cm, a time window of 10 ns must be sufficient.

### (c) Equivalent sampling period

The equivalent sampling period indicates the period at which one would have to sample with a conventional A/D converter. In the case of a sequential sampler, the equivalent sampling period is  $\Delta T$ . In order to do an acquisition without any loss of information one has to respect Shannon's theorem. This means that the equivalent sampling frequency ( $=1/\Delta T$ ) has to be at least twice the highest significant frequency in the emitted signal. In practice however the equivalent sampling frequency is taken much higher than two times the highest significant frequency in the emitted pulse. Typical values of  $\Delta T$  in GPR applications are 10 -100 ps.

### (d) Pulse Repetition Frequency (PRF)

In classic air radar, the PRF is limited by the maximal range at which one wants to detect targets, *i.e.* the maximum unambiguous range. Indeed all echo's from possible targets must be returned before the next pulse is emitted by the radar, otherwise the interpretation of range is incorrect. In GPR technology this is not really a problem. The maximum depth of investigation in the ground is usually limited by the attenuation of the ground and as a consequence will put no restriction on the choice of the PRF. In practice the PRF will be limited by the transmitter technology.

A sequential sampler takes one sample after each emitted pulse, so the PRF will influence the acquisition time of one A-scan. The PRF will also determine the mean power of the GPR pulse generator for a given peak power. Typical values of PRF are

100-1000 kHz. If 512 points are acquired per A-scan, the acquisition of one A-scan would take between 5.12 ms and 0.512 ms.

### **(e) Averaging or stacking**

In general the noise in the received signal can be reduced by averaging (also called stacking) a number of A-scans. Averaging  $S$  A-scans means a noise reduction in amplitude by  $\sqrt{S}$  or an improvement of the signal to noise ratio (SNR) by  $10\log(S)$ .

Normally the stack number  $S$  can be set during acquisition or stacking can be done off-line. When setting the stack number during acquisition, the GPR will automatically output an A-scan which is the average of  $S$  A-scans. Choosing  $S$  too high will considerably slow down acquisition, as well as the maximum displacement speed of the radar for a given grid (or resolution) on the ground. Typical values of  $S$  in GPR applications are 8 - 32, depending on the amplitude of the emitted pulse.

## **2.3. GPR in demining applications**

### **2.3.1. State of the art**

A brief summary of the state of the art in GPR development for minedetection is presented here. Land mine detection and unexploded ordnance (UXO) detection were always of major interest for the GPR research community, since GPR can inherently detect non-metallic as well as metallic objects in the subsurface. The U.S. army already sponsored efforts in this area since the beginning of the seventies. The first use of a GPR in a post conflict situation was reported by the British army after the Falkland war. The attempt however was abandoned because the operational requirements were not fully established. This failure did not discourage the military nor the scientific community to continue research in the area. The difficulty of detecting AP landmines with a GPR may not be underestimated. The size of the

objects is extremely small and the surrounding media can be very complex and rough. Furthermore, the requirements for a mine detector are severe and difficult to meet (see Preface). Therefore the GPR is more and more considered as a complementary sensor to the metal detector to reduce the false alarm rate of the latter and not as a stand-alone detector. There exists already systems which integrate those two types of sensors and which look close to commercialisation. An example of this is the DIGS. DIGS is a handheld wide band stepped frequency GPR, with automatic target recognition algorithms, which is "pluggable" into a standard Schiebel metal detector. A more recent example is the HSTAMIDS, which is a handheld mine detector developed for the U.S. Army and also combines a GPR and a metal detector. In the project planning, the first unit has to be equipped by 2004. The main problem with these types of (army-linked) projects is that it is very hard to get feedback on the performances of the systems.

In Europe there are a lot of governmental (military) and academic research groups doing research on the use of GPR as an AP Landmine detector. Some examples are:

- the Netherlands Organisation for Applied Scientific Research (TNO) [12], who is developing in the scope of the HOM2000 Project a demonstrator for humanitarian demining, combining MD, GPR, IR and vapor detection
- the French-German Research Institute of Saint-Louis (ISL)
- the Defence Evaluation and Research Agency (DERA) in the UK [13]. DERA is working for instance on the integration of a MD, UWB GPR and nuclear quadrupole resonance (NQR) in one sensor (AHHMD project). They also develop the UWB GPR in the project Mineseeker and developed recently a GPR system with an antenna array (4 by 7 bow-tie antennas)
- the Sweden's Defence Research Establishment (FOA) working on metal detector, ground penetrating radar, optical sensors and demining canines [14]
- the Delft University of technology (TU Delft), with departments as IRCTR and ITS which are very active in the domain of GPR and humanitarian demining [15]
- the Norwegian University of Science and Technology where research is done on a stepped frequency GPR for landmine detection [16].

Further almost all ESPRIT projects of the European Commission on humanitarian demining, like Minerec, Demine, Dream, Infield, Hope, Pice and Lotus, include a GPR in their single- or multi-sensor system [17]. The results of the projects are expected for 2001. In Belgium there is besides the RMA [18] also the VUB [19] where research on the use of GPR for AP Landmine detection is undertaken. There are probably more GPR mine detection research groups in Europe than described here. The ones mentioned, are the research groups and projects with whom we have connections.

The literature concerning GPR mine detection is quite extended and all recently written. The main papers describing the use of GPR, the problems and achievements in mine detection, are found in proceedings. First there are of course the conferences that are totally dedicated to Humanitarian demining like the IEE conferences on the detection of abandoned Landmines in October 1996 and 1998, the Mine '99 conference in Florence (It) in 1999, the SusDem conference in Zagreb in Sep. 1997. Recently almost all big conferences in the domain of Electro-Magnetic and Antennas and Propagation and of course the specialised GPR conferences, like the biannual International Conferences on GPRs include special sessions on humanitarian demining.

### **2.3.2. Field trials and conclusions**

In order to test and evaluate different sensors or systems, we installed in collaboration with the Army Forces Bomb Disposal Unit, two test sites: a little one at the Royal Military Academy (RMA) and a larger but still structured one in Meerdaal (near Leuven). The RMA test field contains only 7 AP mines and 6 mine-like targets (can, brick, stone,..) and is mainly for experimental purposes. In Meerdaal we have four identical test fields of 9m by 5m. Each of the four fields contains a different soil type: sand, gravel, local ground (37% sand, 53% silt, and 10% clay) and a mixture of the three previous. In Fig. 2-24 a plan of the test site is given. In Fig. 2-25 one of the four identical test fields is shown in detail. The position of each target is indicated by

wooden pickets around the field (A-D,1-8). The depth of the AP mine depends on its position in the field. The AP mines at position A5, B5 and C5 have a tilt angle of 45°.

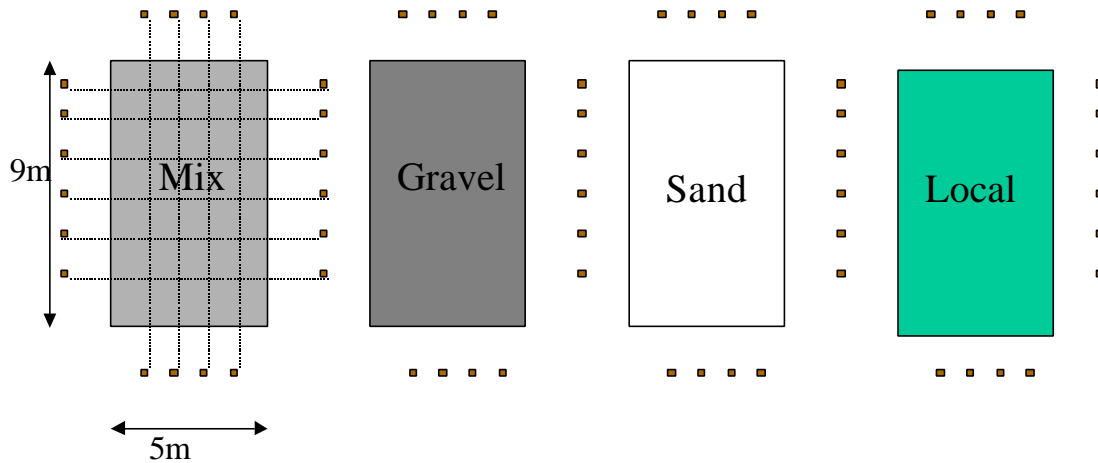


**Fig. 2-24:** Plan of test field in Meerdaal

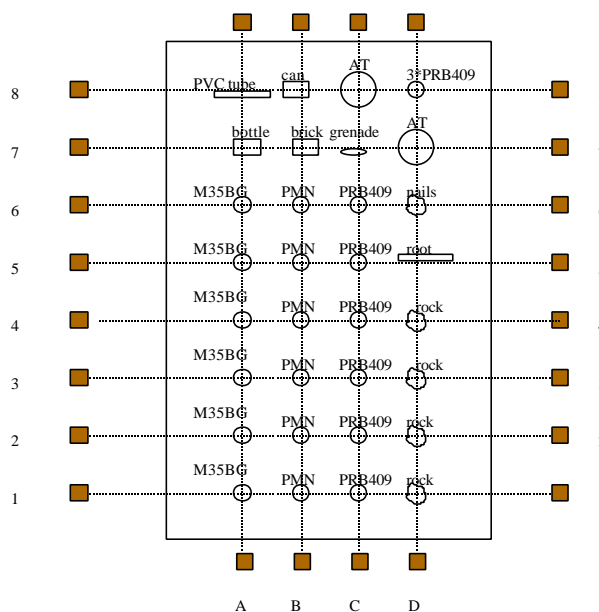


**Fig. 2-25:** Detailed plan of one test field

The Meerdaal test minefields was laid in the spring of 1997. The now more than three years old test field is considered as a good intermediary stage between laboratory conditions and a real mine field. The field is still structured, but the position of the objects is only approximately known, as probably some objects have moved

throughout the years. Furthermore the subsurface of most of the fields is cluttered and the surface in some places can be rough and covered with vegetation. Three different types of AP mines are found in these test fields: the former Soviet PMN mine and two Belgian AP mines the M35BG and the PRB409. The three mines are shown in Fig. 2-26, more details on their dimensions are found in table 2.5. The PMN and the PRB409 are drill mines. The M35BG is made inert by the demining service itself. The primary explosive in the detonator and the TNT have been replaced by a silicone, RTV 3110 from Dow Corning. In the table 2.6 the most important properties relevant for GPR and IR of both the TNT and the silicone are compared.



**Fig. 2-26:** From left to right: PMN AP mine, M35BG AP mine and the PRB409 AP mine

	Radius [mm]	Height [mm]	Explosive
<b>PMN</b>	112	56	200 gram of TNT
<b>M35BG</b>	63.5	38	100 gram of TNT/KNO <sub>3</sub>
<b>PRB409</b>	82	28	80 gram of triallene

Table 2.5: Technical details on the AP mines used in the test field

	TNT	Silicone
Density (g/cm <sup>3</sup> )	1.56	1.17
Dielectric constant at 1GHz	2.89	2.89
loss angle at 1GHz	0.003	0.006
Thermal conductivity W/(m.K)	0.33	0.35
Specific heat cal/(g.°C)	0.234	0.2

Table 2.6: Properties of TNT and silicone

On these test fields, we did several field trials with commercially available GPR systems. The systems we tested are the RAMAC 1GHz, the GSSI SIR-2 with the 1GHz horn antenna , GSSI SIR-2 with the 2.5GHz horn antenna and the ERA with the 1GHz and 2GHz antenna. All of these systems are time domain GPRs. It was not our intention to compare the different GPR systems; we only wanted to gain experience in the use of GPR in this particular application.

The data from the commercially available systems were analysed. In short the following conclusions were drawn.

- The antennas are a critical point. In three out of the five tested systems, the antennas were designed to be in contact with the ground. The antennas coupled to the ground turned out to have a low degree of mobility in a rough and with vegetation covered scene. Two out of the five tested systems had horn antennas, which could be used off-ground. The antennas however were so big and heavy that they were unmanageable in the field. To give an idea of their dimensions, the 2.5 GHz horn antenna, which is the smallest of the two horn antennas, was still 60 cm by 22 cm by 32 cm.
- In the field it is difficult to detect small objects. The antennas must be used in a systematic scan pattern, in order not to miss any spot of the scanned area. If the antennas passed just besides a target, the target was in most of the cases not detected.
- Conventional GPR systems have a poor classification rate. With the bare eye, no difference could be made between a mine-like target and an AP mine.

Furthermore, targets which were shallowly buried or buried flush with the ground were masked by the large air-ground interface reflection. If the air-ground interface was smooth and flat, it was possible to retrieve the targets in the image by simple image processing techniques. But when the air-ground interface was too rough, these simple image-processing techniques failed. Obviously there is a lack of depth resolution in the conventional GPR systems.

## **2.4. Summary**

In this chapter a general description of the conventional GPR is given. The history of the GPR, the different types of GPRs and the physics behind the propagation of electromagnetic waves in a lossy dielectric are discussed. Important to keep in mind for the application is that the attenuation of the electromagnetic waves in a lossy soil increases both with frequency and moisture content of the soil. In a second part of the chapter the state of the art in demining applications, the description of the test fields and the conclusions of the field trials with commercially available systems are presented. The test revealed that the choice of the central frequency and the bandwidth of the GPR are an important issue. Classical GPRs are mostly designed for geophysical applications and use central frequencies below 1GHz. As landmines are small objects and are buried close to the air-ground interface, a larger bandwidth is needed for a better depth resolution and detailed echo. This means the use of an ultra-wideband (UWB) GPR imposes itself. It can be expected that a larger bandwidth also will enhance the classification rate of the GPR. On the other hand, using an ultra-wideband system involves inevitably the use of higher frequencies. These higher frequencies will be strongly attenuated by the lossy soil as shown in this chapter. Furthermore, the use of a large bandwidth has his implications on the hardware of the GPR system. Although the UWB GPR seems a promising sensor for the demining application, the advantages of the ultra-wideband GPR over a conventional GPR and the drawbacks of the use of higher frequencies have to be well balanced against each other.

Therefore we decided to develop a time domain UWB GPR to study its advantages and limitations. The choice of a time domain system over a stepped frequency system was mainly influenced by the fact that a lot of equipment and know-how on UWB time domain systems was already present in our laboratory. In the next chapter we will concentrate on the development of UWB GPR antennas. If we want to use the UWB GPR for the demining application, the antennas have to meet some particular specifications.

## REFERENCES

- [1] W. Stern, "Über Grundlagen, Methodik und bisherige Ergebnisse elektrodynamischer Dickenmessung von Gletschereis," *Z. Gletscherkunde*, vol. 15, pp. 24-42, 1930.
- [2] R. M. Morey, "Continuous subsurface profiling by impulse radar," *Proceedings of the Engineering Foundation Conference on Subsurface Exploration for Underground Excavation and Heavy Construction*, pp. 213-232, Aug. 1974.
- [3] D. J. Daniels, D. J. Gunton and H. F. Scott, "Introduction to subsurface radar," *IEE Proceedings*, vol. 135, no.4, pp. 278-320, Aug. 1988.
- [4] D. J. Daniels, *Surface Penetrating Radar*. London: IEE, 1996.
- [5] OSD/DARPA, Ultra-Wideband Radar Review Panel, *Assessment of Ultra-Wideband (UWB) Technology*. Arlington: DARPA, 1990.
- [6] D. A. Noon, *Stepped- frequency radar design and signal processing enhances ground penetrating radar performance*, Doctoral thesis, University of Queensland, AU, 1996.
- [7] M. Storme, I. Huynen and A. Vander Vorst, "Characterization of wet soils in the 2-18 GHz frequency range," *Microwave and optical technology letters*, vol. 21, no. 5, June 1999.
- [8] A. von Hippel, *Dielectric materials and applications*. Boston: Artech House, 1995.
- [9] G. Turner and A. F. Siggins, "Constant Q attenuation of subsurface radar pulses," *Geophysics*, vol. 59, no. 8, pp. 1192-1200, Aug. 1994.

- [10] M. Piette, *Banc de mesure en régime transitoire de la signature radar d'objets tridimensionnels*, Doctoral thesis, Université catholique de Louvain and Royal Military Academy, Belgium, Oct. 1995.
- [11] W. Murray, C. Lewis, Z. Yang and J. T. A. Pollock, "Development of high resolution GPR hardware in the frequency range 300 MHz - 3.5 GHz," *Sixth International Conference on Ground Penetrating Radar*, Sendai, Japan, pp. 505-510, Sep.-Oct. 1996.
- [12] [http://www.tno.nl/cases/defensie/humanitair\\_ontmijnen.html](http://www.tno.nl/cases/defensie/humanitair_ontmijnen.html)
- [13] <http://www.dera.gov.uk/>
- [14] <http://www.foa.se/>
- [15] <http://irctr.et.tudelft.nl/>
- [16] Egil Eide, *Radar imaging of small objects closely below the earth surface*, Doctoral thesis, Norwegian University of Science and Technology, Norway, Aug. 2000.
- [17] <http://www.cordis.lu/esprit/src/hphdrtd.htm>
- [18] <http://www.sic.rma.ac.be/Projects/Hudem/>
- [19] <http://www.etro.vub.ac.be/>



---

## **Chapter 3. Development of UWB GPR antennas**

---

### **3.1. Introduction**

Antennas may be the most critical point in an impulse GPR system, having a direct influence on its system performance. The antennas have to be specially designed to radiate pulses with given properties into the ground and transduce the backscattered signals from subsurface objects into a useful signal without too much affecting their shape.

They differ from conventional antennas in many aspects. First of all GPR antennas operate near the ground. The presence of the ground in the reactive field or near-field region of the antenna will influence the antenna characteristics. Secondly the antenna often operates in proximity to a second antenna, which gives an additional problem of antenna cross-coupling. Furthermore, the antenna transmits and receives fast transient electromagnetic signals with a large fractional bandwidth. A typical GPR could require an antenna with a fractional bandwidth of 100%. GPR antennas also should have a linear phase characteristic over this band, to limit the distortion of the emitted (or received) signal, and a constant polarisation with frequency.

All these supplementary requirements make that the number of antenna classes, which can be used, is limited. In some cases it also led to the design of new or modified antennas, matching the characteristics of the medium of propagation, the radiated signal and the system requirements.

In this chapter an overview of existing GPR antennas and ultra-wideband antennas will be given. Furthermore we will discuss some design goals of GPR antennas adapted for the application of demining. The design goals are mainly a product of field trials described in Chapter 2. Finally the development of TEM horn antennas for UWB GPR will be described.

## **3.2. Overview of existing GPR antennas**

### **3.2.1. Conventional antennas**

Nowadays, three main types of antennas are used in GPR applications: the element antennas, the frequency independent antennas and the horn antennas. A good overview of GPR antennas is given in [1].

#### *Element antennas*

Element antennas are the most widely used out of the three main types of antennas. Some examples of element antennas are the *monopole*, *dipole* and *bow-tie* antenna. This class of antennas is non-dispersive, and is characterised by linear polarisation, low directivity and some of them have a relatively limited bandwidth. The radiation characteristics of element antennas are well understood. The calculation of the radiated field is based on the approximation of the current distribution on the antenna by a number of elementary currents.

In the system configuration, the transmitting and receiving antenna can have either the same polarity (co-polarised) or an orthogonal polarity (cross-polarised), providing a lower antenna cross-coupling and eventually a better discrimination against certain man-made objects. Due to the low directivity, element antennas are used in close contact to the ground in order to couple as much energy as possible into the ground.

The latter has the disadvantage that the antenna impedance is influenced by the ground properties. Recently some research is done by TU-Delft to try to adapt the antenna to the ground properties [2].

Much effort has gone into techniques to extend the bandwidth of the element antennas. One possible solution is *resistively loading the dipoles*. The loading can be done either by an end loading, by a distributed loading or by a tapered resistive loading. Unloaded dipoles have internal reflections at the open end of the dipole. The resistive loading is essential in causing a rapid decay of current along the antenna to reduce the reflections at the antenna open ends, which results in less distortion or late-time ringing in the tail of the radiated transients. Hence a larger bandwidth is achieved. In 1965, Wu and King were the first to make a study on the tapered loading of a dipole antenna [3]. The profile for this resistive loading is known as the Wu-King profile. An overview of element antennas with resistive loading is given in [4]. Studies comparing a numerical finite difference time domain (FDTD) analysis with experimental measurements can be found in [5] and [6]. A disadvantage of the loading is the reduction of gain and radiation efficiency, although the latter is often considered less disadvantageous than antenna ringing. The radiation efficiency is defined as

$$\frac{\text{energy radiated}}{\text{energy radiated} + \text{energy dissipated}} \quad (3.1)$$

and can in some cases drop down to 29% [6].

Another antenna that can be used as a wideband element antenna is the *bow-tie antenna* [7] (Fig. 3-1). This antenna is in fact a planar version of a finite biconical antenna, determined by a length  $L$  and an angle  $\alpha$ . Bow-tie antennas, together with its many variants like shielded bow-tie, loaded bow-tie, tapered bow-tie etc., are probably the most popular among the element antennas. They can reach fractional bandwidths of 100% and more.

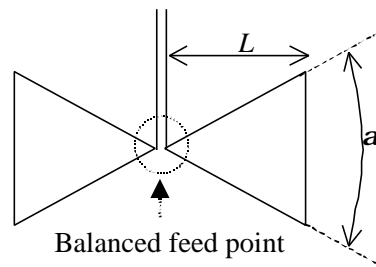


**Fig. 3-1 :** The bow-tie antenna.

### *Frequency independent antennas*

A second main type of antennas used in GPR systems is the frequency independent antenna. An antenna is called frequency independent if it satisfies two principles: the scale principle and the truncation principle. It is known that antenna characteristics like pattern, impedance, etc., are invariant to a change of scale that is in proportion to the change in wavelength. If the shape of an antenna is entirely determined by angles, it would be invariant to a change of scale and hence, the performance of such an antenna would be independent of frequency. Furthermore the antenna has to satisfy the truncation principle, which implies that the current approaches zero at the end of an antenna. Otherwise truncation of the antenna has an effect on the pattern. In practise however, the dimensions of the antenna limit the lower frequency bound. A good overview of the subject is found in [8]. Examples of frequency independent antennas are the *log-periodic antennas* and the *spiral antennas*. An example of a spiral antenna is shown in Fig. 3-2. The formula for the spiral curve in polar coordinates is [8]

$$f = f_0 + \tan A \ln r \quad (3.2)$$

which shows that the antenna is determined only by the angles  $f$  and  $A$ .

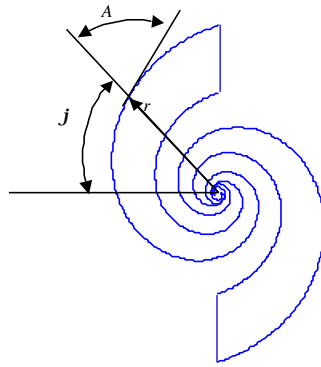


**Fig. 3-2:** Spiral antenna

A new member of the class of frequency independent antennas is the *Vivaldi antenna*. The Vivaldi antenna, introduced by Gibson in 1979 [9], consists of an exponential tapered slot line etched on a dielectric substrate (Fig. 3-3). The structure is usually fed by a micro strip, etched on the other side of the substrate (in dotted line on Fig. 3-3). The antenna characteristics are influenced by a number of parameters, like the dimensions and geometry of the slot line, the thickness and dielectric constant of the substrate, etc. The Vivaldi antenna is extremely wide-banded, bandwidths up to 5 octaves have been reported [9]. The lower cut-off frequency is limited by the dimensions of the antenna aperture. The antenna is characterised by a long electrical length for a reasonable short physical length, and therefore is an interesting antenna for GPR applications.

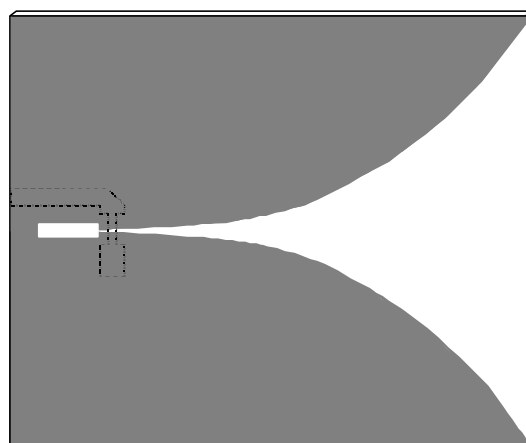


**Fig. 3-3:** Vivaldi antenna with micro strip feed

The frequency independent antennas however have the property of being dispersive. The impulse response of this class of antennas generally results in a chirp-waveform, which makes them unsuited for sending short pulses, as needed in time domain GPR. In stepped-frequency radar, the dispersive behaviour of the antennas can be compensated for. That is why they are only used in combination with this class of GPRs.

### ***Horn antennas***

The third main type of antenna is the *horn antenna*. Classical horn antennas have a fractional bandwidth around 66%, which is normally not enough for a GPR. Larger bandwidths are achieved with double-ridged horns. Horn antennas have the advantage of being directive. This means horn antennas can be used off ground. Examples of commercially used horn antennas are the 1GHz and the 2.5 GHz antenna of GSSI. They were originally developed for road inspection and can be mounted on a vehicle. The disadvantage of this kind of antenna is the size. Usually horn antennas are too large what makes them not user-friendly in rough terrain (e.g. the 1GHz antenna of GSSI are 102 cm \* 22 cm\* 32 cm).

### **3.2.2. Non-dispersive Ultra-wideband antennas**

Thanks to the considerable progress in signal generators and receivers the last decades, the time domain UWB radar has won in interest. The main goal was to achieve higher spatial resolution, an easier target information recovery and a lower probability of interception. In this kind of application it is important that fast electromagnetic transients are radiated, without too much distortion. Therefore non-dispersive UWB antennas are needed, with a fractional bandwidth of 120% or greater. In one of the previous paragraphs we already mentioned the resistive loaded bow-tie antenna, which indeed can be classified in the family of UWB antennas. However if more radiation efficiency and directivity are pursued, the solution must be found in other types of antennas, mostly travelling wave antennas. An antenna is called a travelling wave antenna if the length of the antenna plates is several times larger than

the pulse lengths of the feeding signal. This means the wave actually travels along the antenna plates before it is radiated when reaching the end of the plates.

The *infinitely long biconical antenna* is an ideal radiator for fast electromagnetic transients [10][11][12]. Since its length is infinite and its shape is invariant to a change of scale, the infinitely long biconical antenna is a frequency independent antenna. The infinite biconical antenna is equivalent to a transmission line, guiding a spherical TEM wave. Its characteristic impedance and hence the antenna impedance is only function of  $q_0$  (see Fig. 3-4). In practical use however, the antenna will have a finite length, so that reflections at the antenna end will occur. These unwanted reflections can, just like with the element antennas, be reduced by including resistive material in the antenna structure [13]. Fig. 3-4 shows a finite conical monopole antenna on a ground-plane.

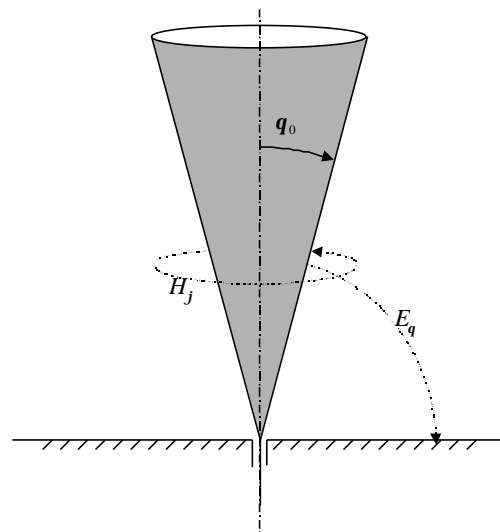


**Fig. 3-4 :** Conical monopole antenna of finite length on a ground-plane

A second type of UWB antenna, based on the biconical antenna is the *travelling wave TEM horn*. A travelling wave TEM horn consists of a pair of triangular conductors forming a V structure (Fig. 3-6), guiding essentially a TEM mode between its antenna plates. The TEM horn is studied in detail in Section 3.4.

A last type of UWB antenna is the *Impulse Radiating Antenna (IRA)*. The IRA antenna is a parabolic antenna with a conical TEM transmission line as primary

source. The conical transmission line will launch essentially a spherical TEM wave towards the reflector. Suppose a step voltage is applied in the feed point of the transmission line. An observer on axis and in the far field of the antenna will first see a pre-pulse, due to the direct (backward) radiation of the feeding transmission line. This is followed by an impulse of short duration and high amplitude. The impulse is proportional to the first temporal derivative of the step on the feeding transmission line. The main impulse is followed by a tail due to reflections on the transmission line end and associated with low frequency components of the feeding signal. These reflections are limited by putting resistors between the transmission line and the reflector. The IRA antenna is represented on Fig. 3-5. This type of antenna is conceived and studied by C.E. Baum and E.G. Farr. More details can be found in [14][15][16].

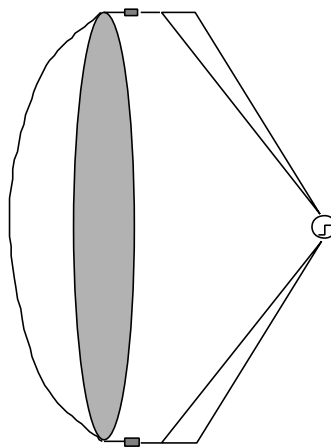


**Fig. 3-5:** The Impulse Radiating Antenna

### **3.3. GPR antenna design goals for the demining application**

As already mentioned in Chapter 2, most GPR antennas are designed for applications other than the demining application and do not meet the specific requirements as needed for the demining application. From the experience obtained by the field trials and taking into account the UWB approach, five technical and practical design goals for UWB antennas are set:

1. The antenna must be able to radiate or receive fast electromagnetic transients with a spectrum between 500 MHz and 4.5 GHz
2. The antenna must be usable off ground, not only for safety reasons but also to improve the mobility of the detector. As a consequence, the antenna must have a high directivity so that it can still couple sufficient energy into the ground to achieve a penetration depth of 20 cm in any soil
3. The antenna must guarantee a high degree of mobility, having an implication on the dimensions and weight of the antenna. Minefields have often a rough surface and are covered with a lot of vegetation. Only little antennas can guarantee a sufficient flexibility in such a scene. Little antennas are also better for hand-held applications
4. The antenna properties must be independent of the ground properties. The influence of the ground will be reduced when using the antenna off ground
5. The antenna must be cheap in production to limit the overall cost of the sensor. This will always be asked for in the case of *humanitarian demining*.

One of the most promising antennas that can meet these design goals, is the travelling wave TEM horn. Therefore we have chosen this type of antenna as the starting point for our study.

### **3.4. Air-filled TEM horn**

#### **3.4.1. TEM horn antennas**

In an effort to increase the directivity or the antenna gain for a broadband and non-dispersive antenna, many researchers have considered a TEM horn. A travelling wave TEM horn consists of a pair of triangular conductors forming a V structure (Fig. 3-6), capable of radiating and receiving a fast transient pulse [4]. It is assumed that the TEM horn guides essentially the TEM mode within the frequency range of interest by maintaining a constant characteristic impedance and that, by neglecting the edge diffraction effect and fringe fields, a linearly polarised spherical wave is radiated. The

operation of a TEM horn is fairly simple. On transmission, the TEM horn radiates a signal that is proportional to the first time derivative of the incident voltage pulse in the feeding point. On reception, the horn outputs a voltage pulse that has the same shape as the incoming electric field (a detailed explanation for this is given in Chapter 4, Section 4.3.3). A conventional TEM horn is completely characterised by three parameters:

- $L$  the length of the antenna plates,
- $\mathbf{j}_0$  the azimuth half-angle,
- $\mathbf{q}_0$  the elevation half-angle.

The characteristic impedance of an infinite long TEM horn ( $L=\infty$ ) is only function of the two angles  $\mathbf{j}_0$  and  $\mathbf{q}_0$ . Theoretically a TEM mode does not have an upper cut-off frequency. In practice however some higher modes exist and will introduce an upper cut-off frequency. The dimension  $L$  of the antenna mainly governs the lower cut-off frequency.

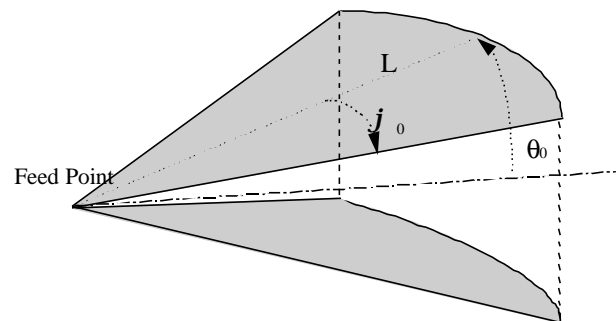


**Fig. 3-6:** The travelling wave TEM Horn

The conventional design of the TEM horn is based on the infinitely long biconical antenna. Many variants are possible, *e.g.* resistive loading of the antenna [17], tapering the antenna plates [18], gradually changing the separation angle between the antenna plates [19], or placing a dielectric lens at the aperture [20].

There is until now no exact theoretical analysis of this structure available. Various approximate analyses and models have been made to allow the antenna design.

### *The antenna impedance*

To calculate the antenna impedance and the surge impedance along the antenna plates, two methods are often found in literature. Both models are based on the approximation that the antenna is infinitely long. In this case, the antenna is equivalent to a conical transmission line. Suppose the origin of co-ordinates in the feed point (apex) of the antenna. For a given value of the two angles  $\mathbf{j}_0$  and  $\mathbf{q}_0$ , the characteristic impedance of the transmission line is constant, independent of the radial co-ordinate  $r$ . Hence, the antenna impedance (for  $r \rightarrow 0$ ), and the surge impedance will then be equal to the characteristic impedance of the transmission line. The surge impedance is defined as the impedance measured in any point of the antenna by means of a step excitation. It does not take into account the backward waves due to reflections at the antennas open end, arriving later.

The characteristic impedance of the transmission line can be found by conformal mapping. In a first step, the two plates are projected by a stereographic projection into two plates of circular arcs. In a second step, the characteristic impedance of the circular arc problem is solved by a standard method of conformal mapping [10][21]. The results are usually given in tables and curves as a function of the two angles  $\mathbf{j}_0$  and  $\mathbf{q}_0$ . This method of conformal mapping can also be used to calculate the field distribution between the antenna plates [22].

A second approach used for the calculation of the characteristic impedance of the infinite TEM horn is based on cascading sections of strip-lines [18][23]. The antenna is split into electrically small segments along its length (Fig. 3-7). Each segment of the antenna is approximated by a parallel twin line and the antenna is modelled as a collection of those parallel twin lines in serie.

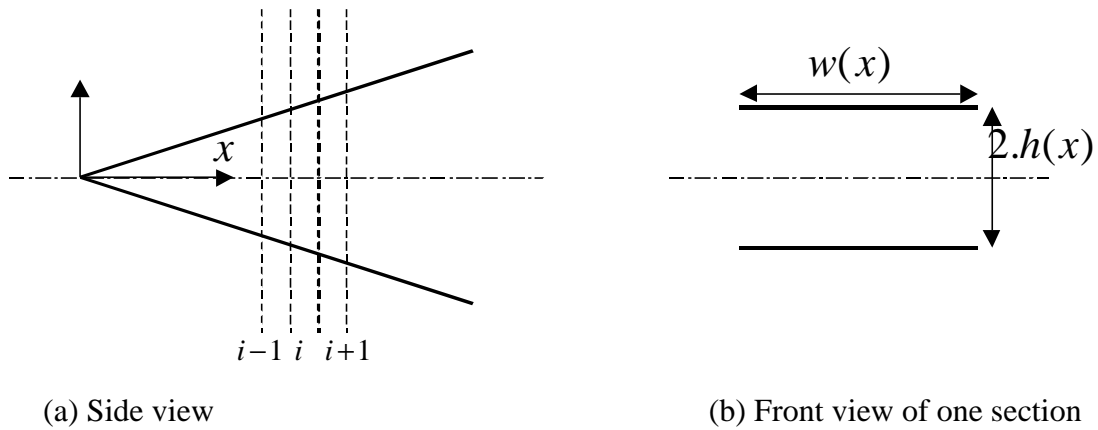


**Fig. 3-7 :** TEM horn as a cascade of strip lines

The characteristic impedance of such a twin line segment is calculated as two times the characteristic impedance of a micro-strip of height  $h$  and width  $w$  in the absence of a dielectric. The characteristic impedance of the micro-strip can be calculated for a given ratio  $w/h$  using the approximated expressions of Hammerstad and Jensen [24].

For a given value of the angles  $\mathbf{j}_0$  and  $\mathbf{q}_0$ , the ratio  $w/h$  is constant and the characteristic impedance of each twin line segment will be the same, hence the surge impedance of the TEM horn will be constant.

### *The radiated far field*

The evaluation of the far field, radiated by a TEM horn, can be done in the frequency domain as well as directly in the time domain. In the frequency domain approach the field is first calculated at the TEM horn aperture, as the field of the TEM mode that would exist in a horn of infinite length. Based on the assumption that the edge diffraction and the fringing field effects are neglected, the spherical field at the horn aperture is given in [4] as

$$E_y(x', y', 0) = \frac{r_0^2}{\sqrt{r_0^2 + x'^2 + y'^2}} \frac{e^{-jk\sqrt{r_0^2 + x'^2 + y'^2 - r_0^2}}}{\sqrt{r_0^2 + y'^2}} \quad (3.3)$$

The origin of co-ordinates is taken in the middle of the antenna aperture (Fig. 3-8). The co-ordinates in the antenna aperture are indicated by primes and  $r_0$  is the distance between the apex and the centre of the aperture. Huygen's principle is used with this field to predict the radiated field outside the aperture.

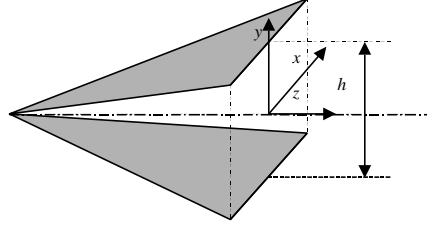


**Fig. 3-8:** Representation of co-ordinate system

A simple time domain model for the TEM horn is given in [25]. In this model, the antenna is considered as an open circuited transmission line. It consists of approximating the antenna by a succession of electric and magnetic dipoles, and summing their contributions. The model is simple but useful to help in the design of a TEM horn or to make comparisons with other antennas. If a step voltage of  $V_0$  is applied at the antenna feed, the radiated electric field on boresight at a distance  $z$  is given by

$$E_y(z, t) = -\frac{V_0}{z} \frac{h}{2\pi c f_g} \left[ \mathbf{d}\left(t - \frac{z+r_0}{c}\right) + \frac{c}{2r_0} \left[ -u\left(t - \frac{z+r_0}{c}\right) + u\left(t - \frac{z+3r_0}{c}\right) \right] \right] \quad (3.4)$$

with  $h$  the distance between the two antenna plates at the aperture (Fig. 3-8),  $c$  the speed of light,  $f_g = Z_c / Z_0$  the geometrical impedance factor,  $Z_0$  the impedance of free space,  $Z_c$  the characteristic impedance of the TEM horn,  $r_0$  the distance between the antenna apex and the origin of co-ordinates and  $u(t)$  the unit step function. Fig. 3-9 shows the graphical representation of the step response given by (3.4). The author also suggests a correction of the model for high frequencies [25].

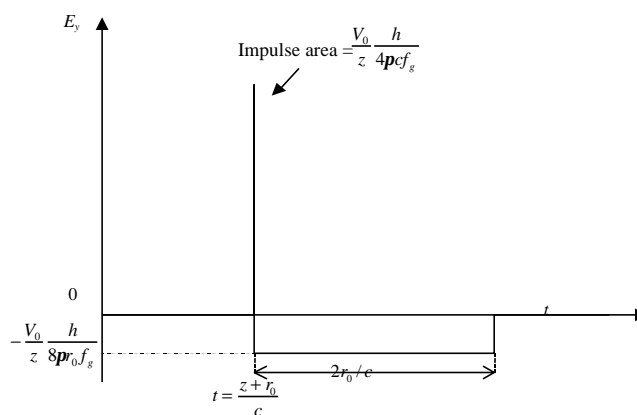


**Fig. 3-9:** Step response on boresight of TEM horn

Another possibility of calculating the antenna impedance and the radiated field are by numerical modelling of the TEM horn using the method-of-moments [4] or finite-difference time-domain (FDTD) code. Some didactic simulations of TEM horns using FDTD are found in [18].

### 3.4.2. Study of the wire Model

An accurate model of the TEM Horn is found in the wire method, where the antenna plates are replaced by a set of infinitely thin wires. The model was originally developed for the electromagnetic performance analysis of Electro-Magnetic Pulse (EMP) simulators [26][27], but can be used as a model for the air-filled TEM horn. The wire method is a time-domain-based method. The transient electromagnetic field emitted by a TEM horn antenna is considered to be the sum of the transient electromagnetic fields emitted by each individual wire.

The advantage of the wire model is that it provides at the same time an analytic expression for the early time radiated far field as for the surge impedance. Furthermore, the expressions of the far field and the antenna impedance are simple which makes them convenient for simulations and design purposes.

In the model the following assumptions are made. The current on the antenna plates is strictly radial and travels with the speed of light. As we are only interested in the TEM

mode of the antenna, this is an acceptable approximation. Furthermore we assume that the waveform and amplitude of the travelling current is constant along the wire, that the wires are infinitely thin and that the current is totally absorbed at the end of the antenna. In reality however a part of the current will bounce back at the antenna-end towards the feed point of the antenna. This phenomenon will cause late time ringing in the antenna, which will be omitted in this approach.

***The radiation by one wire***

In a first step the field radiated by a wire of length  $L$  is studied. The geometry of the wire and the associated co-ordinates are shown in Fig. 3-10. The co-ordinates on the wire are indicated with a prime.

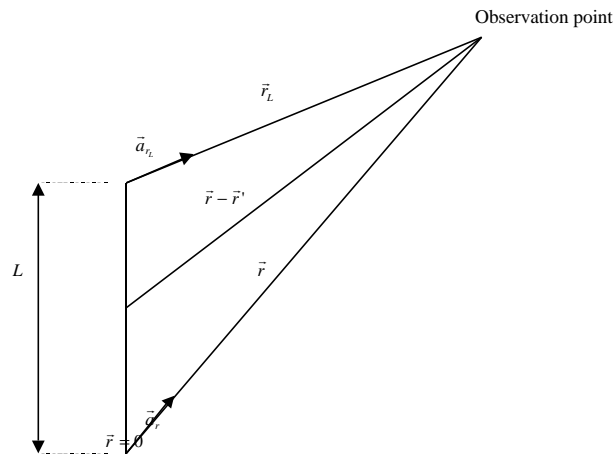


**Fig. 3-10:** Co-ordinate system for the study of the wire

Suppose a current pulse  $I_{wire}(t)$  is applied at the wire at  $\vec{r} = 0$ . The radial current distribution on the wire is then

$$I(r', t) = I_{wire}(t - r'/c) \tag{3.5}$$

with  $r' = |\vec{r}'|$ . The radiated electric field can be written as

$$\vec{E}(\vec{r}, t) = -\vec{\nabla} f(\vec{r}, t) - \frac{\partial \vec{A}(\vec{r}, t)}{\partial t} \quad (3.6)$$

with  $\vec{A}(\vec{r}, t)$  the vector potential and  $f(\vec{r}, t)$  the scalar potential given by

$$\frac{\partial f(\vec{r}, t)}{\partial t} = -c^2 \vec{\nabla} \cdot \vec{A}(\vec{r}, t) \quad (3.7)$$

For a wire of length  $L$ , the vector potential is written as

$$\vec{A}(\vec{r}, t) = \left[ \frac{\mu_0}{4\pi} \int_0^L \frac{I_{wire}(t - r'/c)}{|\vec{r} - \vec{r}'|} dr' \right] \vec{a}_r \quad (3.8)$$

with  $\vec{a}_r$  the unit vector along the wire.

After substitution of (3.7) and (3.8) in (3.6), the electric field radiated by one wire

$\vec{E}_{wire}(\vec{r}, t)$  can be calculated [26] and is expressed as

$$\begin{aligned} \vec{E}_{wire}(\vec{r}, t) = & -\frac{1}{4\pi\epsilon_0} \left\{ \frac{\vec{a}_r}{r^2} q\left(t - \frac{r}{c}\right) - \frac{\vec{a}_{r_L}}{r_L^2} q\left(t - \frac{L+r_L}{c}\right) \right\} \\ & - \frac{Z_0}{4\pi} \left\{ \frac{\vec{a}_{r'} - \vec{a}_r \cdot (\vec{a}_{r'} \cdot \vec{a}_r)}{r(1 - \vec{a}_{r'} \cdot \vec{a}_r)} I_{wire}\left(t - \frac{r}{c}\right) - \frac{\vec{a}_{r'} - \vec{a}_{r_L} \cdot (\vec{a}_{r'} \cdot \vec{a}_{r_L})}{r_L(1 - \vec{a}_{r'} \cdot \vec{a}_{r_L})} I_{wire}\left(t - \frac{L+r_L}{c}\right) \right\} \end{aligned} \quad (3.9)$$

with  $r = |\vec{r}|$ ,  $r_L = |\vec{r}_L|$  the distance between the observation point and the end of the wire,  $Z_0$  the impedance of free space, and  $q$  the charge on the wire given by

$$q(t) = \int_0^t I_{wire}(\mathbf{t}) dt \quad (3.10)$$

For a better insight of the radiation by a wire, we show in Fig. 3-11 some snapshots of the radiated field of one wire on a ground-plane. The snapshots are calculated on a 2mm by 2mm grid using equation (3.9). The vertical oriented wire, shown in white on the snapshots, has a length  $L$  of 10 cm. The feed point of the wire is downwards. In the simulation, the excitation current is a Gaussian pulse with a full width at half maximum (FWHM) of 40 ps. If  $t_a = L/c$  is the time for the current to travel towards the end of the wire, the snapshots are given at  $t = 0.5t_a$ ,  $t = t_a$ ,  $t = 1.5t_a$  and  $t = 2t_a$ . In each snapshot, the electric field is represented in magnitude.

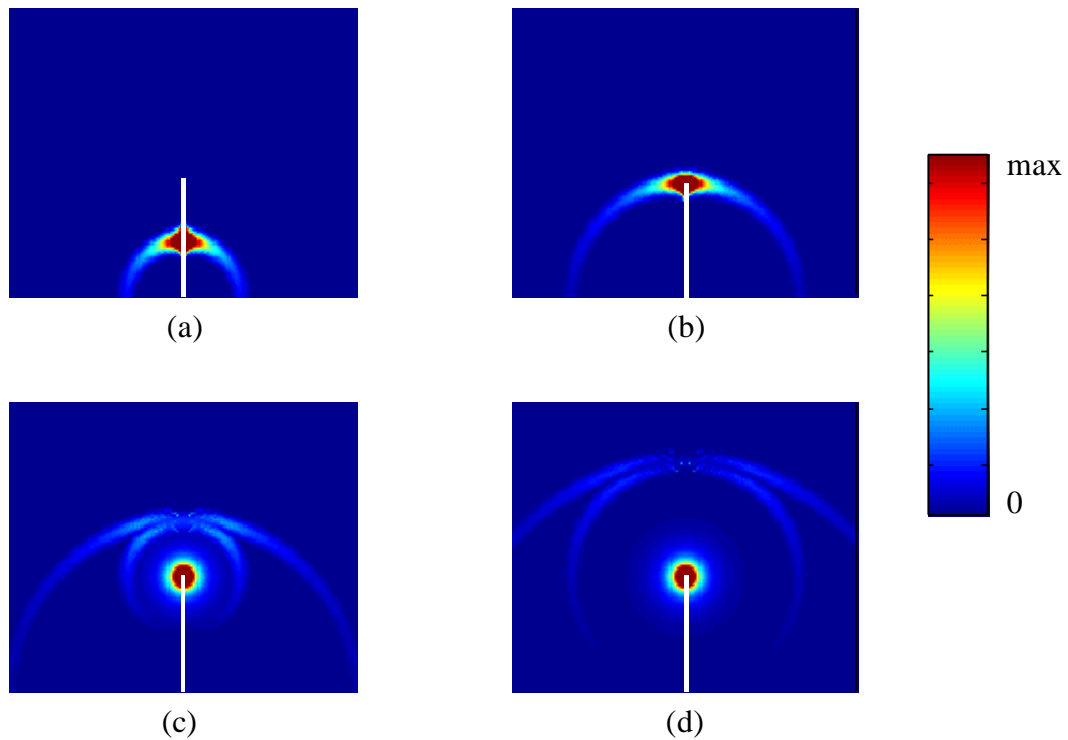


**Fig. 3-11:** Magnitude of the radiated electric field by one wire on a ground-plane.

Snapshots taken at

$$(a) t/t_a = 0.5 \quad (b) t/t_a = 1$$

$$(c) t/t_a = 1.5 \quad (d) t/t_a = 2$$

On the snapshots we see that a first spherical wave, centred at the feed point  $\vec{r} = 0$ , is produced when the current pulse enters the wire. A second spherical wave, centred at  $\vec{r}_L = 0$  is produced when the current reaches the open end of the wire. Because the second wave corresponds with a deceleration of charges, it will have a field opposite to the first wave. This is however not visible on the snapshots because only the field magnitude is shown. The electric field concentrated around the wire end in snapshot (c) and (d) is a static electric field due to the accumulated charges at the open end of the antenna. The charges stay there because in the model the current is absorbed at the wire end. In (3.9) it can be seen that this static field decreases with  $1/r_L^2$ .

A similar analysis in the time domain of the radiated electric field by a wire is found in [28], providing a good physical understanding of radiation phenomena.

### *The current distribution on the antenna plate*

In a next step the current distribution on the antenna plate is considered. The geometry of the antenna plate and the associated co-ordinates are shown in Fig. 3-12. Suppose that a total current  $I_0(t)$  is applied at the antenna feed and that the antenna plate is infinitely thin.

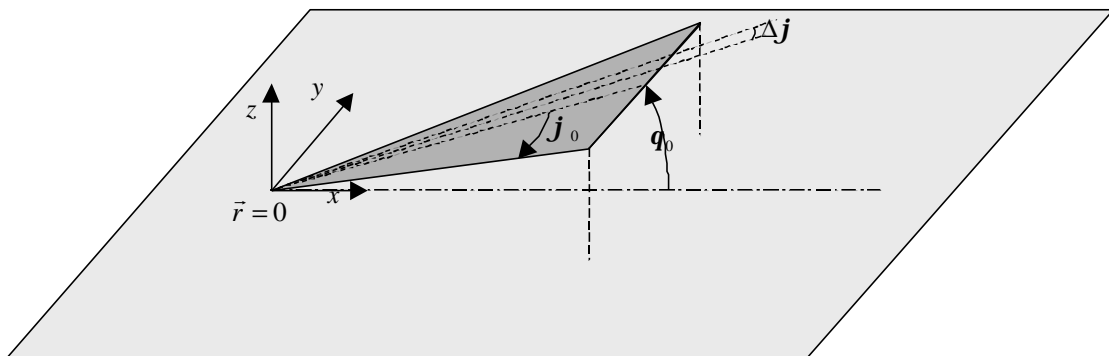


**Fig. 3-12:** The geometry of the antenna plate and the associated co-ordinates

In this case, the current on the plates can be considered as a radial directed current surface density  $\vec{J}_S(\vec{r}', t)$ . The co-ordinates on the plate's surface S are indicated with

a prime. The radial distribution of the current surface density is dictated by  $I_0(t - |\vec{r}'|/c)$ . The azimuth distribution of the current surface density is governed by a function  $F(\mathbf{j} \mathbf{j}_0)$ . According to the current distribution on a micro strip, the current azimuth distribution function is taken [26]

$$F(\mathbf{j} \mathbf{j}_0) = \frac{1}{p\sqrt{\mathbf{j}_0^2 - \mathbf{j}^2}} \quad (3.11)$$

Note that the current azimuth distribution function is normalised, so that

$$\int_{-\mathbf{j}_0}^{\mathbf{j}_0} F(\mathbf{j} \mathbf{j}_0) d\mathbf{j} = 1 \quad (3.12)$$

Fig. 3-13 shows a plot of the azimuth distribution function for  $\mathbf{j}_0 = 30^\circ$ . We notice that the current surface density will be more important near the side edges of the antenna plate.

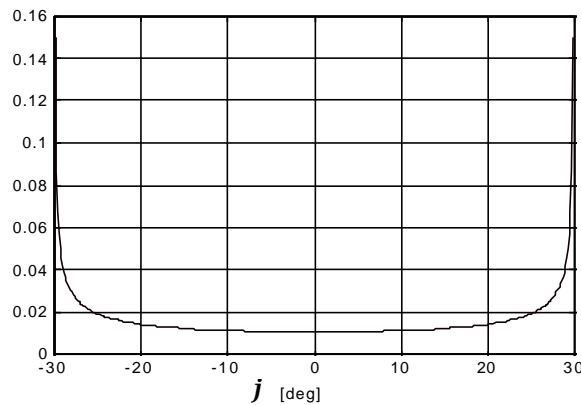


**Fig. 3-13** : Azimuth current distribution function on the antenna plate

***Total field radiated by the TEM horn***

In the next step, the antenna plate is replaced by a mesh of  $N$  radial wires with a common apex. Each wire  $i$  is characterised by an azimuth angle

$$\mathbf{j}_i = (i - \frac{1}{2})\Delta\mathbf{j} - \mathbf{j}_0 \quad i = 1, 2, \dots, N \quad (3.13)$$

with

$$\Delta\mathbf{j} = \frac{2\mathbf{j}_0}{N} \quad (3.14)$$

and an elevation angle

$$\mathbf{q}_i = \arcsin(\sin\mathbf{q}_0 \cos\mathbf{j}_i) \quad (3.15)$$

The current in wire  $i$  is given by

$$I_{\text{wire},i}(t) = I_0(t) \cdot \int_{\mathbf{j}_i - \Delta\mathbf{j}/2}^{\mathbf{j}_i + \Delta\mathbf{j}/2} F(\mathbf{j}, \mathbf{j}_0) d\mathbf{j} \quad (3.16)$$

Finally the total field radiated by the TEM horn is obtained by summing the field expression from each individual wire with its current:

$$\vec{E}_{\text{Tot}}(\vec{r}, t) = \sum_{i=1}^N \vec{E}_{\text{wire},i}(\vec{r}, t) \quad (3.17)$$

Note that, as each wire in the TEM horn has an image wire with an oppositely directed current, all the terms involving the charges  $q(t - r/c)$  are cancelled out.

In Fig. 3-14 a simulation of a TEM horn is shown using the wire model. The antenna has a length  $L$  of 10 cm,  $\mathbf{j}_0 = 25^\circ$  and  $\mathbf{q}_0 = 10.2^\circ$ . In the four snapshots the  $xz$ -plane is represented (see Fig. 3-12). The intersections of the antenna plates with the  $xz$ -plane are shown in white. At  $t = 0$  s a Gaussian current pulse (the same as in the previous simulation with the single wire) is applied at the antenna feed point. The snapshots are given at respectively  $t = 0.5t_a$ ,  $t = t_a$ ,  $t = 1.5t_a$  and  $t = 2t_a$ , with  $t_a$  the time for the current pulse to reach the end of the antenna plates. The magnitude of the electric field is in each snapshot re-scaled and plotted on a colour scale.

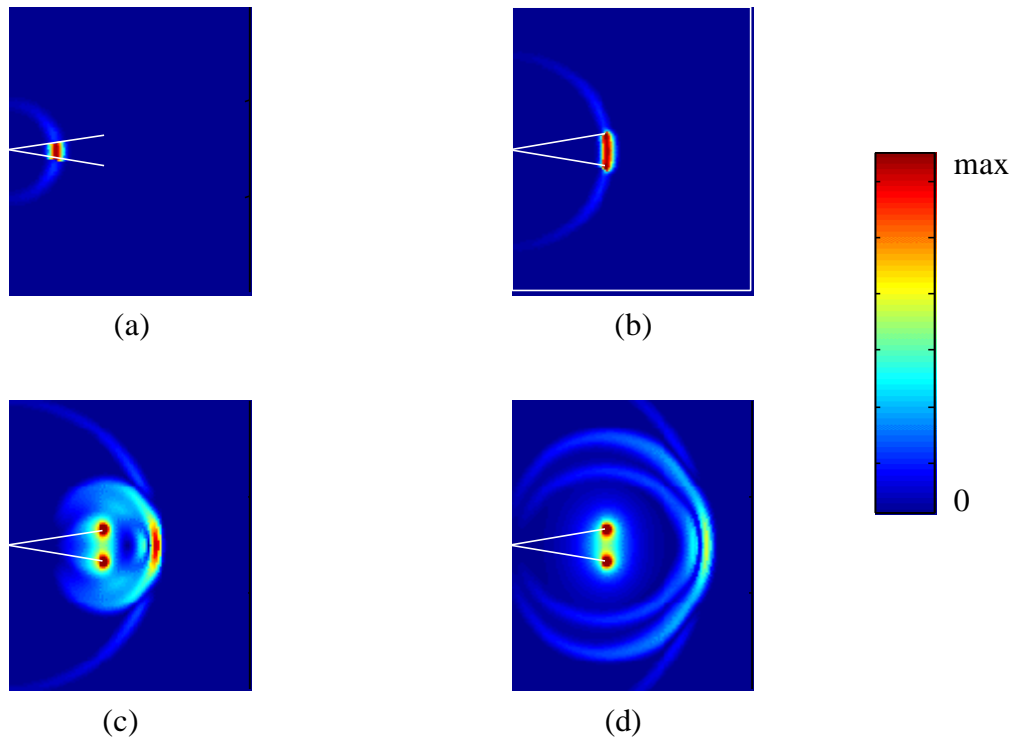


**Fig. 3-14 :** Magnitude of the radiated electric field in the  $xz$ -plane by a TEM horn.

Snapshots taken at

$$(a) t/t_a = 0.5 \quad (b) t/t_a = 1$$

$$(c) t/t_a = 1.5 \quad (d) t/t_a = 2$$

On snapshot (a) and (b) we see the pulse-shaped wave travelling between the antenna plates. Note the wave on the outside of the antenna plates. This is also a spherical

wave centred at the antenna feed, but with an electrical field opposite to the one inside the antenna (the sign is not visible on the snapshots because the magnitude of the field is plotted). This wave is important to explain the negative “pre-pulse” radiated by the dielectric-filled TEM horn (see Section 3.5). It is also at the origin of the pre-pulse encountered by the IRA antenna. On snapshot (c) and (d) the static electric field at the antenna end, due to the accumulation of charges, is visible.

The field radiated on boresight (in the x-direction) has the shape of the first time derivative of the current pulse (this can not be seen in previous figure, as only the magnitude of the field is represented). To show this we plot in Fig. 3-15 the normalised  $E_z$  component of the electric field as function of time in a point on the x-axis at 30 cm from the antenna feed. In Fig. 3-15 (a) the Gaussian current pulse is represented.

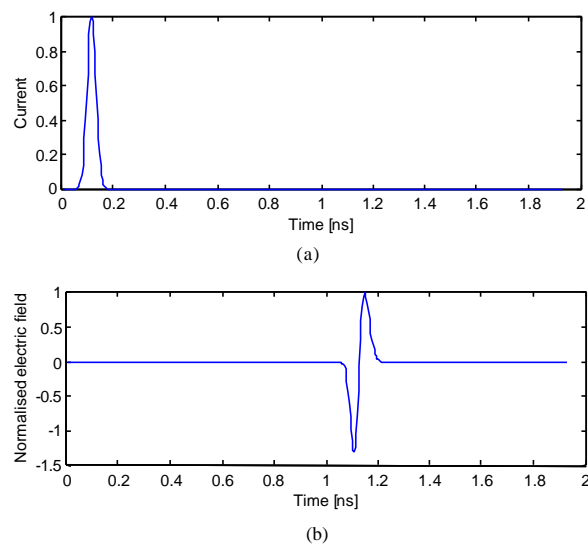


**Fig. 3-15:** (a) The Gaussian current pulse,  
(b) the  $E_z$  component on the x-axis at 30 cm from the antenna feed

### *The surge impedance of the TEM horn*

The wire model can also be used to calculate an analytic expression of the surge impedance of the TEM horn. Therefore we first have to calculate the early time electric field in the antenna, which means

$$t < \frac{L}{c} \quad (3.18)$$

In this case all the terms involving  $r_L$  vanish and the expression of the electric field in the antenna can be simplified. By definition, the surge impedance can be found from

$$Z = \frac{V(r)}{I_0(t - r/c)} = \frac{-\int_{\mathbf{V}} \vec{E}_{in\ antenna} \vec{dl}}{I_0} \quad (3.19)$$

with the integration path  $\mathbf{V}$  chosen as an arc in the xz plane, so

$$Z = \frac{-\int_{-q_0}^{q_0} \vec{E}_{in\ antenna} r \vec{a}_q dq}{I_0} \quad (3.20)$$

In this model the surge impedance (for  $L < \infty$ ), and hence the characteristic impedance along an infinite TEM horn ( $L = \infty$ ), is given by [26]

$$Z = \frac{Z_0}{4p} \sum_{i=1}^N \left[ \ln \frac{1 - \cos \mathbf{j}_i \cos 2\mathbf{q}_i}{1 - \cos \mathbf{j}_i} \int_{j_i - \Delta j / 2}^{j_i + \Delta j / 2} F(\mathbf{j} \mathbf{j}_0) d\mathbf{j} \right] \quad (3.21)$$

with  $F(\mathbf{j} \mathbf{j}_0)$  the azimuth current distribution on the antenna plates,  $N$  the number of wires of the wire mesh and  $\mathbf{j}_i$  and  $\mathbf{q}_i$  the azimuth and elevation angle of the  $i^{th}$  wire. We can see that the surge impedance given by the analytical expression (3.21) is only

function of the angles  $\mathbf{j}_0$  and  $\mathbf{q}_0$ , as we expected. To validate the analytical expression (3.21), we measured the surge impedance of one antenna plate on a ground-plane by time domain reflectometry (TDR) and compared it with the calculated surge impedance. The geometric configuration is the same as shown in Fig. 3-12. The antenna plate has a length of 10 cm and a fixed azimuth half angle  $\mathbf{j}_0$  of  $30^\circ$ . The set-up gave the flexibility of changing the elevation angle  $\mathbf{q}_0$  very easily.

A TDR measurement generates a step with a short rise-time and measures the reflected signal from impedance discontinuities, to determine the reflection coefficient versus time. From this reflection coefficient, the impedance characteristics versus distance of the device under test is calculated. In our TDR measurements, a step with a rise time of 45ps is used.

For different values of the elevation angle  $\mathbf{q}_0$  the surge impedance at the middle of the antenna plate was measured and compared to the values given by (3.21). For the calculation, the number of wires  $N$  used in (3.21) was 400. As the measurement was performed on a half TEM horn (one antenna plate on a ground-plane) the measured surge impedance by TDR will be half the surge impedance of a complete TEM horn (two antenna plates). Therefore, the measured surge impedance has to be multiplied by 2. The results are plotted in Fig. 3-16.

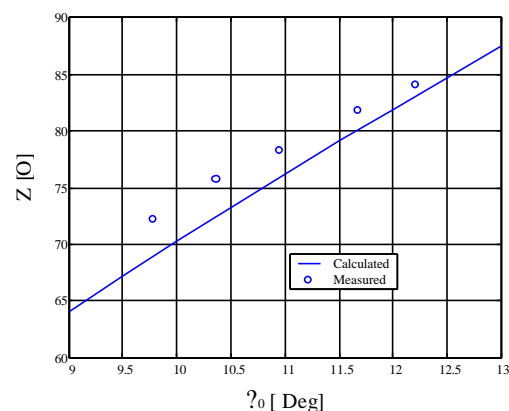


**Fig. 3-16:** Measured and calculated surge impedance of air-filled TEM horn

Expression (3.21) of the surge impedance given by the wire method turns out to be very accurate for predicting the surge impedance. The wire method slightly underestimates the surge impedance. The maximal discrepancy between the theoretical model and the experimental data is 5%. A quick comparison with the two methods given in Section 3.4.1 learns that this method performs better, and is thanks to its analytical form, flexible for design purposes. The small discrepancy is probably due to the fact that the wave guided by the antenna plates is actually not purely TEM. Higher orders can be introduced by a bad feed at the feed point and of course by edge diffraction.

### 3.4.3. Design of air-filled TEM horn

In a first part of the thesis, some work was done on the design of air-filled TEM horns. The purpose was not to develop nor to enhance such an antenna, but to validate the wire model. Further we wanted to study the behaviour of the air-filled TEM horn so that its design could serve as a basis for the development of the dielectric-filled TEM horn. We will not go into all the details of the design, but only discuss aspects that are relevant for the dielectric-filled TEM horn. The air-filled TEM horn will nevertheless be used throughout the work to compare with the performance of the dielectric-filled TEM horn.

For the design of a TEM horn, 3 parameters:  $L$ ,  $\mathbf{j}_0$  and  $\mathbf{q}_0$  have to be determined, and this as a function of the user-defined antenna characteristics like fractional bandwidth, antenna pattern, surge impedance, etc.

In this type of antenna,  $L$  will mainly influence the lower cut-off frequency and the fractional bandwidth [25][29]. It is not easy to extract a value for  $L$  using the discussed models. As a rule of thumb, the length  $L$  must be at least half a wavelength of the lowest frequency [4]. We opted for a small antenna with a length  $L=10$  cm. This means a lower cut-off frequency of 1.5 GHz, which is too high according to the design goal stated in Section 3.3.

The first fundamental question is on the impedance of the antenna. In the past, many antenna designers have tried to match the antenna surge impedance at the antenna end to the wave impedance of free space  $Z_0 = 120\pi$ . In their design they gradually changed the surge impedance from  $50 \Omega$  at the antenna feed to  $377 \Omega$  at the antenna end by continuously changing along the plates the angles  $\mathbf{j}_0$  (flaring out the antenna plates) and/or  $\mathbf{q}_0$  (tapering the antenna plates). The aim of the matching is to avoid reflections at the open end of the antenna. In [18] it is shown by simulation and measurement that the concept of matching the surge impedance to that of free space to eliminate reflections is erroneous and that reflections will occur. Further, tapering and flaring out the antenna plates will disturb the TEM mode in the antenna [19] and hence create higher modes. Later on in this work we want to model the antennas in the time domain. In the application of landmine detection, the targets are relatively close to the antennas ( $\pm 30\text{cm}$ ), and these higher modes will make the model less accurate near the antennas.

For these two reasons we have chosen to keep the surge impedance constant over the whole antenna. This means that no tapering or flaring of the antenna plates is used. In the design of the air-filled TEM horn we opted for an antenna impedance of  $80 \Omega$  and not for the characteristic impedance of the feed cable, *i.e.*  $50 \Omega$ , as is usually done for this kind of antenna. The reasons for this will be explained in Section 3.5.1.

An infinite number of couples  $(\mathbf{j}_0, \mathbf{q}_0)$  that yield a surge impedance of  $80 \Omega$  are possible, so we have to determine one more parameter. In the design phase of the air-filled TEM horn, we used the wire model to optimise the angle  $\mathbf{j}_0$  for a given  $L$  and surge impedance of the antenna. As a criterion for the optimisation we looked at the peak-to-peak value of the radiated E-field and the half-power beamwidth. In Table 3-1 a set of couples  $(\mathbf{j}_0, \mathbf{q}_0)$  leading to a surge impedance of  $80 \Omega$  is given in steps of  $5^\circ$  for the azimuth angle. The couples are calculated using equation (3.21) in an implicit way.

$\mathbf{j}_0$ [ $^\circ$ ]	15	20	25	30	35	40	45
$\mathbf{q}_0$ [ $^\circ$ ]	5.5	7.4	9.5	11.6	14	16.5	19.4

**Table 3-1:** Couples  $(\mathbf{j}_0, \mathbf{q}_0)$  leading to a surge impedance of  $80 \Omega$

For each couple, the radiated transient electromagnetic field is calculated in the H-plane (*i.e.* the xy-plane in Fig. 3-12) at a radius of one meter from the antenna feed point by equation (3.17). The current pulse used in (3.17) has a Gaussian shape with a Full Width at Half Maximum (FWHM) of 80 ps. This means that the radiated field will be a monocycle as shown in Fig. 3-15 (b). For each of the couples ( $\mathbf{j}_0, \mathbf{q}_0$ ) the peak-to-peak value of the radiated E-field (in [V/m]) is plotted on a polar diagram to form a kind of non-normalised radiation pattern (Fig. 3-17).

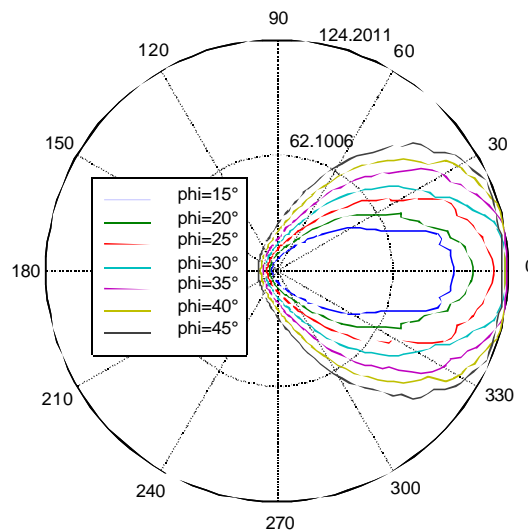


**Fig. 3-17:** Peak-to-peak value of the radiated E-field in H-plane for different values of  $\mathbf{j}_0$

The figure shows clearly a maximum peak-to-peak amplitude on boresight for values of  $\mathbf{j}_0$  between  $30^\circ$  and  $40^\circ$ . The maximum is flat, but for  $\mathbf{j}_0 > 40^\circ$  the peak-to-peak amplitude decreases again and the half-power beamwidth increases. The different values of  $\mathbf{j}_0$  and  $\mathbf{q}_0$  have little effect on the bandwidth. As a conclusion we can say that the optimal angle  $\mathbf{j}_0$  for a surge impedance of  $80 \Omega$ , is found to be  $30\text{-}40$  degrees. In our design we opted for  $\mathbf{j}_0 = 30^\circ$ , which leads to an angle  $\mathbf{q}_0 = 11.2$  (see Fig. 3-16, measured data).

A picture of the air-filled TEM horn is shown in Fig. 3-18. Special attention was paid at the feed-point. The feed point has to be mechanically robust but care must be taken

that it does not introduce a too large impedance discontinuity. A schematic representation of the feed point is given in Fig. 3-19.



**Fig. 3-18:** Picture of the air-filled TEM horn

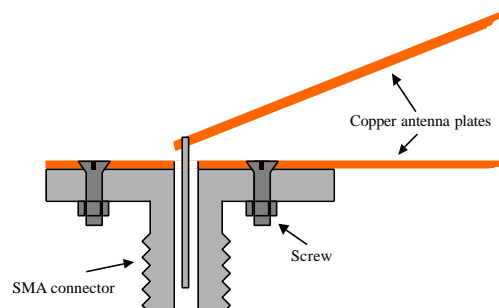


**Fig. 3-19:** Schematic representation of the feed point

To validate the wire model, we compare in Fig. 3-20 the measured antenna pattern in the H-plane at 5 GHz with the antenna pattern, calculated by the wire model. The frequency domain measurements were performed in an anechoic chamber in the University of Leuven. For the calculated pattern, we first calculated the radiated E-field in the time domain and then converted to the frequency domain using an FFT. The wire model turns out to be also very accurate in the calculation of the radiation pattern. The 3-dB beamwidth in the H-plane is around  $45^\circ$ . In Fig. 3-21 the  $|S_{11}|$  parameter of the air-filled TEM horn is shown (reference impedance is  $50 \Omega$ ). From the  $|S_{11}|$  plot, it can be seen that the TEM horn has a very large bandwidth.

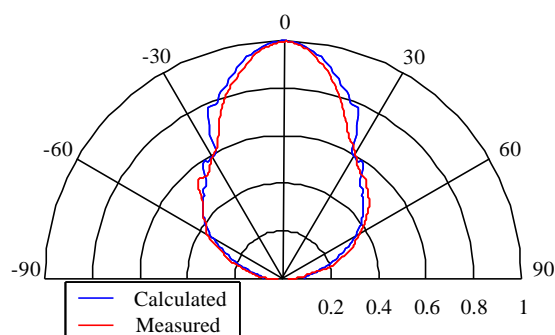


**Fig. 3-20:** Measured (red) and calculated (blue) antenna pattern in H-plane at 5 GHz

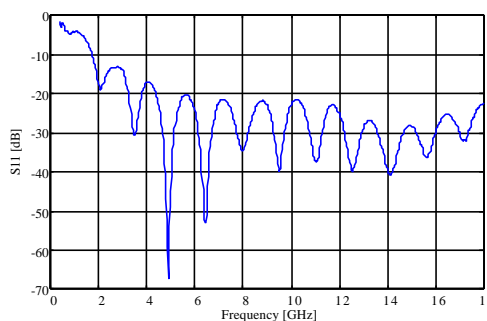


**Fig. 3-21:**  $|S_{11}|$  parameter of air-filled antenna

### 3.5. Dielectric-filled TEM horn

In order to improve directivity and to reduce the physical size of the antenna without limiting too much the bandwidth, we will fill the TEM horns with a dielectric, characterised by a real relative permittivity  $\epsilon_r$  and a loss tangent. Thanks to the dielectric, the propagation speed of the TEM wave between the antenna plates will be divided by  $\sqrt{\epsilon_r}$ , in other words, the electrical length of the antenna will be extended by a factor  $\sqrt{\epsilon_r}$ . Further the dielectric filling will reduce the surge impedance of the antenna by approximately a factor of  $\sqrt{\epsilon_r}$ . To preserve the same surge impedance as before the filling, one can increase the angle  $q_0$ , which again means an improvement of directivity.

#### 3.5.1. Influence of the filling

The infinite air-filled TEM horn is equivalent to a pure TEM transmission line. Filling this transmission line would result in an inhomogeneous quasi-TEM structure. If this inhomogeneous transmission line becomes of finite length, the structure will be very complex to model and a numerical modeling would be more appropriate. In our approach we based the design on the air-filled antenna and on some principles from micro strip theory.

To study the influence of the filling, the air-filled TEM horn from previous section ( $L=10\text{cm}$ ,  $j_0=30^\circ$  and  $q_0=11.2^\circ$ ) is filled with a silicone, characterised by a real relative permittivity  $\epsilon_r$  of 2.89 and a loss tangent of 0.0084 at 1 GHz.

#### *Influence on the surge impedance*

In the static analysis approximation, used in strip-line theory, the characteristic impedance of a strip-line without dielectric decreases with a factor of  $\sqrt{\epsilon_{r,eff}}$  when a substrate with a relative dielectric constant  $\epsilon_r$  is added. The effective relative

permittivity  $\epsilon_{r,eff}$  is introduced as a correction on  $\epsilon_r$  by the fact that the structure becomes quasi-TEM after adding the substrate. An expression for the effective relative permittivity as a function of  $\epsilon_r$ ,  $w$  the width and  $h$  the height of the micro strip is given by Hammerstad and Jensen [24]:

$$\epsilon_{r,eff} = \frac{\epsilon_r + 1}{2} + \frac{\epsilon_r - 1}{2} \left[ 1 + \frac{10h}{w} \right]^{0.555} \quad (3.22)$$

The effective relative permittivity of the silicone used in the design is calculated using (3.22) as  $\epsilon_{r,eff} = 2,55$ . According to strip-line theory, the surge impedance of the TEM horn will be reduced by a factor  $\sqrt{\epsilon_{r,eff}} = 1,6$ . The dielectric-filled TEM horn antenna impedance is chosen to match the  $50 \Omega$  driving cable so that the part of the transient travelling current that bounces back at the antenna aperture towards the excitation source, will meet no mismatches on its way back. In this way antenna ringing will be avoided. If a filled TEM horn with a surge impedance of  $50 \Omega$  is purchased, an empty TEM horn of  $80 \Omega$  is needed, which explains the choice of the surge impedance in Section 3.4. Fig. 3-22 shows the surge impedance of the TEM horn before and after the filling. The measurement is done by TDR, using a step with a rise time of 45 ps. The mismatch at the feed point introduced by the connector is small. The reflection coefficient is less than 5%, which means that only 0.25% of the instantaneous transmitted power at the feeding point is reflected back towards the source. The surge impedance along the antenna varies between 45 and  $55 \Omega$ , so the reduction of surge impedance due to the filling is indeed found to be the expected  $\sqrt{\epsilon_{r,eff}}$ . Note also that the electrical length of the antenna after filling is extended.

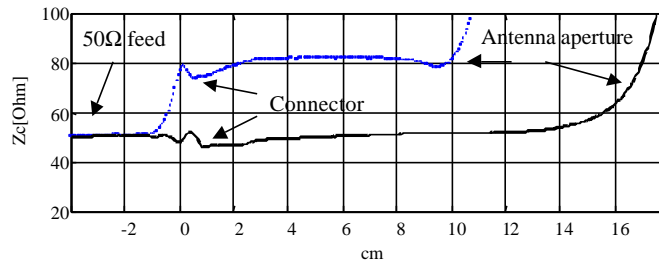


**Fig. 3-22:** Surge impedance of the TEM horn before (dotted) and after (solid) the filling

### *Influence on the antenna pattern and the bandwidth*

The filling of the antenna will certainly have its effect on the antenna pattern and the frequency band of the antenna. As the electrical length of the dielectric-filled horn is extended, it is expected that the antenna will be more directive and that the lower cut-off frequency will decrease. Fig. 3-23 shows the antenna gain of the air-filled TEM horn and the dielectric-filled TEM horn. The gain is measured in an anechoic chamber using calibrated horn antennas, so losses due to the reflection coefficient of the TEM horn is included in the gain. The whole frequency band of the dielectric-filled TEM horn is reduced (approximately by a factor  $\sqrt{\epsilon_{r,eff}}$ ) and has shifted slightly towards the lower frequencies. Fig. 3-24 shows the antenna pattern in the H-plane at 5 GHz. before and after the filling. As expected, the dielectric-filled horn is more directive. This also means that the dielectric-filled TEM horn will be less sensitive to external EM interference, which is an advantage in this application.

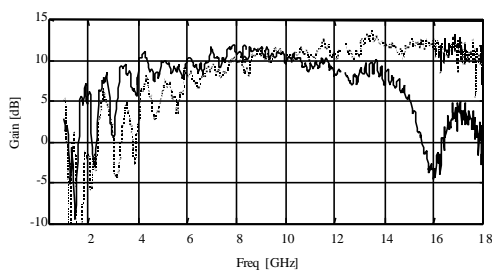


**Fig. 3-23 :** Antenna gain of the air-filled (dotted) and the dielectric-filled TEM horn (solid)

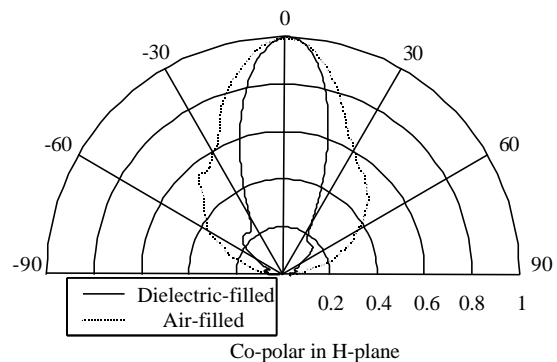


**Fig. 3-24 :** H-plane pattern at 5 GHz before (dotted) and after the filling (solid)

### 3.5.2. Design of the dielectric-filled TEM horn

In previous section the air-filled TEM horn was filled with a dielectric to study the influence of the filling. Antenna measurements showed that even after filling the lower cut-off frequency was still too high to meet our design goals. So in a next (and final) design of a dielectric-filled TEM horn we had to increase the length  $L$  of the antenna. On the other hand, the antenna's dimensions and weight had to stay limited to guarantee a good mobility of the antennas (see design goals). This means we had to compromise on the length and a length  $L$  of 12 cm was chosen.

Further we noticed in previous design a problem with the transition from the unbalanced current in the coax feed cable to the balanced current on the antenna plates. Without precaution an unbalanced current component will be reflected by the antenna feed and appear on the outer conductor of the coax. This current will be the origin of a unwanted TEM mode between the horn conductors and the coax outer conductor. The coax outer conductor will act as an antenna and make the setup sensitive to persons and material in the direct neighborhood of the coax. This situation can be remedied by putting chokes (ferrite cylinders) around the feeding cable. A choke has the following equivalent scheme (Fig. 3-25) and will hence suppress the current pulse on the coax exterior.

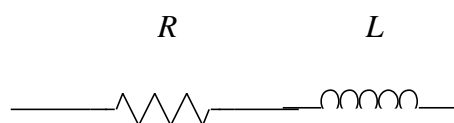


**Fig. 3-25:** Equivalent scheme of choke

Another solution in order to avoid currents on the coax is found in a balun. The problem here is that the balun has to be broad-banded. In literature not many examples of broad-band baluns are found. In [30] some broad-band baluns are proposed, based on the use of ferrite cores. A bandwidth ratio of 20:1 is obtained. In [31] an impedance matching transition from a coaxial line to a balanced two conductor line is accomplished by tapering the outer conductor of the coax towards a line. This

results in a balun with a bandwidth ratio of 100:1, but the balun is too long and not practical to use. In our design we tried out a similar kind of balun. The principle of this balun is based upon an electrostatic reasoning [8]. In a first part of the antenna, an unbalanced configuration of one antenna plate on a ground-plane is imitated (see Fig. 3-26 (a)). The inner conductor of the coax is connected to the upper antenna plate. The currents on the coax outer conductor can only arise from leakage of the field from the upper antenna plate to the coax outer conductor around the edge of the ground-plane. The larger the ground-plane, the smaller the current on the coax outer conductor. This current would be zero for an infinite ground-plane. In the second part of the antenna, the balanced configuration with the two symmetrical antenna plates is achieved (Fig. 3-26 (b)). In between gradual transition from the unbalanced towards the balanced configuration is obtained by tapering the antenna plates (see Fig. 3-27).

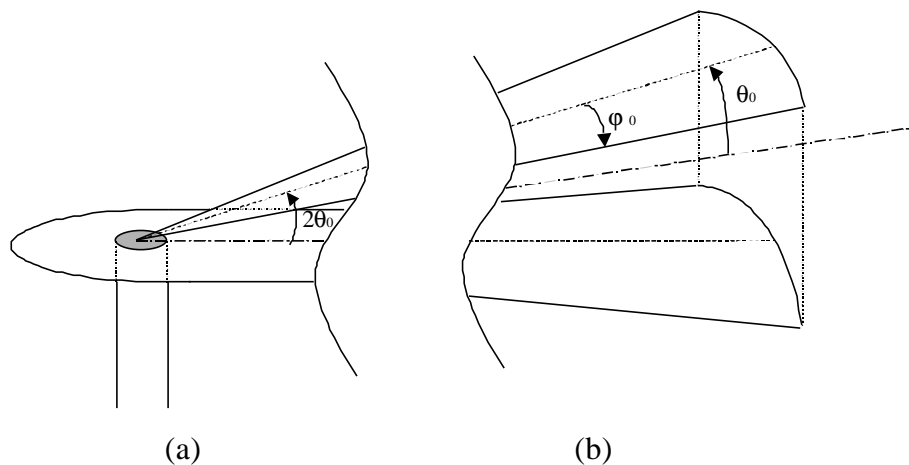


**Fig. 3-26:** (a) unbalanced configuration (b) balanced configuration

The balun influences the surge impedance of the antenna. The transition from the unbalanced towards the balanced configuration will introduce a slight change in surge impedance along the antenna. Expression (3.21) gives the surge impedance of a complete TEM horn, so in the unbalanced part of the antenna (one antenna plate on a ground-plane), the surge impedance is halve the value given by expression (3.21). But the elevation half-angle (angle between one antenna plate and the symmetry plane of the antenna) is  $2q_0$  and not  $q_0$  as in the balanced part of the antenna. The surge impedance of the second part is calculated in a normal way using expression (2.21). In

total, the surge impedance of the unbalanced part is found to be a little inferior to the surge impedance of the balanced part of the antenna.

The antenna impedance of the dielectric-filled TEM horn is chosen to match the  $50 \Omega$  driving cable. Doing so, the part of the transient travelling current that bounces back at the antenna aperture towards the excitation source, will meet no mismatches on its way back and antenna ringing will be avoided. The principle seems to work well for frequencies in the band of the antenna. According to the optimal apex half-angle of the air-filled TEM horn (see previous section), the angle  $\theta_0$  is chosen to be  $30^\circ$  and the physical length  $L$  of the antenna plates, as already discussed, will be 12 cm. In this design, the antenna plates are not made out of a copper sheet, but etched on a printed circuit board (PCB). Etching the antenna plates limits the weight of the plates and increases the precision in fabrication. Inspired by the wire model, the antenna plates are replaced by a set of 41 wires (Fig. 3-27). The distance between the wires is too small to influence the antenna characteristics, but it forces the currents to be radial and it limits the surface of conducting metal. The latter is very important, when using the antennas in combination with a metal detector. Etching the antenna plates on a PCB makes it more difficult to create a good and robust feed-point. A schematic representation in Fig. 3-28 shows how the implementation of the SMA connector in the PCB is done.

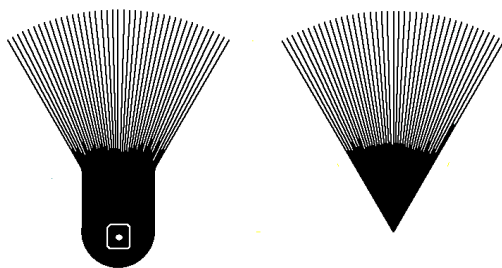


**Fig. 3-27:** Lower and upper antenna plates, etched on a PCB

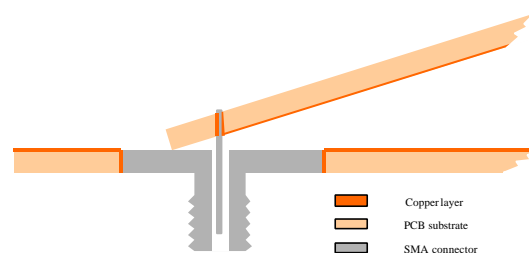


**Fig. 3-28:** Schematic representation of feed point

Taking into account the reduction of the surge impedance due to the filling and taking into account the influence of the balun, an elevation half-angle  $q_0$  (defined in the balanced part) of  $14.5^\circ$  is calculated to match  $50 \Omega$ . This means a surge impedance in the balanced part of  $56 \Omega$ . Summarised, we have  $L=12$  cm,  $j_0=30^\circ$  and  $q_0=14.5^\circ$ , which leads to a physical antenna aperture of 12cm by 6cm.

### 3.5.3. Results of the dielectric-filled TEM horn

Fig. 3-29 illustrates the surge impedance, measured by TDR, along the antenna. Note that the x-axis is calibrated for speed of light. The gradual transition between the unbalanced part (surge impedance around  $55\Omega$ ) and the balanced part (surge impedance around  $65\Omega$ ) is obvious. The reduction of surge impedance due to the filling is again found to be  $\sqrt{\epsilon_{r,eff}}$ . The discrepancy between the measured surge impedance and the wanted one is due to the underestimation of the surge impedance by equation (3.21) (see also Fig. 3-16).

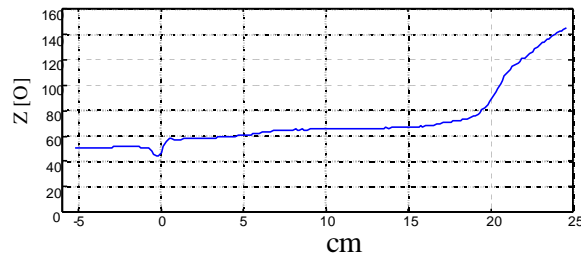


**Fig. 3-29:** Surge impedance of dielectric-filled TEM horn, measured by time domain reflectometry

Most of the antenna characteristics have been measured in the time domain in the installations of the University of Technology in Delft. In Chapter 4 a more accurate description of the antenna is given under the form of its impulse response. For completeness the  $|S_{11}|$  parameter of the antenna is shown in Fig. 3-30. The antenna patterns in H- and E-plane are given in Fig. 3-31. These patterns represent the peak-to-peak value of the radiated impulse in each direction, normalised to one. In this

definition of pattern, **the 3dB beamwidth is  $32^\circ$  in the H-plane and  $65^\circ$  in the E-plane.**

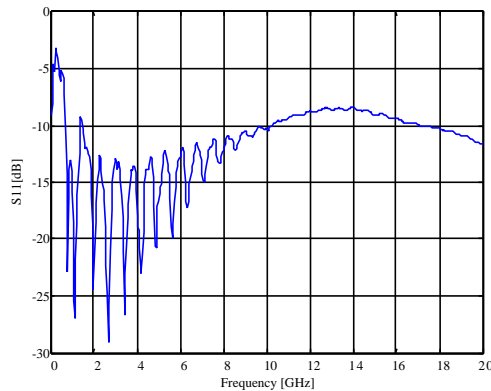


**Fig. 3-30 :**  $|S_{11}|$  parameter of the dielectric-filled TEM horn

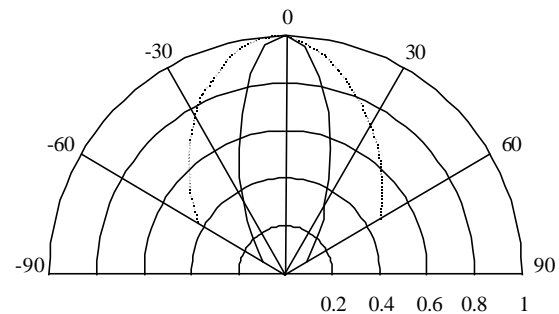


**Fig. 3-31 :** P-t-p antenna patterns in H-plane (solid) and E-plane (dotted)

Interesting to see, because it is closely related to the application, is the main-beam response of two identical antennas. For this time domain measurement the two TEM horn antennas are aligned on boresight of each other. The transmitting antenna is excited with the Gaussian impulse. The received signal is recorded by a 6 GHz digitising oscilloscope. Fig. 3-32 shows the normalised received voltage as a function of time. At  $t < 0.2 ns$  the recorded signal shows a small negative pre-pulse. This pre-pulse is due to the TEM mode that goes in the opposite way around the antenna plates (see simulation in Fig. 3-14). As this wave travels in free space, it will arrive sooner than the wave that travels between the antenna plates. This negative pre-pulse can be reduced by putting radar-absorbing material (RAM) at the outside end of the antenna plates. The RAM also reduces the low frequency ringing of the antenna as we will see in Section 4.5. Around  $t = 1.6 ns$  the reflection on the antenna end is visible. The signal in Fig. 3-32 is taken with the RAM already on the antenna plates. The frequency band of the whole system (transmitter – antennas - receiver), obtained by a time-frequency transformation of the plot in Fig. 3-32, is from 1 GHz up to 5GHz, so the postulated frequency band of 500 Mhz to 4.5 GHz is not reached.

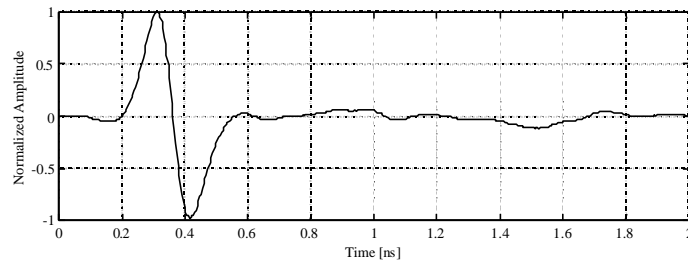


**Fig. 3-32:** Normalised amplitude of the main beam response

### 3.6. Summary

In this chapter, we gave an overview of the exiting GPR antennas and UWB antennas, together with some design goals for GPR antennas in the demining application. The TEM horn seemed to be a good candidate to meet these design goals. In a first step an air-filled TEM horn was studied and developed. An accurate model for design purposes was obtained from the wire method. In order to reduce the physical size of the antenna and to improve the directivity, the antenna was filled with a dielectric. Due to the lack of a good model, the design was based on the air-filled antenna, assuming that the antenna guides a quasi-TEM wave. TDR measurements of the surge impedance showed a slight but acceptable difference with the theory. Antenna measurements revealed that the antennas were more directive and that the frequency range moved towards the lower frequencies. The antenna plates were replaced by a set of wires, which makes them suitable for operating in combination with a metal detector. An ultra-wideband balun was also integrated in the antenna plates. Although we are aware that the actual antennas can still be enhanced, most of the design goals are met. The dimensions of the dielectric-filled TEM horns are small, as needed for the application, and they are capable of radiating and receiving very fast transient pulses, without too much ringing, which is of course important for this application. The cleaner the pulse, the cleaner the backscattered signal, and the more easy it will be to post-process and interpret the data. The antennas, that can be used off-ground, are ready to be integrated in an UWB GPR system.

## REFERENCES

- [1] D. J. Daniels, D. J. Gunton and H. F. Scott, "Introduction to subsurface radar," *IEE Proceedings*, vol. 135, Pt. F, no.4, pp. 278-320, Aug. 1988.
- [2] A. A. Lestari, A. G. Yarovoy and L. P. Ligthart, "Adaptive Antenna For Ground Penetrating Radar," *Eight International Conference on Ground Penetrating Radar*, Gold Coast, Australia, pp. 366-371, May 2000.
- [3] T. T. Wu and R. W. P. King, "The cylindrical antenna with nonreflecting resistive loading," *IEEE Trans. on Antennas Propagat.*, vol. AP-13, pp. 369-373, May 1965. Correction, p.998, Nov. 1965.
- [4] M. Kanda, *Time-Domain Measurements in Electromagnetics*. E. K. Miller, Ed., New York: Van Nostrand Reinhold., 1986, ch. 5.
- [5] J. G. Maloney and G. S. Smith, "A study of transient radiation from the Wu-King resistive monopole – FDTD analysis and experimental measurements," *IEEE Trans. on Antennas Propagat.*, vol. AP-41, no. 5, pp. 668-676, May 1993.
- [6] T. P. Montoya and G. S. Smith, "A study of radiation from several broad-band loaded monopoles," *IEEE Trans. on Antennas Propagat.*, vol. AP-44, no. 8, pp. 1172-1182, Aug. 1996.
- [7] B. Stockbroeck and A. Vander Vorst, "Electromagnetic modes in Conical transmission lines with applications to the linearly tapered slot antenna," *IEEE Trans. on Antennas Propagat.*, vol. AP-48, no. 3, pp. 447-455, March 2000.
- [8] V. Rumsey, *Frequency independent antennas*. New York: Academic Press, 1966.
- [9] B. Stockbroeck and A. Vander Vorst, "Copolar and cross-polar radiation of Vivaldi antennas on dielectric substrates," *IEEE Trans. on Antennas Propagat.*, vol. AP-48, no. 1, pp. 19-25, Jan. 2000.
- [10] R. L. Carrel, "The Characteristic Impedance of Two Infinite Cones Of Arbitrary Cross Section," *IRE Trans. on Antennas and Propagation*, vol. AP-6, pp. 197-201, 1958.
- [11] M. Kanda, "Transients in a Resistively Loaded Linear Antenna Compared with those in a Conical Antenna and a TEM Horn," *IEEE Trans. on Antennas Propagat.*, vol. AP-28, no. 1, pp. 132-136, 1980.

- [12] M. Piette, E. Schweicher and A. Vander Vorst, "An indoor Time-Domain Measurement System for Studying Transient Radar Signatures of Small Scales 3D-Targets," *RADAR '94*, Paris, pp. 518-522, Mai 1994.
- [13] J. G. Maloney and G. S. Smith, "Optimization of a conical antenna for pulse radiation: an efficient design using resistive loading," *IEEE Trans. on Antennas Propagat.*, vol. 41, no. 7, pp. 940-947, July 1993.
- [14] C. E. Baum, "Radiation of impulse-like transient Fields," *Sensor and Simulation Notes*, note 321, Nov. 1989.
- [15] E. G. Farr and C. E. Baum, "Prepulse associated with TEM feed of an IRA," *Sensor and Simulation Notes*, note 337, March 1992.
- [16] C. E. Baum and E. G. Farr, "Impulse radiating antennas," *Ultra-Wideband, Short-Pulse Electromagnetics*, C. E. Baum, H. L. Bertoni, L. Carin, L. B. Felsen, Eds., New York: Plenum Press, 1993, pp. 139-147.
- [17] M. Kanda, "The Effects of Resistive Loading of TEM Horns," *IEEE Trans. Electromagnetic Compatibility*, vol. EMC-24, no. 2, pp. 245-255, 1982.
- [18] K. L. Schlager, G. S. Smith and J. G. Maloney, "Accurate Analysis of TEM Horn Antennas for Pulse Radiation," *IEEE Trans. Electromagnetic Compatibility*, vol. EMC-38, no.3, pp. 414-423, 1996.
- [19] A. P. Lambert, S. M. Booker and P. D. Smith, "Transient Antenna Design parameters for optimising Radiated Pulse," Specialists' Meeting on High Power Microwaves, AGARD, Electromagnetic Wave Propagation Panel, *Proc. 54th*, Ottawa, Canada, ch. 8, May 1994.
- [20] J. F. Aurand, "A TEM-Horn Antenna with Dielectric Lens for Fast Impulse Response," *Ultra-Wideband, Short-Pulse Electromagnetics 3*, C. E. Baum, L. Carin, A. P. Stone, Eds., New York: Plenum Press, 1997, pp. 113-120.
- [21] F. C. Yang and K. S. H. Lee, "Impedance of a Two-Conical-Plate Transmission Line," *Sensor and Simulation Notes*, note 221, 1976.
- [22] F. C. Yang and L. Marin, "Field distribution on a two-conical-plate and a curved cylindrical-plate transmission line," *Sensor and Simulation Notes*, note 229, 1977.
- [23] C. Martel, M. Philippakis and D. J. Daniels, "Time Domain Design of a TEM Horn Antenna for Ground Penetrating Radar," *Millennium Conference on Antennas & Propagation AP-2000*, Davos, Switzerland, vol. II, p. 186, April 2000.

- [24] A. Vander Vorst and D. Vanhoenacker-Janvier, *Bases de l'ingénierie micro-onde*. Brussels: De Boeck & Larcier, 1996.
- [25] E. G. Farr and C. E. Baum, "A Simple Model of Small-Angle TEM Horns," *Sensor and Simulation Notes*, note 340, 1992.
- [26] J. J. A. Klaasen, "An efficient method for the performance analysis of bounded-wave nuclear EMP simulators," *Sensor and Simulation Notes*, note 345, 1992.
- [27] J. J. A. Klaasen, "An efficient method for the performance analysis of bounded-wave nuclear EMP simulators," *IEEE Trans. Electromagnetic Compatibility*, vol. EMC-35, no. 3, pp. 329-338, Aug. 1993.
- [28] G. S. Smith, "Teaching antenna analysis from a time-domain perspective," *Millennium Conference on Antennas & Propagation AP-2000*, Davos, Switzerland, vol. I, p. 435, April 2000.
- [29] B. Scholliers, *Studie van de TEM horn antenna*, Eindwerk, Royal Military Academy, Brussels, BE, 1997.
- [30] C. L. Ruthroff, "Some broad-band transformers," *Proceedings of the IRE*, pp. 1337-1342, Aug. 1959.
- [31] J. W. Duncan and V. P. Minerva, "100:1 bandwidth balun transformer," *Proceedings of the IRE*, pp. 156-164, Feb. 1960.

---

## **Chapter 4. Time domain characterisation of antennas by normalised impulse response**

---

### **4.1. Introduction**

When antennas are excited with a simple harmonic, the frequency dependency of the antenna parameters is usually investigated in the frequency domain over the frequency band of interest. In time domain systems like time domain GPRs, antennas are excited by a fast transient pulse. When using antennas to radiate fast transient pulses, referred to as *time domain antennas*, classical antenna parameters such as gain, radiation pattern, and phase centre, have less meaning [1]. All these parameters are frequency dependent, hence they have to be expressed over the whole frequency band of interest. As time domain antennas have intrinsically a large bandwidth, describing the antenna performances with the frequency dependent parameters is not convenient and most of all not compact. On the other hand, other parameters become more important for time domain antennas, such as ringing in the antenna, maximum amplitude of the received signal, duration of a response, etc. These are all important parameters for an ultra-wideband radar system, where the performance often depends on the quality of the raw data prior to processing. Furthermore, there is a need for describing the antenna performances in a compact way, which can be used for modelling, or for comparing performances of different time domain antennas.

## 4.2. Definitions of terms

### 4.2.1. Impulse response and frequency response function

Every time-invariant linear system is completely described in the time domain by its Impulse Response (IR)  $h(t)$ , which mathematically relates the input  $x(t)$  to the output  $y(t)$  of the system, by the convolution integral

$$y(t) = \int_{-\infty}^{+\infty} h(\mathbf{t})x(t-\mathbf{t})d\mathbf{t} \quad (4.1)$$

where  $x(t)$  is the input signal,

$y(t)$  the output signal,

and  $h(t)$  the impulse response of the system (Fig. 4-1).

Equation (4.1) can be written using the convolution operator  $\otimes$  :

$$y(t) = h(t) \otimes x(t) \quad (4.2)$$

The IR depends on what one takes as input and output of the system. In the frequency domain the corresponding relation is given by the Fourier transformation of (4.2)

$$Y(j\omega) = H(j\omega)X(j\omega) \quad (4.3)$$

where  $X(j\omega)$  and  $Y(j\omega)$  are the respective Fourier transforms of the input  $x(t)$  and the output  $y(t)$ .  $H(j\omega)$ , defined as the *Frequency Response Function*, is the Fourier transform of the impulse response  $h(t)$  :

$$H(j\omega) = \frac{1}{2\pi} \int_{-\infty}^{+\infty} h(t) e^{-j\omega t} dt \quad (4.4)$$

Related by the Fourier transform,  $H(j\omega)$  and  $h(t)$  contain the same information.

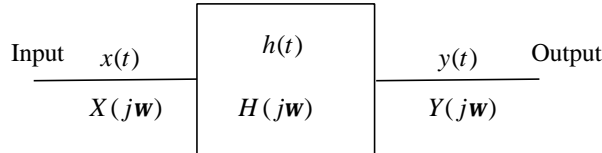


**Fig. 4-1:** Representation of a time-invariant, stable and linear system

According to equation (4.2), if the system is excited by a Dirac impulse  $\mathbf{d}(t)$ , the output becomes  $h(t)$ , hence the name impulse response:

$$\begin{aligned} y(t) &= h(t) \otimes \mathbf{d}(t) \\ &= h(t) \end{aligned}$$

#### 4.2.2. Virtual source of a time domain antenna

In the time domain characterisation of the antennas we will often need the distance from an observation point in the far field to the antenna. Due to the finite but non-zero dimension of the antenna, this distance becomes ambiguous. To solve this, we have defined for our convenience an apparent point in the antenna from which the magnitude of the radiated field  $\vec{E}_{rad}(\vec{r}, t)$  degrades with a factor  $1/R$  (free space loss or spreading loss) in the far field, where  $R$  is the distance from that apparent point. We call this point the "virtual source" of the antenna [2].

The virtual source can be considered as the time equivalent of the phase centre. The phase centre of an antenna is a frequency concept and is defined by IEEE (Std 145-1983) as: "The location of a point associated with an antenna such that, if it is taken as the centre of a sphere whose radius extends into the far field, the phase of a given field component over the surface of the radiation sphere is essentially constant, at

least over that portion of the surface where the radiation is significant.” Equivalent to this definition, we can consider the virtual source to be the origin of a sphere formed by the wave front of the radiated pulse-shaped spherical TEM wave at a certain time.

The virtual source is in general located between the antenna feed and the aperture. In the time domain characterisation of the antennas, the virtual source will serve as origin of the co-ordinate system  $\vec{r} = \vec{0}$ , unless specified otherwise.

### 4.2.3. The far field for time domain antennas

The definition of the far field is a good example of how inconvenient it can be to use classical antenna parameters in the time domain. IEEE defines the far field in Std 145-1983 as “The region of the field where the normalised angular field distribution is essentially independent of the distance from a specified point in the antenna region “. In this region the power density also varies as  $R^{-2}$ . For a narrow band antenna, the far field distance is taken as the distance  $R$  from the antenna phase centre where the phase shift between the ray from the aperture edge and that from the centre is  $22.5^\circ$ . For most narrow band antenna, this distance  $R$  corresponds with

$$R = \frac{2D^2}{\lambda} \quad (4.5)$$

where  $D$  is the aperture dimension in meters and  $\lambda$  the wavelength in free space.

This would mean that for ultra-wideband antennas the far field distance is a function of frequency. In [1] E. G. Farr and C. E. Baum propose an extension of the far field definition into the time domain. To be in the far field of a time domain antenna, the clear time between the arrival of the closest ray and the arrival of the outermost ray should be small compared with the full-width-half-maximum (FWHM) of the pulse (or 10-90% risetime in case of a step). This means

$$\frac{(d_2 - d_1)}{c} \leq \frac{t_{FWHM}}{\mathbf{n}} \quad (4.6)$$

with  $d_1$  and  $d_2$  as defined in Fig. 4-2, and  $\mathbf{n}$  a constant that identifies how much larger the FWHM is than the clear time. The question is how large should  $\mathbf{n}$  be taken? The authors suggest  $\mathbf{n}$  in the region of three to five.

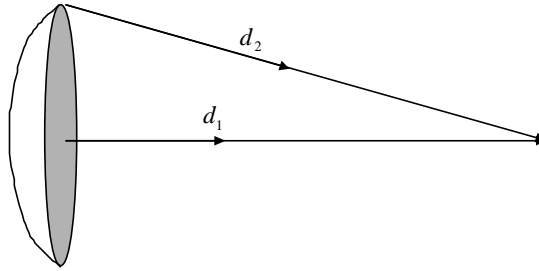


**Fig. 4-2:** Configuration for far field calculation

In this work we will use another definition for the far field of a time domain antenna, more similar to the  $R^{-2}$  dependency of the radiated power in the far field of narrow band antennas. We consider to be in the far field of the time domain antenna if the peak value of the radiated field component varies as  $R^{-1}$ , with  $R$  the distance from the virtual source. In this definition, just like in the definition of E. G. Farr and C. E. Baum, the far field distance will be function of the transient pulse shape.

#### 4.2.4. Electrical boresight

The electrical boresight of a highly directive antenna is the direction at which the largest signal appears. For time domain antennas this definition holds. A TEM horn antenna normally radiates the maximum amplitude in the symmetry axis of the horn. As for the dielectric-filled TEM horn, developed in Chapter 2, the structure is not totally symmetrical due to the integrated balun, the electrical boresight will be slightly different from the symmetry axis. For simplicity however, we consider the electrical boresight in the symmetry axis of the antenna.

#### 4.2.5. Definition of patterns for time domain antennas

The antenna pattern or radiation pattern is defined by IEEE as: “The spatial distribution of a quantity which characterises the electromagnetic field generated by an antenna”. The quantity, which is most often used to characterise the radiation is the directivity. In this case the antenna pattern  $k(\mathbf{q}, \mathbf{j})$  can be written as

$$k = D(\mathbf{q}, \mathbf{j}) / D_M \quad (4.7)$$

where

$D(\mathbf{q}, \mathbf{j})$  is the directivity of the antenna, defined as the ratio of the active power density radiated by the antenna in a given direction to the active power density that would be radiated in the same direction by an isotropic antenna, radiating the same power as the antenna of interest,

$D_M$  is the maximal directivity.

For an UWB antenna this pattern will change as a function of frequency. The antenna will be less directive for lower frequencies and more directive for higher frequencies.

If antennas are used to radiate fast transient pulses, the following quantities seem more useful [3]:

1. The peak power received in a pulse. It does not contain however any information on the change in pulse shape
2. The peak value when the off-axis pulse is correlated with the on-boresighth pulse
3. The power in the pulse, integrated over the length of the pulse
4. The peak-to-peak value of the received pulse.

Each quantity has its advantages, depending on the application. In our application, the most convenient quantity seemed to be the last one. We will refer to it as the p-t-p

antenna pattern, and the quantity which characterises the field is the peak-to-peak value of the received pulse normalised to the peak-to-peak value of the received pulse on boresight.

### 4.3. Time domain antenna equations

A common way of describing systems in the time domain is by means of an impulse response (IR). An antenna can be considered as a linear time-invariant system. For a given defined input and output, the antenna is totally characterised by its IR, relating the input to the output with the convolution integral. This relationship is referred to as an antenna equation in the time domain.

In this section, the antenna equations are expressed first in terms of conventional IR, and later (Section 4.4) in terms of normalised IR. To simplify the expressions, we only consider antenna performance for dominant linear polarisation of the E-field. The extension to the more general case is possible without too much effort. Furthermore we consider the input and output impedance of the laboratory equipment like voltage source, sampling oscilloscope, vector network analyser and cables used, matched to  $50\ \Omega$  (denoted  $Z_c$ ). We define  $V_s$  as the voltage generated by the source in a  $50\ \Omega$  load and  $V_{rec}$  as the voltage measured by an oscilloscope with a  $50\ \Omega$  input impedance (see Fig. 4-3). We also consider that we have two identical antennas.

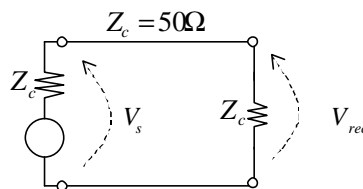


**Fig. 4-3:** Definition of symbols

### 4.3.1. Transmitting antenna

First consider the case of the transmitting antenna, near the co-ordinate origin  $\vec{r} = \vec{0}$ . As input we consider a voltage  $V_s$  applied at the input reference plane (Fig. 4-4).

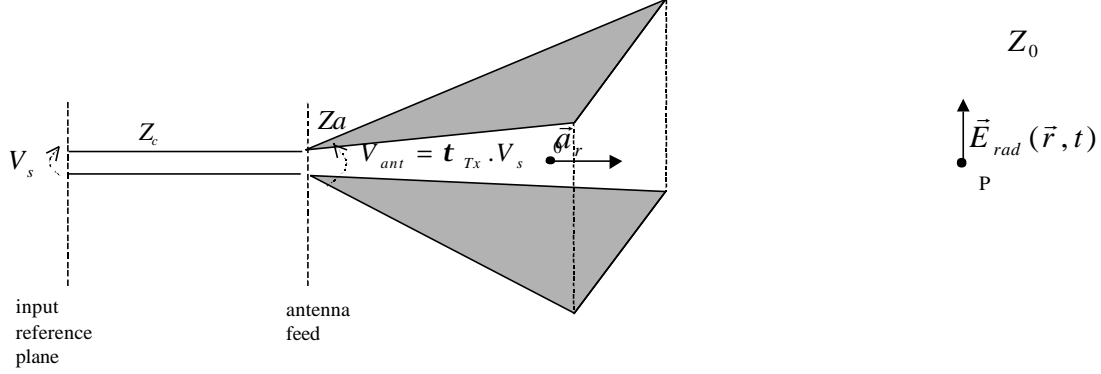


**Fig. 4-4:** Transmitting antenna configuration

The radiated field  $\vec{E}_{rad}(\vec{r}, t)$  in a point P in the far field, for  $\vec{r} \rightarrow \infty$ , can be described as [2] [4] [5]

$$\vec{E}_{rad}(\vec{r}, t) = \frac{1}{2\pi r c f_g} \frac{d\vec{h}_{Tx}(\vec{a}_r, t)}{dt} \otimes V_{ant}(t) \otimes \mathbf{d}(t - t_{d, TX}) \quad (4.8)$$

with  $V_{ant} = \mathbf{t}_{Tx} V_s$ ,  $\mathbf{t}_{Tx} = \frac{2Z_a}{Z_c + Z_a}$ ,  $f_g = \frac{Z_a}{Z_0}$

where  $h_{TX}(\vec{a}_r, t)$  is defined as the IR of the transmitting antenna in the direction  $\vec{a}_r = \frac{\vec{r}}{|\vec{r}|}$ ,  $r$  is defined to be  $r = |\vec{r}|$ ,  $V_{ant}$  is the excitation voltage at the antenna feed,  $\mathbf{t}_{Tx}$  the voltage transmission coefficient from the feed cable to the antenna,  $Z_a$  the antenna input impedance, assumed to be a real constant, and  $Z_0 = 120\pi$ . The convolution with the Dirac-function  $\mathbf{d}(t - t_{d, TX})$  in (4.8) introduces a total delay  $t_{d, TX}$ , which corresponds to the propagation time between the input of the antenna system

where  $V_s$  is applied (input reference plane) and the observation point P where  $\vec{E}_{rad}(\vec{r}, t)$  is evaluated.

For uniformity reasons, we use  $\vec{h}_{Tx}$  as kernel for the convolution in (4.8) and derive the input signal  $V_s$ . In the frequency domain, this corresponds to multiplying the input signal by the complex frequency  $s$  and the derivative of the IR by  $1/s$ . Taking into account the simplification of working only for dominant linear polarisation of the E-field, (4.8) can then be rewritten as

$$E_{rad}(\vec{r}, t) = \frac{t_{Tx}}{2\pi r c f_g} h_{Tx}(\vec{a}_r, t) \otimes \frac{dVs(t)}{dt} \otimes \mathbf{d}(t - t_{d, TX}) \quad (4.9)$$

As discussed in [5], for finite  $r = |\vec{r}|$ , one should limit the highest frequency for such result to be valid. Recognising these limitations, we introduce another problem. Due to the finite but non-zero dimension of the antenna, the location of the coordinate system origin  $\vec{r} = \vec{0}$  becomes ambiguous. To solve this we take the coordinate system origin in the virtual source of the antenna, as defined in Section 4.2.2. When defining the origin of the coordinate system  $\vec{r} = \vec{0}$  in this point, equation (4.9) is valid for finite  $r = |\vec{r}|$ . Assuming that the position of the virtual source is frequency independent over the frequency band of interest (this has been verified experimentally for a dielectric filled TEM horn), it can easily be located (see Section 4.4.2).

A disadvantage of using expression (4.9) is that  $Z_a$  is a function of frequency, so  $t_{Tx}$  and  $f_g$  are not constant. It will be shown that this difficulty can be eliminated by introducing a normalised IR.

### 4.3.2. Receiving antenna

Consider now the case of the receiving antenna, with a uniform plane-wave incident E-field  $\vec{E}_{inc,VS}(t)$ , evaluated in the virtual source point of the receiving antenna (Fig. 4-5). The incident direction is characterised by the unit vector  $\vec{a}_r$ .

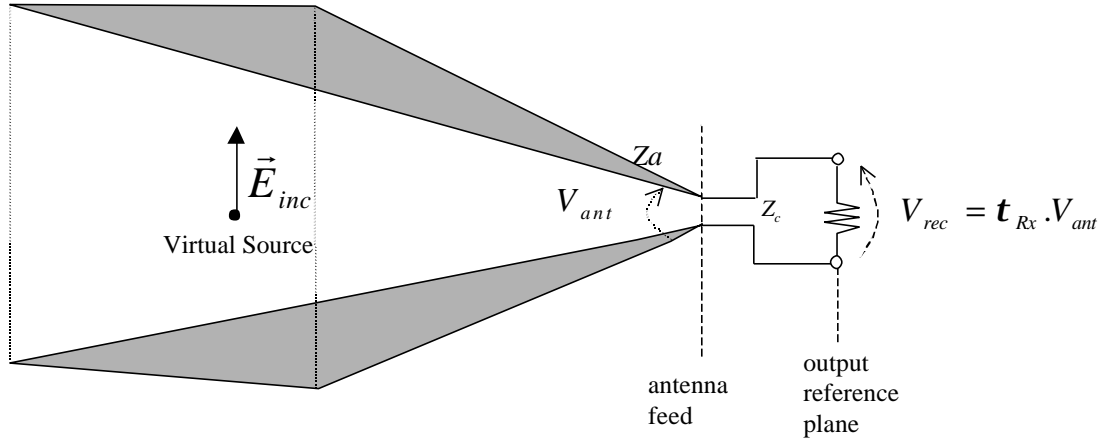


**Fig. 4-5:** Receiving antenna configuration

For dominant polarisation, the output voltage  $V_{rec}(t)$  measured by an oscilloscope in the output reference plane is related to the incident field by [2] [4] [5]

$$V_{rec}(t) = \mathbf{t}_{Rx} h_{Rx}(-\vec{a}_r, t) \otimes E_{inc,VS}(t) \otimes \mathbf{d}(t - t_{d,RX}) \quad (4.10)$$

$$\text{with } \mathbf{t}_{Rx} = \frac{2Z_c}{Z_c + Z_a}$$

where  $h_{Rx}(-\vec{a}_r, t)$  is the impulse response of the receiving antenna in the direction  $-\vec{a}_r$ , and  $t_{d,RX}$  represents the total propagation time between the virtual source point of the receiving antenna and the output reference plane where  $V_{rec}(t)$  is measured.

Expressions (4.9) and (4.10) are defined such that, if the transmitting and receiving antennas are the same,  $h_{Rx} = h_{Tx}$ .

### 4.3.3. Reciprocity of time domain antennas

Let us go for a moment back to the frequency domain. If the same antenna is used to transmit and receive, the frequency response function of the transmitting antenna will not be the same as the frequency response function of the receiving antennas. This can be derived from the Rayleigh-Carson reciprocity theorem [6]. The antenna power gain  $G_t$ , which is a transmission characteristic, and the antenna effective area  $A_e$ , which is a receiving characteristic, are related by

$$G_t = \frac{4p}{I^2} A_e \quad (4.11)$$

Equation (4.11) is a direct consequence of the Rayleigh-Carson reciprocity theorem.

The far field power density  $S$  in [W/m<sup>2</sup>] at a distance  $R$  from the transmitting antenna is given by

$$S = \frac{1}{4pR^2} G_t P_t \quad (4.12)$$

with  $P_t$  the excitation power at the antenna feed. Taking the square root of equation (4.12) and recasting into voltages, yields a relation between the radiated electrical field and the excitation voltage. Hence the frequency response function is proportional to  $\sqrt{G_t(\omega)}$ . On the other hand, when the antenna is used as receiving antenna, the received power as a function of the incoming power density  $S_{inc}$  is given by

$$P_r = A_e S_{inc} \quad (4.13)$$

So the frequency response characteristic, relating the incoming field  $E_{inc}$  to the received voltage at the antenna feed is proportional to  $\sqrt{A_e(\mathbf{w})}$ . Hence, according to (4.11), the ratio of the transmit frequency response function of an antenna to the receive frequency response function of the same antenna, is proportional to  $I^{-1}$  (or to frequency). The above result holds for any antenna [7]. In other words, the IR of the transmitting antenna has to be proportional to the time derivative of the IR of the receiving antenna. This can also be seen by comparing expression (4.8) and (4.10). In Section 4.3.1 we anticipated on this by defining  $\vec{h}_{Tx}$  as IR in (4.9) and derive the input signal  $V_s$ . Doing so,  $h_{Rx} = h_{Tx}$  if the antennas are the same.

## 4.4. Normalised impulse response

The disadvantage of using expressions (4.9) and (4.10) is that in reality  $Z_a$  is a function of frequency, so that  $t_{Rx}$  and  $f_g$  are not real constants. It would be logical and easier to integrate this frequency dependent term  $Z_a$  in the IR, which is in any event unique for each antenna. This can be done by normalising in expressions (4.9) and (4.10) the fields and voltages to the local characteristic impedance [4].

### 4.4.1. Normalisation of the IR

When normalising in the antenna equations the voltages and electric fields to the local characteristic impedance, expressions (4.9) and (4.10) can be rewritten as

$$\frac{E_{rad}(\vec{r}, t)}{\sqrt{Z_0}} = \frac{1}{2\mathbf{p}rc} h_{N,Tx}(\vec{a}_r, t) \otimes \frac{1}{\sqrt{Z_c}} \frac{dV_s(t)}{dt} \otimes \mathbf{d}(t - t_{d,TX}) \quad (4.14)$$

$$\frac{V_{rec}(t)}{\sqrt{Z_c}} = h_{N,Rx}(-\vec{a}_r, t) \otimes \frac{E_{inc,VS}(t)}{\sqrt{Z_0}} \otimes \mathbf{d}(t - t_{d,RX}) \quad (4.15)$$

where  $h_{N,Tx}$  and  $h_{N,Rx}$  are the normalised IRs for transmitting and receiving antenna. They are defined as

$$h_{N,Tx} = \sqrt{\frac{Z_c}{Z_a}} \frac{\mathbf{t}_{Tx}}{\sqrt{f_g}} h_{Tx} \quad \text{and} \quad h_{N,Rx} = \sqrt{\frac{Z_a}{Z_c}} \frac{\mathbf{t}_{Rx}}{\sqrt{f_g}} h_{Rx} \quad (4.16)$$

If the transmitting and receiving antenna are the same, then  $h_{N,Rx} = h_{N,Tx}$ . Combining expressions (4.14) and (4.15), the received voltage, measured with a 50 ohm oscilloscope at the receiving antenna, can be related to the input voltage by

$$V_{rec}(t) = \frac{1}{2pRC} h_{N,Tx}(\vec{a}_r, t) \otimes h_{N,Rx}(-\vec{a}_r, t) \otimes \frac{dV_s(t)}{dt} \otimes \mathbf{d}(t - t_{d,TX} - t_{d,RX}) \quad (4.17)$$

For equation (4.17) the co-ordinate origin is taken in the virtual source of the transmitting antenna, R is defined as the distance between the two virtual sources of the antennas at boresight, and  $t_{d,TX} + t_{d,RX}$  represents the total delay in the combined system. This delay is of importance for the measurement of the normalised impulse response.

Expressions (4.14), (4.15) and (4.17) are extremely simple to use. Due to the elimination of the transmission coefficient between the feed cable and the antenna, and due to the elimination of the antenna impedance in the antenna equations, they can be used without any assumption. Knowing the normalised IR of the antennas, one can calculate, as a function of the input signal, the exact radiated E-field at any point P in the far field of the transmitting antenna. One can also calculate the received voltage for an incoming E-field.

### 4.4.2. Measurement of Normalised IR on boresight

In a first step we will explain how the normalised IR on boresight can be measured. In a second step we show how the normalised IR in any direction can be derived from the normalised IR on boresight and the p-t-p pattern of the antenna.

But before measuring the normalised IR of an antenna, we first have to locate the virtual source of the antenna. This can be done experimentally by using two identical antennas on boresight. The virtual source can be seen as the origin of the radiated impulse, from which the  $1/R$  free space loss is initiated. Let  $d$  be the distance between the two antenna apertures, which is easy to measure (Fig. 4-6). For different values of  $d$ , the measured voltage  $V_{rec}$  degrades with  $1/R$  in the far field.

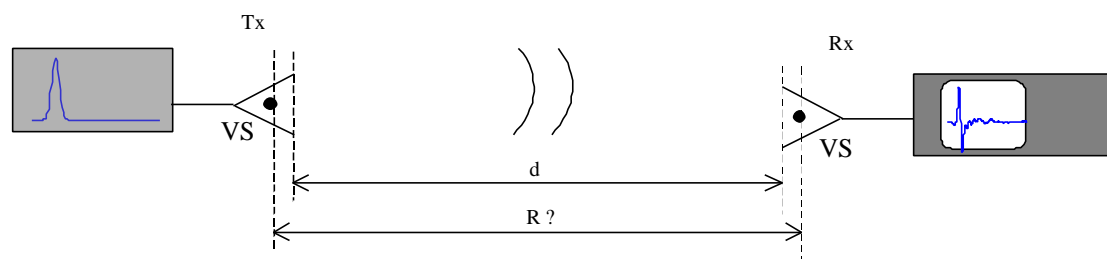


**Fig. 4-6:** Set-up for locating the virtual source (VS) of an antenna

In Fig 4-7 we present  $d$  versus the inverse peak-to-peak value of the received voltage  $V_{rec}$ . The zero of the line fitted through these points in the least-squares sense gives the difference between  $R$  and  $d$ .

In this example  $(R - d)$  is 8 cm, so the virtual source is located at 4 cm from the antenna aperture towards the antenna feed. The knowledge of the exact location of the virtual source is important when (4.14), (4.15) or (4.17) are used near the antennas (but still in the far field) or for exact measurement of the normalised IR of an antenna.

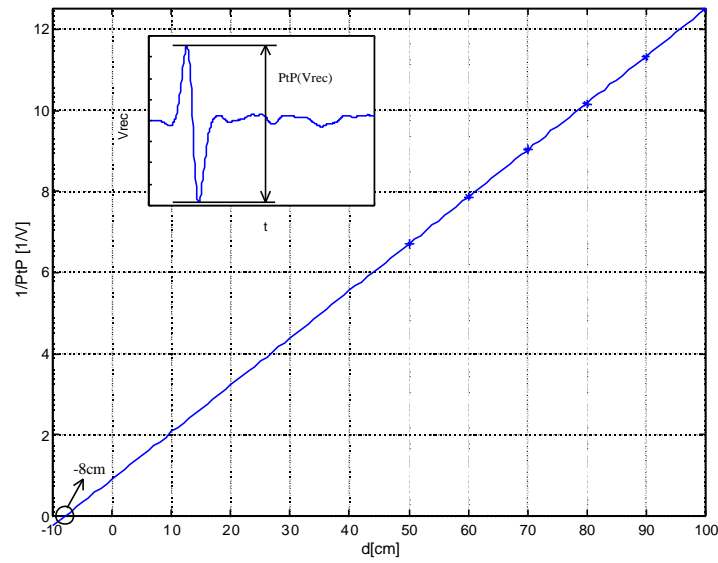


**Fig. 4-7:**  $d$  versus the inverse point to point value of the received voltage  $V_{rec}$

Once the location of the virtual source is known,  $h_{N,Tx}$  and  $h_{N,Rx}$  can be measured by using two identical antennas and a vector network analyser (VNA). Converting (4.17) into the frequency domain, the normalised frequency response function of the antennas is expressed as

$$H_N(\omega) = \sqrt{\frac{2p R c V_{rec}(\omega)}{j\omega V_s(\omega)}} e^{j\omega(t_{d,TX} + t_{d,RX})} \quad (4.18)$$

Considering the two antennas on boresight in the far field, with a distance  $R$  between the two virtual sources, as a two-port, one can measure the  $S_{21}$  parameter with a VNA over the frequency band of interest, covering at least the whole frequency range of the antenna.

The quantity  $t_{d,TX} + t_{d,RX}$ , total delay between the reference planes of port 1 and port 2, can be replaced by  $\frac{R'}{c}$ , where  $R'$  is the distance between the two reference planes of the VNA and  $c$  the speed of light.

Expression (4.18) can then be written as

$$H_N(\mathbf{w}) = \sqrt{\frac{2\mathbf{p}Rc}{j\mathbf{w}} S_{21}(\mathbf{w}) e^{j\mathbf{w}R/c}} \quad (4.19)$$

In expression (4.19) the square root is taken from a complex number. To do so, one first has to unwrap the phase, otherwise the result is non-physical. The unwrapping is far more easy by taking into account the term  $e^{j\mathbf{w}R/c}$ , hence its importance.

Once the discrete frequency vector  $H_N(\mathbf{w})$  is found,  $h_N(t)$  can be extracted by a frequency-time transformation using the following processing scheme:

1. Complete the discrete frequency vector  $H_N(\mathbf{w})$  with zeros for missing frequencies between zero and the start frequency of the VNA
2. Pad zeros after the frequency vector to obtain the desired time resolution after frequency-time transformation. The time step after the transformation will be  $T_s = 1/(2f_{\max})$ , with  $f_{\max}$  the highest frequency after zero padding
3. Take the real part of the inverse DFT of the zero-padded frequency vector. Multiply the real part by 2 to obtain the discrete sequence  $h_N(n)$  with the desired time step  $T_s$
4.  $h_N(t) = h_N(n) / T_s$ .

In step 3, the real part of the inverse DFT is multiplied by 2. The factor two takes into account the lag of the negative frequencies in the frequency vector. The same discrete sequence  $h_N(n)$  would be found if the frequency vector was first completed for negative frequencies before taking the inverse DFT.

It is not necessary to perform step 4, when using the expression (4.14), (4.15) or (4.17) under its discrete form. The division by  $T_s$  in step 4 is explained as follows: when the discrete sequence  $x_s(n)$  contains the exact samples of the analogue signal

$x_a(t)$  sampled with a period  $T_s$ , the discrete Fourier transform of the discrete signal  $X_s$  is then related to the Fourier transform of the analogue signal  $X_a$  by [8]

$$X_s(e^{j\omega T}) = \frac{1}{T_s} \sum_{l=-\infty}^{\infty} X_a \left[ j \left( \frac{\omega + 2\pi l}{T_s} \right) \right] \quad (4.20)$$

In our case the discrete frequency vector  $H_N(\mathbf{w})$  in (4.19) contains the exact samples of its analogue version. So after the inverse DFT, the discrete sequence  $h_N(n)$  will be  $T_s$  times superior to the exact samples of  $h_N(t)$ .

#### 4.4.3. Normalised IR off-boresight

In previous section we showed a procedure to measure the normalised IR of the TEM horn on boresight, *i.e.*  $\mathbf{q} = 0$  and  $\mathbf{j} = 0$  (Fig. 4-8). In this section we will show that this normalised IR on boresight  $h_N(\mathbf{q} = 0, \mathbf{j} = 0, t)$  or short  $h_{N,0}(t)$ , in combination with the antenna pattern, can also be used to describe the behaviour of the TEM horn off-boresight in a given direction  $(\mathbf{q}, \mathbf{j})$ , as far as we stay within the 3dB opening angle of the antenna beam.

The co-ordinate system is shown on Fig 4-8: the origin is defined as usual in the virtual source (VS) of the antenna,  $\mathbf{j}$  is the angle in the H-plane of the antenna, and  $\mathbf{q}$  the angle in the E-plane, both measured from the boresight direction.

In an experimental study we found that the fast transient impulse radiated by the dielectric TEM horn in a given direction only varies in amplitude, but not in shape along the time axis, as far as we stay within the 3dB beamwidth of the antenna. In other words, the pulse shape along the time axis of the radiated signal in a direction  $(\mathbf{q}, \mathbf{j})$  will be identical to the pulse shape of the signal radiated on boresight. The factor  $k$ , representing the variation in amplitude, is by definition given by the p-t-p antenna pattern and can be split in a product of two factors  $k_h$  and  $k_e$ , representing

the pattern in the H-plane and in the E-plane. To simplify the reasoning, we consider a configuration as shown in Fig. 4-9. The transmitting antenna can only rotate in the H-plane. The receiving antenna stays fixed.

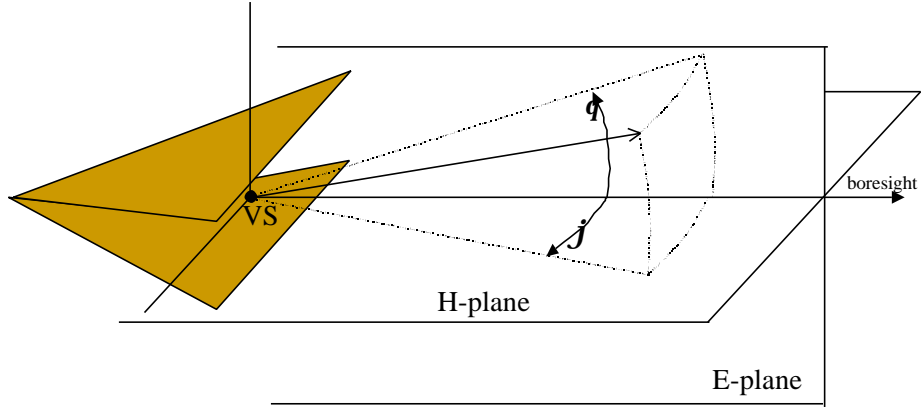


**Fig. 4-8:** Representation of co-ordinate origin,  $\mathbf{q}$  and  $\mathbf{j}$ .

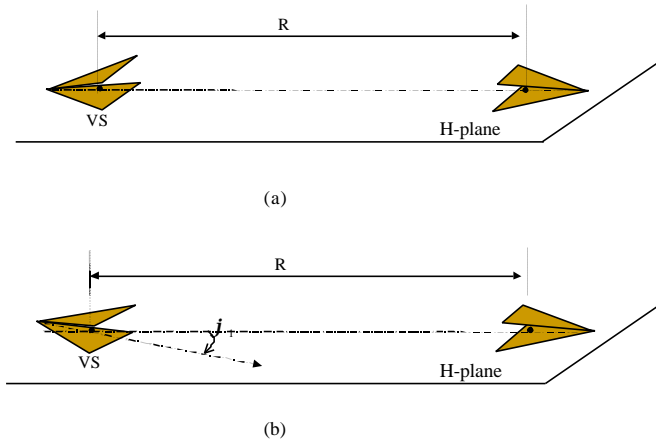


**Fig. 4-9:** Configuration for the experimental study of the normalised IR off-boresight

The received signal in configuration (a) with two identical antennas on boresight and a distance  $R$  between the two virtual sources is given according to (4.17) by

$$V_{rec}(0,0,t) = \frac{1}{2pRc} h_{N,0}(t) \otimes h_{N,0}(t) \otimes \frac{dVs(t)}{dt} \otimes \mathbf{d}(t - t_{d,TX} - t_{d,RX}) \quad (4.21)$$

where  $h_{N,0}(t)$  is the normalised IR on boresight.

If the transmitting antenna is rotated in the H-plane by an angle  $\mathbf{j}_1$  around its virtual source, while the receiving antenna is fixed (Fig. 4-9 (b)), the received voltage is given by

$$V_{rec}(0, \mathbf{j}_1, t) = \frac{1}{2pRc} h_N(0, \mathbf{j}_1, t) \otimes h_{N,0}(t) \otimes \frac{dV_S(t)}{dt} \otimes \mathbf{d}(t - t_{d, TX} - t_{d, RX}) \quad (4.22)$$

where  $h_N(0, \mathbf{j}_1, t)$  is the normalised IR in the direction  $(0, \mathbf{j}_1)$ .

The measured voltage  $V_{rec}(0, \mathbf{j}_1, t)$  differs from  $V_{rec}(0, 0, t)$  by a factor  $k_h(\mathbf{j}_1)$

$$V_{rec}(0, \mathbf{j}_1, t) = k_h(\mathbf{j}_1) V_{rec}(0, 0, t) \quad (4.23)$$

where  $k_h(\mathbf{j}_1)$  is by definition the value of the p-t-p antenna pattern in the H-plane for an angle  $\mathbf{j}_1$ .

When substituting (4.21) and (4.22) in (4.23) and simplifying the expression, the normalised IR in the direction  $(0, \mathbf{j}_1)$  can then be expressed as

$$h_N(0, \mathbf{j}_1, t) = k_h(\mathbf{j}_1) h_{N,0}(t) \quad (4.24)$$

Although the above result is only for a rotation of the antenna in the H-plane, the same result holds for any direction  $(\mathbf{q}, \mathbf{j})$ , hence

$$h_N(\mathbf{q}, \mathbf{j}, t) = k_e(\mathbf{q}) k_h(\mathbf{j}) h_{N,0}(t) \quad (4.25)$$

with  $k_e(\mathbf{q})$  and  $k_h(\mathbf{j})$  the p-t-p pattern in the E- and the H-plane.

The result in expression (4.25) is very important. It means that an antenna is totally characterised in the time domain if its normalised IR on boresight and its p-t-p pattern in E- and H-plane is known, as far as we stay within the 3dB beamwidth of the antenna.

#### 4.4.4. Relation between gain and normalised IR

The normalised IR totally describes the behaviour of the antennas. This means that it must be possible to derive classical antenna parameters from this normalised IR. As an example we express in this section the gain in terms of the normalised IR [9].

We start with the same expression (4.13) and (4.11) in the frequency domain:

$$P_r(\mathbf{w}) = A_e(\mathbf{w})S_{inc}(\mathbf{w}) \quad (4.26)$$

and

$$G_t(\mathbf{w}) = \frac{4\mathbf{p}}{I^2} A_e(\mathbf{w}) \quad (4.27)$$

where  $G_t$  is the antenna power gain,  $A_e$  the antenna effective area and  $S_{inc}$  the incoming power density. Replacing the effective area in (4.26) by (4.27), we can write

$$P_r(\mathbf{w}) = \frac{I^2}{4\mathbf{p}} G_t(\mathbf{w})S_{inc}(\mathbf{w}) \quad (4.28)$$

Taking the square root of equation (4.28) and recasting to voltages results in

$$\frac{|V_{rec}(\mathbf{w})|}{\sqrt{Z_c}} = \frac{I}{2\sqrt{p}} \sqrt{G_t(\mathbf{w})} \frac{|E_{inc}(\mathbf{w})|}{\sqrt{Z_0}} \quad (4.29)$$

Note that, just like in Chapter 3, the losses due to the reflection coefficients of the antenna feed are included in the gain.

If we convert equation (4.15) to the frequency domain and compare it with equation (4.29) we find the relation between the gain and the normalised IR of the antenna:

$$G_t(\mathbf{w}) = \frac{4p}{I^2} |H_N(\mathbf{w})|^2 \quad (4.30)$$

where  $H_N(\mathbf{w})$  is the Fourier transform of the normalised IR (also given by (4.19)).

## 4.5. Results on TEM horns

The normalised IR describes the antenna performances in a very compact way. In this section the performances on boresight of four different TEM horns are compared. For simplicity the antennas are numbered from 1 to 4. Table 4.1 summarises the physical characteristics of the tested antennas. (L is the length of the antenna plates and  $A_{ap}$  the area of the physical antenna aperture). More details on the antennas can be found in Chapter 3.

	L (cm)	$A_{ap}$ (cm <sup>2</sup> )	Filling	RAM
Antenna 1	10	10*4	air	no
Antenna 2	10	10*4	dielectric	no
Antenna 3	12	12*6	dielectric	no
Antenna 4	12	12*6	dielectric	yes

Table 4.1: The physical characteristics of the tested antennas

Antenna 4 is the same as antenna 3 but with RAM placed at the outside end of the antenna plates, to reduce the antenna ringing and to suppress the pre-pulse (see Chapter 3, Section 3.5.3). For each antenna,  $S_{21}$  was measured between 40 MHz and 20 GHz, with a frequency step of 40 MHz, by placing two identical antennas on boresight. The normalised IRs on boresight of the antennas are shown in Fig. 4-10. Note that the dimensions of  $h_N(t)$  are given in m/ns, which corresponds to the dimensions needed in (4.14) and (4.15).

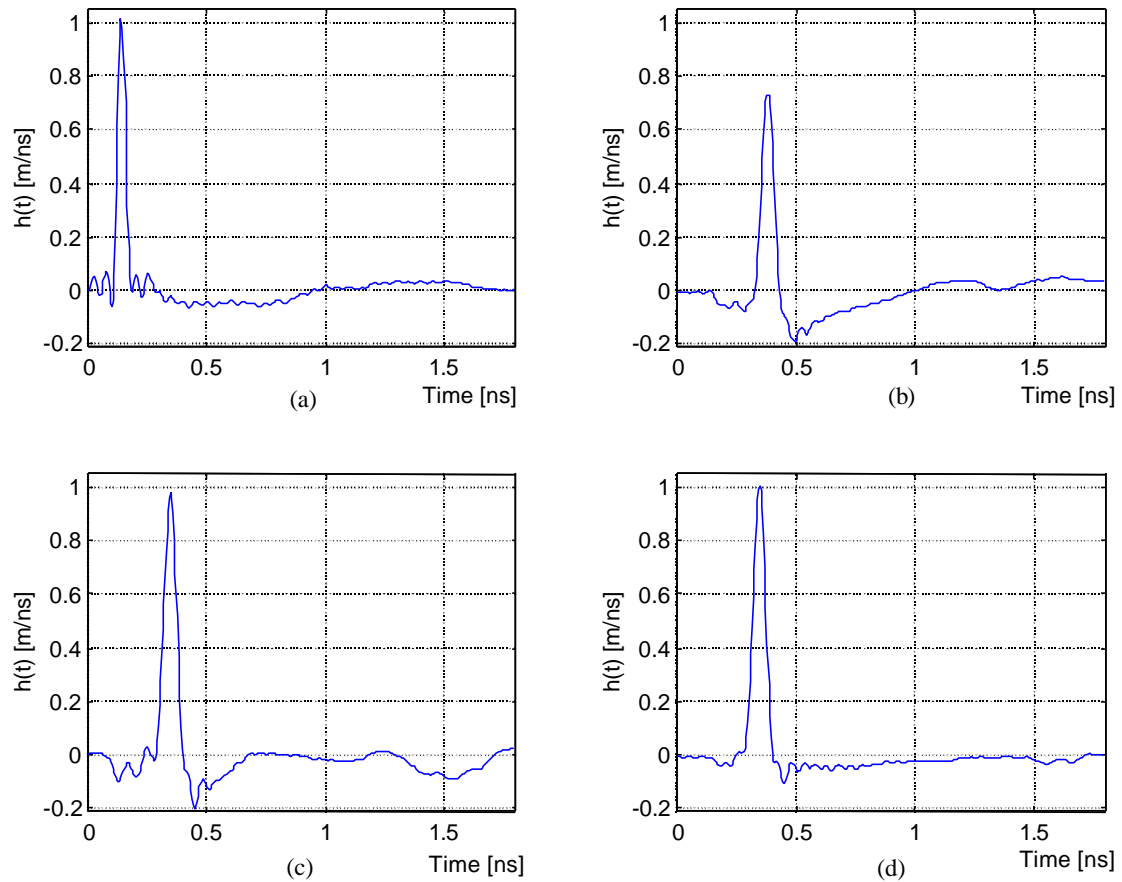


**Fig. 4-10:** (a)  $h_N(t)$  of antenna 1      (b)  $h_N(t)$  of antenna 2  
(c)  $h_N(t)$  of antenna 3      (d)  $h_N(t)$  of antenna 4

For a detailed comparison of the antennas, we summarise some important characteristics of the normalised IR in Table 4.2, *i.e.* the maximum value of the normalised IR, the full width at half maximum value (FWHM) of the impulse, the area under the impulse, and the tail fluctuation as a portion of the maximum value.

	Max of $h_N(t)$ [m/ns]	FWHM [ps]	Area under impulse [m]	tail fluctuation [% of max]
Antenna 1	1.01	38	0.038	13%
Antenna 2	0.73	56	0.041	33%
Antenna 3	0.98	60	0.059	22%
Antenna 4	1.01	60	0.062	11%

Table 4.2: Important characteristics of the normalised IR

The FWHM value of the normalised IR is related to the bandwidth of the antenna. The area under the impulse is related to the effective antenna height [4]. It can be seen that filling the antenna with the dielectric reduces the bandwidth, but increases the area under the impulse. The presence of the absorber material at the end of the antenna plates of antenna 4 has a positive influence on the antenna performance. The comparison with antenna 3 shows that the absorber material does not affect the bandwidth nor the area under the impulse, but it considerably decreases the fluctuations in the tail of the response. Thus antenna 4 will be capable of radiating transient pulses with less ringing. It would be difficult to demonstrate this antenna property with the classical frequency domain characterisation of an antenna. In the implementation of a laboratory UWB GPR, which will be described in Chapter 6, antenna 4 is used.

Fig. 4-11 shows the gain of each antenna derived from the normalised IR (the gain is calculated using expression (4.30)). The gain of the dielectric filled TEM horn (antenna 3 and 4) is 10 dB. The results for antenna 1 and antenna 2 are comparable with the frequency domain measurements of the gain shown in Fig. 3-23 of Chapter 3. The lower cut-off frequency of antenna 4 is about the same as the lower cut-off frequency of antenna 2. This means that the prolongation of the antenna plates with 2 cm does not have much influence.

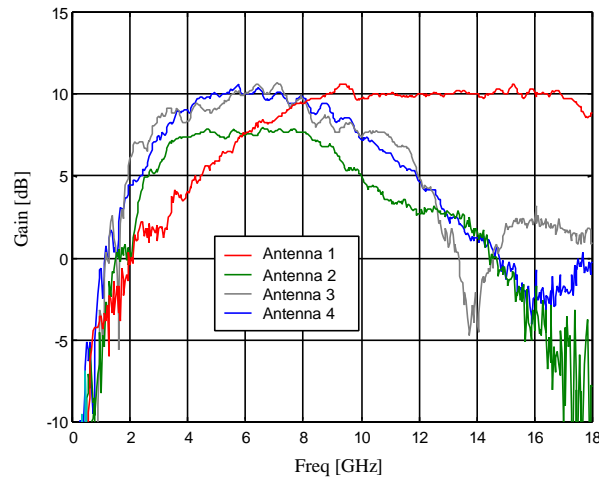


**Fig. 4-11:** Antenna gain of dielectric filled TEM horn

## 4.6. Time domain simulations

The normalised impulse response is a powerful tool that also can be used for simulation and system design purposes. Some examples are presented in this section. For each example the simulated data are compared with measured data. The antenna used in the simulations is antenna 4.

### *Two antennas on boresight*

The first simulation is straightforward. Two antennas are put on boresight at a distance of  $R = 90$  cm. A very short transient impulse with a maximum amplitude of 2.5 V in a  $50 \Omega$  load and a FWHM of 90 ps is used as a driving voltage  $V_s$  (Fig. 4-12 (a)).

The transient voltage signal  $V_{rec}$  at the output of the receiving antenna is calculated using (4.17) and measured using a digitising oscilloscope. Fig. 4-12 (b) shows the calculated waveform and the measured waveform. Both time and voltage data of the two waveforms correspond well.

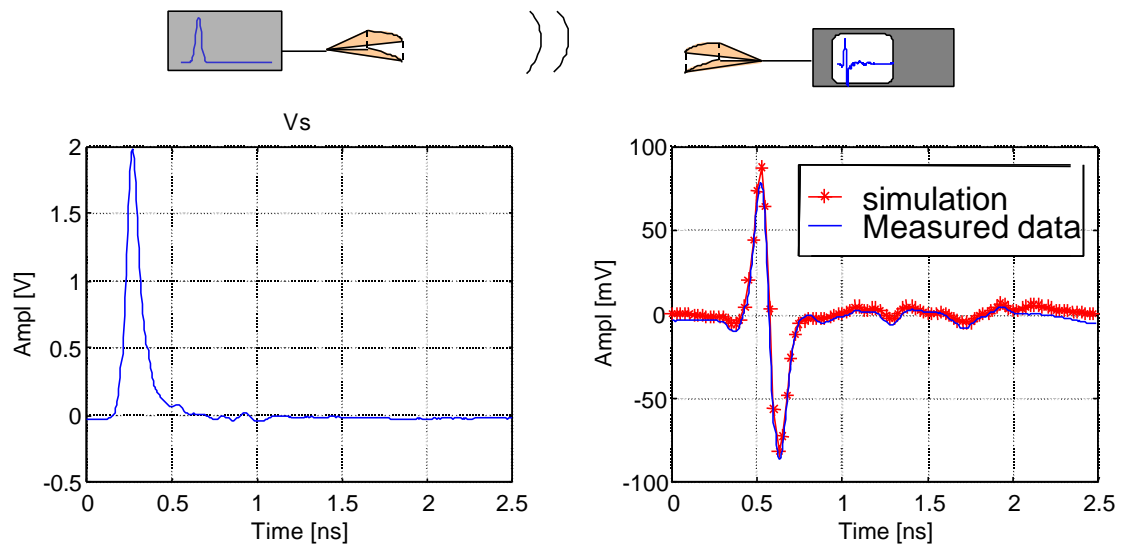


**Fig. 4-12:** (a) Driving signal  $V_s$

(b) Two antennas on boresight, simulated and measured data

***Reflection on a planar air-ground interface***

In a second example the reflection on a planar dry sand interface is simulated. The bistatic configuration, typical for ground penetrating radar, is represented in Fig. 4-13. The two antennas are focused at a point on the interface. The distance between the virtual sources of the TEM horns is 22.8 cm. The H-planes of the antennas are in the same plane and the E-field of both antennas is parallel to the interface (normal to the plane of incidence). The driving voltage  $V_s$  is the same as in the previous simulation.

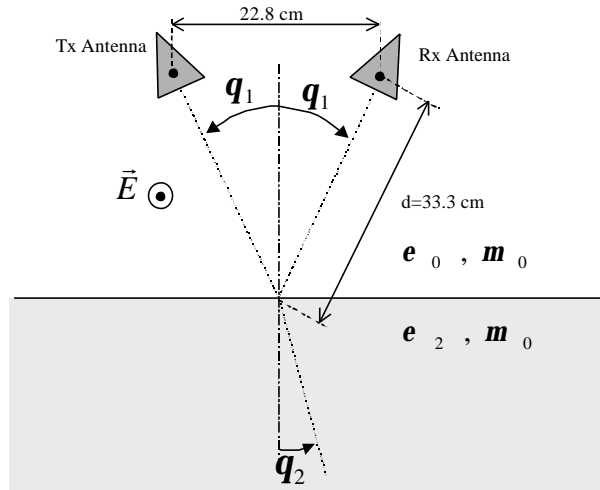


**Fig. 4-13:** Bistatic configuration

The dry sand is characterised by an  $\epsilon_r$  of 2.55 and a  $\mu_r$  of 1 in the frequency band of interest, and is assumed to be homogeneous and loss-less. The reflection coefficient for a polarisation normal to the plane of incidence, is given by

$$\Gamma_{\perp} = \frac{\sqrt{\epsilon_0} \cos q_1 - \sqrt{\epsilon_2} \cos q_2}{\sqrt{\epsilon_0} \cos q_1 + \sqrt{\epsilon_2} \cos q_2}, \text{ which is } -0.248 \text{ in this case.}$$

The total path loss in the simulation is due to the free-space loss over a distance  $2d$  and to the reflection loss from the air-sand interface. The simulated data is obtained by multiplying the result of (4.17) by  $\Gamma_{\perp}$ . Despite the fact that the air-sand interface is near the antennas, the result of the simulation is very similar to the measured data (Fig. 4-14). Note that the direct coupling between transmitting and receiving antennas, which is not taken into account in the simulation, will also introduce errors.

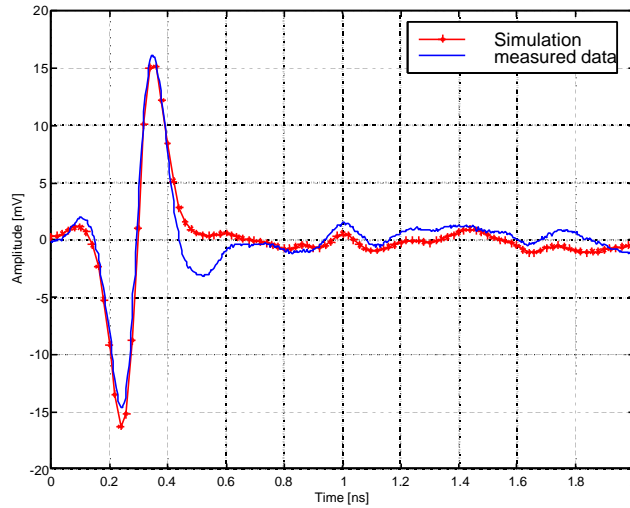


**Fig. 4-14:** Reflection on a planar dry sand interface, simulated and measured data

*Echo of a metallic disc*

In the last simulation, the normalised antenna equations are used in combination with commercial FDTD software. The bistatic antenna configuration, almost the same as in the previous example, is represented in Fig. 4-15. An aluminium disc with a radius of 3.2 cm and 1 cm thick is placed at the focus point of the two antennas.

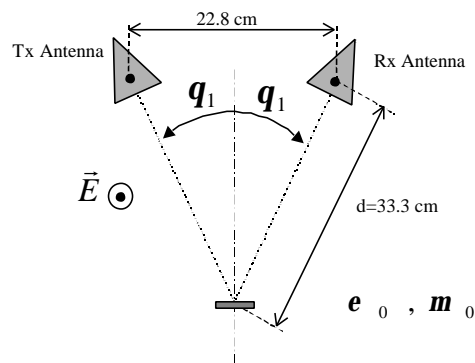


**Fig. 4-15:** Bistatic configuration for metallic disc

Expression (4.14) is used to calculate the radiated E-field at the metallic disc. This wave, assumed to be planar, is introduced in a FDTD programme, which calculates the backscattered field at a point corresponding to the virtual source of the receiving antenna. Using this backscattered field as an incoming field for expression (4.15), we

calculate the received voltage at the output of the receiving antenna. The simulated data and the measured data are given in Fig. 4-16. Again, the correspondence is good. An advantage of this simulation scheme is that we do not need to model the antennas in the FDTD programme.

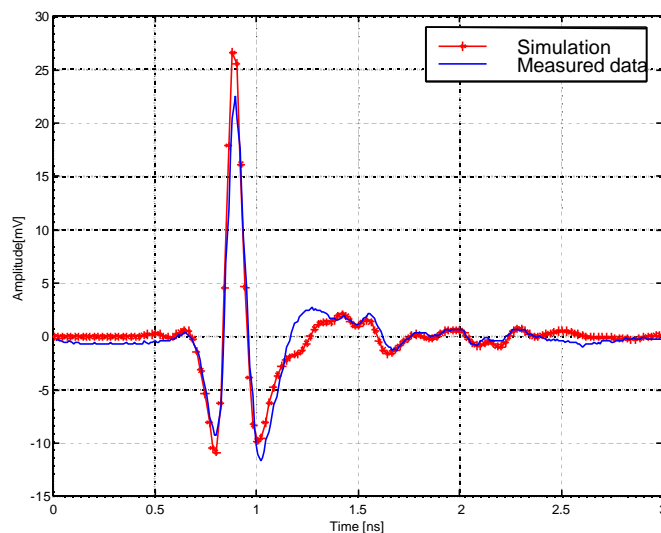


**Fig. 4-16:** Echo of a metallic disc, simulated and measured data

## 4.7. Summary

The normalised IR describes time domain antenna performances, which are sometimes difficult to see in classical antenna parameters, in a compact way. The advantage of using the normalised IR over any other impulse response is that all frequency dependent characteristics are included in the normalised IR. This has two important consequences. First, the time domain antenna equations become very simple and accurate to use, without any assumptions about antenna impedance. Second, the normalised IR permits a comparison between different variants of time domain antennas, taking into account all these frequency dependent terms.

We showed that the normalised IR on boresight is easy to measure, using two identical antennas and a vector network analyser. Furthermore, we showed in an experimental study that the normalised IR off-boresight can be derived from the normalised IR on boresight, using the p-t-p antenna pattern. This means that an

antenna is totally characterised in the time domain by its normalised IR on boresight and its p-t-p pattern. Due to the finite but non-zero size of the antenna, the distance from an observation point to the antenna becomes ambiguous for points close to the antenna. The introduction of an apparent point in the antenna, called the virtual source - which can be seen as the origin of the radiated impulse TEM wave - resolves this shortcoming. The position of the virtual source in the antenna can be easily located.

Thanks to the introduction of the virtual source, the antenna equations can now be used near the antenna, as shown in the examples of the time domain simulations. The simulations also demonstrate the simplicity and accuracy of the time domain antenna equations, using the normalised IR. Similar simulations can also be applied for simulating system performance with different transient impulse generators or for radar range estimation. This will be the subject of Chapter 5.

## REFERENCES

- [1] E. G. Farr and C. E. Baum, "Extending the Definitions of antenna gain and Radiation Pattern into the Time Domain," *Sensor and Simulation Notes*, note 350, 1992.
- [2] B. Scheers, M. Acheroy, A. Vander Vorst, "Time domain simulation and characterisation of TEM Horns using normalised impulse response," *IEE Proceedings - Microwaves, Antennas and Propagation*, vol. 147, no. 6, pp. 463-468, Dec. 2000.
- [3] P. R. Foster, *Introduction to Ultra-Wideband Radar Systems*. J. D. Taylor, Ed., USA: CRC Press, 1995, ch. 5.
- [4] E. G. Farr and C. E. Baum, "Time Domain Characterization of Antennas with TEM Feeds," *Sensor and Simulation Notes*, note 426, 1998.
- [5] C. E. Baum, "General Properties of Antennas," *Sensor and Simulation Notes*, note 330, 1991.
- [6] R. W. P. King, *Theory of linear antennas*. Cambridge, MA: Harvard University Press, 1956.
- [7] M. Kanda, "Transients in a Resistively Loaded Linear Antenna Compared with those in a Conical Antenna and a TEM Horn," *IEEE Trans. on Antennas Propagat.*, vol. AP-28, no. 1, pp. 132-136, 1980.
- [8] A. V. Oppenheim and R. W. Schaffer, *Digital Signal Processing*. New Jersey: Prentice-Hall, 1975.
- [9] L. H. Bowen, E. G. Farr and W. D. Prather, "Fabrication of two collapsible Impulse Radiating Antennas," *Sensor and Simulation Notes*, note 440, 1999.

---

## **Chapter 5. Modelling of the GPR radar range equation in the time domain**

---

### **5.1. Introduction**

For a time domain GPR, a time domain representation is an obvious choice. It allows a compact and more accurate description of the system performances. Therefore we will model in this chapter the radar range equation in the time domain.

Describing performances of a time domain GPR system, using the radar range equation has mainly three drawbacks:

1. The radar range equation contains frequency dependent terms, hence they have to be expressed over the whole frequency band of interest. As time domain systems have intrinsically a large bandwidth, describing the system performance with the frequency dependent parameters is complicated
2. The radar range equation does not specify the nature of the transmitted signal
3. For a time domain system it is more practical to express the minimum detectable signal in terms of peak voltages and/or signal shapes instead of signal power only.

In the previous chapter we explained how time domain antennas can be characterised by their normalised impulse response. By considering the antenna as a convolution operator, we get a mechanism for modelling a whole radar system as a cascade of linear responses, which will lead in this chapter to a time domain equivalence of the radar range equation. Furthermore some modifications will be introduced to adapt the radar equation to the application of the GPR. Each term of the radar range equation in the time domain will be discussed in detail.

## 5.2. Radar range equation

The radar range equation is a useful description of the factors influencing radar performance. It gives the received power at the radar system in terms of the radar characteristics, the illuminated target and the frequency. The basic equation for a monostatic radar in free space illuminating a point scatterer is given by [1]

$$P_r(f) = \frac{P_t(f)G_t(f)}{4\pi R^2} \frac{\mathbf{s}(f)}{4\pi R^2} A_e(f) \quad (5.1)$$

with

$P_r(f)$  : the received signal power

$P_t(f)$  : the transmitted signal power

$G_t(f)$  : the maximum gain of the transmitting antenna

$R$  : the radar-to-target distance

$\mathbf{s}(f)$  : the radar cross section of the target

$A_e(f)$  : the effective aperture area of receiving antenna.

The effective aperture of an antenna is related to the gain and the wavelength by

$$A_e(f) = \frac{G(f)\lambda^2}{4\pi} \quad (5.2)$$

Hence the monostatic radar range equation can be written as

$$P_r(f) = \frac{P_t(f)G^2(f)I^2\mathbf{s}(f)}{(4\mathbf{p})^3 R^4} \quad (5.3)$$

The Radar Cross Section (RCS)  $\mathbf{s}(f)$ , expressed in square meters, is a measure of the equivalent surface area of a target that is seen by the radar [2]. In the definition of the RCS it is assumed that the target is in free space and in the far field of the radar. In a bistatic configuration the RCS of a target will be function of the direction of the incoming field on the target and of the direction towards the receiving antenna, therefore it should be expressed as a function of both incident and scattering angle. The bistatic RCS is mathematically expressed as

$$\mathbf{s}_b(\mathbf{q}, \mathbf{j}; \mathbf{q}', \mathbf{j}') = 4\mathbf{p} \lim_{R \rightarrow \infty} R^2 \frac{|E_s(\mathbf{q}', \mathbf{j}')|^2}{|E_i(\mathbf{q}, \mathbf{j})|^2} \quad (5.4)$$

where

$E_s$  : the scattered field at the receiver

$E_i$  : the incident field on the target

The term  $4\mathbf{p}R^2$  is to factor out the spreading loss. The angles  $\mathbf{q}$  and  $\mathbf{j}$  define the direction of propagation of the incident field and the angles  $\mathbf{q}'$  and  $\mathbf{j}'$  the direction of the scattered field. In the most general case the RCS must also be expressed as a function of the polarisation of the incident and scattered field.

### 5.3. GPR range equation

The GPR system performance is also governed by the radar range equation, but some modifications have to be made. For instance, in the case of a GPR, the transmitting and receiving antennas are physically two separated antennas. Normally the antennas are close to each other, but as the object can be in the neighbourhood of the antenna

configuration, it is more correct to adapt expression (5.3) for the bistatic case. This can be done by replacing the range  $R$  and the RCS of the target by their corresponding bistatic quantities. These corrections are not that important and can, in some cases, be omitted. More important is the introduction of some additional losses, *i.e.* the transmission loss at the air-ground interface, transmission losses associated with any mismatch in the ground (different layers in the ground), propagation loss in the ground and the losses due to an off-boresight position of the target [3]. All these losses are usually introduced in the radar range equation by the factors  $F_t$  and  $F_r$ , called respectively "the pattern propagation factor for transmitting-antenna-to-target path and target-to-receiving-antenna path". The factor  $F_t$  is defined as the ratio of the electric field strength at the target position, to that which would exist at the same distance from the radar in free space and on boresight of the antenna. The factor  $F_r$  is analogously defined [1]. Taking into account the pattern propagation factors, the radar range equation for a GPR system becomes

$$P_r(f) = \frac{P_t(f)G_t(f)}{4\pi R_t^2} \frac{\mathbf{s}_b(f)}{4\pi R_r^2} \frac{G_r(f)I^2}{4\pi} F_t^2 F_r^2 \quad (5.5)$$

with

$G_r(f)$ : the maximum gain of the receiving antenna

$R_t$ : the distance from transmitting antenna to the target

$R_r$ : the distance from receiving antenna to the target

$\mathbf{s}_b(f)$ : the bistatic radar cross section of the target

$F_t(f)$ : the pattern propagation factor for transmitting-antenna-to-target path

$F_r(f)$ : the pattern propagation factor for target-to-receiving-antenna path.

When the GPR is used for relatively small depths, like in the demining application, we can assume constant ground characteristics and no multiple layers between the air-ground interface and the target. In this case the pattern propagation factors  $F_t^2$  and

$F_r^2$  can be split into 4 parts: the transmission loss at the air-ground interface, the retransmission loss for the backscattered signal at the ground-air interface, the two-way propagation losses in the ground, and the off-boresight position of the target.

The transmission power loss  $L_{a-g}$  at the air-ground interface and the retransmission power loss  $L_{g-a}$  at the ground-air are given by

$$L_{a-g} = \frac{Z_{ground}}{Z_0} \left| \frac{2Z_{ground}}{Z_{ground} + Z_0} \right|^2 \quad \text{and} \quad L_{g-a} = \frac{Z_0}{Z_{ground}} \left| \frac{2Z_0}{Z_{ground} + Z_0} \right|^2 \quad (5.6)$$

where  $Z_{ground}$  is the complex characteristic impedance of the ground, given by

$$Z_{ground} = \sqrt{\mathbf{m}/\mathbf{e}^*} \approx \sqrt{\mathbf{m}} / \sqrt{\mathbf{e}'(1 - j \tan \mathbf{d})}$$

The two-way propagation losses in the ground is given by

$$e^{-2\mathbf{a}(R_{t,ground} + R_{r,ground})} \quad (5.7)$$

with  $\mathbf{a}$ : the attenuation constant of the ground as defined in (2.20)

$R_{t,ground}$  and  $R_{r,ground}$ : the parts of the one-way path length in the ground.

## 5.4. Radar range equation in the time domain

In this section, we develop an equivalent radar range equation in the time domain [4]. To make the difference with the conventional radar range equation of (5.5), we denote it as *the time domain radar range equation*. In a first step, the basic time domain equation for a radar in free space is developed. Therefore, we will characterise the antennas by their normalised impulse response, integrating all frequency dependent

antenna characteristics. One of the advantages of considering the UWB antenna as a convolution operator is that we get a mechanism for expressing the radar range equation as a cascade of linear responses.

Consider an electromagnetic configuration as shown in Fig. 5-1. The origin for the coordinates is taken in the virtual source of the transmitting antenna. We define

$\vec{a}_i = \frac{\vec{r}'}{|\vec{r}'|}$  as the direction of radiation of the transmitting antenna towards the target located at co-ordinate  $\vec{r}'$ . It is the incident direction of the field, from the point of view of the target.

$\vec{a}_s = \frac{\vec{r}'' - \vec{r}'}{|\vec{r}'' - \vec{r}'|}$  as the direction of the scattered field from the target towards the receiving antenna. The virtual source of the receiving antenna is located at  $\vec{r}''$ .

When using the normalised impulse response of the antenna, the radiated field in the point  $\vec{r}'$  in the far field is given by (4.14). This field will be the incoming field for the target and is expressed as

$$\frac{E_{inc}(\vec{r}', t)}{\sqrt{Z_0}} = \frac{1}{2\mathbf{p}|r'|c} h_{N,Tx}(\vec{a}_i, t) \otimes \frac{1}{\sqrt{Z_c}} \frac{dV_s(t - |r'|/c)}{dt} \quad (5.8)$$

where  $h_{N,Tx}(\vec{a}_i, t)$  is the normalised impulse response of the transmitting antenna in the direction  $\vec{a}_i$ ,  $V_s$  is the excitation voltage at the antenna feed,  $Z_c$  the impedance of the feed cable, and  $Z_0 = 120\mathbf{p}$ .

We define the Impulse Response (IR)  $\Lambda_{1,1}(\vec{a}_i, \vec{a}_s, t)$  of a given target so that the scattered field in a point  $\vec{r}''$  can be described as

$$E_{scat}(\vec{r}'', t) = \frac{1}{4\mathbf{p}|\vec{r}'' - \vec{r}'|} \Lambda_{1,1}(\vec{a}_i, \vec{a}_s, t) \otimes E_{inc}(\vec{r}', t - |\vec{r}'' - \vec{r}'|/c) \quad (5.9)$$

The impulse response  $\Lambda_{1,1}(\vec{a}_i, \vec{a}_s, t)$  only takes into account the backscattered signal in the same polarisation as the incoming field and is expressed in [m/s]. It can be seen as the time equivalent of the square root of the radar cross section. The factor  $1/|\vec{r}'' - \vec{r}'|$  introduce the spreading loss. The impulse response is described in more detail in Section 5.6.4.

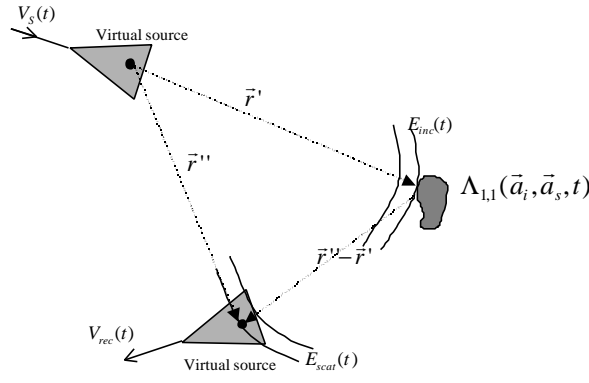


**Fig. 5-1:** Electromagnetic configuration

The received voltage  $V_{rec}(t)$  at the output of the receiving antenna is calculated by (4.15) as

$$\frac{V_{rec}(t)}{\sqrt{Z_c}} = h_{N,Rx}(-\vec{a}_s, t) \otimes \frac{E_{scat}(\vec{r}'', t)}{\sqrt{Z_0}} \quad (5.10)$$

Combining (5.8), (5.9) and (5.10), the basic time domain radar equation for a radar in free space is found as

$$V_{rec}(t) = \frac{1}{8\mathbf{p}^2 R_i R_r c} h_{N,Tx}(\vec{a}_i, t) \otimes \Lambda_{1,1}(\vec{a}_i, \vec{a}_s, t) \otimes h_{N,Rx}(-\vec{a}_s, t) \otimes \frac{dV_s(t)}{dt} \quad (5.11)$$

With  $R_t = |\vec{r}|$  : the total path length from transmitting antenna to the target

$R_r = |\vec{r}'' - \vec{r}'|$ : the total path length from receiving antenna to the target.

Equation (5.11) gives a relation between the excitation voltage (applied at the transmitting antenna) and the received voltage (measured at the receiving antenna) as a cascade of 3 time-invariant linear systems: the transmitting antenna, the target in free space and the receiving antenna, each described by their IR.

Note that in equation (5.11) the total propagation delay  $|\vec{r}| + |\vec{r}'' - \vec{r}'|/c$  is omitted for simplicity. If this delay is important for the application, it has to be included in equation (5.11).

If the minimal detectable transient signal of the receiver is known, expression (5.11) can be used to calculate the range performance of the impulse radar system. The capability of an impulse radar system to detect a scattered signal can be termed in system detectability:

$$D = 20 \log \left( \frac{V_{rec, peak}}{V_{s, peak}} \right) \quad (5.12)$$

In general the limiting factor of detectability is the noise performance of the receiver. The received voltage must be larger than the noise voltage generated by the receiver. In some cases the detectability can be also limited by the coupling between the antennas. The pulse, radiated by the transmitting antenna will couple directly into the receiving antenna and will ring down. Normally this coupling can be compensated for. If not, the ringing can interfere with the useful backscattered signal and limit the detectability of the system.

## 5.5. GPR range equation in the time domain

As for the frequency domain, the time domain radar range equation can be adapted for the GPR. Therefore, expression (5.11) has to be modified to take into account some additional losses. In the scope of demining applications, the antennas are used off-ground, hence we will have to introduce the transmission loss at the air-ground interface and the propagation loss in the ground (Fig. 5-2). The losses due to the off-boresight position of the target are already taken into account by  $h_N(\mathbf{q}, \mathbf{j}, t)$ , representing the normalised impulse response in the direction  $(\mathbf{q}, \mathbf{j})$ . Suppose that the two-way path loss, due to the propagation in the lossy ground is characterised by an impulse response  $g_d(t)$ . In the absence of noise, the complete GPR radar range equation in the time domain can then be written as

$$V_{rec}(t) = \frac{T_{a-g} \cdot T_{g-a}}{8\pi^2 R_t R_r c} g_d(t) \otimes h_{N,Tx}(\bar{\mathbf{a}}_i, t) \otimes \Lambda_{1,1}(\bar{\mathbf{a}}_i, \bar{\mathbf{a}}_s, t) \otimes h_{N,Rx}(-\bar{\mathbf{a}}_s, t) \otimes \frac{dV_s(t)}{dt} \quad (5.13)$$

with

$R_t$  : the total path length from transmitting antenna to the target

$R_r$  : the total path length from receiving antenna to the target

$g_d(t)$  : the impulse response representing the two-way path length loss in the ground

$T_{a-g}$  : the transmission coefficient at the air-ground interface (air to ground)

$T_{g-a}$  : the transmission coefficient at the air-ground interface (ground to air).

Equation (5.13) allows for any excitation signal  $V_s(t)$  to calculate the received voltage  $V_{rec}(t)$  at the receiving antenna as a function of time. Note that, if the excitation signal  $V_s(t)$  for the implementation of equation (5.13) is measured by the receiver, the influence of the IR of the receiver is automatically taken into account in the time

domain GPR range equation. In the next section, all the terms in equation (5.13), except for the normalised IRs of the antennas, will be discussed in detail.

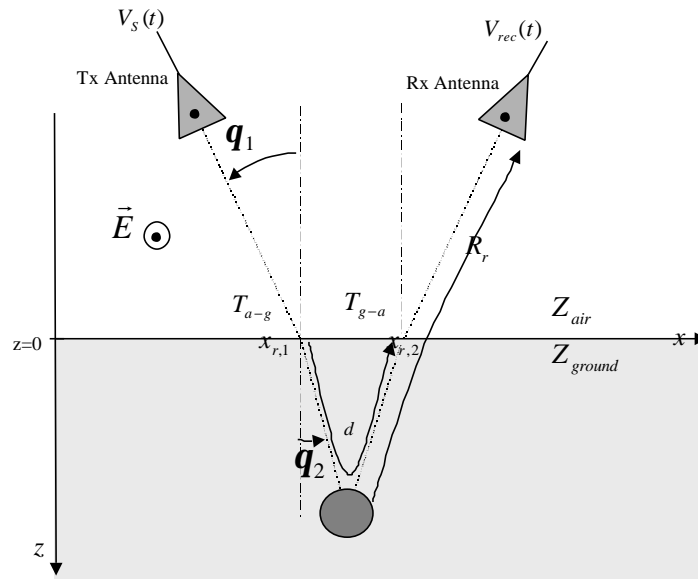


Fig. 5-2: GPR configuration

## 5.6. Calculation of the different terms in the time domain GPR range equation

### 5.6.1. Transmission coefficients on the air-ground interface

The reflection and transmission coefficients of a plane wave at the boundary between two isotropic non-conductive media are described by Fresnel's equations [5]. The coefficients are simply function of the relative permeability and permittivity contrasts between the media and of the angle of incidence. For a complete study, two perpendicular polarisations have to be distinguished, *i.e.* the E-field normal to the plane of incidence (cf. Fig. 5-2), called the normal polarisation and the E-field in the plane of incidence, called the parallel polarisation. In general, geological media have a relative permeability equal 1. In this case, the reflection and transmission coefficients at the boundary between two non-conductive geological media are given by

$$\begin{aligned}
 \Gamma_{\perp} &= \frac{\sqrt{\mathbf{e}_1} \cos \mathbf{q}_1 - \sqrt{\mathbf{e}_2} \cos \mathbf{q}_2}{\sqrt{\mathbf{e}_1} \cos \mathbf{q}_1 + \sqrt{\mathbf{e}_2} \cos \mathbf{q}_2} \\
 T_{\perp} &= \frac{2\sqrt{\mathbf{e}_1} \cos \mathbf{q}_1}{\sqrt{\mathbf{e}_1} \cos \mathbf{q}_1 + \sqrt{\mathbf{e}_2} \cos \mathbf{q}_2} \\
 \Gamma_{//} &= \frac{\sqrt{\mathbf{e}_2} \cos \mathbf{q}_1 - \sqrt{\mathbf{e}_1} \cos \mathbf{q}_2}{\sqrt{\mathbf{e}_2} \cos \mathbf{q}_1 + \sqrt{\mathbf{e}_1} \cos \mathbf{q}_2} \\
 T_{//} &= \frac{2\sqrt{\mathbf{e}_1} \cos \mathbf{q}_1}{\sqrt{\mathbf{e}_2} \cos \mathbf{q}_1 + \sqrt{\mathbf{e}_1} \cos \mathbf{q}_2}
 \end{aligned} \tag{5.14}$$

with

$$\sin(\mathbf{q}_2) = \sqrt{\frac{\mathbf{e}_1}{\mathbf{e}_2}} \sin(\mathbf{q}_1) \tag{5.15}$$

and

- $\Gamma_{\perp}$  : the reflection coefficient for normal polarisation
- $T_{\perp}$  : the transmission coefficient for normal polarisation
- $\Gamma_{//}$  : the reflection coefficient for parallel polarisation
- $T_{//}$  : the transmission coefficient for parallel polarisation
- $\mathbf{q}_1$  : the incident angle
- $\mathbf{q}_2$  : the refraction angle.

In reality, a geological medium is conductive, hence the reflection and transmission coefficients are complex. At radar frequencies, the conductive geological media can be assumed to be free of electric charges and currents, so that conditions for the electric and magnetic fields at the boundaries of the two media are the same as for the non-conductive media case [6]. Hence by analogy, the reflection and transmission coefficients are also given by expression (5.14), providing that the permittivity  $\mathbf{e}$  in (5.14) and (5.15) is replaced by the corresponding complex apparent permittivity  $\mathbf{e}^*$  of the conductive media. If the imaginary part of the conductivity  $\mathbf{s}''$  is neglected, the apparent permittivity  $\mathbf{e}^*$  is approximately given by (2.13) as

$$\mathbf{e}^* = \mathbf{e}'(1 - j \tan \mathbf{d}) \quad (5.16)$$

In the constant  $Q$  model (Section 2.2.3) the loss tangent  $\tan \mathbf{d}$  and the real part of the permittivity  $\mathbf{e}'$  are considered to be independent of frequency, hence the apparent permittivity  $\mathbf{e}^*$  is independent of frequency. In this approximation the reflection and transmission coefficients in (5.14) become independent of frequency. This is an important result, as it means that neither the reflection at a boundary between two conductive media nor the transmission through such boundary will introduce dispersion.

Furthermore, in a study by Lehmann [6], it is stated that for radar frequencies, the reflection and transmission coefficients at boundaries between loss-less media is a good approximation for the reflection and the transmission coefficients for conductive media. The latter has been verified and approved with the soil measurements performed in the scope of the HUDEM project [7]. For example, suppose an interface between air and wet sand with a moisture content of 10% ( $\mathbf{e}'_r = 7.18$  and  $\tan \mathbf{d} = 0.069$  at 2 GHz). In the case were no losses are assumed ( $\tan \mathbf{d} = 0$ ), the transmission coefficient for normal polarisation is calculated to be 0.5224. If the losses are taken into account, the transmission coefficient for normal polarisation is calculated to be  $0.5219 + j*0.0135$ , which means a difference of 0.0068 dB.

To summarise, in the time domain radar range equation (5.13), the transmission coefficients on the air-ground interface can be calculated using (5.14), if we replace  $\mathbf{e}_1$  by  $\mathbf{e}_0$ , the permittivity of free space, and  $\mathbf{e}_2$  by  $\mathbf{e}_2'$ , the real part of the permittivity of the ground. In our configuration (Fig. 5-2), we only work with the electric field normal to the plane of incidence, hence the transmission coefficients as needed for the time domain radar range equation are given by:

$$T_{a-g} = \frac{2\sqrt{\mathbf{e}_0} \cos \mathbf{q}_1}{\sqrt{\mathbf{e}_0} \cos \mathbf{q}_1 + \sqrt{\mathbf{e}_2'} \cos \mathbf{q}_2} \quad (5.17)$$

$$T_{g-a} = \frac{2\sqrt{\mathbf{e}_2'} \cos \mathbf{q}_2}{\sqrt{\mathbf{e}_2'} \cos \mathbf{q}_2 + \sqrt{\mathbf{e}_0} \cos \mathbf{q}_1} \quad (5.18)$$

Note that the transmission coefficients further suppose that the interface is flat and in the far-field of the antennas. In practice these two assumptions are not always respected.

### 5.6.2. Total path length in the air and in the ground

In the GPR range equation given in (5.13), the total path length from the transmitting antenna to the target, the total path length from the target to the receiving antenna and the two-way path length in the ground are needed. In all of the discussions made thus far, we did not mention the refraction on the air-ground interface. For a correct calculation of the above path lengths, the refraction has to be taken into account and the refraction points, denoted  $x_{r,1}$  and  $x_{r,2}$  in Fig. 5-2, on the air-ground interface have to be calculated. Suppose a 2-D configuration as shown in Fig. 5-3. The antenna can move at a fix height  $h$  above the air-ground interface, so the antenna position is characterised by only one co-ordinate  $x$ . The object in the ground is buried at a depth  $d$  at position  $x_2$ . The refraction point  $x_r$  can be calculated according to Snell's refraction law, assuming the air-ground interface is flat and in the far-field of the antennas. This leads to a system of three equations that can be solved by means of iteration:

$$\begin{aligned} \sin(\mathbf{q}_2) &= \sqrt{\frac{\mathbf{e}_1}{\mathbf{e}_2}} \sin(\mathbf{q}_1) \\ \tan(\mathbf{q}_1) &= \frac{|x - x_r|}{h} \\ \tan(\mathbf{q}_2) &= \frac{|x_2 - x_r|}{d} \end{aligned} \quad (5.19)$$

An accurate approximation however for the calculation of the refraction points is found in the following method [8]. Suppose the relative permittivity  $\epsilon_2$  of the second medium is larger than the relative permittivity  $\epsilon_1$  of the first one (this is always the case for the antennas in the air). There are two extreme paths between an antenna and an object in the ground. If  $\epsilon_2 \rightarrow \infty$ , then the refraction point will be at  $x_2$ . If  $\epsilon_2 = \epsilon_1$ , the refraction point will be at  $x_1$ . For values of  $\epsilon_2$  between those two extremes, the refraction point can be linearly approximated by

$$x_r = x_2 + \sqrt{\frac{\epsilon_1}{\epsilon_2}}(x_1 - x_2) \tag{5.20}$$

This simple approximation is very accurate. In the case of antennas scanning at 25 cm above the air-ground interface and an object buried at 10 cm, the maximum error between the approximated position of the refraction point using (5.20) and the real position, is less than 2 mm. This is shown in Fig. 5-4. The position  $x$  of the antenna is represented on the x-axis. The position  $x_r$  of the refraction point is represented on the y-axis. The relative permittivity of the ground is taken  $\epsilon_2 = 9$  for this calculation. The real refraction point is given in red and the approximated one in blue.

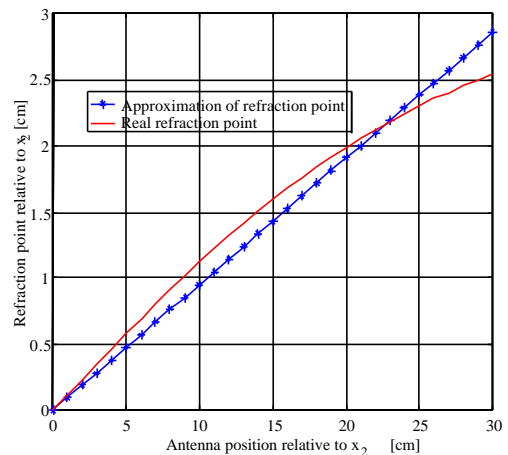
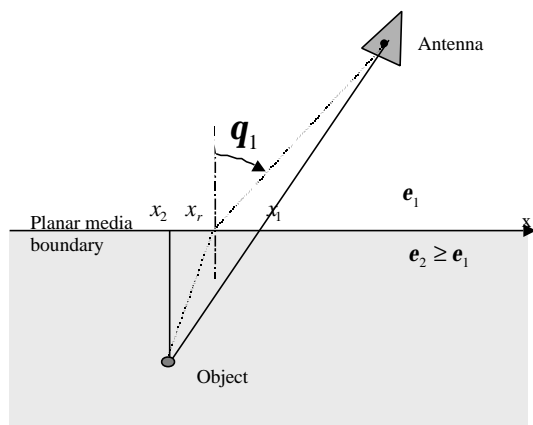


**Fig. 5-3:** Geometry for the calculation of the refraction point **Fig. 5-4:** Validation of the approximation of the refraction point

In the implementation of the GPR range equation, we use the approximation given by (5.20) to calculate the refraction point on the interface for the path between the transmitting antenna to the target and the refraction point on the interface for the path between the target and the receiving antenna. If the second medium is lossy, the real part of  $\epsilon_2$  is used in equation (5.20). Hence the approximated distances  $R_t$ ,  $R_r$ , and  $d$  (the total path length in the ground) can be calculated without too much effort.

### 5.6.3. Ground as a low-pass filter

The propagation losses and dispersion in the ground are not so easy to introduce and need some more explanations. The best way to handle these losses is by representing the ground as a low-pass filter, characterised by its IR  $g_d(t)$  or the corresponding Frequency Response Function  $G_d(\omega)$ . The parameters of this filter are depending on the soil characteristics, *i.e.* the texture of soil, the density and the moisture content, and the two-way path length of the wave in the ground, denoted as  $d$  in Fig. 5-2.

As already discussed in Chapter 2, soils are lossy media characterised by a complex conductivity  $\sigma' - j\sigma''$  and a complex permittivity  $\epsilon' - j\epsilon''$ . The solution to Maxwell's equations describing a harmonic plane wave propagating in a lossy medium is given by

$$\vec{E} = \vec{E}_0 e^{-(\vec{a} + j\vec{b})\vec{r}} \quad (5.21)$$

with

$$\mathbf{a} = \omega \sqrt{\mathbf{m}_0 \epsilon'} \sqrt{\frac{1}{2} \cdot (\sqrt{(1 + tg^2 d)} - 1)} \quad \text{the attenuation constant [Np/m] of the medium}$$

$$\mathbf{b} = \omega \sqrt{\mathbf{m}_0 \epsilon'} \sqrt{\frac{1}{2} \cdot (\sqrt{(1 + tg^2 d)} + 1)} \quad \text{the phase constant [rad/m].}$$

According to (5.21), the propagation of the plane wave over a distance  $d$  meters in the direction of the propagating wave can be characterised as a linear system with a frequency response function

$$G_d(\mathbf{w}) = e^{-(\mathbf{a}+j\mathbf{b})d} \quad (5.22)$$

Note that the same frequency response function would be found in case of spherical waves, because the spreading loss is already taken into account in the radar equation (5.13).

The constants  $\alpha$  and  $\beta$  can be calculated by measuring the complex electrical parameters of the soil over a large frequency band. By an inverse time-frequency transformation or by a filter design method, the impulse response  $g_d(t)$ , representing the losses of a propagation of  $d$  meters in the ground, can be found.

Measuring the electrical parameters over a large bandwidth and designing the filter would be very difficult. Therefore a more convenient way of calculating the filter is presented here. In the constant  $Q$  model (Section 2.2.3), the attenuation constant and the phase constant can be approximated by

$$\mathbf{a} = \mathbf{w}\sqrt{\mathbf{m}\mathbf{e}'} \frac{\tan \mathbf{d}}{2} \quad (5.23)$$

$$\mathbf{b} = \mathbf{w}\sqrt{\mathbf{m}\mathbf{e}'} \quad (5.24)$$

with  $\tan \mathbf{d}$  small and constant with frequency and  $\mathbf{e}'$  constant with frequency. This means that in this approximation  $\mathbf{a}$  and  $\mathbf{b}$  are linear with frequency and that the frequency response function (5.22) can be written as

$$G_d(\mathbf{w}) = e^{-j\mathbf{w}d\sqrt{\mathbf{m}\mathbf{e}'}} e^{-\mathbf{w}d\sqrt{\mathbf{m}\mathbf{e}'}\tan \mathbf{d}/2} \quad (5.25)$$

The first exponential represents the delay due to the propagation through  $d$  meters of soil. The second exponential represents a linear amplitude distortion introduced by the propagation through the ground. The corresponding IR  $g_d(t)$  is found by an inverse Fourier transformation of (5.25) and can be analytically expressed as

$$\begin{aligned} g_d(t) &= \frac{1}{2\mathbf{p}} \int_{-\infty}^{+\infty} G_d(\mathbf{w}) e^{j\mathbf{w}t} d\mathbf{w} \\ &= \frac{1}{2\mathbf{p}} \int_{-\infty}^{+\infty} e^{-\mathbf{a}d} e^{j\mathbf{w}(t-d\sqrt{\mathbf{m}\mathbf{e}'})} d\mathbf{w} \\ &= \frac{d\sqrt{\mathbf{m}\mathbf{e}'(\tan \mathbf{d})}/2}{\mathbf{p}} \left[ \frac{1}{2\mathbf{p}} \int_{-\infty}^{+\infty} \frac{\mathbf{p} e^{-\mathbf{w}(d\sqrt{\mathbf{m}\mathbf{e}'(\tan \mathbf{d})}/2)}}{d\sqrt{\mathbf{m}\mathbf{e}'(\tan \mathbf{d})}/2} e^{j\mathbf{w}(t-d\sqrt{\mathbf{m}\mathbf{e}'})} d\mathbf{w} \right] \end{aligned}$$

Hence :

$$g_d(t) = \frac{d\sqrt{\mathbf{m}\mathbf{e}'(\tan \mathbf{d})}/2}{\mathbf{p} \left[ (t - d\sqrt{\mathbf{m}\mathbf{e}'})^2 + (d\sqrt{\mathbf{m}\mathbf{e}' \tan \mathbf{d} / 2})^2 \right]} \quad (5.26)$$

The calculation of the IR, characterising a propagation through  $d$  meters of soil is made very simple by equation (5.26). As  $\tan \mathbf{d}$  and  $\mathbf{e}'$  are supposed constant with frequency in the constant  $Q$  model, they only have to be measured for one frequency (preferably in the middle of the frequency band of interest).

As an example, we calculate the IR of a wet sandy soil with a moisture content of 10% using (5.26). The real relative permittivity of the soil is  $\mathbf{e}'_r = 8.16$  and a loss tangent  $\tan \mathbf{d} = 0.085$ . Fig. 5-5 shows the impulse response characterising the propagation through a layer of respectively 10 cm and 20 cm of this lossy soil. Fig. 5-6 shows the attenuation and distortion of a transient pulse propagating through the same soil after 10 cm and 20 cm. On the left of the figure (in red), the electric field component of the incoming plane wave is represented. In blue and green the transient pulse is shown at 10 cm and 20 cm in the ground. They are obtained by convolving the incoming pulse (in red) by the IR shown in Fig. 5-5. Both the attenuation in the ground and the dispersive behaviour of the ground, resulting in the broadening of the pulse, are obvious. Note that the decrease in amplitude of the pulse is not due to

spreading loss because a plane wave is assumed. It is only due to the attenuation in the ground.

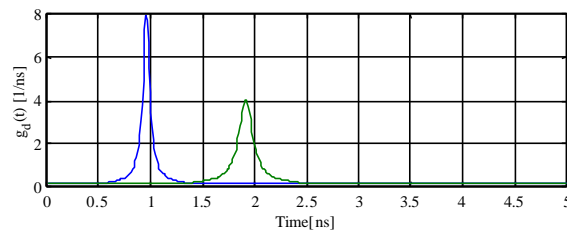


**Fig. 5-5:** Impulse response of wet sandy soil for  $d = 10$  cm (blue) and  $d = 20$  cm (green), using (5.26)

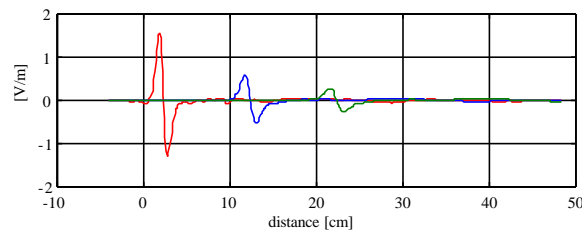


**Fig. 5-6:** Transient pulse before entering the ground (red) and at 10 cm (blue) and 20 cm (green) in the ground

#### 5.6.4. Impulse Response of objects

##### *General*

The IR of an object is defined by the time domain equation (5.9). It can be considered as the time equivalent of the RCS of an object. According to the definition of the RCS in (5.4), that is based on a power ratio of the scattered to the incident field, the IR of an object is based on a ratio of magnitudes of the scattered to incident field. By converting equation (5.9) into the frequency domain, the Frequency Response Function (FRF) of an object, which is defined as the Fourier transform of the IR, can mathematically be expressed, as

$$\Lambda_{1,1}(\vec{a}_i, \vec{a}_s, \mathbf{w}) = 4\mathbf{p} \lim_{R \rightarrow \infty} R \frac{E_s(\vec{a}_s, \mathbf{w})}{E_i(\vec{a}_i, \mathbf{w})} \quad (5.27)$$

with  $E_s(\vec{a}_s, \mathbf{w})$  the scattered field in the direction  $\vec{a}_s$

$E_i(\vec{a}_i, \mathbf{w})$  the incoming field on the object from the direction  $\vec{a}_i$ .

Hence the IR of an object can be written as

$$\Lambda_{1,1}(\vec{a}_i, \vec{a}_s, t) = \mathfrak{F}^{-1} \left\{ 4\mathbf{p} \lim_{R \rightarrow \infty} R \frac{E_s(\vec{a}_s, \mathbf{w})}{E_i(\vec{a}_i, \mathbf{w})} \right\} \quad (5.28)$$

with  $\mathfrak{F}^{-1}$  the inverse Fourier transform.

In (5.27) and (5.28) only one polarisation is assumed. When investigating the complete scattering process of an object, one has to take into account all the polarisations. For an arbitrarily polarised incident plane wave, split into two orthogonal components, the scattered far field can be expressed as

$$\begin{bmatrix} E_s^\perp \\ E_s^\parallel \end{bmatrix} = \begin{bmatrix} S_{1,1} & S_{1,2} \\ S_{2,1} & S_{2,2} \end{bmatrix} \begin{bmatrix} E_i^\perp \\ E_i^\parallel \end{bmatrix} \quad (5.29)$$

or in short

$$\begin{bmatrix} E_s^\perp \\ E_s^\parallel \end{bmatrix} = S \begin{bmatrix} E_i^\perp \\ E_i^\parallel \end{bmatrix} \quad (5.30)$$

where  $E^\perp$  is the polarisation normal to the plane of incidence and  $E^\parallel$  the polarisation parallel to the plane of incidence.  $S$  is called the scattering matrix. The terms  $S_{i,j}$  are the scattering coefficients. The subscripts refer to the two orthogonal polarisation components (normal and parallel). The coefficients  $S_{1,2}$  and  $S_{2,1}$  are the cross-polarisation coefficients. The scattering coefficients are in general complex numbers

and can be represented by an amplitude and phase. The scattering coefficients are directly related to the FRF  $\Lambda_{i,j}(\mathbf{w})$  as

$$\Lambda_{i,j}(\mathbf{w}) = 4pR S_{i,j}(\mathbf{w}) \quad (5.31)$$

In the next chapter, the radar range equation will be used to describe a laboratory UWB GPR. In this set-up, the two antennas are placed with a common H-plane, hence the radiated and received field have the same polarisation (normal to the plane of incidence). This means that in the radar range equation we will only use one polarisation. Therefore the subscript  $i,j$  in the notation of the IR of the target will be omitted in the future.

### ***RCS and Impulse response of a perfect conductive metallic sphere***

As a reference and calibration target in the ground, we often use a metallic sphere. Therefore we discuss its IR in this section. The backscattering on a perfect conductive metallic sphere is given under analytical form by the MIE series [9]. In Fig. 5-7 the RCS of a metallic sphere with a radius of  $a = 5$  cm is given as a function of  $ka = 2\pi a / \lambda$ . The RCS is plotted normalised to the physical cross section of the sphere. In general the RCS of an object is frequency dependent and can be divided into three regions (see Fig. 5-7).

The first region is the *Rayleigh region* or *low frequency region*. In this region the wavelength of the illuminating waveform is large compared to the target dimensions. There is essentially no variation of the phase of the incident wave over the target. The scattered power or the RCS is asymptotically proportional to the fourth power of the frequency.

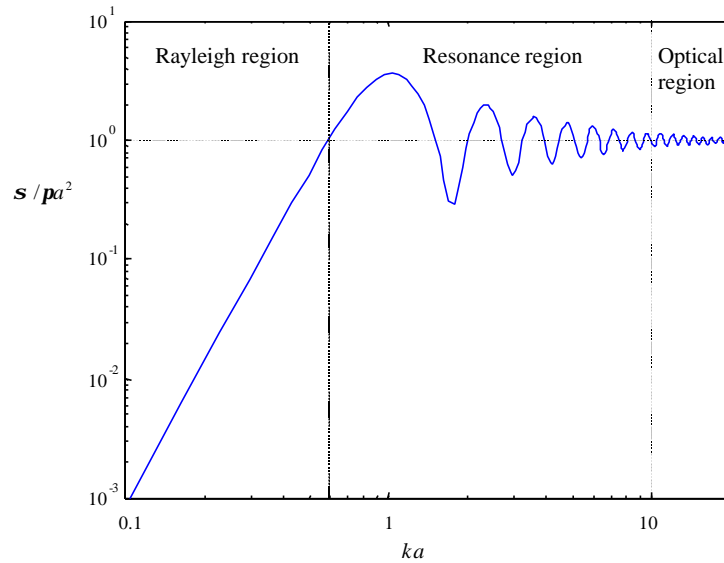


**Fig. 5-7:** RCS of metallic sphere, showing three scattering regimes

The second region is the *resonance region*. In the resonance region, the incident wavelength is of the order of the size of the target. In this region the RCS of a target can be calculated by solving the integral equation relating the induced current on or in the body to the incident field [2]. Normally these induced currents can be represented as damped sinusoids (see also Chapter 7, Section 7.2.2). The peaks and valleys in the resonance region can be seen as respectively the constructive and destructive interference of different backscattering mechanisms on the target. Fig. 5-8 shows five backscattering mechanisms on a *dielectric sphere* [10]:

1. The specular wave is a return from the front of the sphere
2. The axial wave is due to the reflection on the back of the sphere
3. The glory wave is a wave which is first refracted, then reflected on the back and finally refracted into the backscatter direction; for dielectric targets, this wave can be dominant
4. The stationary wave is also a refracted, reflected and then refracted wave, but its ray paths is not exactly in the backscatter direction
5. The creeping wave is a well known backscatter mechanism that is guided by the curved surface of the sphere.

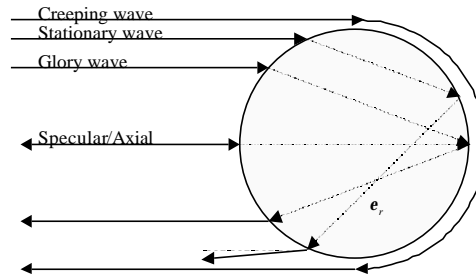


**Fig. 5-8:** backscattering mechanism on a dielectric sphere

The example of a dielectric sphere is chosen here because in general for dielectric targets there are more scattering mechanisms that interfere. For a metallic sphere, as they are non-penetrable, only the specular wave and the creeping wave interfere. The first resonant peak in the RCS of a metallic sphere (Fig. 5-7) appears for  $ka = 1$ . This corresponds to the point where one wavelength of the incident wave is exactly equal to the circumference of the sphere. At this frequency, the creeping wave will constructively add to the specular wave in the backscatter direction, hence the peak.

The last region in the RCS is the *optical region*. In this region the target is much larger than the wavelength of the incident field. For a metallic sphere, the RCS in this region converge to a constant value equal to its physical cross section.

In Fig. 5-9 the monostatic impulse response of the metallic sphere (radius  $a = 5$  cm) is given. The IR is obtained by (5.28), where the scattered field in the backward direction is calculated using the MIE series. The first reflection (at 3 ns) is the specular reflection on the sphere. The amplitude of this reflection is a function of the cross section of the sphere. In the IR of the metallic sphere, a second reflection appears 0.86 ns later. This reflection is the part of the creeping wave that went around the sphere and scatters in the backward direction. The time between the two reflections is given by

$$\frac{a(2+p)}{c} \quad (5.32)$$

Note that the different backscatter mechanisms can lead to scattering centres that appear further (*i.e.* later in time) than the physical cross diameter of the object. This simple example of the metallic sphere shows very well the correspondence between the IR and the RCS of a target.

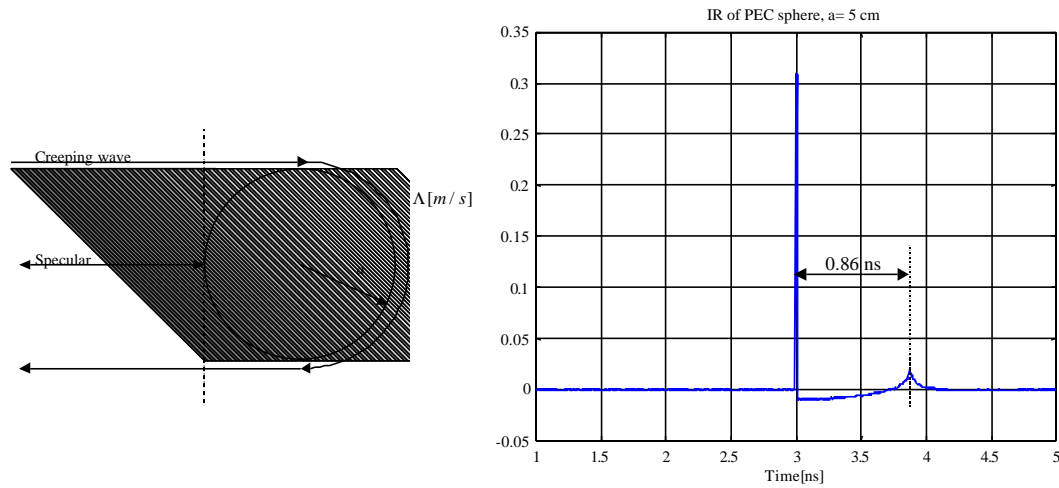


**Fig. 5-9:** IR of a perfect conductive metallic sphere, showing two scattering centres

In the resonance and optical region, the RCS of the metallic sphere varies around its physical cross section  $\pi a^2$ . If we consider as an approximation that this RCS is constant, independent of frequency, then the IR of this fictive target will be a dirac-function. For a radius  $a = 5$  cm, hence  $S = \pi a^2 = 0.0079$  m<sup>2</sup>, the IR of such a target is calculated as

$$\Lambda(t) = 0,314d(t) \tag{5.33}$$

This can also be verified by comparing the definitions of the RCS (5.4) with the definition of the IR (5.28). In the case of a constant RCS, the FRF given by (5.27) is expressed as

$$\Lambda(\omega) = \sqrt{4ps(\omega)} \tag{5.34}$$

Hence :

$$\Lambda(t) = \sqrt{4ps}d(t) \quad (5.35)$$

which corresponds with the solution found in (5.33). Comparing the result of (5.33) with the exact IR of a metallic sphere in Fig. 5-7, we see that the amplitude of the dirac-function corresponds with the amplitude of the specular reflection on the sphere. So equation (5.35) can be used as a good approximation for the metallic sphere.

### *Impulse response of mine-like objects*

In general, the response of any arbitrary target can be split into two parts: the early time response and the late time response. The early time is considered to be the scattering response of the object over a time interval, which is of the order of the wave transit time through the object. The late time response contains all the resonances of the target. These resonances are supposed to be little influenced by the orientation of the object and hence contain valuable information for target recognition.

Mine-like targets are non-canonical dielectric or metallic objects. Hence, it is too difficult to calculate analytical solutions of the IR. Numerical calculation methods, like the Finite Difference Time Domain method (FDTD) [11] or the Method of Moments (MoM) [12] are more appropriate.

An alternative way is to measure the IR. In the early stages of this research we did some measurement of the short pulse response on mine like targets. More details on these measurements are found in appendix A and in [13]. The measurements were done with a Time-Domain Scattering Range (TDSR) that was developed at the RMA [14]. The TDSR is designed to study experimentally the transient backscattering of 3D objects. The measurement set-up is schematically represented in Fig. 5-10. The system consists of the following parts. On the transmitting side, a 2 meter long monocone antenna on a square ground plane (3 x 3 m) is coaxially fed by a fast step generator. On the receiving side, a broadband electric field sensor, which is connected to a 20 GHz digitising oscilloscope through a set of UWB low noise amplifiers, detects the transient wave. The 3D Device Under Test (DUT) is put on the ground

plane and is illuminated by the transient spherical wave radiated between the monocone and the ground plane. The backscattering of the DUT is measured by the E-field sensor. Because the long monocone antenna radiates a step function signal and because the electric field sensor is a time derivative sensor, its output yields in fact the *impulse response* of the DUT.

The step generator generates a repetitive step function voltage (10V/45ps) with a high waveform purity. The generator confers to the TDSR a *subcentimeter radial resolution* on the target in the air, which makes it possible to resolve the different scattering centres of the target and to quantify their relative amplitudes.

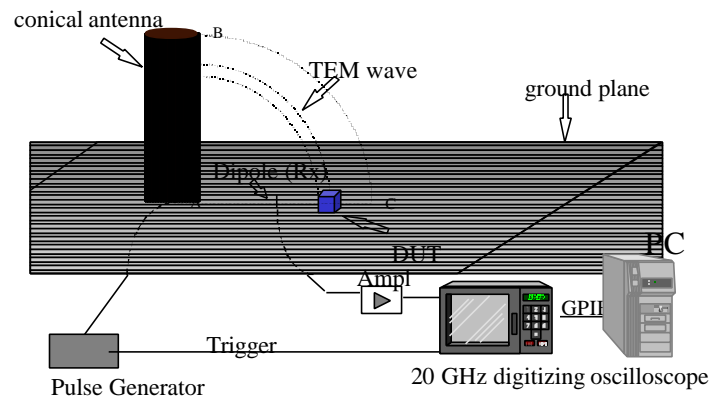


**Fig. 5-10:** The Time-Domain Scattering Range at the RMA

The Time-Domain Scattering Range is also used to measure the Frequency Response Function (FRF) of non-canonical 3D objects using a dual channel analysis technique. The complete study and conclusions are discussed in appendix A.

Fig. 5-11 shows in blue the measurement of the short pulse response by the TDSR on the Teflon cylinder in free space as a function of time. The Teflon cylinder has the same dimensions as a typical AP mine (8 cm diameter and 3.8 cm thick). For verification, the measured short pulse response of the Teflon cylinders is compared with an FDTD simulation. The simulated data of the short pulse response is represented in red in Fig. 5-11. The result shows that the measurements and the

simulations are very similar, which makes us confident in both approaches. In the late time response of the cylinders, the different scattering centres due to the different backscattering mechanisms clearly appear. In Fig. 5-12 the rays of the specular, axial and creeping waves are represented. The additional travelling time of these paths are also projected on Fig. 5-11, with path 1 as a reference in time. The additional travelling time of path 3 is calculated with the propagation velocity in the Teflon, whereas the additional travelling time of path 4 is calculated with the propagation velocity of free space, hence their difference. The additional travelling time of path 2 gives an indication of the physical size of the target on the time axis. It also indicates the end of the early time response and the beginning of the late time response. The reflections on the back of the Teflon cylinder are small compared to the other backscatter mechanisms.

Just like with the metallic sphere, there are scattering centres, which appear later in time than the reflection on the back of the object. The travelling time of path 2 gives an indication of the physical size of the target on the time axis. There are two scatter centres with larger amplitude that appear later in time than the reflection on the back of the cylinder. This indicates that it will be very difficult to retrieve from the backscattered signal accurate information on the size of the target in the range direction (*cf.* the  $z$  direction in Fig. 5-2).

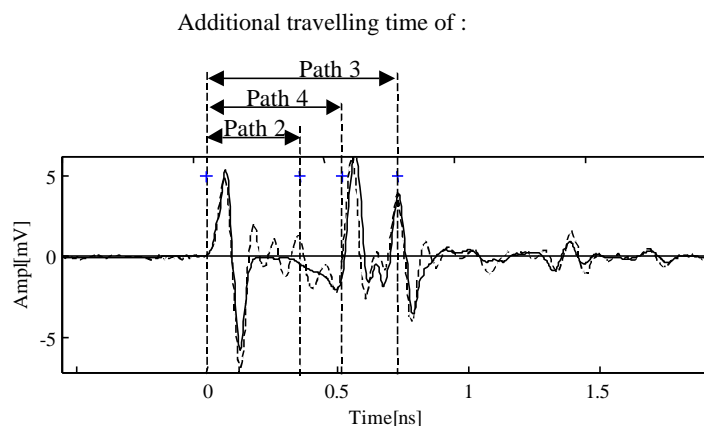


**Fig. 5-11:** Measured (dashed) and simulated (solid) short pulse response on a Teflon cylinder in free-space. The additional travelling time of path 2,3 and 4 are also represented on the figure.

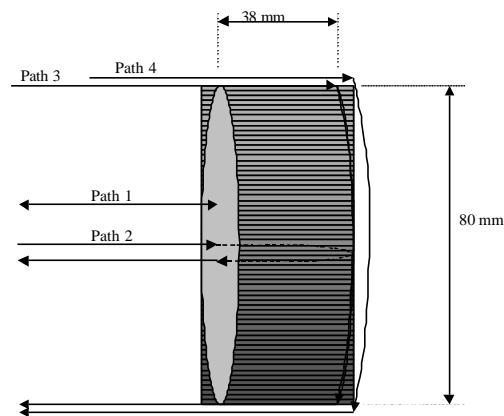


**Fig. 5-12:** Teflon cylinder with some specific rays

A disadvantage of the above method is that the objects were only considered in free space. In the application of demining, the targets are buried in a lossy half-space. As a consequence the IR of a target will not only depend on the shape and orientation of the target but also on the characteristics of the half-space the target is in. In other words the system to be considered is not the target, but the target in its surrounding medium. In reality the number of unknown parameters influencing the IR will often be too large to accurately forward model an IR of a target, even with numerical models. In the literature, studies are found on the influence of the ground on the late time response of targets [12]. The study is in general very difficult and considered being out of the frame of this research.

## 5.7. Summary

Using the radar range equation to describe a time domain system has some disadvantages. The radar range equation contains frequency dependent terms and does not take into account the nature of the transmitted signal. Therefore we modelled in this chapter the total system: GPR-ground-target in the time domain by considering it as a cascade of linear responses, resulting in a *time domain GPR range equation* (5.13). The time domain GPR range equation allows us to calculate the received voltage as a function of time at the output of the receiving antenna in terms of the radar characteristics and the target. The model is adapted for the demining

application, *i.e.* antennas off-ground, no multiple layers, etc. The different parts in this cascade are the pulse generator, the antennas modelled by their normalised impulse response, the spreading losses, the transmission coefficients on the air-ground interface, the propagation through the ground and the scattering on the target in the ground. Fig. 5-13 shows a schematic representation of the different parts of the time domain GPR range equation, summarising the whole chapter. The GPR configuration is as shown in Fig. 5-2 and the target is a metallic sphere with a radius of 5 cm. The influence of each part in the cascade on the signal is visualised.

For the characterisation of the losses in the ground, an analytical expression of the impulse response modelling the propagation in the ground is presented. The expression of the impulse response is calculated from the theoretical frequency response function of the lossy soil and takes into account the attenuation and the dispersive behaviour of the ground. The only three parameters in this expression are the real part of the permittivity, the loss tangent (which are both considered as being independent of frequency for a given soil type and moisture content) and the path length in the ground.

The targets in the ground are also characterised by an IR. We calculated and discussed the exact IR of a metallic sphere and the measured short pulse response of a Teflon cylinder in free space. We showed that the IR is a combination of different scattering mechanism. In general we can say that the dimensions of the targets are of the same order as the wavelengths used in the GPR. This means that we are primarily working in the resonance region of the scattering, leading to scattering centres that appear later in time than the reflection on the back of the target.

In the next chapter we will use the time domain GPR range equation to study and optimise the performance of a laboratory UWB GPR system.

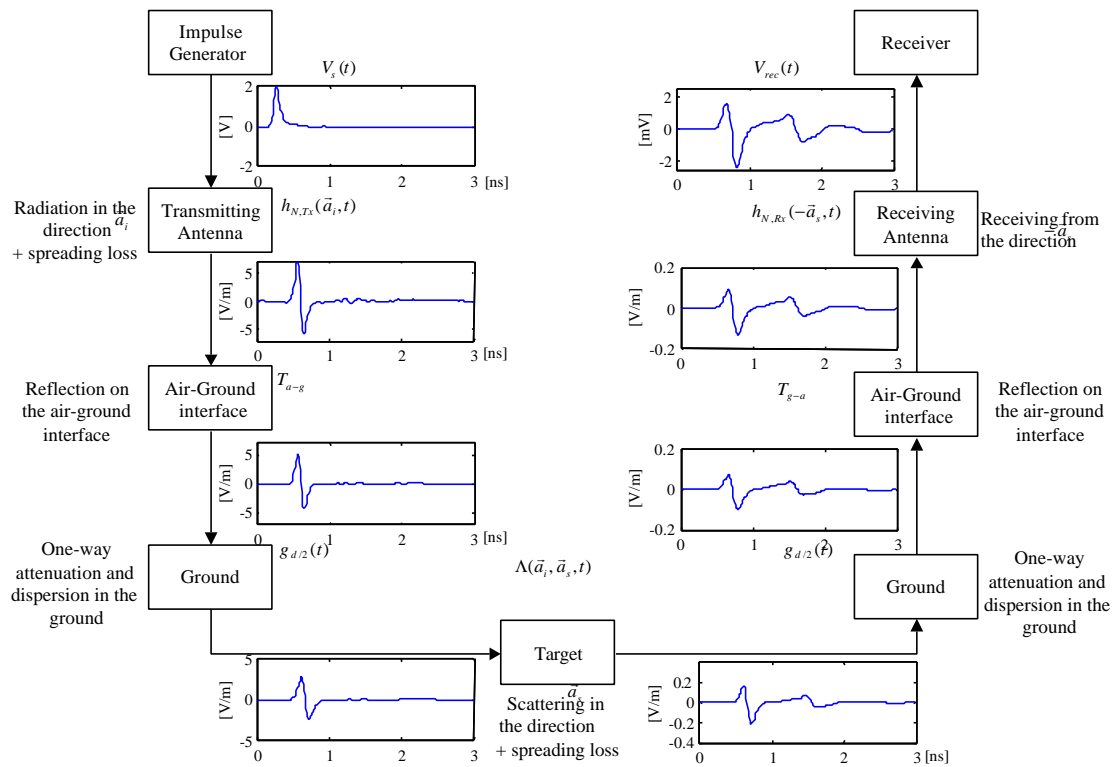


**Fig. 5-13:** Schematic representation of the different parts of the time domain GPR range equation

## REFERENCES

- [1] M. Skolnik, *Radar handbook*. New York: McGraw-Hill, 1990.
- [2] M. L. Van Blaricum, *Introduction to Ultra-Wideband Radar Systems*. J. D. Taylor, Ed., USA: CRC Press, 1995, ch. 9.
- [3] J. L. Davis and A. P. Annan, "Ground-Penetrating Radar for High-Resolution Mapping of Soil and Rock Stratigraphy," *Geophysical Prospecting*, vol. 37, pp. 531-551, 1998.
- [4] B. Scheers, Y. Plasman, M. Piette, M. Acheroy and A. Vander Vorst, "Laboratory UWB GPR system for landmine detection," *Eight International Conference on Ground Penetrating Radar*, Gold Coast, Australia, pp. 747-752, May 2000.
- [5] J. Stratton, *Electromagnetic Theory*. New York: McGraw-Hill, 1941.
- [6] F. Lehmann, "Fresnel equations for reflection and transmission at boundaries between two conductive media, with applications to georadar problems," *6th International Conference on Ground Penetrating Radar (GPR96)*, Japan, pp. 555-559, Sep.-Oct. 1996.
- [7] M. Storme, I. Huynen and A. Vander Vorst, "Characterization of wet soils in the 2-18 GHz frequency range," *Microwave and optical technology letters*, vol. 21, no. 5, June 1999.
- [8] J. Mast and E. Johansson, "Three-dimensional ground penetrating radar imaging using synthetic aperture time domain focusing," *Spie Proceedings on advanced microwave and millimeterwave detectors*, vol. 2275, pp. 205-214, Jul. 1994.
- [9] G. Mie, "Beitrage zur Optik trüber Medien, speziell kolloidaler Metallösungen," *Ann. Physik.*, band 25, pp. 377-445, March 1908.
- [10] S. R. Cloude, A. Milne, C. Thornhill and G. Crisp, "UWB SAR detection of dielectric targets," *IEE Eurel International Conference on The Detection of Abandoned Land Mines*, Edinburgh, UK, pp. 114-118, Oct. 1996.
- [11] K. S. Kunz and R. J. Luebbers, *The finite Difference Time Domain Method for Electromagnetics*. London: CRC Press , 1993.
- [12] S. Vitebskiy and L. Carin, "Resonances of Perfectly Conducting Wires and Bodies of Revolution Buried in a Lossy Dispersive Half-Space," *IEEE Trans. on Antennas and Propagat.*, vol. 44, no. 12, pp. 1575-1583, Dec. 1996.

- [13] B. Scheers and M. Piette, "Short-pulse response of antipersonnel landmines to UWB GPR signals", *Seventh International Conference on Ground Penetrating Radar*, Kansas, USA, pp. 337-341, May 1998.
- [14] M. Piette, *Banc de mesure en régime transitoire de la signature radar d'objets tridimensionnels*, Doctoral thesis, Université catholique de Louvain and Royal Military Academy, Belgium, Oct. 1995.



---

## **Chapter 6. Study of the UWB GPR**

---

### **6.1. Introduction**

At the start of the HUDEM project in 1996, there was no UWB GPR system commercially available. Therefore we decided to develop a laboratory version of an impulse UWB GPR to investigate the feasibility of enhancing the depth resolution and classification capability of UWB systems. Further the system would provide us with the necessary UWB data for the evaluation of signal- and image processing algorithms, developed by other researchers in the scope of the HUDEM project. In this chapter we will give a detailed description of the system and its acquisition software, together with a study of the antenna set-up and the range performance of the system, using the time domain model from the previous chapter. Finally some raw data on surrogate mines are shown and preliminary results are drawn.

### **6.2. General description of the system**

The components of the laboratory UWB GPR are mainly off-the-shelf laboratory equipment. Only the antennas are developed in the RMA. A schematic representation of the UWB GPR system is given in Fig. 6-1.

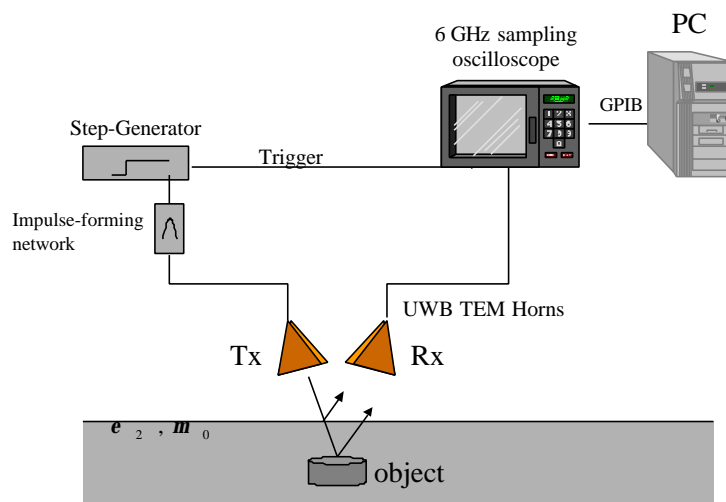


**Fig. 6-1:** Schematic representation of the UWB GPR system

### *Transmitter*

On the transmitting side a Picosecond Pulse Labs step-generator type PSPL 4050B is used, followed by an impulse-forming-network. The PSPL 4050B is a step-generator based on the combination of an avalanche transistor and a Step Recovery Diode (SRD). The avalanche transistor is used as a fast switch, allowing a rapid discharge of the energy stored in a transmission line. The rise time of the generated fast transition is later on enhanced by a SRD. In the PSPL 4050B this SRD is implemented in a box outside the generator as shown in Fig. 6-2.



**Fig. 6-2:** The Picosecond Pulse Labs step-generator, type PSPL 4050B

The pulse repetition frequency (PRF) of the generator can be manually set from 10 Hz to 1 MHz. The delay between the trigger output and the step is adjustable by four switches on the front panel between 0 and 110 ns. The delay uncertainty or jitter of

the generator is inferior to 3 ps [1]. The generated step has an amplitude of 10 V, a very short rise-time and a high waveform purity. The step, recorded by a 20 GHz sampling oscilloscope is shown in Fig. 6-3. The measured rise-time is 60 ps.

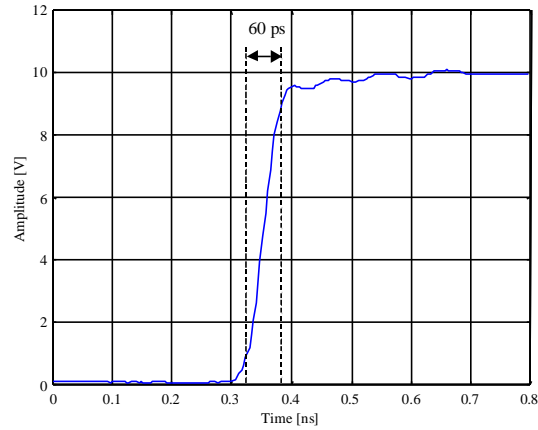


**Fig. 6-3:** Waveform generated by the step-generator PSPL 4050B

The fast transient step is transformed by an impulse-forming-network to a pulse with a maximal amplitude of 2.55 Volts. Experience learned that using a pulse as input signal for the antennas works better than using a step. It limits in time the cross coupling between the antennas. The pulse waveform, measured by a 6 GHz sampling oscilloscope is shown in Fig. 6-4. The Full Width at Half Maximum (FWHM) is 82 ps and the oscillations in the tail of the pulse do not exceed 90 mV or 3.6 % of the full scale.

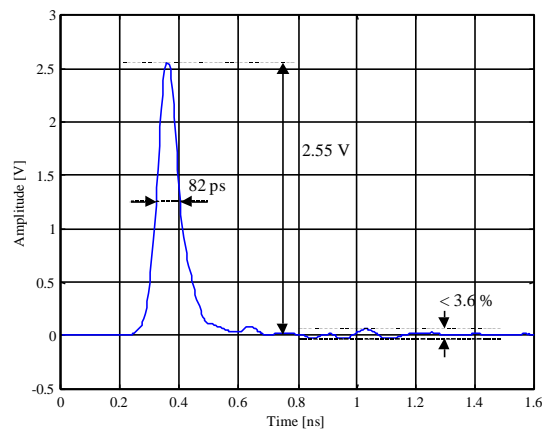


**Fig. 6-4:** Pulse waveform after the impulse-forming-network

### ***Antennas***

The pulse coming from the impulse-forming-network is fed to a pair of two identical TEM horn antennas, with a dielectric filling. A photo of the antennas is shown in Fig. 6-8. The antennas used in the laboratory UWB system are referred to as *Antenna 4* in Chapter 4, Section 4.5. We opted for these antennas because they meet almost all the design goals for the demining application as stated in Chapter 3, Section 3.3. The dimensions of the antennas are small, they are capable of radiating and receiving fast transient pulses without too much ringing and they can be used off-ground. To reduce the ringing in the antennas, a RAM is placed at the outside end of the antenna plates. The normalised IR of the antennas is given in Chapter 4, Fig. 4-10 (d). In the configuration of the UWB GPR, the two antennas are put side by side. More details about the antenna configuration will be given in Section 6.3.

### ***Receiver***

On the receiver side, the 6 GHz sampling oscilloscope TDS820 from Tektronix is used to digitize the backscattered signal. The oscilloscope has only a 14 bit resolution. To increase its dynamic range, the oscilloscope has a possibility of averaging up to 10.000 times. Without averaging, the dynamic range of the oscilloscope would be limited by the 14 bit resolution to 84 dB, while commercial GPR receivers have dynamic ranges of at least 100 dB. A disadvantage of using an oscilloscope is that it has no time-varying gain. As a whole we can say that the oscilloscope is not an ideal receiver for a GPR, but given its bandwidth and its price it was the only realistic solution for the laboratory system. The data coming from the oscilloscope are collected by a computer, using a GPIB bus. The most important technical details of the sampling oscilloscope are resumed in Table 6.1

Name	Description
Number of channels	2
Number of digitising bits	14
Input connector type	SMA
Input impedance	$50 \Omega \pm 1 \Omega$
Sensitivity	2 mV/Div - 200mV/Div
Input range	$\pm 2V$
Random channel noise	$\leq 1.2 \text{ mV RMS}$
Time range	20ps/Div – 2ms/Div
Delayed time base	between 16ns and 20 ms
Delay jitter	$< 9\text{ps}$ for delay of 200 ns
Input bandwidth	6 GHz
Maximum rise time	$57.8 \pm 0.1\text{ps}$ per $^{\circ}\text{C}$
Number of averaging	up to 10.000 times

**Table 6.1:** Technical details of the Tektronix TDS820



**Fig. 6-5:** The Tektronix TDS820 6GHz sampling oscilloscope

### *Total system bandwidth*

To have an idea of the overall bandwidth of the system the two TEM horn antennas are aligned on boresight of each other and the main-beam response is measured. The transmitting antenna is excited with the impulse coming from the impulse-forming-network (see Fig. 6-4). The received signal is recorded by the 6 GHz sampling oscilloscope. Fig. 6-6(a) shows the normalised received voltage as a function of time.

In Fig. 6-6 (b) the power spectrum of this normalised received signal is shown, which gives an idea of the overall bandwidth of the system. The 3 dB frequency band of the whole system (transmitter – antennas - receiver) is from about 1 GHz up to 5 GHz.

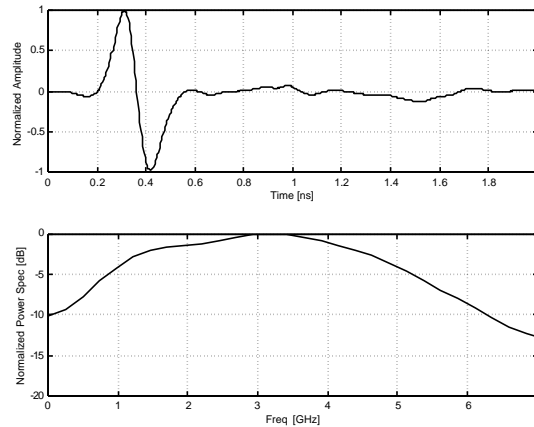


**Fig. 6-6** (a) Normalised amplitude of the main beam response  
(b) Normalised power spectrum of the main beam response

### *XY-scanners*

The antennas of the laboratory UWB GPR can be mounted on two different xy-scanners. In both cases the whole set-up is controlled by a computer, which commands via a serial connection the position of the xy-scanner and meanwhile collects the data (A-scans) from the 6 GHz oscilloscope via a GPIB connection.

The first scanning platform is an indoor xy-table of 2 m by 2.5 m and 2 m high. The xy-table is computer-controlled and has a minimum displacement step of less than 0.1 mm. In the scanning area of the table, two sandboxes are placed, 1.5 m by 1.5 m each and 0.8 m deep. The first one is filled with sand, the second one with loam. The permittivity of both types of soil is fully characterised as a function of frequency and moisture content. The indoor xy-table is represented in Fig. 6-7.



**Fig. 6-7:** Set-up of the UWB GPR system on the indoor xy-table

The second xy-scanner is a small platform, mounted on a robot of the type HUNTER. The robot itself is remote controlled and can be moved in adverse terrain. The scanning area of the platform is 50 cm by 70 cm. The set-up gives the opportunity of doing trials outside. Fig. 6-8 shows a photo of the antennas mounted together with the metal detector on the HUNTER.

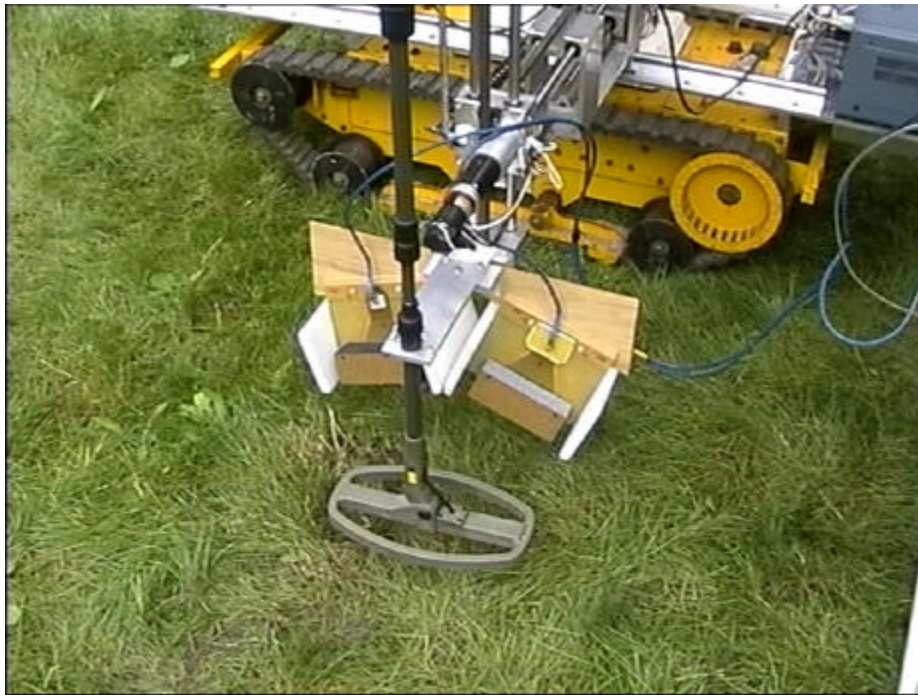


**Fig. 6-8:** Set-up of the UWB GPR system on the HUNTER robot

## 6.3. Study of the antenna configuration

In the design of the laboratory UWB GPR, a study was made to optimise the position and orientation of the Tx and Rx antennas. In commercial GPR systems, the antennas are usually put side by side with their boresight parallel to each other. Putting the antennas side by side seems a logical choice, but whether the parallel boresight is the optimal choice, is not evident. Further, in the demining application we want to use the antennas off ground, so we also have to determine their height.

### 6.3.1. Height above the ground

For the choice of the height of the antennas above the ground, we took into account three factors: the far field of the antenna, the distance from the antennas to the target and the fact that the system will be used in a demining application.

The height of the antennas above the ground is partially dictated by the application. For the demining application the degree of mobility of the antennas must be high. Minefields have often a rough surface and are covered with a lot of vegetation. Therefore we opted to use the antennas not closer than 20 cm to the ground. For the same reason of mobility, the two antennas will be put as close as possible to each other.

A second parameter influencing the choice of the height is the far field of the antennas. In a lot of GPR applications, the antennas are used in the near field. Indeed, to detect an object, the object does not have to be in the far field of the GPR antennas. However, in the time domain model, presented in Chapter 4, we always supposed the objects in the far field of the antennas. If we want to use the time domain model to tune signal processing algorithm, it is better that the antennas operate in the far field. Hence, the knowledge of the far field region becomes important. In Chapter 4, an alternative definition of the far-field region for a time domain antenna was proposed. It stated that in the far field of a time domain antenna, the peak value of the radiated transient field varies as  $R^{-1}$ , with  $R$  the distance to the virtual source of the antenna.

To get an idea of the far field region of the antennas, we have put the two antennas on boresight of each other and measured for decreasing values of  $R$  the peak value of the signal at the receiving antenna. The inverse of the value is plotted in Fig. 6-9 as a function of  $R$  and a line is fitted through the measured points. For values of  $R$  down to 30 cm the points are still on a line. This indicates that the far field region of the antennas begin at least at a distance of 30 cm from the antenna's virtual source, but probably even sooner. Unfortunately we did not perform measurements below 30 cm to determine the exact far field region. As the TEM horns guide essentially a TEM mode, it was expected that the far fields region would begin close to the antenna.

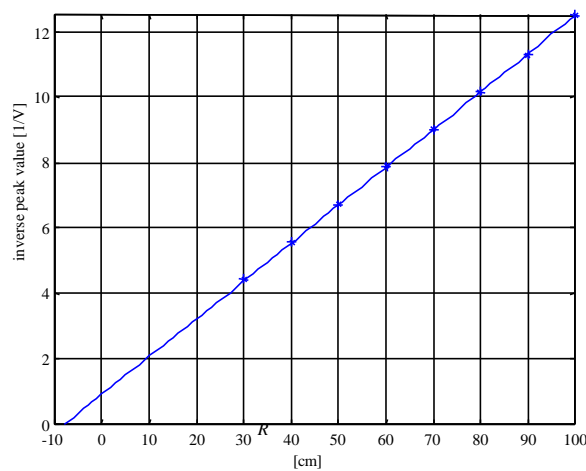


**Fig. 6-9:** Determination of the far field region of the antennas

A last parameter influencing the height of the antenna is the  $R^{-1}$  free space loss or spreading loss. Without going into detail one can intuitively understand that the closer the antennas are to the ground, the closer the antennas will be to the objects, and thus the easier it will be to detect them.

The conditions on the mobility and the far field of the antennas are in contradiction with the condition on the free space loss, so a compromise urges itself. We want the objects in the far field of the antennas, but not too far from the antennas and we want the antennas at least 20 cm above the ground to guaranty their mobility. Therefore we have chosen the height of the antennas for the laboratory UWB GPR to be 25 cm above the ground. Hence, if the targets are shallow buried, we have to keep in mind

that they will be at the under-limit of the far field of the antennas, and that the time domain model will be less accurate.

### 6.3.2. Antenna Coupling

Part of the energy radiated by the Tx antenna will directly couple into the receiving antenna, without being reflected on any object. This phenomenon is called antenna cross-coupling or in short antenna coupling. Antenna coupling can create a ringing between the two antennas. This means that the duration of the antenna coupling can be larger than the duration of the excitation pulse applied on the transmitting antenna. Therefore antenna coupling is usually also expressed as a function of time.

In principle antenna coupling is not critical and can be compensated for. Once the antenna coupling is measured (with the two antennas radiating in free space), the coupling can be subtracted from each measured A-scan. Nevertheless it is better to keep the antenna coupling as small as possible in amplitude and in duration. If the ringing between the two antennas lasts too long, it can interfere with the useful backscattered signal. Furthermore, every backscattered incoming signal on the antennas will make the antennas radiate again due to mismatches in the antenna. Hence the backscattered incoming signals will themselves be sources of ringing between the antennas, which can of course not be compensated for, since they are stochastic.

For the laboratory UWB GPR we choose to measure only the co-polarised backscattered field, *i.e.* the backscattered field in the same polarisation as the radiated field. In this case, the TEM horn antennas can be put in two trivial configurations: either they are put with a common E-plane, *i.e.* the E-field of the transmitting antenna and the receiving antenna are aligned, or they are put with a common H-plane, *i.e.* the H-field of the two antennas are aligned. The top view of the two configurations are shown schematically in Fig. 6-10.

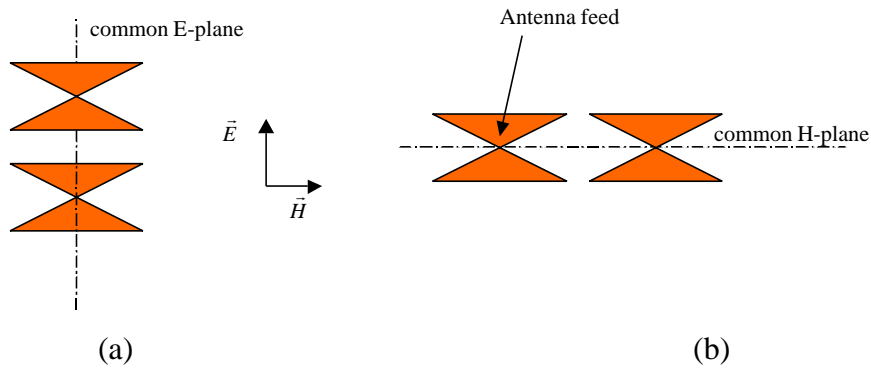


**Fig. 6-10:** (a) Top view of common E-plane configuration

(b) Top view of common H-plane configuration

In general an E-field coupling between two antennas is larger than an H-field coupling, so one could expect a larger coupling in the common E-plane configuration. This is verified with measurements. Fig. 6-11 shows in dashed line the coupling between the two antennas in the common E-plane configuration and in solid line the coupling between the two antennas with a common H-plane. In both cases the distance between the virtual sources of the two antennas was taken to be 22.8 cm. The coupling is measured as the response at the receiving antenna when the transmitting antenna is excited by a pulse. The two antennas were radiating towards RAM to avoid reflections from the surrounding structures. It is clear that the coupling in the common H-plane case is inferior in amplitude compared to the coupling in the common E-plane case. To be complete, each of these configurations can be further subdivided in two more configurations by turning one of the antennas by a  $180^\circ$ , *i.e.* the two SMA connectors pointing in the same direction or in opposite direction. As the antennas are balanced, this makes no significant difference in the amplitude nor in the duration of the coupling.

A third possible configuration is putting the Rx antennas out of the E- and H-plane of the Tx antenna. A quick test learned that this does not decrease considerably the coupling, compared to the common H-plane configuration.

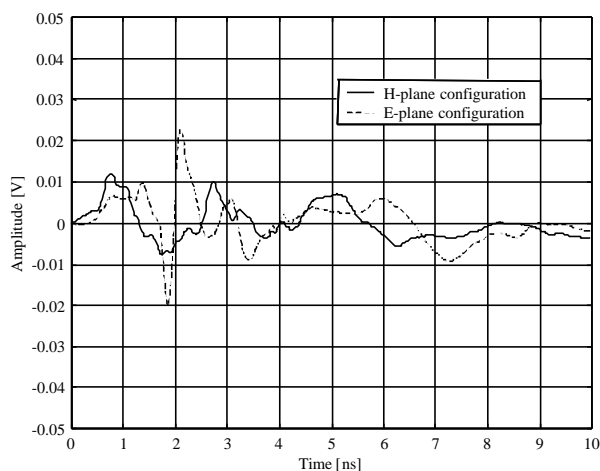


**Fig. 6-11:** Coupling between the two TEM horns in the common E-plane and common H-plane configuration

In the laboratory UWB GPR, the configuration with the lowest coupling, *i.e.* the common H-plane configuration (in solid line on Fig. 6-11), is taken. In this case the coupling will not exceed  $-27$  dB. A spectrum analysis of the coupling reveals that the H-plane coupling between the two antennas is primarily a low frequency coupling with a maximum energy around a frequency of 500 MHz. This frequency is out of the frequency range of the antennas, but has a very low reflection coefficient at the antenna feed point (see Chapter 3, Fig. 3-30), which means that the antenna will radiate around this frequency with a very low directivity.

### 6.3.3. The 3 dB footprint of the antennas

The 3 dB footprint of an antenna on a plane perpendicular to the boresight direction is defined as the region where the field, measured in the plane, is within the 3 dB of the maximum field measured in the same plane (normally on boresight of the antenna). The footprint of an antenna is schematically represented in Fig. 6-12. The footprint will be function of the height of the antenna above the plane. Fig. 6-13 shows the measured footprint of the TEM horn on a horizontal plane at 25 cm below the antenna. The footprint is 24 cm by 16 cm. The footprint was measured with a Bdot-sensor, *i.e.* a sensor that measures the time derivative of the magnetic field.

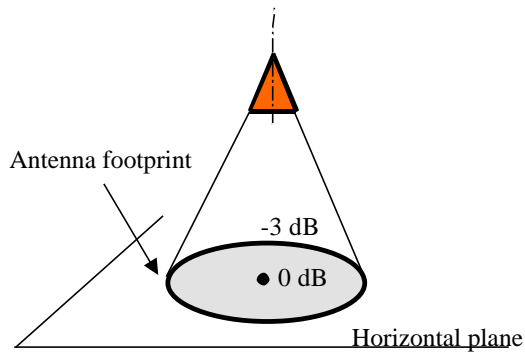


**Fig. 6-12:** Schematic representation of the antenna footprint

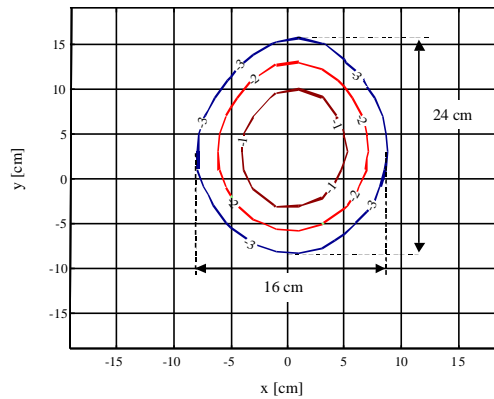


**Fig. 6-13:** Measured footprint of TEM horn

### 6.3.4. Optimisation of the antenna off-set angle

Due to the beam-width of transmit and receive antenna, a point target in the ground is already seen by the GPR system even when the point target is not exactly under the antennas. As a consequence, the reflections on the target will be smeared out over a broad region in the recorded data. However, the two-path length between the antennas and the target is larger when the target is not exactly under the antennas, hence the reflection will appear later in time, as schematically represented in Fig. 6-14. It can easily be verified that the obtained structure in the B-scan is a hyperbola (see Chapter 2). There exist a number of signal processing algorithms, called migration, which correct for this defocusing. In the ideal case, the migration algorithm will focus all the energy back into the true position and physical shape of the target.

An important parameter in the Tx-Rx antenna configuration is the combined antenna footprint – *i.e.* the footprint of the two antennas considered as one antenna. The resulting 3dB footprint of the two antennas is obviously a function of the offset angle  $\alpha_1$  as represented in Fig. 6-15. Note that a larger 3 dB footprint produces larger hyperbolas in the B-scan. The question is if this increases the detectability of objects or not.

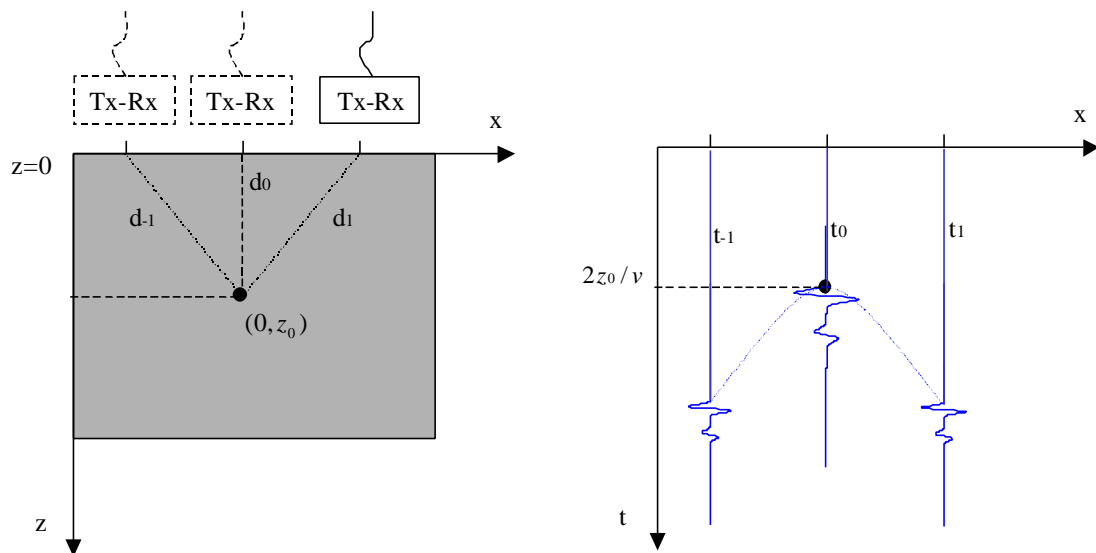


**Fig. 6-14:** Schematic representation of defocusing on a point target

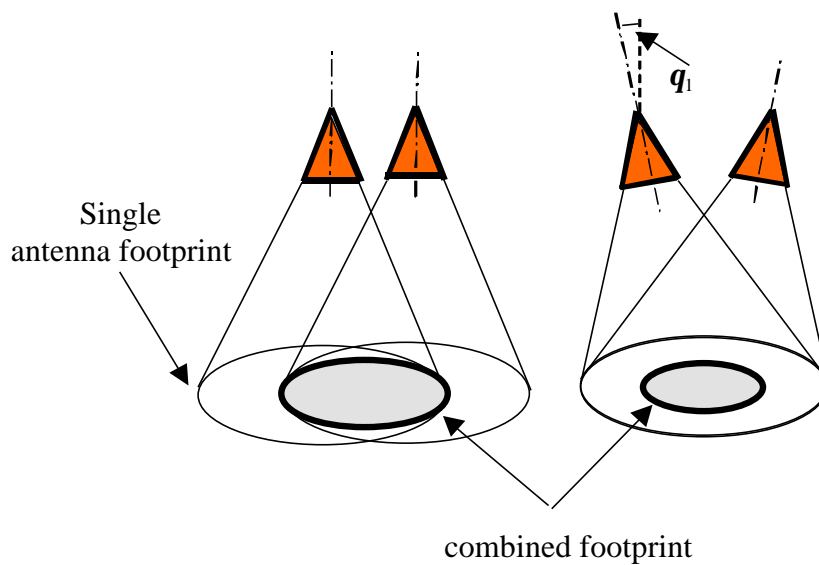


**Fig. 6-15:** Combined antenna footprint

The aim of the study in this section is to find the optimum offset angle  $q_1$  of the antennas for a given configuration, *i.e.* height of the antenna, depth of the object and soil type. As a criterion for the optimisation we consider the total energy found in the hyperbolic shaped response of a point target. This total energy represents in some sense the expected energy of the point target in a B-scan, after enhancing the B-scan by an optimal migration method. For this reason, we simulated 31 different synthetic

B-scans of a point scatterer at 6 cm in the ground, for different offset angles  $\mathbf{q}_1$  between  $0^\circ$  and  $30^\circ$  in steps of  $1^\circ$ . The fictive point scatterer is represented by a bistatic impulse response  $\Lambda = \mathbf{d}(t)$ . The configuration is shown in Fig. 6-16. For each position  $x$  between  $-50$  cm and  $50$  cm of the antenna pair, the backscattered signal  $V_{rec}(t)$  is calculated using the time domain GPR range equation (5.13). The backscattered signals  $V_{rec}(t)$  for all the antenna positions are then represented as a B-scan, as shown in Fig. 6-17. In the simulations, the transmission losses and the influence of the ground are also taken into account, although they have no influence on the interpretation of the result, as they are the same for all offset angles. Fig. 6-17 shows the result of the simulation for an offset angle  $\mathbf{q}_1 = 20^\circ$ .

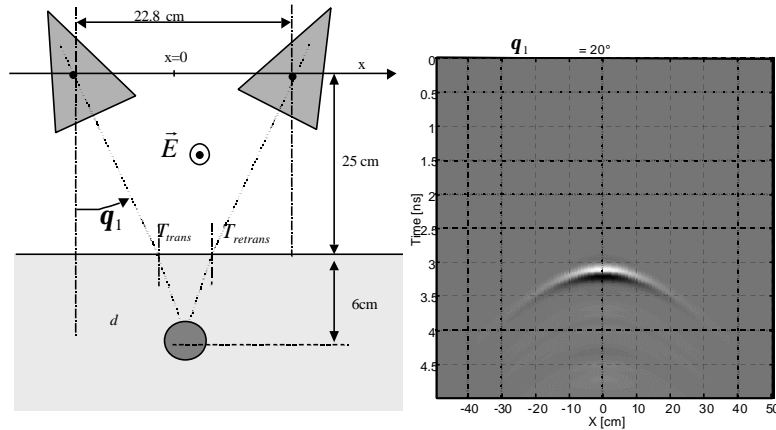


**Fig. 6-16:** Antenna configuration

**Fig. 6-17:** Synthetic B-scan for  $\mathbf{q}_1 = 20^\circ$

For each of the 31 synthetic B-scans, the total energy in the hyperbolic shaped response of the target is calculated as

$$E_{tot} = \int \int_x |V_{rec}(t)|^2 dt dx \quad (6.1)$$

Fig. 6-18 shows the total energy in the hyperbolic response of the point target as a function of the offset angle  $\mathbf{q}_1$ . The total energy in the hyperbola increases for increasing values of the offset angle. But when the offset angle becomes too large, the energy in the hyperbola decreases. The maximal energy in the hyperbola is found for

an offset angle of  $20^\circ$ , which for this configuration (object depth and soil type) corresponds to the angle that focuses the antennas on the target, taking into account the refraction. The same result is obtained for other object depths and soil types. In general we can conclude that the optimum offset angle, with respect to the total backscattered energy on a point target, is the angle that focuses the antennas on the target. Although the obtained conclusion seems trivial, it is not straightforward to confirm. The above simulation however gives an objective verification.

In reality the depth of the object is *a priori* unknown, but is expected to be between 0 and 20 cm. However, the graph in Fig. 6-18 indicates that the maximum in the energy is rather flat, meaning that the choice of the optimal offset angle is not too critical. In the design phase of the laboratory UWB GPR, a most probable depth for an AP mine of 6 cm was assumed, leading to an offset angle  $q_1$  of  $20^\circ$ .

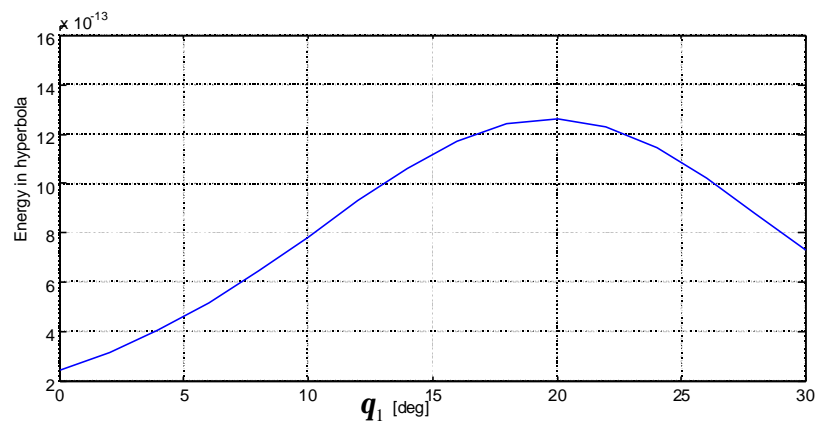


**Fig. 6-18:** Total energy in the hyperbolic shaped response of a point target at 6 cm of depth

Table 6.2 resumes the choices on the antenna configuration, resulting from the study made in this section. Fig. 6-19 shows a photo of the antenna configuration as used in the laboratory UWB GPR system.

<b>Configuration characteristic</b>	<b>Expression</b>
Preferred height of the antennas above the ground	25 cm
Distance between the two virtual sources	22.8 cm
Polarisation	H-field of the two antennas aligned (common H-plane)
Offset angle	20°

**Table 6.2:** Antenna configuration



**Fig. 6-19:** Photo of antenna configuration

## 6.4. Study of the range performance

In the design phase of a GPR system it is indispensable to study the range performance or penetration depth of the system. In the literature one can find multiple examples of such studies [2][3]. Unfortunately they all start from the radar range equation in the frequency domain. As already mentioned in the introduction of Chapter 5, describing the range performances of time domain system, using frequency dependent signal power has some drawbacks. The radar range equation contains frequency dependent terms, hence they have to be expressed over the whole frequency band of interest. Further, to estimate the range performance, one has to specify the minimum detectable signal power of the receiver at a given frequency. For a time domain system it is more practical to express the minimum detectable signal of

the receiver in terms of peak voltages instead of frequency dependent signal power. The study of the range performance of a time domain GPR system can be done with far more accuracy by modelling the whole UWB GPR in the time domain. Once the minimal detectable peak amplitude of the receiver is known, the time domain GPR range equation (5.13) can be used to calculate the range performance of the impulse radar system for a given configuration, *i.e.* soil type and target.

In this section an evaluation of the range performance is done for our laboratory UWB GPR. The range performance is studied for the following configuration: the target is a metallic sphere with a radius of 5 cm, buried in a sandy soil. The soil, coming from Cambodia, has a texture composition of 69% of sand, 24% of silt and 7% of clay. This sandy soil represents a regular agriculture soil with which deminers are confronted. The complex permittivity of the soil was measured by the UCL [4] in function of the moisture content and frequency. Table 6.3 shows the real relative permittivity, the loss tangent and the attenuation constant  $\alpha$  for 3 different moisture contents at a frequency of 2 GHz. The first two values are sufficient to calculate for each moisture content the impulse response of the soil using the analytic expression (5.26).

<b>Moisture content</b>	<b>Real relative permittivity</b>	<b>Loss tangent</b>	<b>Attenuation [dB/m]</b>
0%	2.55	0.01	2.9
5%	4.45	0.056	21.4
10%	8.16	0.085	44.1

Table 6.3: Characteristics of a sandy soil coming from a rice field in Cambodia at 2 GHz

In the study we introduced some simplifications without loss of generality. Because we are only interested in the peak value of the backscattered signal, we can replace the IR of the metallic sphere by  $\Lambda(t) = 0.314 \mathbf{d}(t)$ , representing the IR of a fictive metallic object, which is comparable to the IR of the metallic sphere with a radius of 5 cm by only taking into account the specular reflection (see also equation (5.35)). Further we assume that the bistatic RCS of the target is independent of the bistatic

angle and that the air-ground interface is flat. A schematic representation of the configuration for the study of the range performance is shown in Fig. 6-20. The virtual source of the antennas are at 25 cm from the ground and the two antennas are separated by 22.8 cm. The air-ground interface is at  $z = 0$ . The excitation waveform  $V_s(t)$  is the Gaussian pulse generated by the step generator, followed by the impulse-forming network (Fig. 6-4).

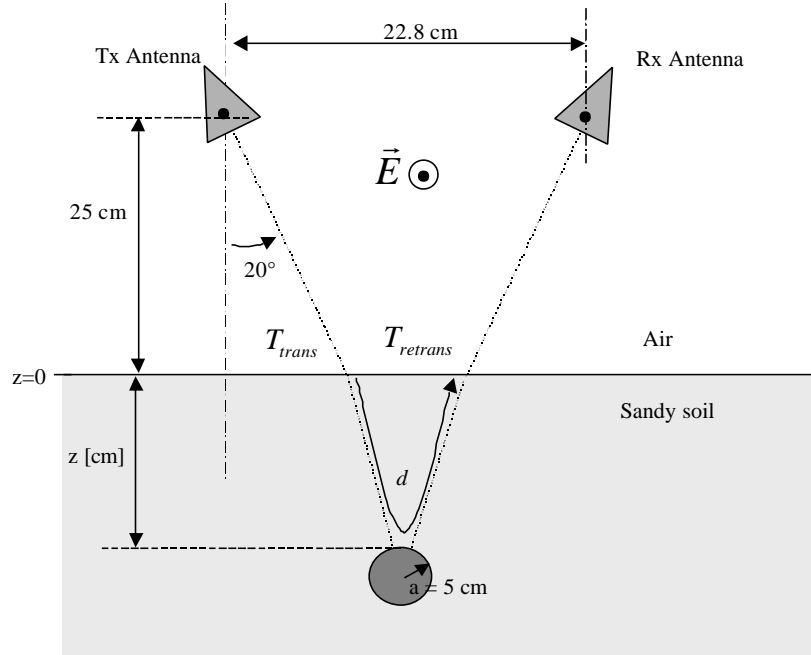


**Fig. 6-20:** Configuration for range performance

First, for a given target depth and moisture content, the backscattered signal  $V_{rec}(t)$  is calculated using equation (5.13). Fig. 6-21 shows as an example the simulated backscattered signal for the target at a depth of 5 cm and moisture content of 0%. From this signal, the peak amplitude is taken and expressed in dBm as

$$V_{rec,peak} [dBm] = 10 \log \left( \frac{V_{rec,peak}^2 [Volt] 10^3}{50} \right) \quad (6.2)$$

$V_{rec,peak}^2 [Volt]/50$  corresponds with the maximum instantaneous peak power of the signal. In our example the peak amplitude of the backscattered signal is 8.6 mV or – 28 dBm.

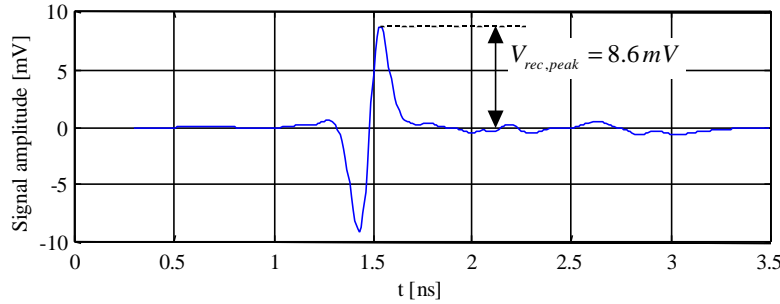


**Fig. 6-21:**  $V_{rec}(t)$  for the target at a depth of 5 cm and a moisture content of 0%.

This is repeated for all target depths and moisture contents. The results are globalised in Fig. 6-22, showing the maximum signal amplitude in dBm, at the receiver of the UWB system as a function of depth of the metallic sphere in a lossy sandy soil.

The minimal peak amplitude that can be detected by the receiver is in general limited by its noise performance. For the 6 GHz oscilloscope the RMS value of the random channel noise is measured to be less than 1mV or –47 dBm. This measurement is done according to the test procedures of the supplier, by measuring two times the same input signal, one without averaging and one with averaging 128 times, subtracting these two measurements and calculating the RMS value of the subtraction. Assuming that the noise is a white noise, the noise level of the receiver can be improved by averaging. Averaging  $N$  times improves the noise level by

$$20\log(\sqrt{N}) \quad (6.3)$$

For example, averaging 32 times, which is commonly used for GPRs, improves the noise level with 15 dB. According to Skolnik [5], for a probability of detection of 99% and a false alarm rate of  $10^{-5}$ , a signal-to-noise ratio of 14 dB is needed. If we

apply the same ratio to our time domain receiver, the minimal detectable peak amplitude of the 6 GHz oscilloscope, with 32 times averaging, will be

$$-47 \text{ dBm} - 15 \text{ dB} + 14 \text{ dB} = \mathbf{-48 \text{ dBm}}$$

The determination of the minimal detectable peak amplitude of a receiver is quite subjective and can be source of discussion. In practice the minimal detectable peak amplitude depends on more factors than the noise floor of the receiver only. For instance the ringing in the antennas or the residual cross-coupling between the antennas after compensation, exceeding the level of  $-48 \text{ dBm}$ , could possibly mask small reflections on targets. On the other hand the above reasoning is done for the GPR system in one physical position. Normally, the GPR is used to acquire B- or C-scans. In this case a point target will generate a hyperbolic response in the image, which could increase the detectability of the object. Further, signal processing techniques on the B- or C-scans will also increase the detectability of targets. It is difficult to estimate the total influence of all these factors on the minimal detectable peak amplitude, therefore in this example we only take into account the noise performance of the receiver.

Once the minimal detectable peak amplitude of the receiver is determined, the maximum range at which the target can be detected can be read from the plot in Fig. 6-22. Doing so, one of the main disadvantages of an UWB GPR clearly appears. For the same sandy soil, the maximal range (penetration depth) decreases from 50 cm when the soil is dry over 20 cm when the soil has a moisture content of 5% to only 11.5 cm for 10 % moisture content. Note that the range performances of our laboratory UWB GPR system could be increased by replacing the driving source  $V_s(t)$ . For the moment the driving source is limited to a maximum amplitude of only 2.5 V and does not make use of the full dynamic range of the receiver. Further the performance can be increased by increasing the bit resolution of the receiver and by integrating a time varying gain.

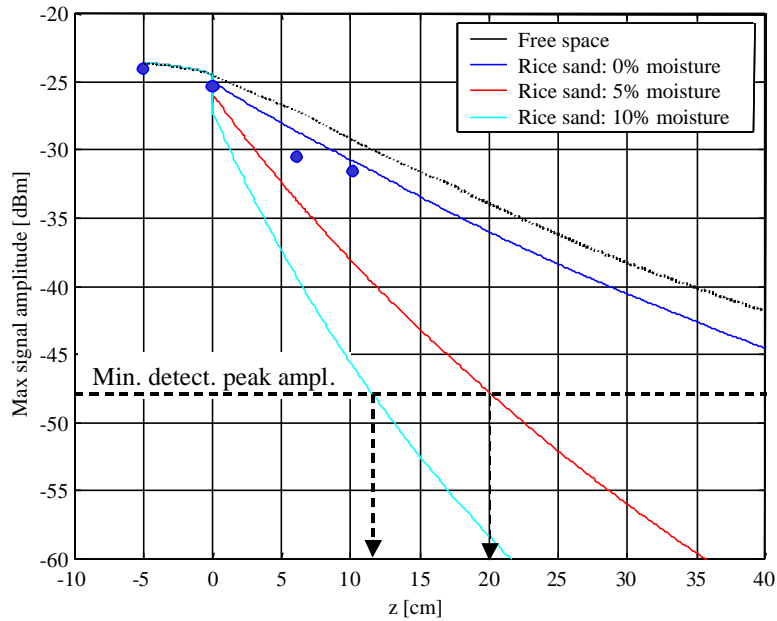


**Fig. 6-22:** Peak amplitude of the reflection on the target [dBm] as a function of the depth  $z$  [cm] for a sandy soil with respectively 0%, 5% and 10% moisture content

In the beginning of this section we stated that the range performance of a time domain GPR could be done with more accuracy by using the time domain GPR range equation. To give an idea of the accuracy of the time domain model we performed measurements on a metallic sphere with a radius of 10 cm according to the measurement set-up as shown in Fig. 6-20. The metallic sphere was buried at respectively  $z = -5$  (top of the sphere at 5 cm above the ground level),  $z = 0$ ,  $z = 6.2$  and  $z = 10.2$  cm in dry sand (0% moisture content). The dry sand is characterised by a permittivity and loss tangent that is comparable with the sandy soil used for the calculations. For each depth the peak amplitude was measured and plotted on Fig. 6-22. The calculated curve for the 0% moisture case (in blue) overestimates a little the measurement points, but the largest difference, found for the dept of 6.2 cm, does not exceed 2 dBm.

## 6.5. Experimental results

### 6.5.1. Acquisition software

For the acquisition of the data, two software programs have been developed: one for a B-scan and one for a C-scan. The programs control, via a serial connection, the position of the xy-table, collect the data (A-scan) from the oscilloscope via a GPIB connection and provide the man-machine-interface toward the user. Further the software allows the user to visualise the data, to perform basic signal and image processing and to save the data to disk. The data is taken on a regular grid, where the step in x- and y-direction is set by the user. Before the acquisition starts, the programs asked for a compensation of the antenna coupling. The user must put a RAM under the antennas to simulate the free space. In this case only the antenna coupling is measured. The program takes one acquisition and will keep this acquisition to subtract it from all future taken A-scans to compensate for the antenna coupling. Fig. 6-23 shows the user interface of the program for the acquisition of B-scans.

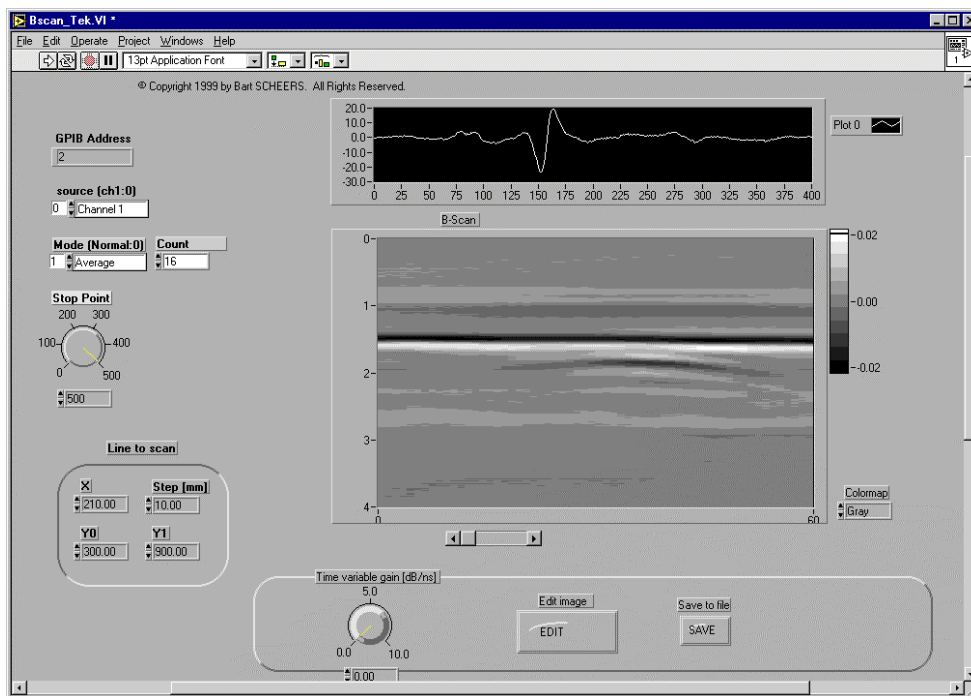
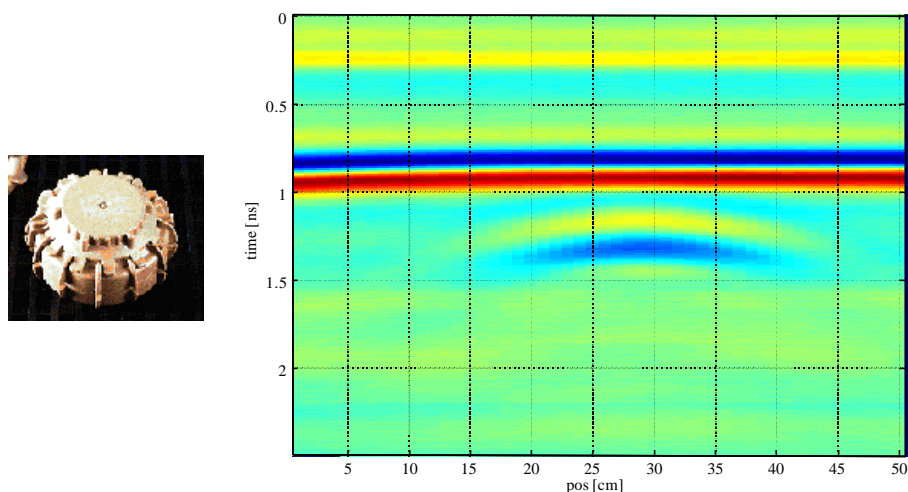


Fig. 6-23 : User interface of the program for the acquisition of B-scans

### 6.5.2. Results

The system can now be used to acquire B-scans and C-scans of AP mines. At this point we can already draw some conclusions concerning the advantages and disadvantages of the UWB approach. In the next three figures we show B-scans taken by the laboratory UWB GPR. On the horizontal axis the displacement of the antennas is given in centimetres; the vertical axis represents the time in ns. The images represent raw data, so no signal processing was performed on the data, except for the compensation of the antenna coupling.

Fig. 6-24 shows an Italian VS/50 AP mine buried in sand at a depth of 2 cm. The mine appears very clearly on the image and can be distinguished from the air-ground interface despite of the fact that it is shallow buried. With a conventional GPR system, the echo of the air-ground interface would mask the echo coming from the mine and additional signal processing would be needed to recover the target in the image. We can conclude that the UWB GPR is capable of detecting shallow buried objects.



**Fig. 6-24 :** VS/50 mine buried in sand at a depth of 2 cm

In the next two figures, we show a PMN mine buried in loam a depth of 5 cm. In the first case, shown in Fig. 6-25, the loam is moistened. As expected, the signal is strongly attenuated in the wet soil and the mine is hardly visible. We then waited for two days to give the ground time to dry and took a B-scan of the same scenario again.

The result is shown in Fig. 6-26. The PMN mine is now more visible. This qualitative test demonstrates that the performances of the UWB GPR decrease dramatically in wet soils. One can compensate for the attenuation by the ground by a time-varying gain in the receiver part of the system. This is usually done in commercial GPR systems. In an oscilloscope however, this option is not available. The result can also be improved by bringing the antennas closer to the ground. Lowering the antennas means reducing the antenna footprint on the ground, so more energy will be reflected by the small mine. Reducing the antenna footprint can also be done by making antennas with a larger antenna aperture. But this means larger and heavier antennas, which is in contradiction with our design goals.

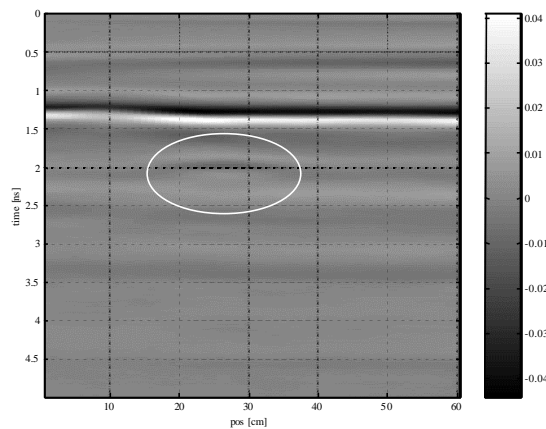


**Fig. 6-25:** PMN mine buried in wet loam a depth of 5 cm

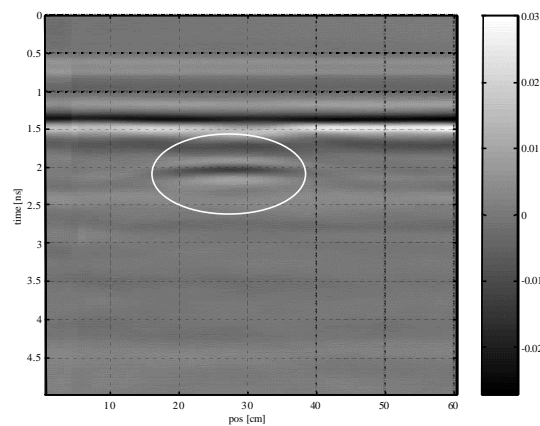


**Fig. 6-26:** Same PMN mine as in previous figure after two days

In none of the above B-scans the signature of a mine is visible. From these images of the raw data it is already clear that for classification of the object some signal and/or image processing will be needed.

## 6.6. Summary

In the frame of this research we have built a relatively simple UWB GPR systems, using mainly off-the-shelf equipment. The system can be mounted on a xy-table for indoor trials or on a robot for outdoor trials. The main purpose of this system was to provide the group with UWB data on AP mines. Further it gave the opportunity to evaluate the time domain model. Measurements on a metallic sphere showed a good correspondence with the simulations. Some shortcomings of the UWB GPR system are the weak instantaneous power in the impulse (maximum amplitude of 2.5 V) and the lack of a time varying gain in the receiver part.

The antenna configuration of the UWB GPR was studied in detail using the time domain radar range equation. The study revealed that the optimal offset angle for the antennas is the one that focuses the antennas on the target. In this case, the total reflected energy on a point target could become several times larger than when the two antennas have their boresight parallel to each other. Further the range performance of the system was investigated for a given target in a given soil. The range performance of a time domain GPR was found to be very accurate by using the time domain GPR range equation. From this study we could conclude that the range performance of the UWB system will be limited by the moisture content of the soil. This is due to the dramatically increasing attenuation of the radiated signal by the soil as a function of frequency and moisture content. In a sandy soil with a moisture content of 10 %, the UWB GPR can detect a metallic sphere with a radius of 5 cm down to a burial depth of only 11.5 cm.

Some tests were done on AP mines. At this point we can already draw some preliminary conclusions concerning the advantages and disadvantages of the UWB approach. First of all, as expected the tests showed the capability of detecting

shallowly buried mines. The tests also confirmed that when mines are buried deeper and the soil has a high moisture content, the visual detection becomes almost impossible.

Although the data on the targets has a better depth resolution and contains more frequency information on the target, the visual classification of objects in the B- and C-scans is not feasible. However, this extra information is present in the data and can hopefully be explored using advanced signal and image processing algorithms like time-frequency analysis and analysis of resonance in the late time response of the objects.

## REFERENCES

- [1] M. Piette, *Banc de mesure en régime transitoire de la signature radar d'objets tridimensionnels*, Doctoral thesis, Université catholique de Louvain and Royal Military Academy, Belgium, Oct. 1995.
- [2] D. J. Daniels, *Surface Penetrating Radar*. London: IEE, 1996, pp. 11-18.
- [3] J. L. Davis and A. P. Annan, "Ground-Penetrating Radar for High-Resolution Mapping of Soil and Rock Stratigraphy", *Geophysical Prospecting*, vol. 37, pp. 531-551, 1998.
- [4] M. Storme, I. Huynen and A. Vander Vorst, "Characterization of wet soils in the 2-18 GHz frequency range," *Microwave and optical technology letters*, vol. 21, no. 5, June 1999.
- [5] M. Skolnik, *Radar handbook*. New York: McGraw-Hill, 1990, p. 2.20.



---

## Chapter 7. UWB Signal processing

---

### 7.1. Introduction

In the last chapter of this work, we discuss some signal processing techniques used on GPR data. Until now we only have treated hardware aspects of the UWB GPR and we have modelled the system in the time domain. The question is if we can use this additional information on the hardware of the system for adapting or developing signal processing algorithms.

Further there is the question if the UWB approach in the demining application yields the necessary advantages over the conventional GPR. Many authors suggest that there is a lot of information in the early- and especially in the late-time response (also called the resonant part) of buried objects to short transient pulses. This information could be very useful for the classification of targets. The verification of this statement however is not straightforward. In the previous chapter we saw that UWB GPR was able to detect shallow buried mines. But despite the better depth resolution and the fact that the backscattered signal contains more frequency information on the target, the visual classification of objects in the B- or C-scans is not feasible. In this chapter, we will report some conclusions concerning the use of signal processing techniques that are more adapted to UWB signals.

Signal processing on the raw data coming from a conventional GPR has mainly two objectives. First it can be used to reduce the clutter. Clutter can be defined as

backscattered signals that are not from possible targets, but occur in the same time window and have similar spectral characteristics. In GPR applications some examples of clutter sources are the air-ground interface, multiple reflections between antenna and ground, reflections from side-lobes and discontinuities in the ground like stones and roots. Unlike conventional radar systems, the targets and clutter sources are both static, so clutter removal techniques like moving target indicator (MTI) can't be used. In the scope of the HUDEM project, work has been done in the domain of clutter reduction on UWB data [1].

A second objective of the signal processing is in general to enhance the quality of the images, so that the interpretation by a human operator becomes easier and more correct. Noise reduction methods [2] as well as focussing techniques to reduce the influence of the antenna beamwidth, called migration techniques, belong to this class of signal processing techniques.

Another way of classifying the signal processing algorithms is by the type of signals to which they are applied. Signal processing techniques can be applied to A-scans, B-scans or C-scans. In the next section a brief overview of a few basic signal processing techniques on A-scans will be given. The overview is far from complete, only the techniques, used or developed in the scope of this work, are restrained. Furthermore we report on two well-known signal processing techniques on A-scans that are more adapted to UWB signals and discuss briefly their target classification capability, without addressing the problem of classification itself. In the following section, an overview of migration techniques is given. This section must be seen as an introduction to the last section of this chapter where a fast and computational not intensive migration technique is described. The novelty of the algorithm is that the characteristics of the GPR system and the ground are taken into account in the algorithm. This is normally not the case in the conventional migration techniques.

## 7.2. A-scans processing

### 7.2.1. Overview of A-scan processing

#### *DC offset removal*

From the physical point of view, the mean value of an A-scan has to be zero or close to zero. Many receivers however have a DC offset that is different from zero and eventually slowly drifting as a function of time. Therefore it is advised to compensate for this offset. In the assumption that the offset stays constant over the time duration of the A-scan, it can be removed by

$$a'(n) = a(n) - \frac{1}{N} \sum_{i=0}^{N-1} a(i) \quad \text{for } n : 0 \rightarrow N-1 \quad (7.1)$$

where

$a(n)$  is the raw A-scan,

$a'(n)$  the A-scan after DC offset removal,

$n$  the sample number of the A-scan, and

$N$  the total number of samples per A-scan.

#### *Background subtraction*

In many GPR data, there is clutter present that always appears at the same time in an A-scan or in a series of neighbouring A-scans. Examples of this kind of clutter are a flat air-ground interface, a horizontal layer in the ground, or antenna ringing. These clutter sources create horizontal lines in the B- or C-scans and can in some cases obscure a target. The reduction of this kind of clutter can be achieved by subtracting from each A-scan the average of a number of neighbouring A-scans or even the average of all the A-scans in a B-scan. The algorithm is mathematically described as

$$a'_i(n) = a_i(n) - \frac{1}{K} \sum_{k=0}^{K-1} a_k(n) \quad (7.2)$$

where

$a_i(n)$  is the  $i^{\text{th}}$  A-scan in the raw data,

$a'_i(n)$  the  $i^{\text{th}}$  A-scan of the processed data,

$K$  the number of A-scans to be averaged before subtraction. In general, the neighbouring A-scans are taken symmetrically around the A-scan that is processed.

If the clutter is present in the whole B-scan, the number  $K$  is often taken equal to the total number of A-scans in the B-scan, so that the average of the whole B-scan is subtracted from each individual A-scan.

Note that other mathematical operations than the average, as for instance the median, are also possible and sometimes lead to better results.

Care has to be taken with the background subtraction, as it can create artefacts in the image and sometimes inversion in the intensity of the A-scans, leading to an inversion of the colour in the B-scan. Fig. 7-1 shows a B-scan of a Belgian AP mine, type PRB-409, buried at a depth of 5 cm in loam. The PRB-409 is a very flat and difficult to detect AP mine. In the unprocessed image on the left, the antenna coupling and the air-ground interface is clearly visible. In the processed image at the right, the little AP mine becomes more visible. In this example, the average of the whole B-scan is taken to be subtracted from each individual A-scan.

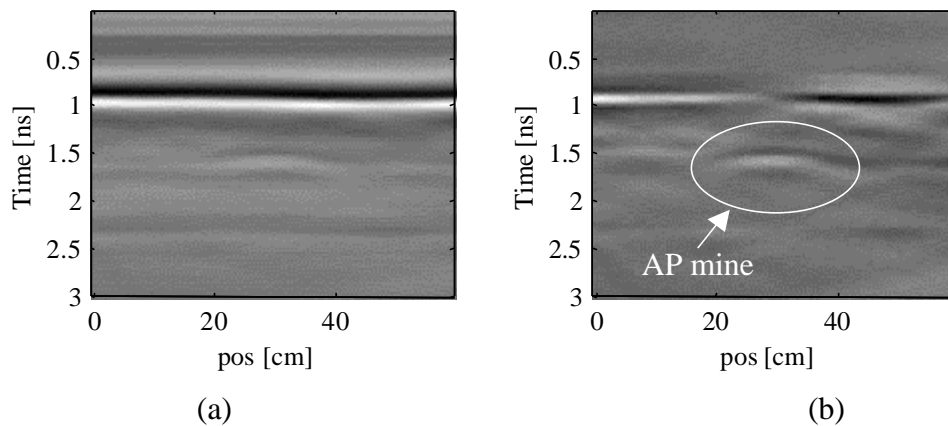


**Fig. 7-1:** B-scan of a PRB-409 AP mine (a) before and (b) after background subtraction

### *Time-varying gain*

As already mentioned in Chapter 2, the received signal is attenuated by the losses in the ground and by the spreading losses. The later in time the reflection appears in an A-scan, the further it has travelled in the ground, hence the more it was attenuated by the above mentioned losses. This can be compensated for by applying a time-varying gain. As our receiver had no such gain implemented in hardware, it can also be done software wise. The disadvantage of this approach however is that the noise and clutter in the A-scan are also amplified, therefore we will almost never apply this signal processing technique to our data.

### *Extraction of the scattering centres*

In radar applications, it is well known that the backscattering from a complex target can be approximately modelled by a discrete set of scattering centres. A method to extract the scattering centres of the target, and thereby enhancing depth resolution, is by deconvolving the signal source and antenna IR from the backscattered signal. Due to the band limited nature of the emitted wave and the effects of noise, deconvolution of the signal source and antenna IR is an ill-posed problem. Furthermore with the deconvolution one cannot take into account the dispersive behaviour of the ground.

Indeed, an additional problem to extract the scattering centres in an A-scan is the broadening of the reflected signal due to the dispersive behaviour of the ground. An often-used deconvolution technique is the *Wiener filter* or a variant of this filter. More details about the Wiener filter can be found in Section 7.4. A disadvantage of this filter is that the noise spectral density and the signal spectral density must be known.

In this section we present a processing technique for extracting the scattering centres, which is more robust to noise and can partially compensate for the dispersive behaviour of the ground [3][4]. The method is based on the Continuous Wavelet Transformation (CWT) [5] and uses the dilatation properties of the wavelets to counteract the dispersive behaviour of the ground. The knowledge of the exact source signal and the antenna IR is basic in this method.

For clarity reasons let us summarise a somewhat simplified version of the time domain radar range equation (5.13). The received voltage due to a reflection on one buried object can be described by

$$V_{rec}(t) = K g_d(t) \otimes h_{N,Tx}(t) \otimes \Lambda(t) \otimes h_{N,Rx}(t) \otimes \frac{dV_s(t)}{dt} \quad (7.3)$$

where

$K$  is a constant taking into account the spreading loss, the transmission coefficients, the off boresight position of the target, etc.,

$h_{N,Tx}(t)$  is the normalised impulse response of the transmitting antenna on boresight,

$h_{N,Rx}(t)$  the normalised impulse response of the receiving antenna on boresight,

$g_d(t)$  the impulse response representing the two-way path length loss in the ground,

$\Lambda(t)$  the impulse response of the buried target, and

$V_s$  the excitation voltage at the antenna feed.

If more than one target is present in a scene and the targets are considered to be independent of each other, the total received voltage at the receiver can then be written as a sum of the received voltages of each individual (and independent) target.

Furthermore, in this method we assume that if  $k$  scattering centres approximately model a scenario of complex targets and planner interfaces, then the received A-scan can always be written as a sum of  $k$  individual normalised wavelets:

$$a(t) \approx \sum_{p=1}^k B_p h_{a_p, t_p}(t) \quad (7.4)$$

where  $h_{a_p, t_p}(t)$  represents the backscattered wavelet on scattering centre  $p$  and  $B_p$  its amplitude. According to the time domain radar range equation (7.3), and neglecting for the moment the influence of the ground, the backscattered wavelet  $h_{a_p, t_p}(t)$  must have the shape of

$$h_{N,Tx}(t) \otimes h_{N,Rx}(t) \otimes \frac{dV_s(t)}{dt} \quad (7.5)$$

In the case of the laboratory UWB GPR, expression (7.5) resembles a derivative of a Gaussian pulse. To extract these individual wavelets from  $a(t)$ , the Continuous Wavelet Transformation (CWT) is used. The CWT is a time-frequency analysis technique that gives in a time-scale plane the correspondence between a time signal  $a(t)$  and a basic wavelet  $h_{a_p, t_p}(t)$ , delayed by  $t$  and scaled by a dilatation coefficient  $a$ . The basic wavelet for this transformation is chosen to fit the shape of expression (7.5). Normalising the energy in the wavelet, results in the basic wavelet

$$h_{a_p, t_p}(t) = \frac{1}{\sqrt{a_p}} \sqrt{\frac{2}{\sqrt{p}}} \left( \frac{t - t_p}{a_p} \right) e^{-\frac{1}{2} \left( \frac{t - t_p}{a_p} \right)^2} \quad (7.6)$$

The delay  $t_p$  takes into account the two-way travelling time between the antennas and the scattering centre  $p$ . The dilatation coefficient  $a_p$  scales the wavelet and thereby partially compensates for the broadening of the reflection on the scattering centre due to the dispersive behaviour of the ground. The coefficients  $B_p$  are found one at a time by an iterative procedure. One begins at stage  $p=1$ . The CWT of received signal is computed, using (7.6) as basic wavelet. The parameter  $B_1$  is found as the maximum wavelet coefficient of the transformations, with  $a_1$  and  $t_1$  as corresponding dilatation coefficient and time-delay of the wavelet. Then  $B_1 h_{a_1, t_1}(t)$  is subtracted from the received signal. This procedure is iterated to generate as many coefficients as needed to accurately represent the original received signal. Fig. 7-2 shows the result of this method on an A-scan, representing a PMN mine in loam at 5 cm of depth. In this example only five scattering centres are calculated.

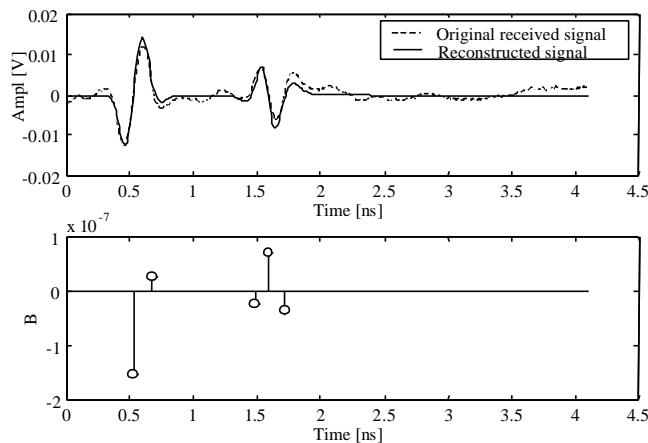


**Fig. 7-2:** (upper) Approximation of A-scan as a sum of normalised wavelets, (lower) coefficients  $B_p$  of the five scattering centres

The lower plot of Fig. 7-2 can be seen as the deconvolved version of the solid curve in the upper plot of Fig. 7-2. The first two scattering centres in the lower plot of Fig. 7-2 represent the reflection on the air-ground interface, the last three scattering centres represent the reflection on the object.

In [6] it is suggested that the scattering centres of an object are characteristic of that object. Hence the last three scattering centres in the lower plot of Fig. 7-2 can be used

as a template to look for similar objects (in this case PMN mines) in other A-scans. A more detailed study on the data coming from the UWB GPR revealed that the template of an object indeed does not alter too much as a function of the depth of the object [3]. However, the relative amplitude of the scattering centres, the time interval between the scattering centres and even the number of scattering centres is very sensitive to variations in inclination of the object and to variations in the surrounding media of the objects. Furthermore, once the energy in the reflection on the target becomes too small, because the target is too deep or the attenuation in the ground too high, the retrieval of a stable template is almost impossible. As a whole the method was not found robust enough to retrieve reliable features for classification algorithms for buried objects on our data.

A possible application of this processing technique for extracting the scattering centres is to use it as a method to reduce the amount of data. A problem often encountered when working with C-scans is that the amount of data becomes too large. A way of reducing this amount of data is to only store the information on the scattering centres per A-scan. It is seen that in most of the cases an A-scan is accurately represented by a sum of 5 wavelets. Each wavelet is characterised by one triplet  $(B_p, t_p, \mathbf{a}_p)$ . This means that for an A-scan of 512 points, only 15 values have to be stored instead of 512, hence a data reduction of 1/34. The complete A-scan can always be reconstructed from those 15 values. The extraction of the scattering centres is very fast and can easily be implemented in real time. A decomposition of an A-scan of 512 points in a sum of 5 wavelets takes only 0.39 sec in MatLab code on a PC.

Fig. 7-3 shows a 3D plot of a C-scan of a buried mine by only representing the scattering centres of each A-scan. The amplitudes of the coefficients  $B_p$  of the scattering centres are represented by colours.

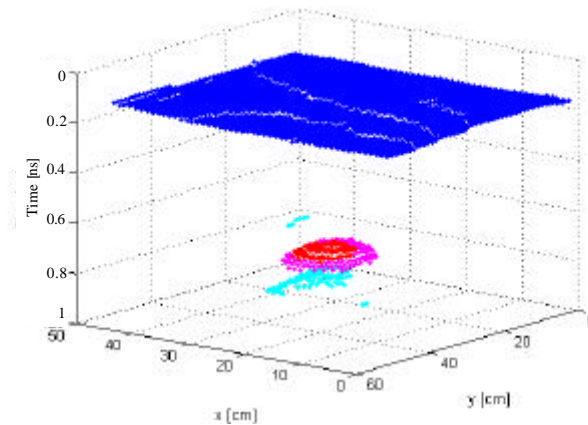


**Fig. 7-3:** 3D plot of a C-scan by only representing the scattering centres

### 7.2.2. UWB signal processing on A-scans

In Chapter 5 we mentioned that the response of an object on a fast transient impulse can be split into two parts: the early time response and the late time response. The late time response is considered to begin after a time interval, which is of the order of the wave transit time through the object. The late-time response (also called the resonant part) is governed by the complex natural resonances of the object. These complex natural resonances are supposed to be independent of the orientation of the object, and contain valuable information for target recognition and clutter reduction.

#### *Pole extraction*

A technique for extracting the natural resonance frequencies of the late-time transient response, is given by Prony-type methods. In Prony-type methods it is assumed that the late-time response of a target can be modelled as an all-pole system, and hence can be written as a summation of complex exponentials:

$$y(n) = \sum_{i=1}^p D_i e^{s_i n T} \quad (7.7)$$

where

$y(n)$  is a vector (sequence) of equally spaced data points,

$N$  the total number of data points,

$T$  the sampling period,

$s_i$  the  $i^{th}$  complex pole,

$D_i$  the residue of the  $i^{th}$  complex pole, and

$p$  the total number of poles.

In 1795 Prony gave a method of solution for finding the complex poles to fit a vector of equally spaced data points with length  $N = 2p$  [7]. This method however performs poorly in the presence of noise [8]. To overcome the problem, improved Prony-type methods have been developed. Equation (7.7) can be written as a recursive differential equation

$$y(n) = -\sum_{k=1}^p a(k)y(n-k) \quad \text{for } n \geq p \quad (7.8)$$

This auto-regressive recurrence equation, also called the forward linear prediction equation can be written for the different measured data points

$$\begin{bmatrix} y(p) & y(p-1) & \cdots & y(1) \\ y(p+1) & y(p) & \cdots & y(2) \\ \vdots & \vdots & \ddots & \vdots \\ y(N-1) & y(N-2) & \cdots & y(N-p) \end{bmatrix} \begin{bmatrix} a(1) \\ a(2) \\ \vdots \\ a(p) \end{bmatrix} = -\begin{bmatrix} y(p+1) \\ y(p+2) \\ \vdots \\ y(N) \end{bmatrix} \quad (7.9)$$

or in short

$$Ya = h$$

The matrix  $Y$  is called the data matrix and the vector  $h$  is called the observation vector. The unknown complex amplitude vector  $a$  can be calculated by solving the

linear prediction equation (7.9) for  $N > 2p$  in the sense of least squares [9]. Once the amplitude vector  $a$  has been found, the complex poles of the system can be calculated as the zeros of the polynomial

$$1 + a(1)z^{-1} + a(2)z^{-2} + \dots + a(p)z^{-p} \quad (7.10)$$

The residues  $D_i$  can be found by solving using equation (7.7) in the sense of the least squares. The same can be done using the backward linear prediction equation or a combination of both [9]. Other improved prony-type methods based on linear prediction are found in [10][11].

Another problem besides the measurement noise is the lack of *a priori* knowledge on the exact number of poles of the system, *i.e.* the order  $M = p$  of the system. In [12][13], the estimation of  $M$  is done based on the singular value decomposition (SVD) of the data matrix  $Y$ . If no noise is present in the data, the rank of  $Y$  will be equal to  $M$  and only  $M$  eigenvalues will be found different from 0. In our study, we implemented the Total Least Square method (TLS) [13]. In this approach the noise in the data matrix and the observation vector is reduced simultaneously. The number of poles will be estimated by use of the SVD of the augmented matrix  $[Y|h]$ ; only the poles with a sufficiently high energy are kept.

In an experimental study [3], the TLS method is tested on the backscattered signals of metal discs and of different types of AP mines. The aim of the study was to verify if the location of the poles is characteristic for an object, and if the location can be used for the classification or even recognition of that object. The study showed that the location of the poles is not stable and this for mainly two reasons. The first reason is the large damping of the resonances. AP mines are so called low- $Q$  targets, *i.e.* targets with a large damping factor. This damping factor is related to the target shape, the dielectric contrast and the surrounding medium [14]. As a consequence the usable length of the data vector  $y(n)$  becomes shorter and the results from the TLS method become highly unstable. A second problem is related to the choice of the starting point of the data vector  $y(n)$ . In theory Prony-type methods must be applied only on

the late time response, as the early time response is a function of the orientation of the object. AP mines however are relatively small compared to the duration of the incoming pulse that is used, hence the end of the early time response interferes with the beginning of the late time response. Indeed, we observed that in practice it is almost impossible to separate the early time response from the late time response and that the position of the poles found by the TLS method is very sensitive to changes of the starting point of the data vector. As a whole we concluded that the results of the pole extraction algorithm are not robust enough to be used for the classification of AP mines in practical applications.

### *Time-frequency analysis*

Time-frequency analysis is a well adapted signal processing technique for analysing non-stationary data and has recently been applied with success to electromagnetic UWB scattering data [15][16]. A problem encountered with the spectrum analysis of a signal using a Fourier transform is that the signal is supposed to be stationary. With the data coming from an UWB GPR, this assumption is not true. The non-stationary character of the data in an A-scan makes that time-frequency analysis techniques like Short-Time Fourier Transform (STFT) and Continuous Wavelet Transformations (CWT) would perform better than the conventional Fourier transformations. These techniques give a spectrum analysis that is more localised in time, hence they are good candidates for the analysis of the late time response of targets.

The Short-Time Fourier Transform (STFT) is a technique where a sliding window (often a Gaussian window) is applied to the data in order to limit the signal in time. A Fourier Transform is then performed on the windowed data for each position of the window. The STFT on a time signal  $x(t)$  results in a two dimension function, time *versus* frequency, and is expressed as

$$G(\mathbf{t}, \mathbf{w}) = \frac{1}{\sqrt{2ps}} \int_{-\infty}^{+\infty} x(t) e^{-(t-\mathbf{t})^2/2s^2} e^{j\mathbf{w}t} dt \quad (7.11)$$

where  $\mathbf{t}$  is the centre of the sliding Gaussian window and  $\mathbf{s}$  the standard deviation.

The Continuous Wavelet Transformations (CWT) is a technique where the time signal  $x(t)$  is decomposed into a continuous set of wavelets, which are derived from a basic wavelet by expansion (contraction) and shifting in time. The CWT is expressed as

$$W(\mathbf{t}, a) = \frac{1}{\sqrt{|a|}} \int_{-\infty}^{+\infty} x(t) h\left(\frac{t - \mathbf{t}}{a}\right) dt \quad (7.12)$$

where  $h(t)$  is the basic wavelet (also called the mother wavelet),  $\mathbf{t}$  is the time shift of the wavelet and  $a$  the scale factor. The result of a CWT on an A-scan gives a two dimensional representation of the signal, time *versus* scale-factor. In analogy with the power spectrum representation of a Fourier transformation, a CWT is often represented in what is termed a scalogram, defined as

$$SCAL_w(\mathbf{t}, a) = |W(\mathbf{t}, a)|^2 \quad (7.13)$$

An important point in CWT is the choice of the mother wavelet [16]. For seismic applications the Morlet wavelet is often used [5]. In our research, we also used the Morlet wavelet and tested it on the data coming from the UWB GPR [17]. Although CWT could give an indication of the presence of a target, the results of CWT with respect to the classification of objects was found to be limited, probably because of the same reasons as mentioned in the paragraph on pole extraction.

Fig. 7-4 shows two scalograms: one of an A-scan with only a reflection on the air-ground interface, and one of an A-scan with a target present.

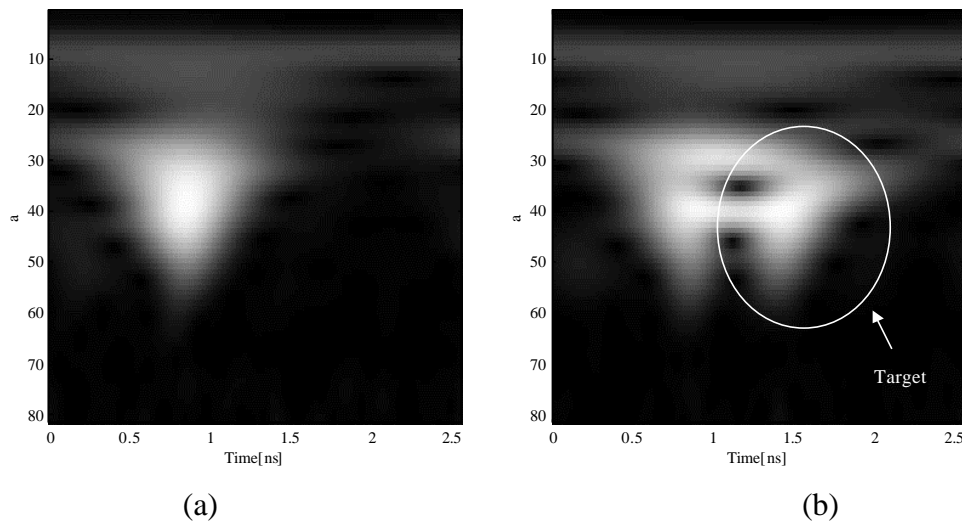


**Fig. 7-4 :** (a) Scalogram of an A-scan without target, (b) scalogram of an A-scan with target

The study of UWB signal processing techniques on A-scans coming from the UWB GPR was mainly experimental. The first conclusions drawn from this study were not promising enough for us to continue research in this direction. From this point, an important reorientation of the work in the domain of signal processing was done. Until now we hoped to find sufficient information on the target in an A-scan, because the UWB GPR could then be used in the same way as a metal detector, *i.e.* producing an alarm when a mine or a mine-like target is detected. Considering our rather disappointing experience with the UWB signal processing techniques on A-scans, we decided to concentrate our work more on the interpretation of C-scans, to retrieve information on the shape and dimensions of the buried target.

## 7.3. Migration

### 7.3.1. General

The data coming from a GPR, even after optimal A-scan processing will still be unfocussed. Because of the beam-width of the transmitting and receiving antenna, the reflections on a structure will be smeared out over a broad region in the recorded data.

The family of processing algorithms that try to reconstruct, from the recorded B- or C-scans at the surface, the reflecting structure present in the sub-surface, is called *migration*. The aim of migration techniques is to focus reflections in the recorded data back into the true position and physical shape of the target. In this respect, migration can be seen as a form of spatial deconvolution that increases spatial resolution.

The migration techniques received much attention in the last 30 years in seismic and geophysical engineering. The first migration methods were geometric approaches. After the introduction of the computer, more complex techniques, based on the scalar wave equation, were introduced. A good overview of these techniques is given in [18] and [19].

Migration techniques applied on GPR images are sometimes called 1D-SAR imaging techniques. Indeed, migration uses data coming from different antenna position and increases azimuth (cross range) resolution. In this perspective the name 1D-SAR technique is correctly chosen. Note that SAR techniques used in radar usually make more approximations than the migration techniques in seismic. In seismic most of the migration algorithms are based on a backpropagation (inverse extrapolation) of the wave field, described by a scalar wave equation. Until the late 1980s, SAR techniques were based on differences in travel time (or phase) and used plane wave approximations. It is only recently that processing techniques, similar to migration algorithms in seismic, are used in synthetic aperture radars [20].

In Section 7.3.3 some existing migration techniques, applicable on GPR data, will be introduced. Although most of the techniques are originally developed for acoustic sounding, using scalar pressure-wave propagation theory, they are applied with success to electromagnetic sounding. In electromagnetic sounding the fields have a vectorial character and hence the scalar seismic processing algorithms can in theory not be used. In practice however, as most GPRs only radiate and measure one scalar component of the EM field, the seismic migration techniques for scalar fields perform well. In this chapter, to simplify the analysis, we will also make this approximation and replace the vector field by a scalar one. Another difference between electromagnetic and acoustic sounding is the way in which the data are recorded. In the GPR case, the distance between the transmitting antenna and the receiving antenna

is always constant. In seismic terminology, this is called constant-offset data. If the distance between the two antennas is negligible, this is called zero-offset data. Further, with the laboratory UWB GPR, the antennas are used off the ground. This means that the migration algorithm must be modified to take into account the different velocities of the two media (air and ground) and the diffraction on the air-ground interface. If possible, we will suggest such a modification. More mathematical details on the migration algorithm are found in Appendix B.

### 7.3.2. Exploding source model

A model often used in seismics to explain the mathematics behind some of the methods, is the model of the exploding source. We present the model here because it allows some definitions of terms and illustrates well the migration problem. The geometry of the model is represented on Fig. 7-5. The exploding source is located in the  $xz$ -plane, denoted the *object plane*. At time  $t = 0$ , the sources in the object plane explode and send out waves. The waves propagate as a function of time, represented on a horizontal axis, and reach the surface. The receivers, located along the  $x$ -axis, at  $z = 0$ , record the data. The plane in which the data is recorded is defined as the *data plane*. The recorded data are denoted  $b(x, z = 0, t)$  or in short  $b(x, t)$ .

The ideal migration method transforms the data  $b(x, z = 0, t)$  from the data plane back into the object plane  $b(x, z, t = 0)$ . Due to a number of unknowns, the reduced data set, the complexity of the subsurface and the noise present in the data, a complete inversion is difficult and computational intensive. In many cases it is even impossible, or can lead to unreliable results. All migration algorithms are based on a linearisation of the wave scattering problem. This means that the interaction of the field inside the scatterer and between different scatterers present in the scene is neglected. This approximation is known from optics as the Born approximation [21]. The result of the migration method on the recorded data is called the migrated image  $\hat{O}(x, z)$ . The migrated image is an estimation of the object plane. Sometimes the migrated image is not represented as a function of the depth  $z$ , but as a function of time. One reason for this is that the estimation of the propagation velocity in the subsurface is limited in

accuracy. The migration process resulting in the data  $\hat{O}(x,t)$  is then called *time migration*. If the propagation velocity of the medium is known, there is a direct relation between the time and the depth.

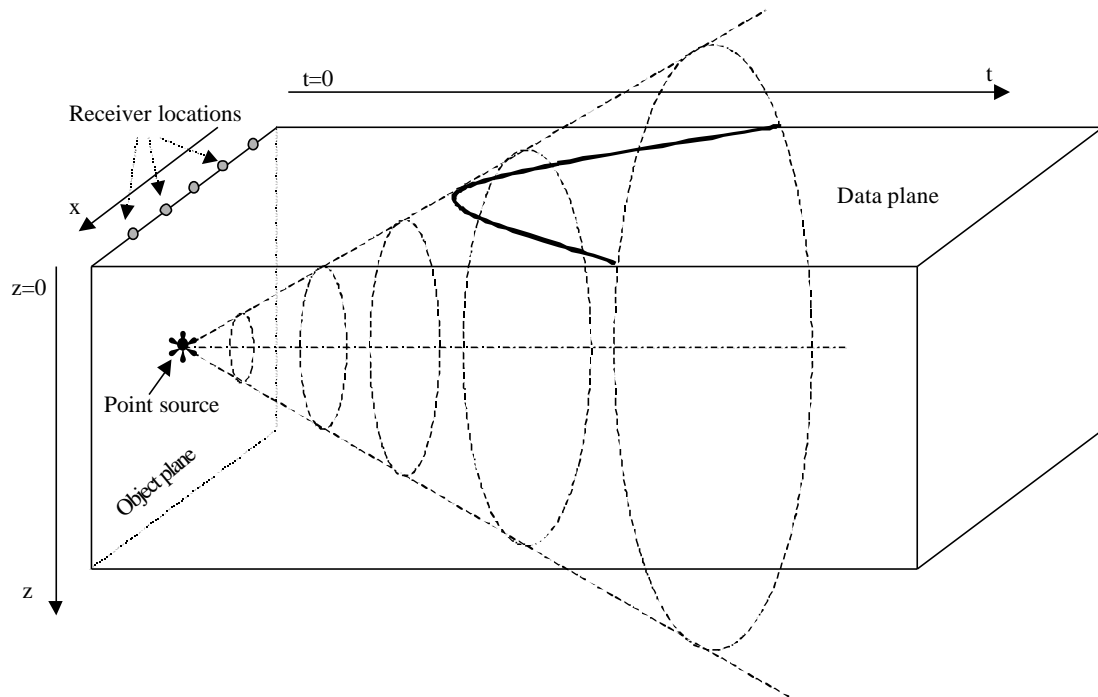


**Fig. 7-5:** The geometry of the exploding sources model

The data, resulting from an exploding source model is largely equivalent with the zero-offset data of a GPR, with one important distinction. The zero-offset data is recorded as two-way travelling time, while the data from the exploding source model represents the one-way travelling time. To make the data comparable, one can always imagine that the velocity of propagation is half the value of the actual medium velocity in the exploding source model.

Note that the notions *data-* and *object planes* are represented here as 2D planes. This will only be the case if B-scans are recorded. For C-scans, the dimension of the data increases by one, and the two planes have to be considered as volumes.

Further we assume that the propagation velocity in the ground remains constant with depth and that we only want to migrate the top region of the recorded data down to a depth of 20 cm. These two assumptions introduce some simplifications in a lot of the

methods. An extension to a variable propagation velocity in depth and even cross-range is not possible in all of the methods.

### 7.3.3. Overview of existing migration methods

#### *Diffraction-summation*

The first technique is a relatively straightforward method, but it illustrates well the general principle of migration. Consider a 3D data set  $b(x, y, t)$  recorded in the data plane. Each point in the migrated image  $\hat{O}(x, y, z)$  is the result of a summation of the recorded amplitudes in the data-plane along a diffraction hyperbola, whose curvature is governed by the medium velocity and the depth of the point to be migrated. If there is an object in the apex of the diffraction hyperbola, the amplitudes will add. If not, the summation of the non-coherent data along the diffraction hyperbola tends to zero.

Suppose the data  $b(x, y, t)$  is recorded with a monostatic GPR by moving the antennas on the ground in the  $xy$ -plane, taking a measurement  $b(x_j, y_k, t)$  at position  $(x_j, y_k, 0)$ , with  $j = 1, 2, \dots, J$  and  $k = 1, 2, \dots, K$ . The migrated image  $\hat{O}(x, y, z)$  is then calculated by

$$\hat{O}(x, y, z) = \sum_{j=1}^J \sum_{k=1}^K b(x_j, y_k, \frac{2R_{j,k}}{v}) \quad (7.14)$$

where

$R_{j,k}$  is the distance between the measuring position  $(x_j, y_k, 0)$  and the point

$(x, y, z)$  that is to be migrated,

$v$  the propagation velocity of the medium.

The time  $\frac{2 \cdot R_{j,k}}{v}$  represents the total travelling time from the transmitting antenna to the point  $(x, y, z)$  and back.

For the UWB GPR data, using the antennas off-ground, the two-way travelling time in equation (7.14) has to be modified to take into account the different velocities of the two media (air and ground) and the diffraction on the air-ground interface. This can be done by calculating for each point in the object plane the corresponding migration template in the recorded data. To obtain the point in the migrated image, the summing must be performed along the migration template. This must be repeated for all points in the object plane.

The result of the above described diffraction migration method on a B-scan, recorded with the UWB GPR is shown in Fig. 7-6. The B-scan represents a metal disc with a radius of 5 cm, buried at 6 cm in dry sand. The diffraction hyperbolas on the top of the metal disc are clearly visible in Fig. 7-6 (a). On the migrated image however, the diffraction hyperbolas disappear and the physical dimensions of the targets approach the real dimensions of the target. Note the presence of some artefacts in the migrated image at the left and the right side above the target. These artefacts, typical for the method, are explained by the fact that the summation of the data along a diffraction hyperbole not always tends to zero when no target is present.

The diffraction migration algorithm is easy to implement, but computationally intensive, because the diffraction template on which we have to sum has to be recalculated for each depth. In practice however, the shape of the diffraction hyperbola does not change very much with depth and the same hyperbola can be used for a broad depth range. On the other hand, diffraction migration does not take the physics of wave propagation into account. Therefore more complex algorithms will be introduced.

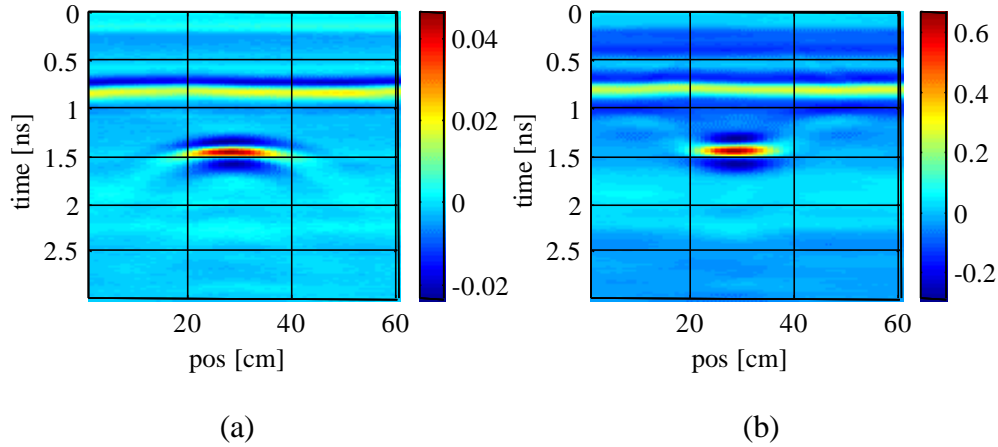


**Fig. 7-6:** (a) B-scan of metal disc, buried at 6 cm in dry sand, (b) result after migration, using the diffraction migration algorithm

### *Kirchhoff-migration*

The basic idea in the Kirchhoff-migration is to back-propagate the wavefront, measured in the data-plane (as defined in the exploding source model, see Fig. 7-5), to the object plane at  $t=0$ , using an integral solution method to the scalar wave equation. So this migration method involves back-propagation or inverse extrapolation to remove the effects of wave field propagation. In fact the array of receivers recording the data  $b(x', y', z'=0, t')$  in the data plane, denoted here as  $S'$ , will be replaced by an array of secondary sources, each driven in reverse time by the recorded data. Doing so the migrated image  $\hat{O}(x, y, z)$  is calculated as

$$\hat{O}(x, y, z) = \frac{2}{4\pi v} \iint_{S'} \dot{b}(x', y', z'=0, |\bar{r} - \bar{r}'|/v) \frac{\cos(\mathbf{q})}{|\bar{r} - \bar{r}'|} dS' \quad (7.15)$$

where  $\dot{b}(x', y', z'=0, t')$  is the time derivative of the data recorded in the data plane  $S'$ ,

$\bar{r} = (x, y, z)$  the point to be migrated, and

$\mathbf{q}$  the angle between the direction  $\bar{r}' - \bar{r}$  and the normal to the data plane  $S'$ .

The complete development of (7.15) is found in Appendix B.

Comparing the result of the diffraction migration method in (7.14) with the Kirchhoff migration given by (7.15), three differences are observed. First there is the oblique factor  $\cos(\mathbf{q})$ , that takes into account the fact that the normal to the wave front is not parallel to the normal of the measuring surface. Second there is the spreading factor

$\frac{1}{|\bar{r} - \bar{r}'|}$ , dealing with the spreading losses of spherical waves. Last, the summation over the diffraction hyperbola has to be taken on the time derivative of the recorded data. So before summation, the time derivative of each A-scan has to be calculated.

Equation (7.15) has to be adapted for the data coming from the UWB GPR with the two antennas off-ground. The same principle as in the diffraction-summation method is used, *i.e.* the summing is performed on a migration template. In (7.15) the travelling time  $\frac{|\bar{r} - \bar{r}'|}{v}$  is replaced by the actual travelling time (from transmitting antenna towards the point  $(x, y, z)$  to be migrated and back to the receiving antenna). For the calculation of the angle  $\mathbf{q}$ , the refraction on the air-ground interface has to be taken into account.

For comparison purposes, the Kirchhoff migration algorithm has been applied to the same B-scan as in the previous method. The B-scan in Fig. 7-7 (a), recorded with the UWB GPR, represents a metal disc with a radius of 5 cm, buried at 6 cm in dry sand. The result after migration is shown in Fig. 7-7 (b). The result is obviously better than with the diffraction summation method. The target is more focussed and there are almost no artefacts left on the top of the metal disc.

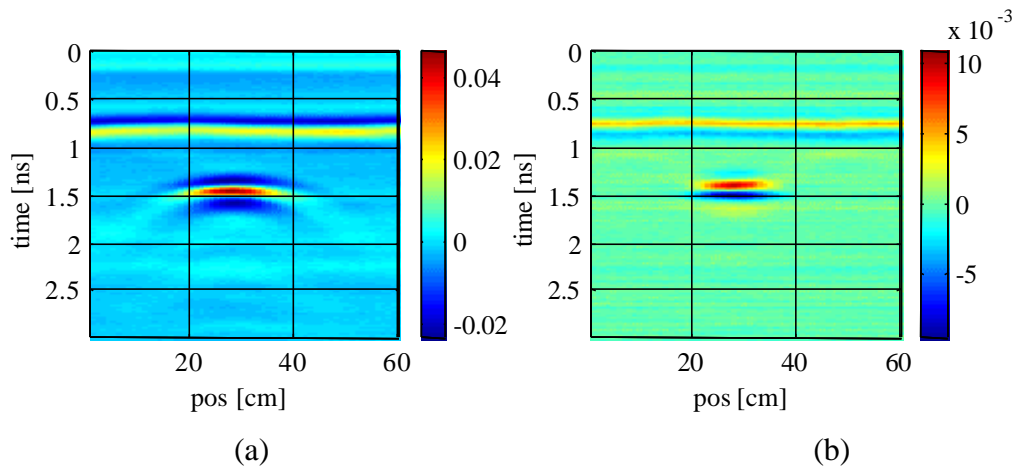


**Fig. 7-7:** (a) B-scan of metal disc, buried at 6 cm in dry sand, (b) result after migration, using the Kirchhoff migration algorithm.

### *Finite-Difference Migration*

The finite-difference migration is, just as the Kirchhoff migration, a method that back-propagates the wavefront, measured in the data-plane towards the object plane at  $t = 0$ . The main difference with the Kirchhoff method is the way of solving the scalar wave equation. The finite-difference migration is based on the differential solution. From the wavefront at time  $t$ , it calculates the wavefront at time  $t - \Delta t$ , using finite-difference approximations, and backpropagates until  $t = 0$ .

### *Frequency-Wavenumber Migration*

In 1978, Stolt [22] introduced a Fourier transform approach in migrations. Since then, variants on the methods on the original Stolt migration appeared. All these methods are grouped under the name *Frequency-Wavenumber Migration*, or in short f-k migration.

The method is, just like the former two, based on the back-propagation of the scalar wave-equation and can thereby best be explained using the exploding source model. More details about the calculation are found in Appendix B.

If  $B(k_x, k_y, 0, \mathbf{w})$  is the Fourier transformation of the data recorded in the data plane, with respect to the  $x, y$  and the  $t$  co-ordinate, then the migrated image can be calculated as

$$\hat{O}(x, y, z) = \iiint B(k_x, k_y, 0, \mathbf{w}) e^{-i(k_x x + k_y y + k_z z)} dk_x dk_y d\mathbf{w} \quad (7.16)$$

where  $k_z$  is a wavenumber defined as

$$k_z = \text{sgn}(\mathbf{w}) \sqrt{\frac{\mathbf{w}^2}{v^2} - k_x^2 - k_y^2} \quad (7.17)$$

Equation (7.16) is the general representation of the f-k migration, also called the *Phase Shift Migration*. The method can deal with variations of velocity as a function of depth. The *Stolt Migration* is a variant on the *Phase Shift Migration*, for a constant propagation velocity. In the special case where  $v(z) = v = cst$ , equation (7.16) can be further developed by a change of variables from  $\mathbf{w}$  to  $k_z$ . The migrated image becomes

$$\hat{O}(x, y, z) = v^2 \iiint \frac{k_z}{\mathbf{w}} B(k_x, k_y, 0, \mathbf{w}) e^{-i(k_x x + k_y y + k_z z)} dk_x dk_y dz \quad (7.18)$$

The advantage of (7.18) over (7.16) is that (7.18) can be calculated using an inverse Fourier transformation of  $B(k_x, k_y, 0, \mathbf{w})$ , scaled by  $\frac{v^2 k_z}{\mathbf{w}}$ , i.e. the Jacobian of the transformation from  $\mathbf{w}$  to  $k_z$ . This implies a serious reduction of the number of floating point operations for the migration and a gain of calculation time.

Fig. 7-8 (b) shows the result of the Stolt migration on the B-scan representing a metal disc with a radius of 5 cm, buried at 6 cm in dry sand (Fig. 7-8 (a)). In the configuration of the UWB GPR, as the antennas are used off-ground, there is a change in the vertical propagation velocity, and normally the Stolt migration given by (7.18)

can not be used. To solve this problem, a constant mean velocity, somewhere between the propagation velocity in air and in ground, is used for the migration. This is probably the reason why the method performs less good than to the Kirchhoff migration. The artefacts on the left and the right side above the ground are due to the Fourier transformation. They can be avoided by windowing the data, prior to migration.

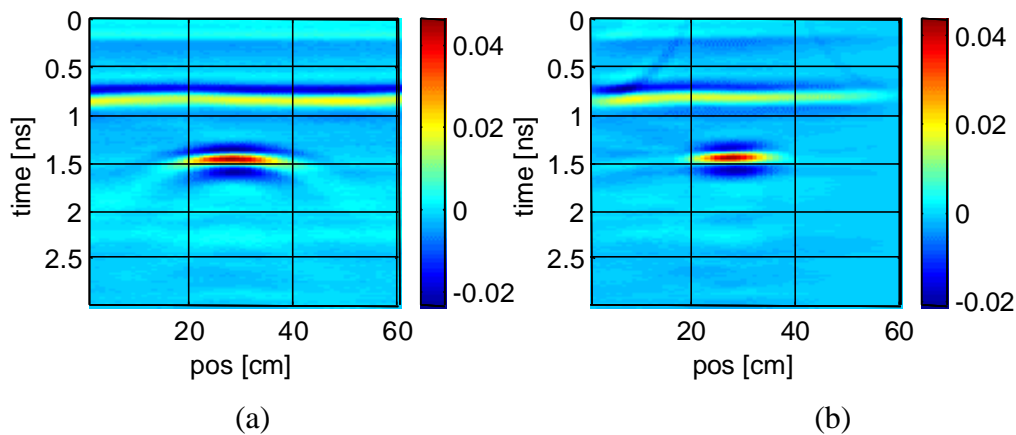


**Fig. 7-8:** (a) B-scan of metal disc, buried at 6 cm in dry sand, (b) result after migration, using the Stolt migration algorithm

## 7.4. Migration by deconvolution

In previous section we have concentrated on some existing migration methods. Most of these methods are based on backpropagation of waves. Almost none of these methods however include system aspects of the GPR like the waveform of the excitation source, the impulse response of the antennas, the antenna pattern, etc. Furthermore most of the migration methods consider the ground as being loss-less and without dispersion. It can be expected that an imaging technique that takes into account the characteristics of the system and possibly the characteristics of the ground would perform better. The migration scheme presented in this section is a backpropagation technique based on the deconvolution of the recorded C-scans with the point spread function of the system. This point spread function is a synthetic C-

scan of a fictive point target at a given depth. It includes all the above mentioned system and ground characteristics. The point spread function can be found by forward modelling. By doing so, a very simple and fast migration algorithm, integrating system and ground characteristics, is obtained.

### 7.4.1. Development of the method

The development of the method is done in the time domain, using the time domain description of the system, presented in Chapter 5. The migration by deconvolution makes only sense if the acquisition process by the GPR is a convolution between the structure present in the subsurface and the point spread function of the system. This can be demonstrated under certain assumptions.

Suppose a co-ordinate system as represented in Fig. 7-9. The antenna configuration is a bistatic configuration and there are only variations in propagation velocity in the downward direction. The 3D data  $b(x, y, z = 0, t)$  are recorded on a regular grid by moving the antennas in the  $xy$ -plane at  $z = 0$ .

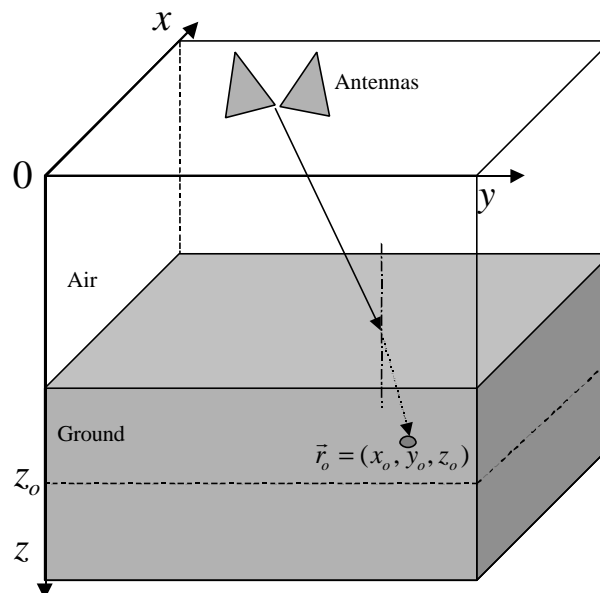


**Fig. 7-9:** Configuration and representation of the co-ordinate system

Assume in a first time that there is only one small isotropic point scatterer present in the subsurface, located at  $\vec{r}_o = (x_o, y_o, z_o)$  and characterised by an impulse response (IR)  $\Lambda_o(t)$ , independent of the incident direction. Note that, in the most general case, the IR of the localised isotropic point scatterer does not necessarily have to be a Dirac impulse as a function of time. For the antennas at any position  $\vec{r}_a = (x_a, y_a, z = 0)$ , the received voltage, representing an A-scan, can be written according to (5.13) as

$$b(\vec{r}_a, t) = \frac{T_{a-g} T_{g-a}}{8\mathbf{p}^2 R_t R_r c} g_d(t) \otimes h_{N,Tx}(\vec{a}_i, t) \otimes \Lambda_o(t) \otimes h_{N,Rx}(-\vec{a}_s, t) \otimes \frac{dVs(t-t_d)}{dt} \quad (7.19)$$

where  $t_d$  represents the exact two-way travelling time between the antennas and the point target, taking into account the different propagation velocities in the media.

By grouping all the factors, except for the IR of the point target, in one factor  $w(\vec{r}_a, \vec{r}_o, t)$ , equation (7.19) becomes

$$b(\vec{r}_a, t) = w(\vec{r}_a, \vec{r}_o, t) \otimes_t \Lambda_o(t) \quad (7.20)$$

The symbol  $\otimes_t$  is introduced to clearly indicate that the convolution in (7.20) is a convolution in time:  $b(\vec{r}_a, t) = \int_t w(\vec{r}_a, \vec{r}_o, t - \mathbf{t}) \Lambda_o(\mathbf{t}) d\mathbf{t}$ . For a given configuration, all the factors in (7.19) are known, hence  $w(\vec{r}_a, \vec{r}_o, t)$  can be easily calculated. Furthermore, for the antennas at  $z = 0$  and the point scatterer at a fixed depth  $z = z_o$ , the response  $w(\vec{r}_a, \vec{r}_o, t)$  is a function of  $\vec{r}_o$  and  $\vec{r}_a$  only by their difference, and (7.20) can be written as

$$b(\vec{r}_a, t) = w(\vec{r}_a - \vec{r}_o, t) \otimes_t \Lambda(r_o, t) \quad (7.21)$$

If an object can be modelled by a set of independent small isotropic point scatterers, all at approximately the same depth  $z = z_o$ , the output voltage  $b(\vec{r}_a, t)$  will be a

combination of the contribution of each individual point scatterer, that is clearly a convolution in space if we assume that the operation is linear:

$$b(x_a, y_a, t) = \iint_{x,y} \int_t w(x_a - x, y_a - y, z_o, t - \mathbf{t}) \Lambda_{z_o}(x, y, \mathbf{t}) d\mathbf{t} dx dy \quad (7.22)$$

Equation (7.22) represents a space-time convolution along the co-ordinates  $x$ ,  $y$  and  $t$ , and can be written as

$$b(x, y, t) = w(x, y, z_o, t) \otimes_{x,y,t} \Lambda_{z_o}(x, y, t) \quad (7.23)$$

where  $\Lambda_{z_o}(x, y, t)$  is a 3D matrix, called the scattering matrix [19], and contains the responses associated with the distributed point scatterers at approximately a depth  $z_o$ . The symbol  $\otimes_{x,y,t}$  denotes a space-time convolution along the co-ordinates  $x$ ,  $y$  and  $t$ . The 3D matrix  $w(x, y, z_o, t)$  represents the point spread function of the UWB GPR system for a depth  $z_o$  and is found by replacing the scattering matrix in (7.23) by a Dirac impulse in space and time:

$$\Lambda_{z_o}(x, y, t) \equiv \mathbf{d}(x, y, z - z_o) \mathbf{d}(t) \quad (7.24)$$

In practice the 3D point spread function  $w(x, y, z_o, t)$  is calculated by using (7.19) for different antenna positions  $\vec{r}_a$  on a regular grid in the  $xy$ -plane at  $z = 0$  and a small fictive point scatterer with IR  $\mathbf{d}(t - t_d)$ , at a depth  $z_o$ . In other words it can be seen as a synthetic C-scan of a small fictive point scatterer. Fig. 7-10 shows the 3D point spread function of the system at a depth of 6 cm below the air-ground interface (with the antennas 25 cm above the ground). In the point spread function, as it is obtained by forward modelling, all the information on the system like the waveform of the source, the IR of the antennas, the antenna pattern, the attenuation and dispersion in the ground, etc. are included. Note that for the implementation of (7.23), the apex of the hyperboloid in Fig. 7-10 has to be centred in the origin of the 3D image, *i.e.* the

top corner of the 3D volume. If not, the convolution with the point spread function will introduce a displacement of the objects in the scattering matrix.

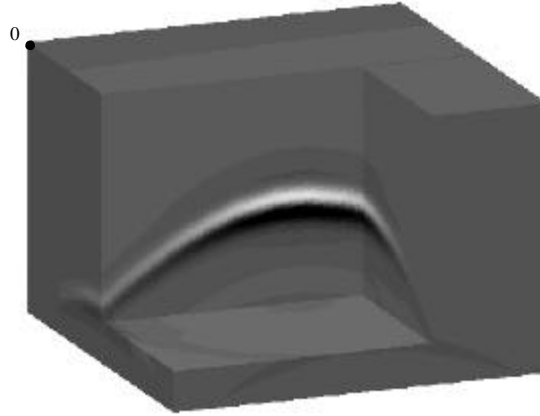


**Fig. 7-10:** Synthetic C-scan of a fictive point scatterer at a depth of 6 cm below the air-ground interface

Although the point spread function  $w(x, y, z_o, t)$  is space variant (function of  $z_o$ ), its shape will not change very much with depth. In practice, the point spread function for a given depth can be used for a broad depth range. As a consequence, the space-time convolution (7.23) can be considered as space (depth) invariant and the image of the 3D scattering matrix  $\hat{\Lambda}(x, y, t)$  can be calculated in one step by

$$\hat{\Lambda}(x, y, t) = b(x, y, t) \otimes_{x,y,t}^{-1} w(x, y, z_o, t) \quad (7.25)$$

where  $\hat{\Lambda}(x, y, t)$  denotes the spatial image of  $\Lambda_{z_o}(x, y, t)$ , *i.e.* the migrated image,

$b(x, y, t)$  is the recorded C-scan that is to be migrated,

$w(x, y, z_o, t)$  the point spread function for a fixed depth  $z = z_o$ , and

$\otimes_{x,y,t}^{-1}$  a deconvolution in  $x$ ,  $y$  and  $t$ .

### 7.4.2. Implementation of the migration method

From the mathematical point of view, solving equation (7.25) can cause some problems. Because of the band-limited nature of the system and the effects of noise, equation (7.25) is a classical ill-posed problem. A fast and computational not intensive mathematical solution for the deconvolution is to perform it in the frequency-wavenumber domain, by means of a Wiener filter [23]. A Wiener filter is an optimal filter that minimises the variance of the error between the restored image and the original image before degradation, under the assumption of a signal-independent noise, a linear degradation and stationarity of the images.

Let  $B(k_x, k_y, \mathbf{w})$  be the 3D Fourier transform of the data recorded  $b(x, y, t)$ , with respect to the  $x$ ,  $y$  and the  $t$  co-ordinates:

$$B(k_x, k_y, \mathbf{w}) = \iiint b(x, y, t) e^{ik_x x + ik_y y - i\mathbf{w}t} dx dy d\mathbf{w} \quad (7.26)$$

Taking the Wiener filter approach, the restored image in the frequency-wavenumber domain is given by

$$\hat{\Lambda}(k_x, k_y, \mathbf{w}) = \frac{B(k_x, k_y, \mathbf{w}) W^*(k_x, k_y, \mathbf{w})}{W(k_x, k_y, \mathbf{w}) W^*(k_x, k_y, \mathbf{w}) + \frac{P_n(k_x, k_y, \mathbf{w})}{P_\Lambda(k_x, k_y, \mathbf{w})}} \quad (7.27)$$

where  $W(k_x, k_y, \mathbf{w})$  is the 3D Fourier transformation of the calculated point spread function,

$W^*(k_x, k_y, \mathbf{w})$  its complex conjugate,

$P_n(k_x, k_y, \mathbf{w})$  the spectral density of the noise in the image, and

$P_\Lambda(k_x, k_y, \mathbf{w})$  the spectral density of the original image.

The main problem with the Wiener filter is that it can be difficult to get a good estimation of the spectral density of the noise and the spectral density of the image before degradation, which is *a priori* not known. A classical solution is to replace the ratio of the two power spectral densities by a constant parameter  $\mu$ , also called water level parameter. It will prevent (7.27) of becoming too large for very small values of  $W(k_x, k_y, \mathbf{w})$ .

Finally the migrated image is given by the inverse 3D Fourier Transform of  $\hat{\Lambda}_{zo}(k_x, k_y, \mathbf{w})$ :

$$\hat{\Lambda}(x, y, t) = \frac{1}{2\mathbf{p}} \iiint \hat{\Lambda}(k_x, k_y, \mathbf{w}) e^{-i(k_x x + k_y y - \mathbf{w} t)} dk_x dk_y d\mathbf{w} \quad (7.28)$$

The migration scheme is resumed in the following steps:

1. The point spread function is calculated for a given soil type and depth. The depth is chosen to be the most likely depth for an object. In our application a burial depth of 6 cm is always chosen. The calculation of the point spread function only has to be done once.
2. The 3D Fourier transform of the recorded data is calculated by (7.26).
3. The data is filtered by the Wiener filter as in (7.27).
4. The inverse 3D Fourier Transform of the filtered data is calculated, represented in (7.28), resulting in the migrated image.

As already mentioned, this migration scheme is very simple and not computational intensive. Suppose a C-scan of 32\*32\*256 points representing an area of 64 cm by 64 cm with a step of 2 cm in both lateral directions. The 3D Fourier transformation, the filtering and the inverse transformation of this C-scan (steps 2-4 of the migration scheme) only takes 76 Mflops, which means that it can easily be implemented in real time. The migration of a C-scan of 64\*64\*256 points takes approximately 246 Mflops.

### 7.4.3. Discussion

#### *Influence of the spatial invariance approximation of the point spread function*

The key-point of the whole migration method lies in the approximation of considering the point spread function as space invariant. It permits to calculate  $\hat{\Lambda}(x, y, t)$  by (7.25) in one step. This approximation is based on the assumption that the shape of the point spread function does not change very much with depth. Suppose there is only one object in the ground, at approximately a depth of 10 cm. Ideally, the deconvolution of the raw C-scan should be done with a point-spread function, calculated for objects at 10 cm of depth. As *a priori* we do not know the depth of the buried object, the raw C-scan will be deconvolved with a point spread function calculated for the most probable depth of an object, *i.e.* 6 cm. To have an idea of the influence of this error on the migration results, the following verification was done. The point spread function is calculated for a depth of 6 cm. This point spread function is then used to migrate synthetic images of point targets respectively at 2 cm, 6 cm, 10 cm and 15 cm of depth in the ground. For all of the three cases, the same water level parameter  $m$  is used in the Wiener filter to perform the deconvolution. The results after migration are shown in Fig. 7-11. The migrated image of the point target at 6 cm (Fig. 7-11 (b)) gives the best focussed image, which is logical because the point spread function, used for the deconvolution, was calculated for targets at 6 cm of depth. The results after migration of the other three point targets at 2 cm, 10 cm and 15 cm of depth give less focussed but still acceptable results.

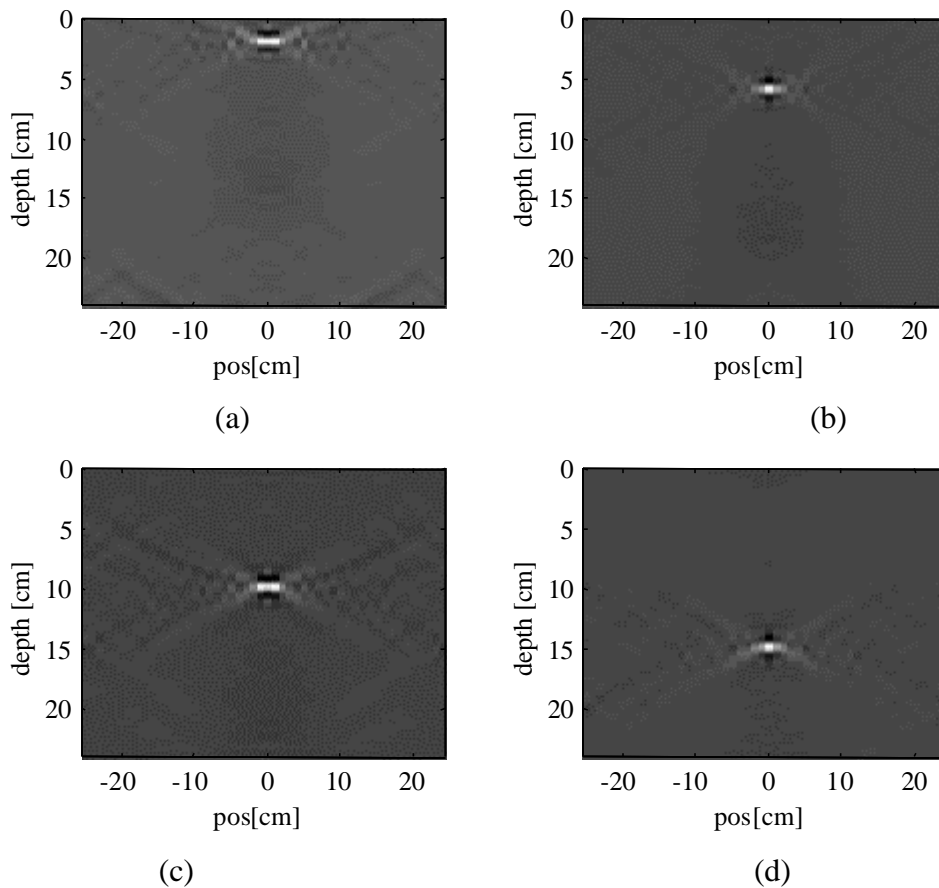


**Fig. 7-11:** The influence of the space invariant approximation of the point spread function

- (a) migrated image of the point targets at 2 cm
- (b) migrated image of the point targets at 6 cm
- (c) migrated image of the point targets at 10 cm
- (d) migrated image of the point targets at 15 cm

For comparison, the result of the Kirchhoff migration method on the synthetic image of the point targets at 6 cm is given in Fig. 7-12. It is clear that the result after the Kirchhoff migration is less focussed than any of the results in Fig. 7-11, which brings us to the conclusion that the approximation of considering the point spread function as space invariant is acceptable.

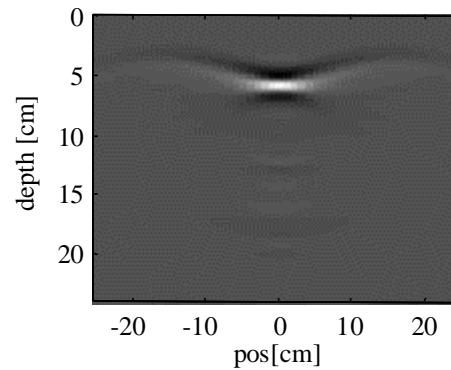


**Fig. 7-12:** Migrated image of the point targets at 6 cm after Kirchhoff migration

Note that for the migration of the synthetic images, the Kirchhoff migration method is put in an unfair position compared to the migration by deconvolution. The synthetic images are obtained by forward modelling, using the same model as for the calculation of the point spread function. Applying the migration methods on real images however, we also noticed that the migration by deconvolution gave systematically better focussed images than the Kirchhoff migration. Fig. 7-13 shows a B-scan of a PMN mine at 5 cm of depth, after migration by deconvolution (Fig. 7-13 (a)) and after Kirchhoff migration (Fig. 7-13 (b)). It can be seen that the image on the left is slightly more focussed. Furthermore on images with a lot of clutter or a very weak reflection of the object, the object is in general more visible when the image is restored by the migrated by deconvolution method than by the Kirchhoff migration method.

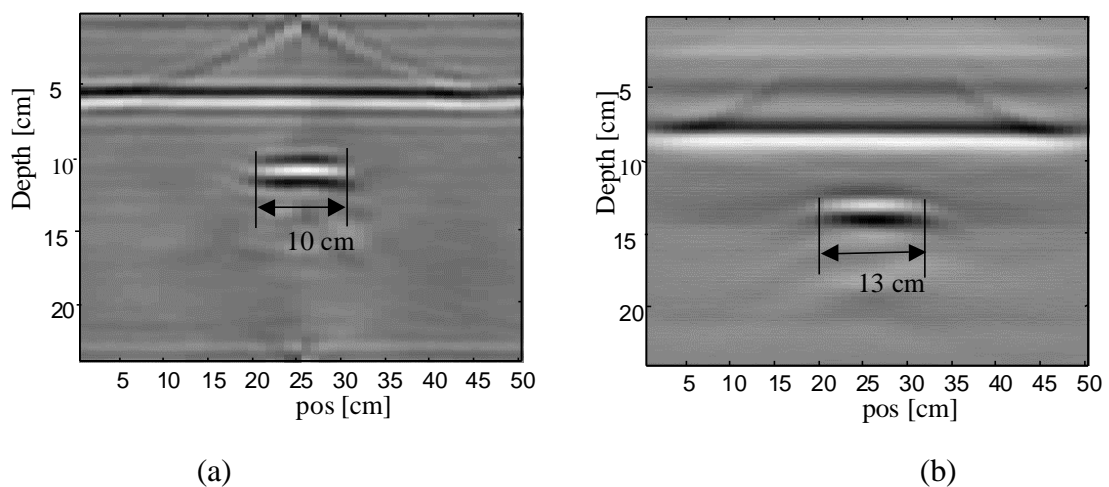


**Fig. 7-13:** PMN at 5 cm of depth, (a) after migration by deconvolution, and (b) after Kirchhoff migration

### *Spatial resolution in x- and y- direction*

In general, the spatial resolution of a GPR system depends on a lot of system and ground parameters, *e.g.* the dimensions of the combined antenna footprint, the bandwidth of the system, the migration method that is used, the losses in the ground, etc. The migrated image in Fig. 7-11 (b) gives an idea of the spatial resolution one could expect from the laboratory UWB GPR after migration by deconvolution. The spatial resolution in the  $x$ -direction of the single point target in Fig. 7-11 (b) is 2 cm (the spatial resolution is measured as the 3dB width of the grey-values of the target in the migrated image). Two point scatterers with equal strength can be easily distinguished from each other if they are separated by 4 cm, as shown in Fig. 7-14. Note that these resolution figures must be considered as best cases. First of all, the deconvolution is done with the point spread function calculated for the exact depth. Secondly the results are obtained on synthetic images generated by the same system model and with very little noise present in the images, hence the deconvolution with the Wiener filter will be very successful, leading to a high resolution. If more noise is present in the images, the resolution of the migrated image will decrease due to a decreasing bandwidth of the Wiener filter. Further, the resolution will also decrease if the ground becomes more lossy. Higher losses will reduce the width of the hyperbole, which is equivalent to a reduction of the length of the synthetic antenna.

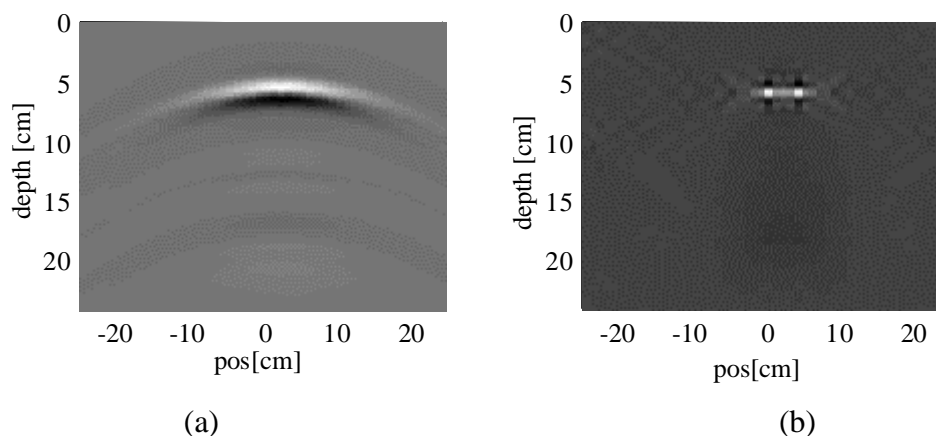


**Fig. 7-14:** (a) Synthetic B-scan of two point targets at 6 cm of depth, separated by 4 cm, (b) same B-scan after migration by deconvolution

***Analogy with imaging techniques***

It is shown in Section 7.4.1 that under certain assumptions the acquisition process by the GPR is a convolution between the structure present in the subsurface and the point spread function of the system. Similar conclusions are found in the electromagnetic imaging theory, using the same assumptions, but a different target modelling. Electromagnetic imaging is a linearised inversion scheme that approximates the field inside the scatterer by the incoming field and thereby can be seen as a subclass of the inverse scattering problems. In electromagnetic imaging, three domains are defined: the source and receiver domain where respectively the sources and receivers are located and the scattering domain, where the objects are located. The objects are modelled by an object function, also called a contrast function  $\mathbf{c}(\vec{r})$ , which is related to the constitutive parameters of the object. In general, the scattered field in the frequency domain  $E_{sct}(\vec{r}, \mathbf{w})$  at a point  $\vec{r}$  belonging to the receiver domain is described by an integral representation

$$E_{sct}(\vec{r}, \mathbf{w}) = - \int_{\vec{r}' \in D_{sct}} g(\vec{r}, \vec{r}', \mathbf{w}) \mathbf{c}(\vec{r}') E(\vec{r}', \mathbf{w}) d\vec{r}' \quad (7.29)$$

where  $g(\vec{r}, \vec{r}', \mathbf{w})$  is the Green function and  $D_{sct}$  the scattering domain. Note that for simplicity, the scalar version is described.  $\mathbf{c}(\vec{r})$  serves as an unknown in the inverse scattering problem. A way to linearise the inversion problem is to introduce the Born approximation [21]. For weak scatterers, *i.e.* scatterers with a low contrast, the total field in the volume integral in (7.29) can be approximated by the incoming field,

$$E(\vec{r}', \mathbf{w}) \approx E_{inc}(\vec{r}', \mathbf{w}) \quad (7.30)$$

Hence (7.29) becomes

$$E_{sct}(\vec{r}, \mathbf{w}) = - \int_{\vec{r}' \in D_{sct}} g(\vec{r}, \vec{r}', \mathbf{w}) \mathbf{c}(\vec{r}') E_{inc}(\vec{r}', \mathbf{w}) d\vec{r}' \quad (7.31)$$

It is shown in [24] that by considering a monostatic GPR configuration and describing the finite length antennas with an effective point source approximation, equation (7.31) can be rewritten as

$$E_{sct}(\vec{r}, \mathbf{w}) = -\int_{\vec{r}' \in D_{sct}} W(\vec{r}, \vec{r}', \mathbf{w}) \mathbf{c}(\vec{r}') S(\mathbf{w}) d\vec{r}' \quad (7.32)$$

where  $W(\vec{r}, \vec{r}', \mathbf{w})$  is called the two-way wave field extrapolator, describing the propagation of the scalar field from the source to the location  $\vec{r}'$  in the scattering domain, and back to the receiver.  $S(\mathbf{w})$  contains the frequency information of the source. For antennas at a fixed height above the ground and the object at a given depth  $z = z_o = cst$ , and no lateral variation of the propagation velocity in the subsurface, the two-way wave field extrapolator is only function of the difference  $\vec{r} - \vec{r}'$  and (7.33) can be written as

$$E_{sct}(x_a, y_a, \mathbf{w}) = -\int_{D_{sct}} W(x_a - x_o, y_a - y_o, z_o, \mathbf{w}) S(\mathbf{w}) \mathbf{c}(x_o, y_o) dV \quad (7.33)$$

where  $(x_a, y_a, z_a = cst)$  are the co-ordinates of the antennas, and

$(x_o, y_o, z_o = cst)$  are the co-ordinates of the object.

This means that in the space-frequency domain the scattered field can be presented as a spatial convolution between the contrast function at a depth  $z_o$  and the two-way wave field extrapolator for that depth  $z_o$ . Note that for this result the same assumptions had to be made as in Section 7.4.1, *i.e.* objects at a fixed depth and no lateral variations in the propagation velocity.

### ***Consideration on the modelling of the target***

In the electromagnetic imaging approach the target is modelled by a contrast function and the Born approximation is applied. This means that the scattering sources are

considered to be independent of each other. In the approach we took in Section 7.4.1, the object is modelled by a set of independent point scatterers, each characterised by an IR  $\Lambda_o(\vec{r}_o, t_o)$  that can be different from a Dirac function in time. In both cases it is shown that the acquisition process by a GPR is a convolution, but due to the difference in modelling the object, the interpretation of the results after migration are different. The difference however between the two models and the interpretation of the results is subtle. The space that we want to image has in reality four dimensions:  $x$ ,  $y$ ,  $z$  to indicate the position of targets, and the time dimension  $t$ , containing information on the two-way travelling time to the targets and on their impulse responses. If raw C-scan data are recorded the number of dimensions is reduced from four to three by considering the time axis parallel to the  $z$ -axis. Doing so we make a mistake that leads to an unfocussed image. To avoid this defocusing, migration methods are applied in order to physically bring the time axis parallel to the  $z$ -axis. If we now represent the migrated C-scan in a three dimensional space, the image will be focussed, but we will still be unable to separate the  $z$  co-ordinate from the time variable. In the electromagnetic imaging this ambiguity is solved by taking an object function  $c(\vec{r}')$  that is only function of the spatial co-ordinates and not function of  $w$ . As a consequence, each reflection in the migrated image at a given depth has to be produced by a change in contrast at that depth. This model will work good if the Born approximation holds. In the application of AP mines, the Born approximation does not always hold. In actual applications, a permittivity contrast of over a 100% is easily obtained and the boundaries of an object will be overestimated. In the development of the migration method in Section 7.4.1 we anticipated on this by modelling the object as a set of small point scatterers, each with an IR  $\Lambda_{z_o}(t)$  different from a Dirac function. In this approach the ambiguity between time and depth is deliberately not solved. Each reflection in the migrated image is a scattering centre produced by a point scatterer at that location or above that location, because each isotropic point scatterer can have an IR different from a Dirac function. As already said, the difference lies in the interpretation of the migrated image. In our approach we recognise that the depth information on an object does not correspond with the physical dimensions of the object. To illustrate the above, let us go back to Fig. 5-2 in Chapter 5, representing the backscattered time domain signal on a dielectric cylinder in free space. In the signal, certain scattering centres appeared later in time than the

reflection on the back of the target. In the Born approximation, this would mean that there are reflections coming from behind the object, where there is no dielectric contrast present. This is physically impossible. The explanation is simple. The scattering centres, which appear later in time, are the products of other scattering mechanisms like creeping waves etc., which in the Born approximation are not allowed. In the modelling we applied in our migration method, we can deal with these other scattering mechanism by considering impulse responses that can be different from a Dirac impulse. The only scattering centre of which we are sure that it will be correctly positioned in each A-scan is the scattering centre corresponding with the specular reflection on the object, indicating the top contour of the object.

#### 7.4.4. Results of the migration method

Considering the poor results of the UWB signal processing techniques on A-scans, we decided to concentrate our work on the interpretation of C-scans in the hope to retrieve information on the shape and dimensions of the buried target. In the previous section we concluded that the depth information is ambiguous, hence the most reliable information on the shape and dimensions of the object will be found in the  $x$  - and the  $y$ -directions. Therefore we will systematically show projections of the whole (or a part of the) C-scans on a horizontal plane. The projections are the results of the summation of the energy per A-scan:

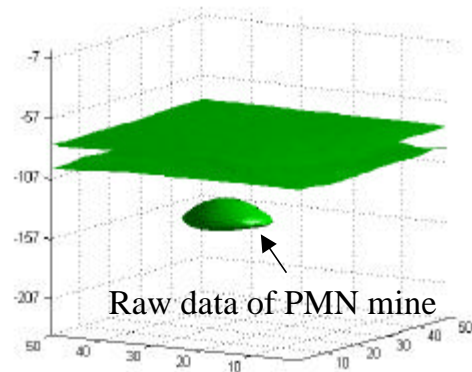
$$c(x, y) = \sum_{i=n_1}^{n_2} b(x, y, i)^2 \quad \text{with} \quad 1 \leq n_1 < n_2 \leq N \quad (7.34)$$

***Results of indoor trials***

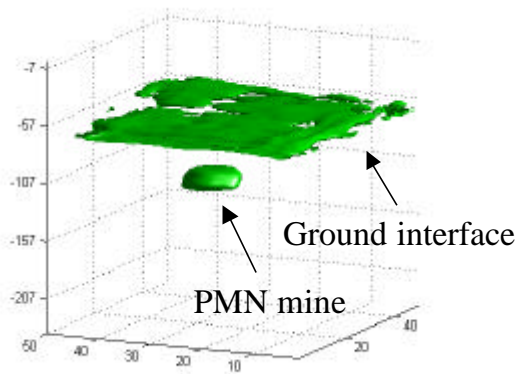
The migration by deconvolution is applied on data taken by the laboratory UWB GPR, with the antennas mounted on the indoor xy-scanning table, as described in Chapter 6. The data are acquired over an area of 50 cm by 50 cm with a step of 1 cm in both  $x$ - and  $y$ -direction. Fig. 7-15, Fig. 7-16 and Fig. 7-17 show respectively the results of the migration method on a PMN mine, a brick of dimensions 15\*9\*6 cm and a piece of 20 cm barbed wire, all buried at 5 cm of depth in sand. The 3D representations of the raw data (subplots (b)) and the migrated data (subplot (c)), are obtained by performing a Hilbert transform on each individual A-scan to find its envelope. The data are then plotted by the iso-surface 3D plot function of MatLab, highlighting all the pixels of a given intensity. The vertical axis is a time axis in  $10^{\text{th}}$  of ps. In the lower right corner of each image, the two-dimensional C-scan representation, given by (7.34), of the migrated image is shown. For clarity, the ground reflection is omitted in Fig. 7-16 and Fig. 7-17. Looking on the objects from above, the round shape of the PMN mine becomes very clear, whereas the shape of the brick is more rectangular. This means that the (oval) footprint of the antennas has successfully been deconvolved from the recorded data. The shape of the barbed wire in Fig. 7-17 (d) can be easily distinguished from the other two shapes and even contains the three sets of pins, present on the real wire. Note that the dimensions of the objects in the migrated images approach the  $x$ - and  $y$ -dimensions of the real objects. These three examples show that it is possible to extract the shape and dimensions of a buried object out of the migrated data collected by the UWB GPR. The same three data sets were also migrated by the Kirchhoff migration method. The migrated images were less focussed and the oval shape of the antenna footprint was still visible in the migrated image.



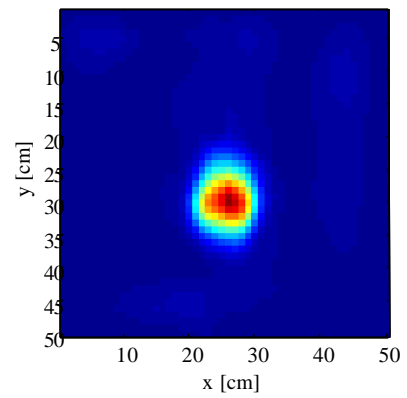
(a)



(b)



(c)



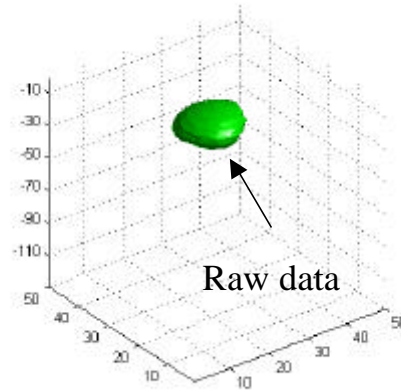
(d)

**Fig. 7-15:** Migration by deconvolution applied on a PMN mine (diameter of 11 cm) buried at 5 cm

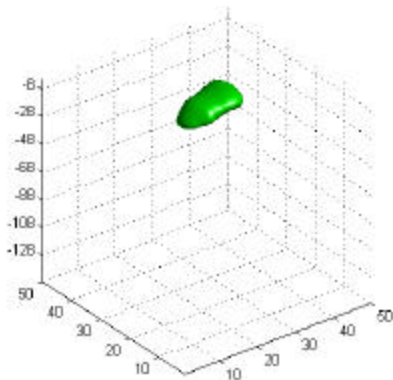
- (a) Photo of PMN mine
- (b) 3D C-scan representation of raw data
- (c) 3D C-scan representation of migrated data
- (d) 2D C-scan representation of migrated data



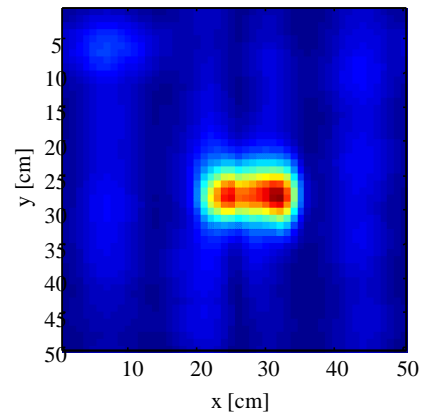
(a)



(b)



(c)



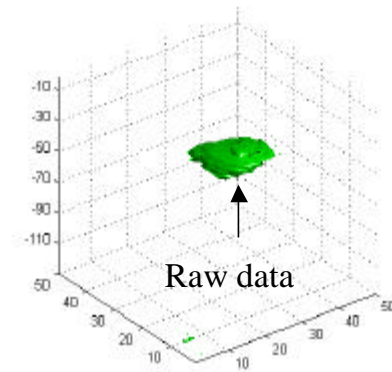
(d)

**Fig. 7-16:** Migration by deconvolution applied on a brick (15\*9\*6cm) buried at 5 cm

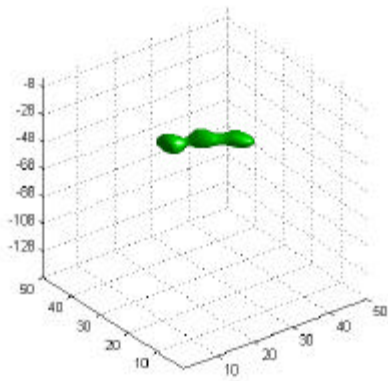
- (a) Photo of the brick
- (b) 3D C-scan representation of raw data
- (c) 3D C-scan representation of migrated data
- (d) 2D C-scan representation of migrated data



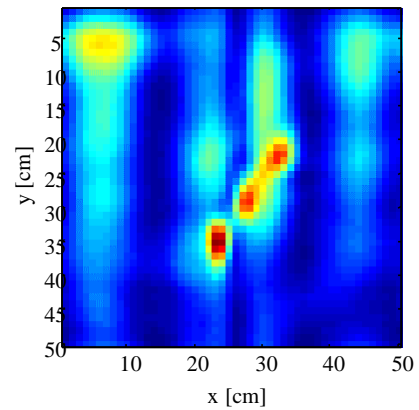
(a)



(b)



(c)



(d)

**Fig. 7-17:** Migration by deconvolution applied on barbed wire (length of 20cm) buried at 5 cm

- (a) Photo of the barbed wire
- (b) 3D C-scan representation of raw data
- (c) 3D C-scan representation of migrated data
- (d) 2D C-scan representation of migrated data

The aim of migration is to focus reflections on objects back into the true physical shape of the object but also into its true position. To illustrate the latter, we show in Fig. 7-18 (a) the raw data on an oblique mine. The mine was buried under an angle of about  $30^\circ$  in dry sand, with the highest point of the mine at a depth of 5 cm. In the raw B-scan at the left, the strongest reflections on the mine are found in the lower right corner of the image, whereas in reality the mine is situated in the middle of the image, indicated by the rectangular box in the image. The explanation for this shift is simple. When the antennas are right above the oblique mine, the mine will have a strong reflection in a direction away from the receiving antenna. For the antennas in the direction perpendicular to the flat top of the mine, the reflections on the mine towards the receiving antenna will be stronger than in the case the antennas are right above the oblique mine, leading to a displacement of the target in the raw data. After migration by deconvolution however, the target is found in its true position, as shown in Fig. 7-18 (b). The migrated image not only shows the object in its true position, but also clearly shows that the object is oblique. Indeed, due to the different backscatter mechanism in the object, the dimensions of the object in the  $z$ -direction can be overestimated, but the position (in time or space) of the first reflection on the object (the specular reflection) will be correct and reliable. Hence the reconstruction of the top contour of buried objects will be correct. Other migration methods, like Kirchhoff migration and Stolt migration were also applied on the same data, but with less good results than the migration by deconvolution method. Fig. 7-18 (c) shows the result after Kirchhoff migration. The migrated image is better than the raw one, but the Kirchhoff migration is not able to bring the target completely back in its actual position.

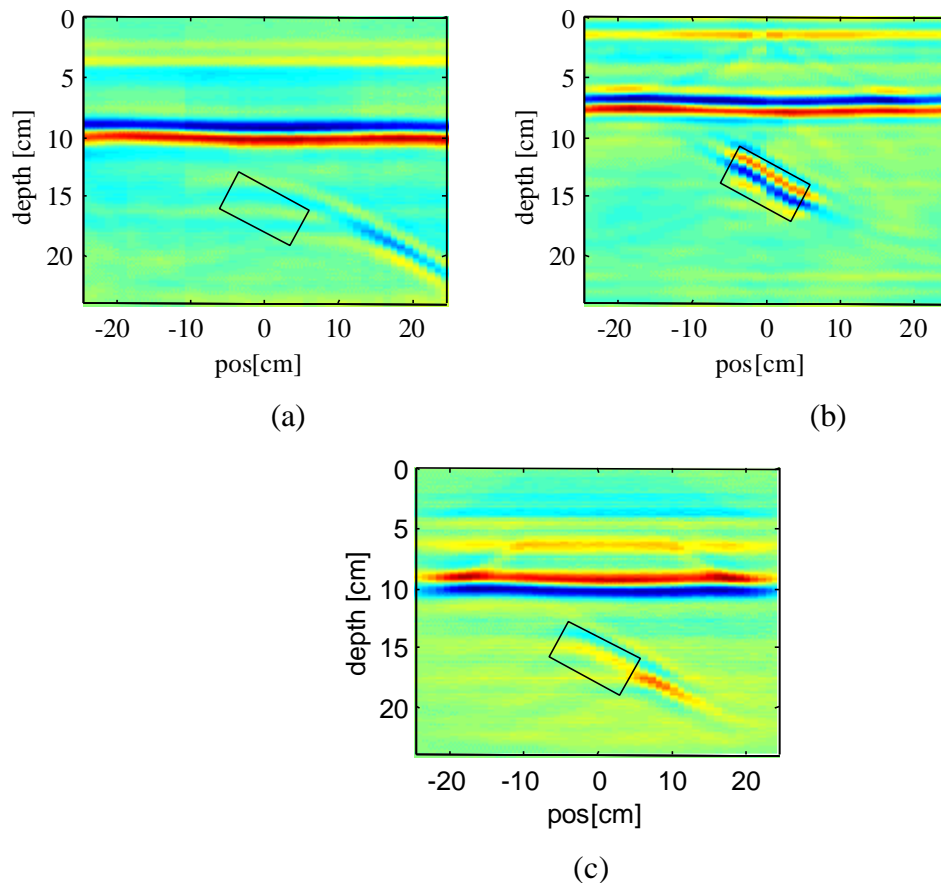


**Fig. 7-18:** Oblique PMN mine under an angle of  $30^\circ$

- (a) Raw data
- (b) After migration by deconvolution
- (c) After Kirchhoff migration

### *Results of outdoor trials*

The previous results are obtained on data that is acquired in the laboratory, where all conditions are well controlled and where the air-ground interface is flat. In reality this is not the case. Ground characteristics like permittivity and attenuation are often not known and have to be estimated. The air-ground interface can be very rough and can introduce additional clutter, which eventually might interfere with the reflections on the target, like presented on Fig. 7-19. Furthermore, the ground is not always homogeneous and it can be expected that the UWB GPR, which yields a high resolution, is sensible to these inhomogeneities.

In this subsection some results of outdoor trials are presented. The trials were held on the test site in Meerdaal, in August 2000. At that moment, the objects were already more than three years in place. After a lot of rain during the summer, the soil was quite wet and it seemed that the attenuation of the soil was too high to get good results on the smallest AP mines. We already discussed this problem, which is partially due to the laboratory UWB GPR. The larger AP mines and mine-like targets gave good results.

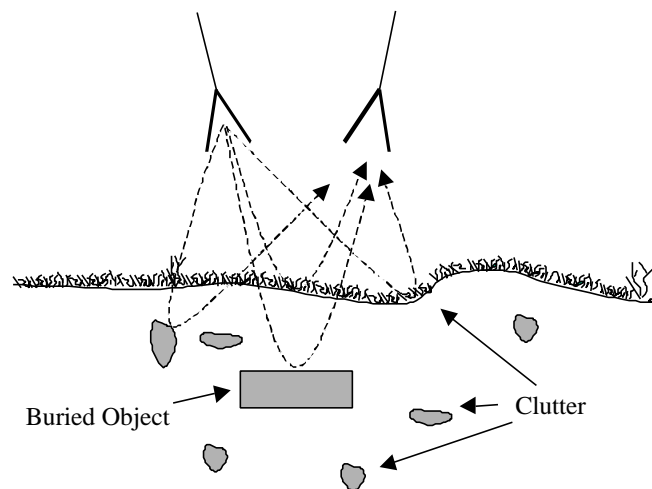


**Fig. 7-19:** Clutter introduced by the rough air-ground interface and inhomogeneities in the ground

The data represented in the next three figures is acquired over an area of 50 cm by 50 cm in steps of 2 cm (which is still small enough to avoid aliasing in the  $x$ - and  $y$ -direction).

Fig. 7-20 shows a 2D representation of a B-scan and a C-scan of a PMN mine, buried in gravel at a depth of 5 cm, before and after migration. In the images of the raw data there is a lot of clutter present and the shape of the mine is not clear. After migration, most of the clutter disappeared and the circular shape and dimensions of the mine becomes correct.

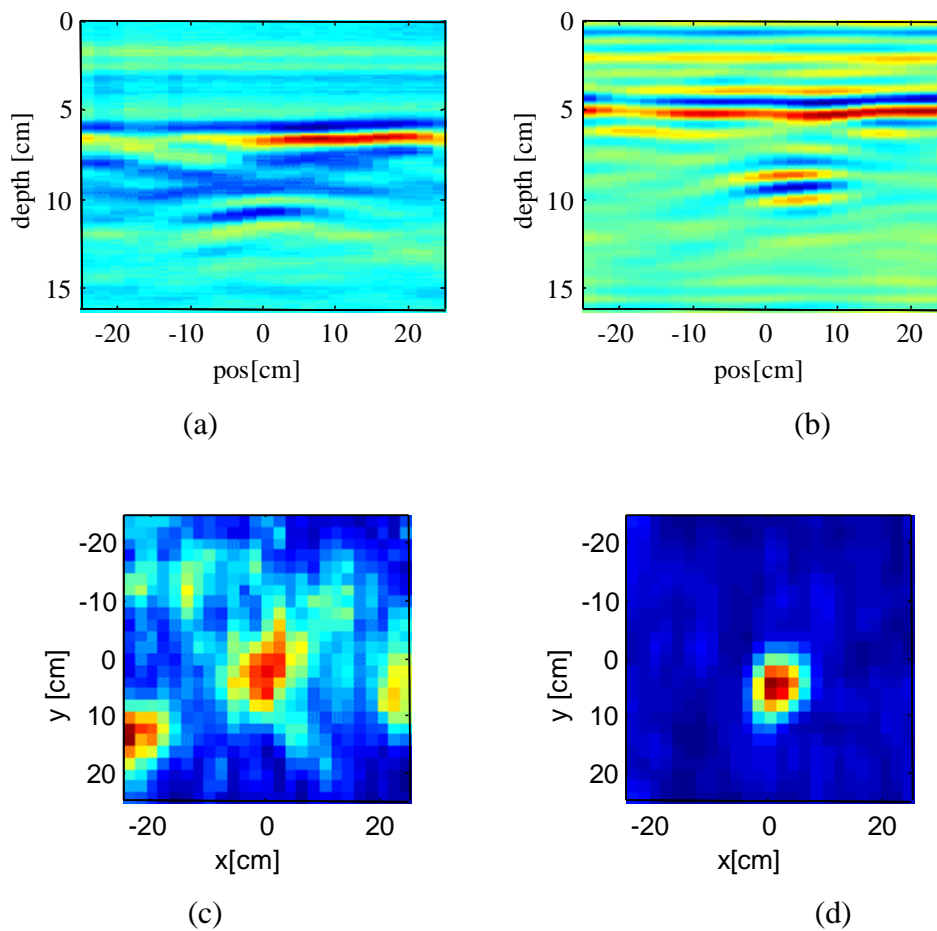


**Fig. 7-20:** PMN mine in gravel at 5 cm of depth

- (a) B-scan of raw data
- (b) B-scan of migrated data
- (c) 2D C-scan representation of raw data
- (d) 2D C-scan representation of migrated data

Fig. 7-21 shows a PMN mine that was laid on the surface of the ground. On the migrated B-scan, the mine is clearly distinguishable from the air-ground interface. The migrated B-scan even shows that the mine is a little oblique. Just like in previous figure, the shape of the target becomes more clear in the 2D C-scan representation after migration.

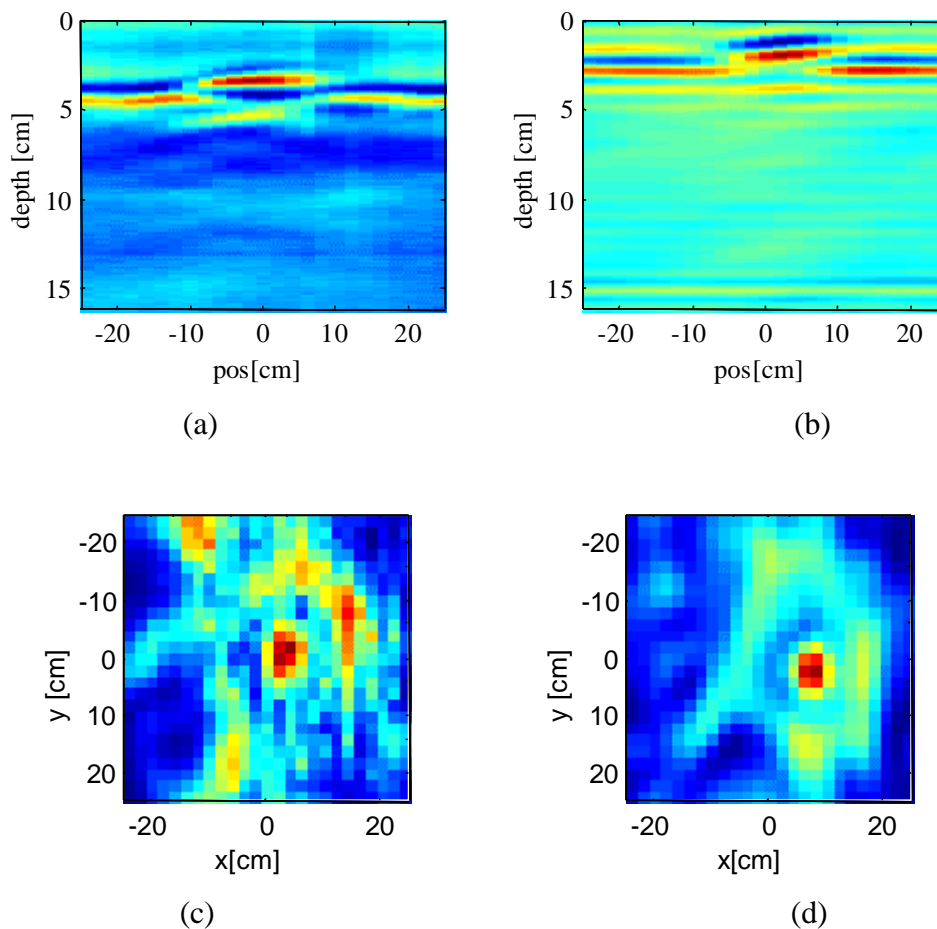


**Fig. 7-21** : PMN mine laid on the surface

- (a) B-scan of raw data
- (b) B-scan of migrated data
- (c) 2D C-scan representation of raw data
- (d) 2D C-scan representation of migrated data

Fig. 7-22 shows the result on an (empty) wine bottle buried in sand at a depth of about 7 cm. During the years the bottle is probably partially filled with sand, which explains the low contrast in the images, even after migration.. The result after migration however is interesting. The 2D C-scan representation of the migrated data reveals that the shape of the object is not round and that the object is oriented from the left to the right in the image and not vertically like one could expect from the 2D C-scan representation of the raw data.

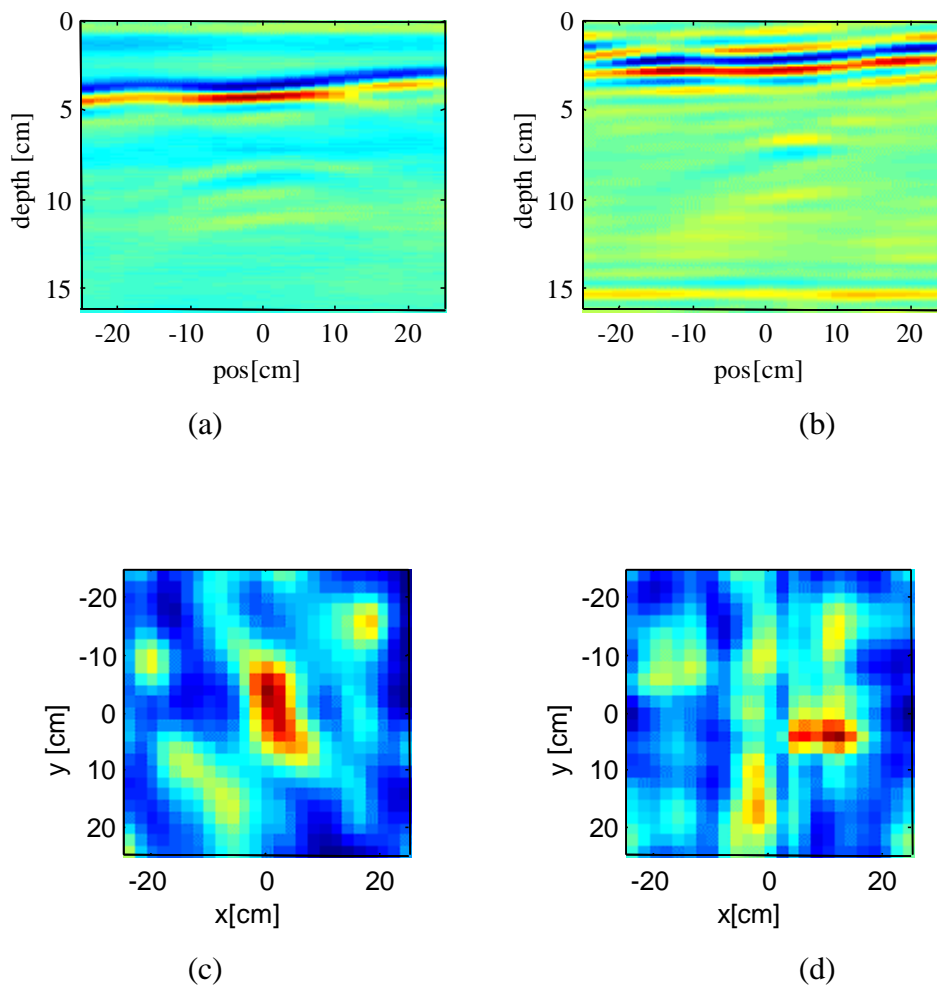


**Fig. 7-22 :** Bottle in sand at a depth of 7 cm

- (a) B-scan of raw data
- (b) B-scan of migrated data
- (c) 2D C-scan representation of raw data
- (d) 2D C-scan representation of migrated data

## 7.5. Summary

Because anti personnel landmines are small objects and often shallowly laid, a large bandwidth is needed for a better depth resolution and a more detailed echo. In a first part of the chapter we presented some UWB signal processing techniques on A-scans, based on Prony-type methods and on time-frequency analysis. Despite the larger bandwidth of the system, UWB signal processing techniques on the A-scans seem to have limited success. This is probably due to the low Q factor of the targets. None of these methods seems to be robust enough to be used for classification purposes. The conclusions drawn out of the study on the UWB signal processing techniques on A-scans are considered as preliminary. However they did not convince us to invest more in this direction.

We therefore oriented our work towards the exploitation of the C-scans, to investigate the possibility of retrieving information on the shape and dimensions of the targets. The raw C-scans recorded by a GPR are often difficult to interpret for an operator. Due to the beam-width of the antennas, a target in the ground is already seen by the GPR system even when it is not exactly under the antennas. As a consequence, the recorded data will be unfocussed. Focussing techniques to reduce the influence of the beamwidth of the antennas are called migration techniques. Most of the existing migration techniques however do not take into account the characteristics of the acquisition system and the ground characteristics. We therefore proposed a migration technique, called the migration by deconvolution. The novelty of the algorithm is that it uses the time domain model of the GPR and hence does take into account the system and ground characteristics. The migration method is simple and fast. We calculate by forward modelling a synthetic point spread function of the UWB GPR. This point spread function is then used to be deconvolved from the recorded data. The method is evaluated on data coming from the UWB GPR and aspects like spatial resolution and the influence of the assumptions are discussed. Results of this migration method on cluttered data, obtained by the UWB GPR system during in- and out-door trials are found to be very good. Not only does the UWB GPR give enough depth resolution to distinguish the reflections on the targets from the air-ground reflections, but it has, after migration of the data, also enough resolution in the lateral

directions to give an idea of the shape and, in favorable circumstances, of the dimensions of the buried object.

## REFERENCES

- [1] L. Van Kempen, H. Sahli, J. Brooks and J. Cornelis, "New results on clutter reduction and parametric estimation for landmine detection using GPR," *Eight International Conference on Ground Penetrating Radar*, Gold Coast, Australia, pp. 872-879, May 2000.
- [2] A. Pizurica, W. Philips, I. Lemahieu and M. Acheroy, "Speckle Noise Reduction in GPR Images," *Proc. of the International Symposium on Pattern Recognition, "In Memoriam Pierre Devijver"*, Brussels, Belgium, pp. 162-165, Feb. 1999.
- [3] Y. Plasman, *Analyse en verwerking van signalen, komende van een ultra-wideband GPR*, Eindwerk, Royal Military Academy, Brussels, Belgium, 1999.
- [4] B. Scheers, Y. Plasman, M. Piette, M. Acheroy and A. Vander Vorst , "Laboratory UWB GPR system for landmine detection," *Eight International Conference on Ground Penetrating Radar*, Gold Coast, Australia, pp. 747-752, May 2000.
- [5] S. Mallat, *A wavelet tour of signal processing*. San Diego: Academic Press, 1998, ch. 1.
- [6] S. R. Cloude, A. Milne, C. Thornhill and G. Crisp, "UWB SAR detection of dielectric targets," *IEE Eurel International Conference on The Detection of Abandoned Land Mines*, Edinburgh, UK, pp. 114-118, Oct. 1996.
- [7] R. Prony, "Essai expérimental et analytique ... ", *L'Ecole Polytechnique*, Paris, vol. 1, no. 2, pp. 24-76, 1795.
- [8] M. L. Van Blaricum and R. Mittra, "Problems and solutions associated with Prony's method for processing transient data," *IEEE Trans. on Antennas Propagat.*, vol. AP-26, no. 1, pp. 174-182, 1978.
- [9] S. M. Kay, *Modern spectral estimation, theory and application*. New Jersey: Prentice-Hall Signal Processing Series, 1988, pp. 217-227.

- [10] M. L. van Blaricum and R. Mittra, "A technique for extracting the poles and residues of a system directly from its transient response," *IEEE Trans. on Antennas Propagat.*, vol. AP-23, no. 6, pp. 777-781, Nov. 1975.
- [11] R. Kumaresan and D. W. Tufts, "Improved spectral resolution III: Efficient realisation," *IEEE proceedings*, vol. 68, no. 10, pp. 1354-1355, Oct. 1980.
- [12] D. W. Tufts and R. Kumaresan, "Estimation of frequencies of multiple sinusoids: Making linear prediction perform like maximum likelihood," *IEEE proceedings*, vol. 70, no. 9, pp. 975-989, Sep. 1982.
- [13] M. A. Rahman and K. B. Yu, "Total least square approach for frequency estimation using linear prediction," *IEEE trans. Acoustic, Speech and Signal Processing*, vol. 35, pp. 1440-1454, Oct. 1987.
- [14] C.-C. Chen and L. Peters, *Design and Development of Enhanced Ground Penetrating Radar Systems for the Detection and Classification of Unexploded Ordnances and Land Mines*, Joint Technical Report 733346-1, 733946-1, 730181-3, the Ohio State University, Ohio, USA, Sep. 1997.
- [15] L. Carin, L. B. Felsen, D. R. Kraj, H. S. Oh, W. C. Lee and S. U. Pillai, "Wave-oriented signal processing of dispersive time-domain scattering data," *IEEE Trans. on Antennas Propagat.*, vol. AP-45, no. 4, pp. 592-600, April 1997.
- [16] L. C. Trintinalia and H. Ling, "Feature extraction from electromagnetic backscattered data using joint time-frequency processing," *Ultra-Wideband, Short-Pulse Electromagnetics 3*. C. E. Baum, L. Carin and A. P. Stone, Eds., New York: Plenum Press, 1997, pp. 305-312.
- [17] B. Scheers, M. Piette and A. Vander Vorst, "The detection of AP mines using UWB GPR," *IEE Second International Conference on The Detection of Abandoned Land Mines*, Edinburgh, UK, pp. 50-54, Oct. 1998.
- [18] Ö. Yilmaz, *Seismic data processing*. Tulsa, USA: Society of Exploration Geophysicists, 1987.
- [19] A. J. Berkhout, "Wave field extrapolation techniques in seismic migration, a tutorial," *Geophysics*, vol. 46, no. 12, pp. 1638-1656, Dec. 1981.
- [20] M. Soumekh, *Synthetic aperture radar signal processing*. New York: John Wiley & sons, 1999.
- [21] Egil Eide, *Radar imaging of small objects closely below the earth surface*, Doctoral thesis, Norwegian University of Science and Technology, Norway, Aug. 2000.

- [22] R. H. Stolt, "Migration by Fourier Transform," *Geophysics*, vol. 43, no. 1, pp. 23-48, Feb. 1978.
- [23] H.C. Andrews and B.R. Hunt, *Digital Image Restoration*. New Jersey: Prentice Hall, 1977.
- [24] J. van der Kruk, C. P. A. Wapenaar and J. T. Fokkema, "Multi-component 3-D imaging of ground penetrating radar data using matrix inversion in the spatial Fourier domain," *Eight International Conference on Ground Penetrating Radar*, Gold Coast, Australia, pp. 508-513, May 2000.



---

## **Chapter 8. Conclusions and future work**

---

### **8.1. Conclusions**

The work reported in this thesis on the use of the ultra-wide band (UWB) GPR as a possible demining sensor was made in the frame of the Belgian HUDEM project. The potential of detecting non-metallic objects makes GPR complementary to a metal detector in the application of AP landmine detection. At the moment, the use of conventional GPR in real demining operations is negligible, mainly due to three drawbacks. The first drawback concerns the antennas used in commercially available GPR systems. In most cases, GPR antennas have a low directivity and therefore perform best when they are in contact with the ground, in order to couple as much energy as possible into the ground. For safety reasons, deminers do not want to use a sensor that is in direct contact with the ground. The second drawback is the limited depth resolution of conventional GPR systems. The range resolution (in this case depth resolution) of a GPR is, just as in any other radar system, directly related to its bandwidth. As anti personnel landmines are often shallowly laid, conventional GPR can have difficulties in discriminating the target echoes from the air-ground interface, especially when the surface is rough. In this case, more depth resolution is needed, which means a larger bandwidth of the system. A third problem with the conventional GPR systems is the inability of discriminating between a mine and a mine-like target. This problem, also related to the frequencies used by the GPR system, has to be solved by using appropriate signal processing. To investigate the feasibility of possible solutions for all of these drawbacks, we have built a relatively simple UWB

GPR systems, using mainly off-the-shelf equipment. The system uses frequencies between 1 and 5 GHz, with a central frequency of 3 GHz. The upper cut-off frequency seems to be a good compromise between the resolution of the system and the attenuation of the higher frequencies in the ground. In accordance with the philosophy of the HUDEM project, the intention of this work is not to produce a ready-to-use mine detector. The work consists in a contribution to UWB GPR in order to help industrial designers in the development of this kind of sensor for mine detection.

In agreement with the above mentioned problems, three main personal contributions have been made in association with this work:

1. the development and testing of small UWB GPR antennas, which can be used off-ground,
2. the modelling of the UWB GPR system in time domain, and
3. the development of a novel migration algorithm, using the time domain model of the system.

As one can see, this work is not limited to only hardware or software aspects of the UWB GPR, but a more overall system approach is followed, starting from the development of some critical hardware parts, over system modelling towards signal processing, integrating the knowledge of the system in the processing part. The latter is probably one of the most original parts of the work.

### **8.1.1. UWB antennas**

The demining application imposes specific requirements to the GPR antennas, the most important of which being the mobility of the antennas and the bandwidth. As minefields have often a very rough surface and can be covered with a lot of vegetation, the antennas have to be mobile. This means that they have to be small, light-weighted and directive, so that they can be used off-ground. The TEM horn seemed to be a good candidate to meet these design goals. In a first step an air-filled TEM horn was studied and developed. It is shown that the wire model is an accurate

model for the design of such an antenna. The wire model is not too complicated to implement and it permits to simulate accurately the peak-to-peak antenna pattern as well as the surge impedance. In order to reduce the physical size of the antenna and to improve the directivity, the antenna was filled with a dielectric. Due to the lack of a good model, the design was based on the air-filled antenna, assuming that the antenna guides a quasi-TEM wave. Time domain reflectometry measurements of the surge impedance showed a slight but acceptable difference with the theory. Antenna measurements revealed that the dielectric-filled antenna is indeed more directive compared to an air-filled antenna of the same dimensions and that the frequency range moved towards the lower frequencies. The antenna plates were replaced by a set of wires, which makes them suitable for operating in combination with a metal detector. An ultra-wideband balun was also integrated in the antenna plates. The dielectric-filled TEM horns are capable of radiating and receiving very fast transient pulses, without too much ringing, which is of course important for this application. The cleaner the pulse, the cleaner the backscattered signal, and the more easy it will be to post-process and interpret the data.

### **8.1.2. Time domain modelling of the GPR**

A second main contribution was made in the domain of system modelling. Normally, the performances of radar systems are characterised in the frequency domain. In this work we described the whole system, *i.e.* GPR system, ground and target, in the time domain by considering it as a cascade of linear responses, resulting in a *time domain GPR range equation*. The time domain GPR range equation allows us to calculate the received voltage as a function of time at the receiver in terms of the radar, ground and target characteristics. The time domain model is used to optimise the offset angle for the GPR antennas. The study revealed that the optimal offset angle for the antennas is the one that focuses the antennas on the target. Furthermore, the range performance of the UWB GPR system is calculated by the time domain GPR range equation, for a given target in a given soil. It was shown that the moisture content of the soil limits drastically the range performance of the UWB system.

A key element in the modelling of the radar is the description of the antennas in the time domain by means of the normalised IR. This explains why a whole chapter was dedicated to this topic. In that chapter we showed how the normalised IR describes in a compact way the time domain antenna characteristics, which are sometimes difficult to see in classical antenna parameters. The success of the normalised IR is that it includes all frequency dependent characteristics. This gives two important advantages. First, the time-domain antenna equations become very simple and accurate. Second, the normalised IR permits a comparison between different variants of time domain antennas. Due to the finite but non-zero size of the antenna, the distance from an observation point to the antenna becomes ambiguous for points close to the antenna. Therefore we introduced an apparent point in the antenna, called the virtual source, which can be seen as the origin of the radiated impulse TEM wave. The knowledge of the position of the virtual source is important when the antenna equations are used near the antennas or for the measurement of the normalised IR of the antennas. The normalised IR on boresight is easy to measure, using two identical antennas and a vector network analyser. We also showed that, within the 3dB opening angle of the antenna, the normalised IR off-boresight can be derived from the normalised IR on boresight, using the p-t-p antenna pattern. This means that within the 3dB opening angle an antenna is totally characterised in the time domain by its normalised IR on boresight and its p-t-p pattern.

Another important term in the time domain radar range equation, besides the IR of the antennas, is the IR of the lossy ground. In this work we proposed an analytical expression of the impulse response, modelling the propagation in the ground. The expression of the impulse response is calculated from the theoretical frequency response function of the lossy ground and takes into account the attenuation and the dispersive behaviour of the ground.

The targets in the ground are also characterised by an IR. In general we can say that the dimensions of the targets are of the same order of magnitude as the wavelengths in the ground used by the GPR. This means that we are primarily working in the resonance region of the scattering, leading to scattering centres that appear later in time than the reflection on the back of the target.

As a whole, the time domain modelling was found to be a powerful and accurate tool for describing and studying a time domain system and this type of modelling is recommended to all those who work with time domain systems.

### **8.1.3. Migration**

A last main contribution was made in the domain of the 3D signal processing. Most of the existing migration techniques do not take into account the characteristics of the acquisition system and the ground characteristics. As we dispose of a good time domain description of our UWB GPR, we proposed a novel migration method that integrates the time domain model of the UWB GPR in the migration scheme. We calculate by forward modelling a synthetic 3D point spread function of the UWB GPR, *i.e.* a synthetic C-scan of a small point scatterer. This 3D point spread function, containing system characteristics like the waveform of the excitation source, the combined antenna footprint and the IR of the antennas, is then used to deconvolve the recorded data. Results of this migration method on real data obtained by the UWB GPR system show that the migration method is able to reconstruct the top contour of small targets like AP mines, in some cases even with the correct dimensions. The method is also capable of migrating oblique targets into their true position. The migration scheme is not computational intensive and can easily be implemented in real time.

## **8.2. Conclusions on the use of a UWB GPR as a mine detector**

From the experience we have obtained by working with the UWB GPR for mine detection, we learned that the difficulty of detecting small objects in an inhomogeneous background is often underestimated. One should not forget that, in contradiction to many other imaging techniques, the number of measuring points with a GPR is limited. One can only measure by moving the antennas in a half-space above the target. Furthermore, the subsurface that is to be imaged can contain a lot of clutter

and the air-ground interface can be very rough, which makes the interpretation of the images difficult. Therefore, the UWB GPR will most likely **never be used as a stand-alone mine detector**, but always in combination with other sensors.

In this research the advantages as well as the shortcomings of the UWB GPR as a mine detector are addressed. As a summary we can say that, as expected, the UWB GPR is capable of detecting shallow buried mines and even mines that are laid on the surface. The tests also confirmed that when mines are buried deeper and the soil has a high moisture content, the detection becomes almost impossible. This means that in practice the UWB GPR can only be used as **a detector for shallow buried objects**. Despite the large bandwidth of the system, signal-processing techniques on A-scans have limited success. None of these methods seems to be robust enough to be used for classification purposes. The by the author **recommended way of using the UWB GPR is to record C-scans**. After migration, the buried objects are replaced into their true positions and the 3D images have enough resolution for extracting the shape of the object. If not too much noise and clutter is present in the recorded data, it is even possible to retrieve the exact dimensions of the buried object. This additional information on location, shape and dimensions of the target will drastically reduce the number of false alarms and thereby speed up the mine clearance.

### **8.3. Future work**

The way towards a reliable, robust, cheap and field usable hand-held version of an UWB GPR is long and there is still a lot of research and development to do. In this respect the topics of possible future work are inexhaustible. In this section we limit us to some topics which are considered by the author as not fully finished in his work or in a logic continuation of his work.

A first topic of future work resides in the field of antennas. Although the TEM horn antennas that are developed in the scope of this work meet almost all of the design goals, it is still possible to enhance the TEM horn antennas (*e.g.* resistive loading in combination with the dielectric filling) or to explore other types of antennas. A

promising candidate, which currently gains in interest for the stepped frequency ground penetrating radar, is the Vivaldi antenna. The Vivaldi antenna is light-weighted and small, has a very large bandwidth and can also be used off-ground. The question here is how the antennas will perform in a time domain system. Other interesting types of antennas are antennas with circular polarisation. These antennas would permit full-polarised measurements without additional effort and loss of time in the measurement process. Another challenge is the integration of GPR antennas in the search coil of a metal detector (MD). The integration contains two difficulties. First, the metal in the antenna plates may not disturb the good functioning of the MD, but more difficult, the search coil of the MD may not introduce additional ringing in the GPR measurements.

A second interesting research topic lies in the domain of signal processing. For the moment the migration by deconvolution uses the Wiener filter to deconvolve the point spread function from the recorded data. The Wiener filter is an optimum filter under certain assumptions, which are not necessarily fulfilled in our case. Further there is in this method the problem of estimating the spectral densities of the noise and the original image. It is possible that there exist better techniques to perform the deconvolution in the migration scheme.

Related to the signal processing is the presentation of the processed 3D data. Until now only a few researchers have concentrated on this topic, but a clear and simple man-machine interface is difficult to build and a lot of work can still be done in this domain.

The last topic we propose is only relevant in case the UWB GPR should be integrated in a hand-held system. In Section 8.2 we recommend to record C-scans, which will then be processed before showing to a human operator for interpretation. For the processing of the data, it is necessary that the exact position of each recorded A-scan is known. This means there is a need for a precise, light-weighted and cheap positioning system that has to be integrated with the UWB GPR and the other sensors. The positioning system must not only provide the exact position of the search head, but also its orientation.



---

# **Appendix A. Measurement of short pulse response and frequency response function of non-canonical 3D objects**

---

## **A.1. Measurement set-up**

In order to study experimentally the transient backscattering of 3D objects, a Time Domain Scattering Range (TDSR) has been developed at the RMA [1]. The system consists of the following parts (Fig. 1). On the transmitting side, a 2 meter long monocone antenna on a square ground plane (3 m x 3 m) is coaxially fed by a fast step-function generator. On the receiving side, a broadband electric field sensor, which is connected to a 20 GHz digitising oscilloscope through a set of UWB low noise amplifiers, detects the transient wave. The 3D Device Under Test (DUT) is put on the ground plane and is illuminated by a transient spherical wave, radiated between the monocone and the ground plane. The backscattering on the DUT is measured by the broadband electric field sensor. Because the long monocone antenna radiates a step function and because the electric field sensor is a time derivative sensor, its output yields in fact the impulse response of the device under test.

Three solid state generators are available in the laboratory to feed the antenna. The first two generators generate a repetitive step function (50V/350ps, 10V/45ps) with a high waveform purity. The third generator yields a 2kV/200ps impulse waveform. The fastest generator (10V/45ps) confers to the TDSR a sub-centimetre radial

resolution on the target, which makes it possible to resolve the different scattering centres of the target and to quantify their relative amplitudes. The oscilloscope is coupled to a personal computer for collecting and analysing the data.

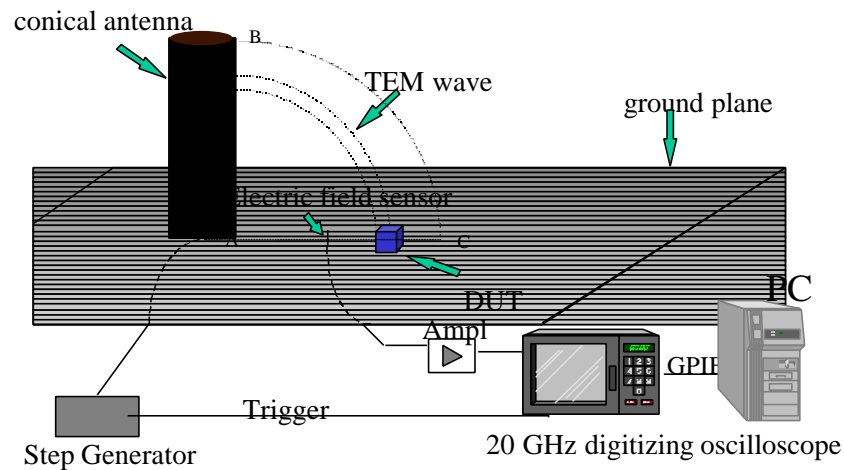


**Fig. 1:** The Time Domain Scattering Range at the RMA

## A.2. Measurement of the FRF of 3D objects by dual channel analysis

The main objective in dual channel systems analysis is to measure input-output relationships of linear systems. In our case the 3D object in free space will be considered as a linear system. Two fundamental functions of this analysis, the Frequency Response Function (FRF) and the Coherence Function, are dealt with in some detail.

Every time-invariant, stable and linear system is completely described in the time domain by its Impulse Response (IR)  $h(t)$ , which mathematically relates the input  $x(t)$  and the output  $y(t)$  of the system according to the convolution integral. In the frequency domain this relationship is given by

$$Y(f) = H(f)X(f) \quad (\text{A. 1})$$

where  $X(f)$  and  $Y(f)$  are the Fourier transform of input  $x(t)$  and the output  $y(t)$ .  $H(f)$  is called the Frequency Response Function.  $H(f)$  and  $h(t)$  are related by the Fourier transform and contain the same information.

Theoretically, the FRF  $H(f)$  can be calculated using (A.1) by dividing  $Y(f)$  by  $X(f)$ . In practice this is impossible because (A.1) degrades very fast in the presence of noise. The best way to handle the noise problem is to perform multiple measurements of input and output and estimate the FRF in the least squares sense to obtain the best linear fit in the frequency band covered by the input signal  $x(t)$ . There exist different FRF estimators [2]. In our application the power of the output signal is far less than the power in the input signal, so the S/N ratio of the output signal will be very low. In this case the best estimator is

$$\tilde{H}_1 = \frac{\sum_{k=1}^K YX^*}{\sum_{k=1}^K XX^*} \quad (\text{A. 2})$$

where  $*$  indicates the complex conjugation and  $K$  the number of measurements of input and output signal.

Equation (A.2) will minimise uncorrelated measurement noise at the output in a least square sense.

For  $K \rightarrow \infty$  equation (A.2) becomes

$$\tilde{H}_1 = \frac{S_{yx}}{S_{xx}} \quad (\text{A. 3})$$

with  $S_{xx}$  and  $S_{yx}$  the autospectrum and the cross-spectrum of the input and output signals.

Another useful Dual Channel function is the so-called Coherence Function  $g^2(f)$ , given by

$$g^2(f) = \frac{|S_{xy}|^2}{S_{xx}S_{yy}} \quad \text{with } 0 < g^2(f) < 1 \quad (\text{A. 4})$$

For a given frequency, a low Coherence ( $< 0.8$ ) will indicate that one or more of the following conditions exist:

- extraneous noise is present in the measurement at that frequency
- the system is not linear
- there are other inputs, besides  $x(t)$ , influencing the output.

Hence  $g^2(f)$  will give an idea of the quality of the measurements and of the assumptions that are made about the system. A coherence  $g^2(f) > 0.8$  is needed for an accurate interpretation of the measured data.

The measurement set-up for the dual channel analysis is represented in Fig. 2.

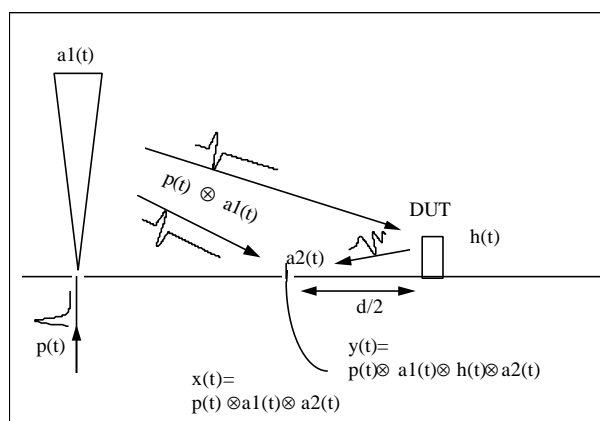


**Fig. 2:** Measurement set-up for dual channel analysis

Assume the 3D target as a linear system with Impulse Response  $h(t)$ . Let  $a_1(t)$  be the IR of the transmitting antenna,  $a_2(t)$  the IR of the electric field sensor, and  $p(t)$  the signal generated by the source. Not taking into account the spreading loss in the free space, one can say that

$$\begin{aligned} \frac{Y(f)}{X(f)} &= \frac{P(f)A_1(f)H(f)A_2(f)e^{-jw\frac{d}{c}}}{P(f)A_1(f)A_2(f)} \\ &= H(f)e^{-jw\frac{d}{c}} \end{aligned} \quad (\text{A. 5})$$

with  $X(f)$  the Fourier transform of the pulse sent by the monocone and captured by the electric field sensor.  $Y(f)$  is the Fourier transform of the signal backscattered by the target, and captured by the electric field sensor, taking into account the delay caused by the travelling time of the signal.  $d$  is twice the distance between the target and the electric field sensor. By measuring  $K$  times the input  $x(t)$  and the output  $y(t)$ , (A.2) yields an estimation of the FRF  $\tilde{H}(f) e^{-jw\frac{d}{c}}$  of the 3D object. The delay  $e^{-jw\frac{d}{c}}$ , which only influences the phase, is a function of the travelling time and can be calculated.

The advantage of this test set-up is that one can measure the input and the output signals, separated in time by  $\frac{d}{c}$ , with the same sensor. This means that the measured FRF of the 3D object does not depend on the IR  $a_2(t)$  of the electric field sensor. The excitation signal  $p(t) \otimes a_1(t)$  is of great importance because the measured FRF is only meaningful at the frequencies excited by this input signal. Since the noise spectral density can be regarded as more or less uniform over the frequency range of interest, the signal to noise ratio will become too small for frequencies with too little power and, as a consequence, the coherence function will be less than 0.8. Fig. 3. shows the coherence function of a typically dual channel measurement performed with the TDSR when the fastest generator (10V/45ps) is used. At frequencies less than 800 MHz or above 13 GHz the coherence function is less than 0.8, meaning that

the TDSR at the RMA can only be used to measure the FRF of 3D objects in that frequency range.

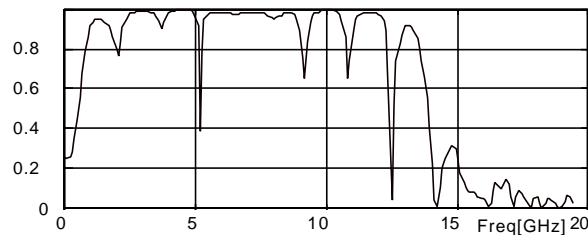


**Fig. 3:** Coherence function

### A.3. Measurement results on Teflon cylinders and AP mines in free space

In a first step, tests are performed on three Teflon cylinders with dimensions comparable to a typical AP mine. The dimensions (in mm) of the cylinders are given in Fig. 4.

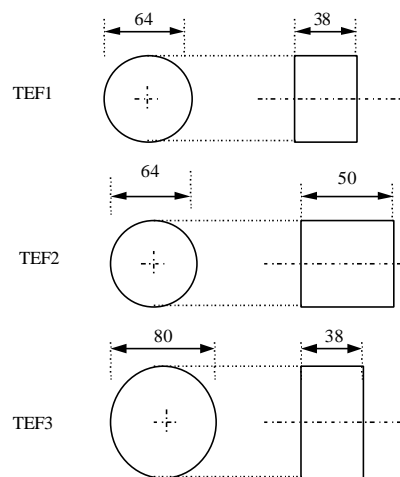


**Fig. 4:** The three Teflon cylinders

The cylinders are positioned on the ground plane such that the top of the cylinder is oriented towards the transmitting antenna (their surface is perpendicular to the propagation direction of the incoming wave). Fig. 5, Fig. 6 and Fig. 7 show for each

of these cylinders the backscattered signal as a function of time (upper plot) and the magnitude of the FRF as a function of frequency (lower plot). Note that the magnitude of the FRF is not represented in dB's!

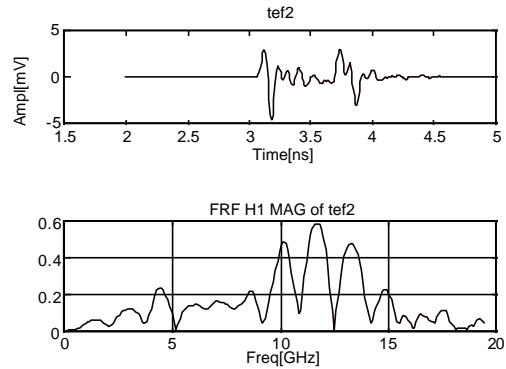
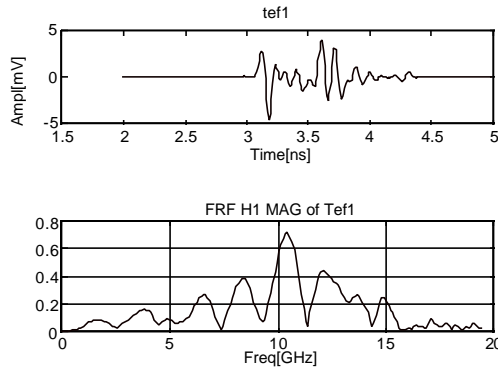


**Fig. 5:** Short pulse response and FRF of Tef 1

**Fig. 6:** Short pulse response and FRF of Tef 2

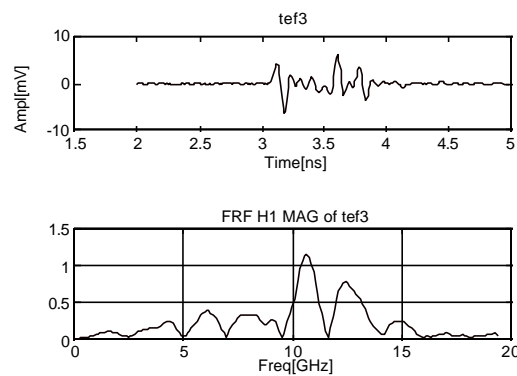


**Fig. 7:** Short pulse response and FRF of Tef 3

In a second step, tests were performed on two types of AP mines. The first type is the Belgian PRB M35 mine, which is a small AP mine. The dimensions of the PRB M35 are the same as the dimensions of TEF1 ( $\varnothing$  64mm, height 38mm). The TNT of the mine is replaced by a silicone with electrical parameters comparable to those of TNT. The second type of AP mine is a PMN mine ( $\varnothing$  115mm, height 55mm). Fig. 8 and Fig. 9 show for each of these AP mines the backscattered signal as a function of time (upper plot) and the magnitude of the FRF as a function of frequency (lower plot).

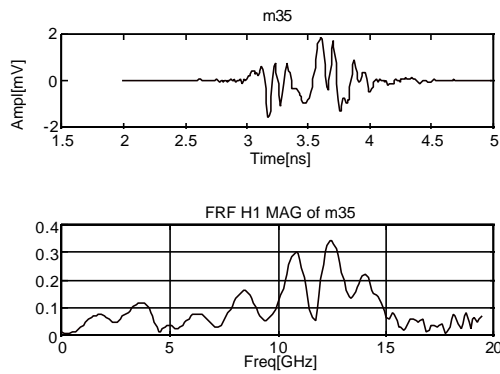


**Fig. 8:** Short pulse response and FRF of PRB M35

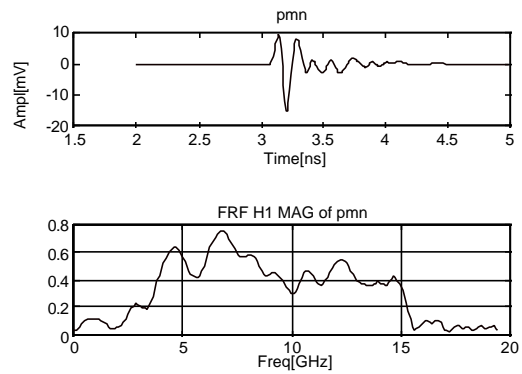


**Fig. 9:** Short pulse response and FRF of PMN

## A.4. Discussion

Tests have been performed on Teflon cylinders and on AP mines in free space. In the backscattered signal of the objects, the scattering centres or the different backscattering mechanisms clearly appear. On the other hand, looking at the magnitude of the FRFs of the different objects, the peaks in the FRF are not sharp. This indicates that the resonances in the late time response of the objects are damped instantaneously in free space.

## REFERENCES

- [1] M. Piette, *Banc de mesure en régime transitoire de la signature radar d'objets tridimensionnels*, Doctoral thesis, Université catholique de Louvain and Royal Military Academy, Belgium, Oct. 1995.
- [2] A. Preumont, *Random Vibration and Spectral Analysis*. Brussels: Kluwer Academic, 1999, pp. 135-141.

---

## Appendix B. Kirchhoff and Stolt migration

---

### B.1. Kirchhoff migration

The Kirchhoff migration technique finds its origin in the field of seismics. Although the Kirchhoff migration has been developed for the backpropagation of scalar pressure wavefields, it is often applied (with success) to electromagnetic waves. The basic idea in the Kirchhoff-migration is to back-propagate the scalar wavefront, measured in the data-plane (as defined in the exploding source model), to the object plane at  $t = 0$ , using an integral solution method to the scalar wave equation.

Suppose a scalar field  $b(\vec{r}, t)$ , satisfying the scalar 3D wave equation

$$\nabla^2 b(\vec{r}, t) - \mathbf{m} \frac{\partial^2}{\partial t^2} b(\vec{r}, t) = 0 \quad (\mathbf{B. 1})$$

The configuration and the co-ordinate system are shown in Fig. 1. The array of receivers recording the data  $b(\vec{r}', t')$  in the data plane at the air-ground interface (denoted here as  $S'$ ), will be replaced by an array of secondary sources, each driven in reverse time by the recorded data. In the configuration:

$\vec{r}$  is the co-ordinate of the observer,

$t$  the real time of the observer,

$\bar{r}'$  the co-ordinate of the sources,

$t'$  the real time of the sources,

$S'$  the data plane, containing the secondary sources

$b(\bar{r}, t)$  the scalar wavefield

$b(\bar{r}', t')$  represents the measurements of this scalar field in the data plane.

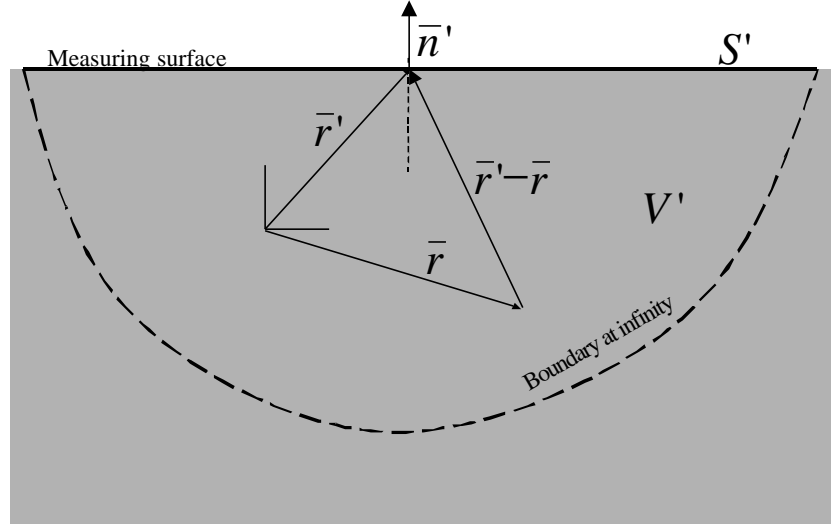


**Fig. 1:** Configuration and co-ordinate system for the Kirchhoff migration

In seismics, the air-ground interface is considered as a perfect reflector, hence the problem has the following boundary conditions:

$$b(\bar{r}, t)|_{S'} = 0$$

$$b(\bar{r}, t) \rightarrow 0 \quad \text{for } |\bar{r}| \rightarrow \infty \quad (\mathbf{B. 2})$$

The backwards Green's function  $G(\bar{r}, t | \bar{r}', t')$  for the scalar wave equation in half space medium without losses is given by

$$G = g(x, y, z, t | x', y', z', t') - g(x, y, z, t | x', y', -z', t') \quad (\mathbf{B. 3})$$

with

$$g(\bar{r}, t | \bar{r}', t') = \frac{\mathbf{d}(t - t' + |\bar{r} - \bar{r}'|/v)}{|\bar{r} - \bar{r}'|} \quad (\text{B. 4})$$

the Green's function for an imploding point source in a homogeneous medium.  $v = 1/\sqrt{\mathbf{m}\mathbf{e}}$  is the propagation velocity of the medium.

The field solution  $b(\bar{r}, t)$  is given by the integral Kirchhoff [1], derived from Green's theorem as

$$b(\bar{r}, t) = -\frac{1}{4\mathbf{p}} \int dt' \oint_{S'} b(\bar{r}', t') \frac{\partial G}{\partial n'} - G \frac{\partial}{\partial n'} b(\bar{r}', t') dS' \quad (\text{B. 5})$$

where  $n'$  is the vector normal to the surface  $S'$  and pointing outwards. The term  $\frac{\partial G}{\partial n'}$  in (B.5) can be written as

$$\frac{\partial G}{\partial n'} = 2 \frac{\partial g}{\partial n'} \quad (\text{B. 6})$$

Introducing (B.6) together with (B.3) into (B.5), the latter equation can be simplified to

$$b(\bar{r}, t) = -\frac{2}{4\mathbf{p}} \int dt' \oint_{S'} b(\bar{r}', t') \frac{\partial g}{\partial n'} dS' \quad (\text{B. 7})$$

The partial derivative of the Green's function  $g(\bar{r}, t | \bar{r}', t')$  equals

$$\begin{aligned}\frac{\partial g}{\partial n'} &= \frac{\partial g}{\partial z'} = \frac{1}{|\bar{r} - \bar{r}'|} \frac{\partial \mathbf{d}(t - t' + |\bar{r} - \bar{r}'|/v)}{\partial z'} + O\left(\frac{1}{|\bar{r} - \bar{r}'|^2}\right) \\ &= \frac{-1}{v|\bar{r} - \bar{r}'|} \frac{\partial \mathbf{d}(t - t' + |\bar{r} - \bar{r}'|/v)}{\partial t'} \frac{d|\bar{r} - \bar{r}'|}{dz'} + O\left(\frac{1}{|\bar{r} - \bar{r}'|^2}\right)\end{aligned}\tag{B. 8}$$

If necessary, the second order term in  $|\bar{r} - \bar{r}'|^{-2}$  can be taken into account [2], but in the far field the second order term is neglected.

The term  $\frac{d|\bar{r} - \bar{r}'|}{dz'}$  can be transformed in

$$\frac{d|\bar{r} - \bar{r}'|}{dz'} = \frac{(z - z')}{|\bar{r} - \bar{r}'|} = \cos(\mathbf{q})\tag{B. 9}$$

with the angle  $\mathbf{q}$  as defined in Fig. 1.

Substituting (B.8) and (B.9) in equation (B.7), the field solution  $b(\bar{r}, t)$  becomes

$$\begin{aligned}b(\bar{r}, t) &= \frac{2}{4\mathbf{p}v} \int dt' \iint_{S'} b(\bar{r}', t') \frac{\partial \mathbf{d}(t - t' + |\bar{r} - \bar{r}'|/v)}{\partial t'} \frac{\cos(\mathbf{q})}{|\bar{r} - \bar{r}'|} dS' \\ &= \frac{2}{4\mathbf{p}v} \iint_{S'} \frac{\partial b(\bar{r}', t + |\bar{r} - \bar{r}'|/v)}{\partial t'} \frac{\cos(\mathbf{q})}{|\bar{r} - \bar{r}'|} dS'\end{aligned}\tag{B. 10}$$

Finally, the migrated image is found from the wavefield  $b(\bar{r}, t)$  in (B.10) at time  $t = 0$ , hence

$$\hat{O}(x, y, z) = \frac{2}{4\mathbf{p}v} \iint_{S'} \dot{b}(x', y', z'=0, |\bar{r} - \bar{r}'|/v) \frac{\cos(\mathbf{q})}{|\bar{r} - \bar{r}'|} dS'\tag{B. 11}$$

## B.2. Stolt migration

The method is, just like the Kirchhoff migration, based on the back-propagation of the scalar wave equation and can thereby best be explained using the exploding source model. Important here is that only upcoming waves are assumed. Note also that the propagation velocity used in the exploding source model is half the value of the true medium velocity.

Consider a scalar field component  $b(x, y, z, t)$  resulting from an exploding source. This component has to satisfy the scalar wave equation

$$\nabla^2 b(x, y, z, t) - \mathbf{m} \frac{\partial^2}{\partial t^2} b(x, y, z, t) = 0 \quad (\text{B. 12})$$

Applying a Fourier transformation on (B.12), with respect to the  $x$ ,  $y$  and the  $t$  coordinate, results in

$$\frac{\partial^2}{\partial z^2} B(k_x, k_y, z, \mathbf{w}) = \left(-\frac{\mathbf{w}^2}{v^2} + k_x^2 + k_y^2\right) B(k_x, k_y, z, \mathbf{w}) \quad (\text{B. 13})$$

The Fourier transformation along the  $x$  and  $y$  co-ordinates only makes sense if the propagation velocity does not vary in the  $x$  and  $y$  directions. In the Fourier transformation, the following sign convention is used. For the forward transformation, the sign of the argument in the exponential is negative if the variable is time and positive if the variable is space. So the 3 dimensional forward Fourier transformation of  $b(x, y, z, t)$  is defined as

$$B(k_x, k_y, z, \mathbf{w}) = \iiint b(x, y, z, t) e^{ik_x x + ik_y y - i\mathbf{w}t} dx dy dt \quad (\text{B. 14})$$

Defining a wavenumber  $k_z$  as

$$k_z = \text{sgn}(\mathbf{w}) \sqrt{\frac{\mathbf{w}^2}{v^2} - k_x^2 - k_y^2} \quad (\text{B. 15})$$

and substituting (B.15) in (B.13), equation (B.13) has as general solution

$$B(k_x, k_y, z, \mathbf{w}) = Ce^{ik_z z} + De^{-ik_z z} \quad (\text{B. 16})$$

The constants C and D in (B.16) are found using the following two boundary conditions:

- assuming only upward coming waves, the first constant becomes  $C = 0$ .
- for  $z=0$ , the Fourier transformation of the measured data is found, hence  $D = B(k_x, k_y, 0, \mathbf{w})$ .

Finally (B.16) becomes

$$B(k_x, k_y, z, \mathbf{w}) = B(k_x, k_y, 0, \mathbf{w})e^{-ik_z z} \quad (\text{B. 17})$$

Equation (B.17) represents the Fourier transform of the wavefront at depth  $z$ . The migrated image will be the inverse Fourier transform of (B.17) at time  $t = 0$ :

$$\hat{O}(x, y, z) = b(x, y, z, 0) = \iiint B(k_x, k_y, 0, \mathbf{w}) e^{-i(k_x x + k_y y + k_z z)} dk_x dk_y d\mathbf{w} \quad (\text{B. 18})$$

Equation (B.18) is the general representation of the f-k migration, also called the *Phase Shift Migration*. The method can deal with variations of velocity in function of depth. In the special case where  $v(z) = v = cst$ , equation (B.18) can be further developed by a change of variables from  $d\mathbf{w}$  to  $dk_z$ . According to the definition of  $k_z$  in (B.15)

$$\mathbf{w} = -k_z v \sqrt{1 + \frac{k_x^2 + k_y^2}{k_z^2}} \quad (\text{B. 19})$$

hence  $d\mathbf{w}$  can be written as:

$$d\mathbf{w} = \frac{k_z v^2}{\mathbf{w}} dk_z \quad (\text{B. 20})$$

Replacing  $d\mathbf{w}$  in (B.18) by the expression in (B.20), the migrated image becomes

$$\hat{O}(x, y, z) = v^2 \iiint \frac{k_z}{\mathbf{w}} B(k_x, k_y, 0, \mathbf{w}) e^{-i(k_x x + k_y y + k_z z)} dk_x dk_y dk_z \quad (\text{B. 21})$$

The advantage of (B.21) over (B.18) is that (B.21) can be calculated using an inverse 3D Fourier transformation of the measured data  $B(k_x, k_y, 0, \mathbf{w})$ , scaled by  $\frac{v^2 k_z}{\mathbf{w}}$ , *i.e.* the Jacobian of the transformation from  $\mathbf{w}$  to  $k_z$ . This means a serious reduction of the number of floating point operations for the migration and a gain in calculation time.

Although the method seems to be simple, the implementation of the Stolt's migration algorithm can be tricky. The Fourier transformation with respect to the  $x$ ,  $y$  and the  $t$  co-ordinate of the measured data provides equally spaced samples of  $B(k_x, k_y, 0, \mathbf{w})$  on a rectangular grid in the  $(k_x, k_y, \mathbf{w})$  domain. This data is mapped into the  $(k_x, k_y, k_z)$  domain by the change of variables given by (B.19), where  $k_z$  is a non-linear function of  $k_x$ ,  $k_y$  and  $\mathbf{w}$ , resulting in an unevenly spaced data set. This mapping is graphically represented in Fig. 2. For simplicity we consider only the 2D case with the co-ordinates  $x$  and  $t$ . Fig. 2 shows the mapping of the evenly spaced points in the  $(k_x, \mathbf{w})$  domain, identified by black squares, into the unevenly spaced points in the  $(k_x, k_z)$  domain, identified by circles. The unevenly spaced data set in the  $(k_x, k_z)$  domain represents a problem for the inverse Fourier transformation.



## REFERENCES

- [1] A. J. Berkhout, "Wave field extrapolation techniques in seismic migration, a tutorial," *Geophysics*, vol. 46, no. 12, pp. 1638-1656, Dec. 1981.
- [2] Ö. Yilmaz, *Seismic data processing*. Tulsa, USA: Society of Exploration Geophysicists, 1987, ch. 4.
- [3] M. Soumekh, *Synthetic aperture radar signal processing*. New York: John Wiley & sons, 1999, ch. 4.